

Stochastic thermodynamics of information processing: bipartite systems with feedback, signal inference and information storage

Von der Fakultät Mathematik und Physik der Universität Stuttgart
zur Erlangung der Würde eines Doktors der
Naturwissenschaften (Dr. rer. nat.) genehmigte Abhandlung

vorgelegt von

DAVID MICHAEL HARTICH

aus Backnang

Hauptberichter : Prof. Dr. Udo Seifert
Erster Mitberichter : Prof. Dr. Siegfried Dietrich
Zweiter Mitberichter : Prof. Dr. Massimiliano Esposito
Vorsitzender : Prof. Dr. Clemens Bechinger

Tag der Einreichung : 23.01.2017
Tag der mündlichen Prüfung : 15.03.2017

II. Institut für Theoretische Physik der Universität Stuttgart

2017

Abstract

Stochastic thermodynamics is a theoretical framework that extends the laws of classical thermodynamics to small system at the molecular and cellular scale. In particular processing information at these scales is continuously corrupted by thermal fluctuations. Examples involve translating information from DNA to proteins, bacteria that sense their environment or neurons that fire action potentials. In all of these examples, energy is consumed to process information or to shield the process against thermal fluctuations. This thesis investigates the relation between information and thermodynamics in physical systems.

We develop a framework for two continuously coupled systems, which is called stochastic thermodynamics of bipartite systems. This framework includes information and refines the standard second law of thermodynamics. In the first part we consider feedback-driven engines, where one subsystem is controlled by a second subsystem that constitutes the feedback controller. The feedback controller continuously acquires information about the controlled subsystem and uses it to rectify thermal fluctuations, i.e., to “convert information into energy”. We compare two information theoretic quantities that characterize the performance of the feedback controller the transfer entropy rate and the learning rate. We find that only the latter both (i) bounds the rate of energy extraction from the medium due to the controlled subsystem and (ii) is itself bounded by the thermodynamic cost to maintain the dynamics of the feedback controller. This insight is one of the main results and provides a modern view on classical thought experiments first proposed by Maxwell.

In the second part, we discuss implications to cellular information processing, whereby a stochastic time dependent signal is measured by a sensory network. In contrast to feedback-driven engines, here a sensor dissipates energy to acquire information about a signal, i.e., “it converts energy into information”. We define an efficiency that relates the information which a sensor acquires to the energy which is dissipated by the sensor. Models that are inspired by the sensory system of *Escherichia coli* chemotaxis are used to illustrate our findings. Moreover, a purely information theoretic quantity, which is called sensory capacity, is introduced. The sensory capacity is bounded by one and given by the ratio of the learning rate of the sensor and the transfer entropy rate from the signal to the sensor. The sensory capacity is maximal if the instantaneous state of the sensor knows as much about the signal as its full time history. We show that the sensory capacity can be increased with an additional dissipative memory, where the increase of the sensory capacity characterizes the performance of the memory. A general tradeoff between the sensory capacity and the efficiency is shown, which demonstrates that a sensor cannot be both: a perfect noise filter and energetically efficient.

The third subject considers binary sensors (e.g., receptors) measuring a stochastic signal (e.g., ligand concentration). For this setup we study the information loss of inference strategies that are solely based on time-averages of the sensor state. We show that simple

time-averaging strategies lose up to 0.5 bit of information compared with the full time history of the sensor. This result holds for an arbitrary number of sensors measuring the same signal independently. Furthermore, we show that the same information loss occurs if one approximates a discrete chemical master equation by a continuous Brownian motion.

In the last part, we discuss nonequilibrium receptors that are driven out of equilibrium by an ATP hydrolysis reaction. It is shown that the sensitivity of the receptor to concentration changes can be increased with the nonequilibrium reaction, whereby the increase in sensitivity is related to the chemical energy released in the hydrolysis of one ATP molecule. It turns out that there is an analogy between nonequilibrium receptors and kinetic proofreading, which is a dissipative mechanism to reduce errors in a polymerization process. This part demonstrates that investing chemical energy can improve the capability to process information.

Contents

Publications	8
Zusammenfassung	9
1 Introduction	14
2 Foundations of stochastic thermodynamics	19
2.1 Thermodynamic quantities on a single trajectory	19
2.2 Stochastic entropy and Fluctuation theorems	22
3 Stochastic thermodynamics of bipartite systems with feedback	24
3.1 Introduction	24
3.1.1 Historical overview: Maxwell’s demon and Landauer principle	24
3.1.2 Recent experimental advances for feedback systems	27
3.1.3 Second law and fluctuation theorems with feedback	28
3.2 Bipartite systems and entropy production	29
3.2.1 Basic definitions and Shannon entropy	29
3.2.2 Entropy production of the subsystem	30
3.2.3 Interpretation of subsystem “y” as a Maxwell’s demon	32
3.2.4 Learning rate and thermodynamic consistency	33
3.3 Transfer entropy in bipartite systems	35
3.3.1 Causal influence between two random processes	35
3.3.2 Analytic upper bound on transfer entropy rate	37
3.3.3 Rate of mutual information and Shannon entropy rates	38
3.4 Main results and Examples	40
3.4.1 Summary of important inequalities	40
3.4.2 Biased random walk with stochastic feedback control	41
3.4.3 Bipartite four state system	42
3.4.4 Four state system with time scale separation	44
3.4.5 Further related research	46
3.5 Conclusion	46
Appendices to chapter 3	48
3.A Transfer entropy versus learning rate	48
3.A.1 Rewriting transfer entropy rate	48
3.A.2 Finishing the proof	48
3.A.3 Comments on the proof	49
3.B Calculating Shannon entropy rates	49
3.B.1 Path weight and continuous time Shannon entropy rates	49

3.B.2	Random matrices and path weight of coarse-grained processes . . .	51
3.B.3	Shannon entropy rates of coarse-grained processes	53
3.C	Continuous variables	54
4	Cellular information processing in bipartite systems	56
4.1	Introduction to cellular information processing	56
4.2	Efficiency of cellular information processing	58
4.2.1	Processing time dependent signals for bacterial chemotaxis	58
4.2.2	Bipartite process: Signal and Sensor	59
4.2.3	Learning rate and thermodynamic efficiency of a sensor	61
4.2.4	Coarse-grained learning rate	63
4.3	Examples systems from <i>E. coli</i> chemotaxis	64
4.3.1	Toy model	65
4.3.2	Single receptor model	67
4.3.3	Model with adaptation	73
4.4	Sensory capacity	79
4.4.1	Optimal noise filtering	79
4.4.2	Transfer entropy rate and sensory capacity	80
4.4.3	Sensor with a memory	81
4.5	Cellular two-component network	83
4.5.1	Model definition with memory and fluctuating signal	83
4.5.2	Bare sensor	87
4.5.3	Memory increases sensory capacity	90
4.6	Trade-off between sensory capacity and efficiency	92
4.6.1	Trade-off for linear two-component network	92
4.6.2	General trade-off	93
4.6.3	Estimate of sensory capacity and refined efficiency	96
4.7	Conclusion	97
	Appendices to chapter 4	99
4.A	Linear noise approximation for cellular two-component network	99
4.A.1	Diffusion approximation	99
4.A.2	Small signal variation and linear noise approximation	100
4.B	Entropic rates for Gaussian linear process	102
4.C	Uncertainty from time series	104
5	Optimal inference strategies and approximation schemes	107
5.1	Introduction to chemoreception	107
5.2	Sensor measuring a stochastic concentration	108
5.2.1	Model for binary sensor	108
5.2.2	Main result	109
5.3	Dispersion of random variables	113
5.3.1	Generating function and first two moments	114
5.3.2	Mutual information for weak Gaussian signals	116
5.3.3	Long time limit for arbitrary signal distribution	118
5.3.4	Method from References [198, 203, 204] for joint dispersion	121

5.4	Continuous approximation schemes	124
5.5	Discussion and outlook	126
6	Nonequilibrium sensing and its analogy to kinetic proofreading	128
6.1	Introduction	128
6.2	Nonequilibrium receptor model	129
6.3	Integrated sensitivity	131
6.4	Analogy with kinetic proofreading	134
	6.4.1 Kinetic proofreading	134
	6.4.2 Non-equilibrium sensing vs. kinetic proofreading	135
6.5	Effect of the occupancy of the receptor on phosphorylation and dephosphorylation rates	137
	6.5.1 Single receptor	137
	6.5.2 Generalization to an arbitrary number of binding sites	140
6.6	Conclusion	141
7	Concluding perspectives	143
	Bibliography	146
	Danksagung (Acknowledgement)	158

Publications

- D. Hartich, A. C. Barato, and U. Seifert, *Stochastic thermodynamics of bipartite systems: Transfer entropy inequalities and a Maxwell's demon interpretation*, *J. Stat. Mech.* (2014) P02016.

© 2014 IOP Publishing Ltd and SISSA Medialab srl. Chapter 3 is based on this publication.

- A. C. Barato, D. Hartich, and U. Seifert, *Efficiency of cellular information processing*, *New J. Phys.* **16**, 103024 (2014).

© 2015 IOP Publishing Ltd and Deutsche Physikalische Gesellschaft. Published under the terms of the [Creative Commons Attribution 3.0 licence](#). DOI: [10.1088/1367-2630/16/10/103024](https://doi.org/10.1088/1367-2630/16/10/103024). Parts of chapter 4 are adopted from this publication.

- D. Hartich, A. C. Barato, and U. Seifert, *Nonequilibrium sensing and its analogy to kinetic proofreading*, *New J. Phys.* **17**, 055026 (2015).

© 2015 IOP Publishing Ltd and Deutsche Physikalische Gesellschaft. Published under the terms of the [Creative Commons Attribution 3.0 licence](#). DOI: [10.1088/1367-2630/17/5/055026](https://doi.org/10.1088/1367-2630/17/5/055026). Chapter 6 is adopted from this publication.

- D. Hartich, A. C. Barato, and U. Seifert, *Sensory capacity: An information theoretical measure of the performance of a sensor*, *Phys. Rev. E* **93**, 022116 (2016).

© 2016 American Physical Society. Parts of chapter 4 are based on this publication.

- D. Hartich and U. Seifert, *Optimal inference strategies and their implications for the linear noise approximation*, *Phys. Rev. E* **94**, 042416 (2016).

© 2016 American Physical Society. Chapter 5 is based on this publication.

Zusammenfassung

Die stochastische Thermodynamik ist ein theoretisches Grundgerüst, welches die Gesetze der Thermodynamik auf kleine Systeme erweitert. Vor allem Prozesse, die auf molekularer und zellulärer Ebene Information verarbeiten, werden permanent durch thermische Fluktuationen beeinträchtigt. Beispiele hierfür sind die Proteinsynthese, bei der Information von der DNA beziehungsweise mRNA kopiert wird, Bakterien, die ihre Umgebung wahrnehmen oder Neuronen, die ein Aktionspotential versenden. In all diesen Beispielen wird Energie aufgewandt, um Information zu verarbeiten oder den Prozess vor thermischen Fluktuationen zu schützen. In dieser Arbeit wird die Rolle der Information für die Thermodynamik untersucht.

Entwickelt wird eine allgemeine Rahmentheorie für zwei kontinuierlich gekoppelte Systeme, die stochastische Thermodynamik zweigeteilter Systeme genannt wird (*stochastic thermodynamics of bipartite systems*). Diese Rahmentheorie berücksichtigt Information, die zwischen den beiden Teilsystemen ausgetauscht wird, um den zweiten Hauptsatz der Thermodynamik zu verallgemeinern. Im ersten Teil werden feedback-getriebene Maschinen betrachtet, wobei ein Teilsystem kontinuierlich von einem zweiten Teilsystem (dem Feedback-Controller) durch Rückkopplung kontrolliert wird. Der Feedback-Controller erhält kontinuierlich Information über den Zustand des zu kontrollierenden Systems und nutzt diese, um thermische Fluktuationen auszurichten beziehungsweise um "Information in Energie umzuwandeln". Es werden zwei informationstheoretische Größen untersucht, die Transferentropierate sowie Lernrate genannt werden und die die Leistung des Feedback-Controllers charakterisieren. Es stellt sich heraus, dass nur die Lernrate allgemein die beiden folgenden Eigenschaften erfüllt: (i) Sie beschränkt die Energie, die vom kontrollierten Teilsystem aus dem umgebenden Medium extrahiert wird und (ii) sie wird selbst durch die thermodynamischen Kosten, den Feedback-Controller zu betreiben, beschränkt. Diese Erkenntnis stellt eines der Hauptergebnisse dieser Arbeit dar und bietet eine moderne Sicht auf klassische Gedankenexperimente, wie sie zuerst von J. C. Maxwell vorgestellt wurden und erst vor kurzem experimentell realisiert werden konnten.

In einem zweiten Teil werden zeitabhängige Signale betrachtet, die von einem sensorischen Netzwerk gemessen werden. Im Gegensatz zu feedback-getriebenen Maschinen wird hier "Energie in Information umgewandelt", wobei ein Sensor Energie dissipiert, um Information über das Signal zu erhalten. Es wird eine Effizienz definiert, die sich aus dem Verhältnis der Lernrate und der Energiedissipationsrate des Sensors ergibt. Die Effizienz gibt an, wie effizient chemische Energie verwendet wird, um Information über ein Signal zu gewinnen. Die Ergebnisse werden anhand verschiedener Modelle illustriert, die an das sensorische Netzwerk des Chemotaxisystems von *Escherichia coli* angelehnt sind. Es werden Ähnlichkeiten zu molekularen Motoren aufgezeigt, wobei anstatt der Umwandlung von chemischer in mechanische Energie hierbei chemische Energie in Information umgewandelt wird. Darüber hinaus wird eine rein informationstheoretische Größe definiert,

die Sensorische Kapazität genannt wird und sich formal aus dem Verhältnis zwischen Lernrate des Sensors und der Transferentropierate vom Signal zum Sensor berechnet. Die Sensorische Kapazität eines Sensors erreicht ihr Maximum 1, falls der instantane Zustand des Sensors die selbe Information über das Signal enthält wie die Zeitserie des Sensors. Die Sensorische Kapazität kann durch Hinzufügen eines dissipativen Speichers die Leistungsfähigkeit eines Sensors erhöhen, wobei die Information von der Zeitserie des Sensors im instantanen Zustand des Speichers festgehalten wird. Es stellt sich eine Kompromissbeziehung zwischen der Effizienz und der Sensorischen Kapazität eines Sensors heraus, die es allgemein verhindert, dass ein Sensor zugleich ein perfekter Rauschfilter sowie energetisch effizient sein kann.

In einem dritten Themenbereich werden binäre Sensoren (z.B. Rezeptoren) betrachtet, die ein stochastisches Signal (z.B. Stoffkonzentration) messen. Hierbei wird der Informationsverlust von Inferenzstrategien untersucht, die ausschließlich auf der Zeitintegration des Sensorzustands basieren. Es wird gezeigt, dass diese einfachen Inferenzstrategien Information verlieren, die nur aus der kompletten Zeitserie des Sensorzustands gewonnen werden kann. Der Informationsverlust beträgt abhängig vom physikalischen Modell des Sensors bis zu 0.5 bit pro Messung. Der gleiche Informationsverlust tritt auch für beliebig viele Sensoren auf, die unabhängig ein Signal messen. Außerdem stellt sich heraus, dass der selbe Informationsverlust bei Approximationsverfahren auftritt, bei denen die Dynamik eines diskreten chemischen Netzwerks, durch eine kontinuierliche Brown'sche Bewegung angenähert wird.

Im letzten Teil der Arbeit werden Nichtgleichgewichtsrezeptoren untersucht, die durch eine ATP Hydrolyse aus dem Gleichgewicht getrieben werden. Es wird gezeigt, dass die Sensitivität des Rezeptors gesteigert werden kann durch die chemische Energie, die bei der Aufnahme eines ATP-Moleküls frei wird. Des Weiteren wird eine Analogie zwischen *kinetic proofreading* und Nichtgleichgewichtsrezeptoren hergestellt.

Die Dissertation ist wie folgt aufgebaut: Kapitel 1 bildet die Einführung in das Thema. Daraufhin werden einige Grundlagen zur stochastischen Thermodynamik in Kapitel 2 kurz dargestellt. Anschließend folgen die unten genannten Hauptkapitel, wobei Kapitel 7 die Ergebnisse der Dissertation zusammenfasst sowie einige Ausblicke bietet.

Kapitel 3: (Stochastische Thermodynamik zweigeteilter Systeme mit Rückkopplung). In diesem Kapitel wird in die Thermodynamik zweier gekoppelter mikroskopischer Systeme eingeführt. Hierbei wird zunächst der Fall betrachtet, in dem ein Teilsystem benutzt wird, um Arbeit von einem Wärmebad zu extrahieren, während es von einem zweiten Subsystem kontrolliert wird. Schon in der Entstehung der klassischen Thermodynamik wurde dies als scheinbarer Widerspruch von Maxwell erkannt, weshalb das zweite kontrollierende Subsystem auch als "Maxwell'scher Dämon" bezeichnet wird. Daraus lässt sich eine neue Theorie entwickeln, die eine besonders transparente Beschreibung eines sogenannten Maxwell'schen Dämons auf mikroskopischer Ebene erlaubt. Zu diesem Zweck wird eine thermodynamisch konsistente Informationsrate eingeführt, welche Lernrate (engl. *learning rate*) genannt wird. Diese charakterisiert die Reduktion der Unbestimmtheit des kontrollierten Systems aufgrund der Wechselwirkung mit dem "Maxwell'schen Dämon". Es stellt sich als zentrales Ergebnis heraus, dass die Rate, mit der Arbeit vom kontrollierten Teilsystem extrahiert werden kann, durch die Lern-

rate begrenzt wird. Es wird ferner gezeigt, dass die Lernrate selbst durch die dissipierte Wärme des zweiten Subsystems (“Maxwell’scher Dämon”) beschränkt wird und daher eine zusätzliche Investition von chemischer oder mechanischer Arbeit erfordert.

Die Lernrate wird mit einer weiteren etablierten Informationsrate, der Transferentropie, verglichen, die unter anderem für feedback-getriebene Maschinen verwendet wird und die die extrahierbare Arbeit des kontrollierten Systems beschränkt. Außerdem ist die Transferentropierate einerseits sensitiv für die kausale Wechselwirkung zwischen zwei Teilsystemen, andererseits berücksichtigt sie zeitliche Korrelationen der “Messungen” des kontrollierenden Teilsystems. Es wird bewiesen, dass die Lernrate strikt kleiner ist als die Transferentropierate. Außerdem ist letztere nicht durch den Arbeitsaufwand des “Maxwell’schen Dämons” beschränkt, wie anhand eines einfachen Vierzustandssystems verdeutlicht wird. Auch im Gleichgewicht, in dem keinerlei Energie dissipiert wird, kann die Transferentropierate im Gegensatz zur Lernrate ungleich Null sein. Basierend auf den entwickelten theoretischen Konzepten wird im folgenden Kapitel 4 die Signal- und Informationsverarbeitung in zellularen Prozessen untersucht.

Kapitel 4: (Informationsverarbeitung zellulärer Sensoren). In diesem Kapitel werden die Konzepte verwendet, die in Kapitel 3 entwickelt wurden. Hierbei wird jedoch eine andere Problemstellung verfolgt, nämlich das Messen von Signalen. Es wird ein zeitlich variierendes stochastisches Signal betrachtet, welches von einem Sensor gemessen wird. Die Lernrate des Sensors gibt an, mit welcher Rate die Unbestimmtheit des Signals durch die Sensordynamik verkleinert wird. Es wird gezeigt, dass die Lernrate des Sensors durch die Energie beschränkt ist, welche durch den Sensor dissipiert wird. Dies erlaubt die Definition einer Effizienz, die positiv und durch 1 beschränkt ist und die die sensorische Leistungsfähigkeit (charakterisiert durch die Lernrate) mit den thermodynamischen Kosten (charakterisiert durch die Entropieproduktion) vergleicht. Es werden einfache Modelle mit steigender Komplexität untersucht, die dem sensorischen Netzwerk von *Escherichia Coli* entnommen sind. Diese Modelle erlauben es, die Entropieproduktion mit der chemischen Energie, die in der Zelle verbraucht wird, und der Arbeit, die durch das Signal hinzugeführt wird, zu identifizieren. Sie beinhalten im Speziellen die Aktivierung und Deaktivierung von Proteinen, ein klassisches Monod-Wyman-Changeux-Modell für Rezeptorkomplexe und/oder Adaptionsmechanismen.

Darauf aufbauend wird die Sensorische Kapazität eines Sensors eingeführt, die formal das Verhältnis zwischen Lernrate und Transferentropierate darstellt. Die Sensorische Kapazität ist eine rein informationstheoretische Größe, welche positiv und durch 1 beschränkt ist. Die Sensorische Kapazität eines Sensors erreicht ihr Maximum 1, falls der instantane Zustand des Sensors die gleiche Information über das Signal beinhaltet wie die gesamte Zeithistorie des Sensorzustandes. Die Sensorische Kapazität kann beispielsweise durch das Hinzufügen eines Speichers erhöht werden, indem er Information über das Signal aus der Zeithistorie des Sensors speichert. Es wurde eine interessante Kompromissbeziehung zwischen der Sensorischen Kapazität und der Effizienz eines Sensors entdeckt: Ein Sensor mit maximaler Kapazität 1 dissipiert Energie mit mindestens der zweifachen Lernrate, was zur Folge hat, dass die Effizienz kleiner oder gleich $1/2$ sein muss. Diese Kompromissbeziehung verbietet es einem Sensor, ein perfekter Rauschfilter sowie energetisch effizient zu sein. Mithilfe eines zweikomponentigen Netzwerks wurde beispielhaft ein Sensor mit

Speicher realisiert, der eine fluktuierende Molekülkonzentration misst. Eine Approximation des Netzwerks mittels einer stochastischen Differentialgleichung ermöglicht eine analytische Lösung des Problems.

Kapitel 5: (Optimale Inferenzstrategien und Approximation stochastischer Prozesse). Es wird der Informationsverlust einer Klasse von Inferenzstrategien untersucht, die ausschließlich auf der zeitlichen Integration des Sensorzustandes basieren. Für eine Anordnung mehrerer binärer Sensoren (z.B. Rezeptoren), die ein Signal (z.B. Molekülkonzentration) messen, ist dieser Informationsverlust bis zu 0.5 bit pro Messung unabhängig von der Anzahl gleichzeitig messender Sensoren. Von der lokalen *detailed balance* Relation wird eine genaue Beziehung hergeleitet, die den zusätzlichen Informationsinhalt angibt, welcher ausschließlich aus der Anzahl der Sensorübergänge, nicht aber aus der zeitlichen Integration des Sensorzustandes gewonnen werden kann. Falls die Änderung der freien Energiedifferenz, die durch das Signal hervorgerufen wird, symmetrisch auf die vorwärts- und rückwärtsgerichtete Übergangsrate verteilt wird, enthält die Anzahl der Sensorübergänge keine weitere Information über das stochastische Signal. In diesem Fall ermöglichen einfache Zeitintegrationsmechanismen eine Inferenz des Signals mit höchster Präzision.

Als eine weitere Anwendung wird eine Verbindung zu Approximationsverfahren gefunden, mithilfe derer die Dynamik chemischer Netzwerke mittels einer kontinuierlichen Brown'schen Bewegung angenähert werden kann. Durch die Vereinfachung der Dynamik geht hierbei jedoch Information im Vergleich zur ursprünglichen Dynamik verloren, welche exakt der Information entspricht, die sich ausschließlich aus der Anzahl der diskontinuierlichen Übergänge des Sensors ergibt. Falls das Signal jedoch einen symmetrischen Einfluss auf die vorwärts- und rückwärtsgerichteten Übergangsraten hat, sind solche kontinuierlichen Näherungsverfahren sogar bis auf die Trajektorienebene genau.

Kapitel 6: (Nichtgleichgewichtssensoren und deren Analogie zu *kinetic proofreading*). Für ein typisches Modell aus der bakteriellen Chemotaxis wird untersucht, wie die Sensitivität eines Rezeptors erhöht werden kann, falls dieser aus dem Gleichgewicht getrieben wird. Ein solches Nichtgleichgewicht taucht auf, wenn die Aktivierung des Rezeptors durch die Hydrolyse von Adenosintriphosphat (ATP) stattfindet. Es wird aufgezeigt, dass die Sensitivität durch den Verbrauch chemischer Energie erhöht werden kann, was eine sogenannte Ultrasensitivität ermöglicht. Hierbei ist die Erhöhung der Sensitivität, integriert über einen Konzentrationsbereich, direkt begrenzt durch die chemische Energie, die bei der Aufspaltung eines ATP-Moleküls frei wird. Diese Relation verdeutlicht, wie der Verbrauch chemischer Energie zu einer erhöhten Leistungsfähigkeit zellulärer Sensoren führen kann.

Darüber hinaus wird ein Fehlerkorrekturmechanismus (*kinetic proofreading*) untersucht, der Fehler beim Kopieren von Information aus der DNA verhindert. Hierbei wird chemische Energie investiert, um thermische Fluktuationen aktiv zu unterdrücken. Dies ermöglicht es, Kopierprozesse genauer ablaufen zu lassen beziehungsweise Fehler um mehr als das 100-fache zu verkleinern. Dabei wird eine interessante Analogie zwischen Nichtgleichgewichtssensoren und dem Mechanismus des *kinetic proofreading* entdeckt: die Erhöhung der Sensitivität durch zugeführte chemische Energie bei Nichtgleichgewichtssensoren.

soren ist analog zu der Fehlerreduktion bei *kinetic proofreading*.

Kehrt man die chemischen Kräfte in einem Netzwerk um, so kann auch die Sensitivität von Nichtgleichgewichtssensoren verkleinert werden. Ähnlich ließen sich auch aktiv Fehler bei Kopierprozessen erhöhen, was einem sogenannten *anti-proofreading* entspräche. Im Allgemeinen können chemische Kräfte von Reaktionen, die fernab vom Gleichgewicht stattfinden, eingesetzt werden, um die Sensitivität eines Rezeptors für externe Konzentrationsfluktuationen gezielt zu erhöhen oder zu verkleinern.

1 Introduction

Thermodynamic fluctuations are ubiquitous in micro-sized or nano-sized systems, for example, in molecular motors, biomolecules (enzymes) and colloidal particles. Extending the laws of thermodynamics to such systems has been a subject of research within the last two decades. Thermal interaction between these small systems and their surrounding renders their motion stochastic. In particular, heat exchanged with the environment and chemical and mechanical work delivered to the system become fluctuating functionals that can be evaluated along a single stochastic trajectory [1–3], which are key ingredients in the first law accounting for energy conservation. Moreover, fluctuation theorems have been discovered [4–8] that hold for systems driven far away from equilibrium and include, amongst other things, the identification of a stochastic entropy term [6, 8] that is evaluated along a single trajectory. These fluctuation theorems provide a more detailed understanding of the second law of thermodynamics, for which Jarzynski’s equality [4] and Crook’s detailed fluctuation theorem [6] allowed to derive new diagnostic tools to determine free energy differences in finite time experiments that are performed far away from equilibrium. Experimental tests of these fluctuation theorems involve, for example, RNA unfolding experiments [9, 10], optically driven defect centers in diamond [11, 12], colloidal particles in a laser trap [13–15], and experiments with electric circuits at low temperatures [16, 17]. These advances have shaped a powerful framework that is called stochastic thermodynamics [18].

In this thesis we include new information theoretic aspects into stochastic thermodynamics. The leading question will be: How much energy is necessary to process or copy information, i.e., to reduce fluctuations?

One illustrative and important example is the replication of DNA, where information from one double strand of DNA is copied to generate two identical DNA strands, see, e.g. [19]. This process is important to pass genetic information from one cell to another during cell division. The information in a DNA molecule is encoded in a sequence of nucleotides, adenine (A), thymine (T), cytosine (C) and guanine (G). It has been found that A pairs with T and C pairs with G, which constitutes “correct” pairings, whereas “wrong” pairings correspond to TG or CA, see Fig. 1.1 for an illustration. The free energy difference between a correct pairing and wrong pairing is “so small” that at body temperature ($\sim 37^\circ\text{C}$) the Boltzmann factor would predict one error in 10^4 nucleotides due to energetic discrimination. Errors in this process will lead to mutations that could cause cancer. The real error rates in the DNA polymerization, however, are astonishingly smaller than one would naïvely expect, namely, only one error in every 10^9 nucleotides, i.e., more than 10^5 times fewer errors than one would expect from energetic discrimination. This discrepancy has firstly been theoretically explained by Hopfield and Ninio [20, 21], who have found that a non-equilibrium mechanism, which consumes chemical energy, is necessary to shield the process against thermal fluctuations. This process is termed “kinetic proofreading”,

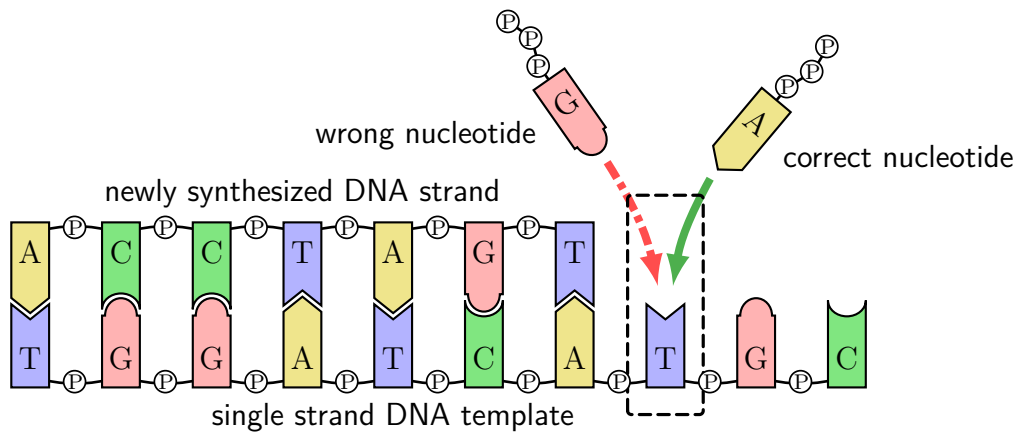


Figure 1.1 | DNA replication with kinetic proofreading. Errors are reduced by many orders of magnitude at the expense of chemical energy. Individual nucleotides are adenine (A), thymine (T), cytosine (C) and guanine (G). Each nucleotide triphosphate can bind to the DNA template at the position of the DNA polymerase (dashed box). Two phosphate groups P are released along the polymerization of one nucleotide, which are crucial for kinetic proofreading, i.e., low error rates.

where each nucleotide is checked multiple times before it is incorporated. This example, illustrates that chemical energy can be used to copy information more reliably.

Information processing is not restricted to just copying information. Thermodynamics of computation is another topic in the interface between information theory and physics that has been pushed forward by Landauer [22]. He has realized the importance of irreversible logical operations in a computer that have not a single valued reverse, as for example, the erasure of a bit $0, 1 \rightarrow 0$. Such logically irreversible operations are accompanied by a minimum amount of heat generation according to what is nowadays called Landauer’s principle. For instance, a computer must dissipate at least $k_B T \ln 2$ of energy to erase a single bit, where k_B is Boltzmann’s constant and T the temperature. This insight provides a fundamental thermodynamic constraint on the performance of a computer. First experimental tests of Landauer’s principle have been realized just recently with micro-sized particles in a double-well potential [23, 24]. Adopting these ideas to stochastic thermodynamics will allow us to obtain, amongst other things, a more detailed understanding of the thermodynamic cost of cellular information processing, which will be of central importance in this thesis. Thereby, irreversibility arises from chemical reactions that are driven out of equilibrium resulting in a constant rate of energy consumption. The fact that acquiring and processing information does cost energy, emphasizes that information can be regarded as a “quantity of value”, which cannot be attained for free.

The third and last example of the importance of information for thermodynamics, is quite an old discussion concerning the limitations of the second law. The second law of thermodynamics, for example, forbids that thermal fluctuations (heat) can be rectified to convert it into useful directed energy (work), i.e., running an engine or a refrigerator requires external energetic inputs. In 1871 Maxwell realized that if one has microscopic information about a system, say information about the velocity and position of individual molecules, one could exploit this information by implementing a feedback mechanism that

uses this information to rectify thermal fluctuations [25]. A simpler and more quantitative gedankenexperiment was proposed by Szilard in 1929, which involves an ideal gas with one single molecule and a measurement that just provides a binary outcome [26], i.e., one single bit of information. It could be shown that the amount of work that can be extracted at constant temperature T with a feedback mechanism that uses the information from a single binary valued measurement is bounded by $k_B T \ln 2$. This bound constitutes the first quantitative relation between microscopic information and the amount work that can be extracted by using this information. Further thought experiments and theoretical advances have been developed in the last years, whereas an experimental realization seemed to be dreams of the future. However, considerable experimental progress has been made, which has allowed to realize the first feedback-driven engine in 2010 [27]. In this experiment a polystyrene bead (less than a micron in diameter) has been pushed upwards a staircase-like potential by a feedback mechanism that converts the information from a measurement into useful work. This feedback mechanism blocks the motion of the particle downwards the potential, whereas it allows the particle to move “freely” if it is moving upwards the potential. This experiment has shown that such thought experiments involving the conversion of information into energy have become of practical importance. This example will be discussed in more detail later on.

In this thesis we built a general framework for continuously coupled processes that can be used to study cellular information processing, feedback-driven engines and thermodynamics of a memory that stores information. Thereby information will be considered as a quantity of value, which can be acquired at the expense of chemical or mechanical energy (work). Conversely, microscopic information about a system can be exploited to rectify thermal fluctuation to extract useful energy (work) with a feedback-driven engine.

The thesis is organized as follows, see also Fig. 1.2. Chapter 2 introduces the main concepts of stochastic thermodynamics. We use a colloidal particle as a paradigm to introduce a stochastic version of the first law of thermodynamics, where heat, work, and energy are stochastic functionals of trajectories. Moreover, the local detailed balance relation is discussed, which links the dynamics of a discrete chemical master equation to thermodynamics. In the second section (Sec. 2.2) we briefly introduce the concept of stochastic entropy and fluctuation theorems.

In chapter 3, we focus on feedback-driven engines, involving the so-called Maxwell’s demon. We give a more detailed overview over historical achievements and recent research involving Maxwell’s demon and Landauer’s principle, including further experimental results. After introducing basic concepts of information theory, we establish the framework for continuously coupled systems, which we call stochastic thermodynamics of bipartite systems. This framework allows for particularly transparent interpretation of Maxwell’s demon (i.e., a feedback-driven system), where one part of the systems constitutes a feedback controller. For example, the thermodynamic cost of feedback control is easily accessible. With the interpretation of a Maxwell’s demon, we derive a new set of inequalities that characterize the performance of a feedback-driven engine that is continuously coupled to a feedback controller. A simple four state system is used to illustrate the main findings.

The results from chapter 3 are not restricted to feedback driven systems. We consider in chapter 4 another problem, namely, a cell or a sensor that is measuring or computing a

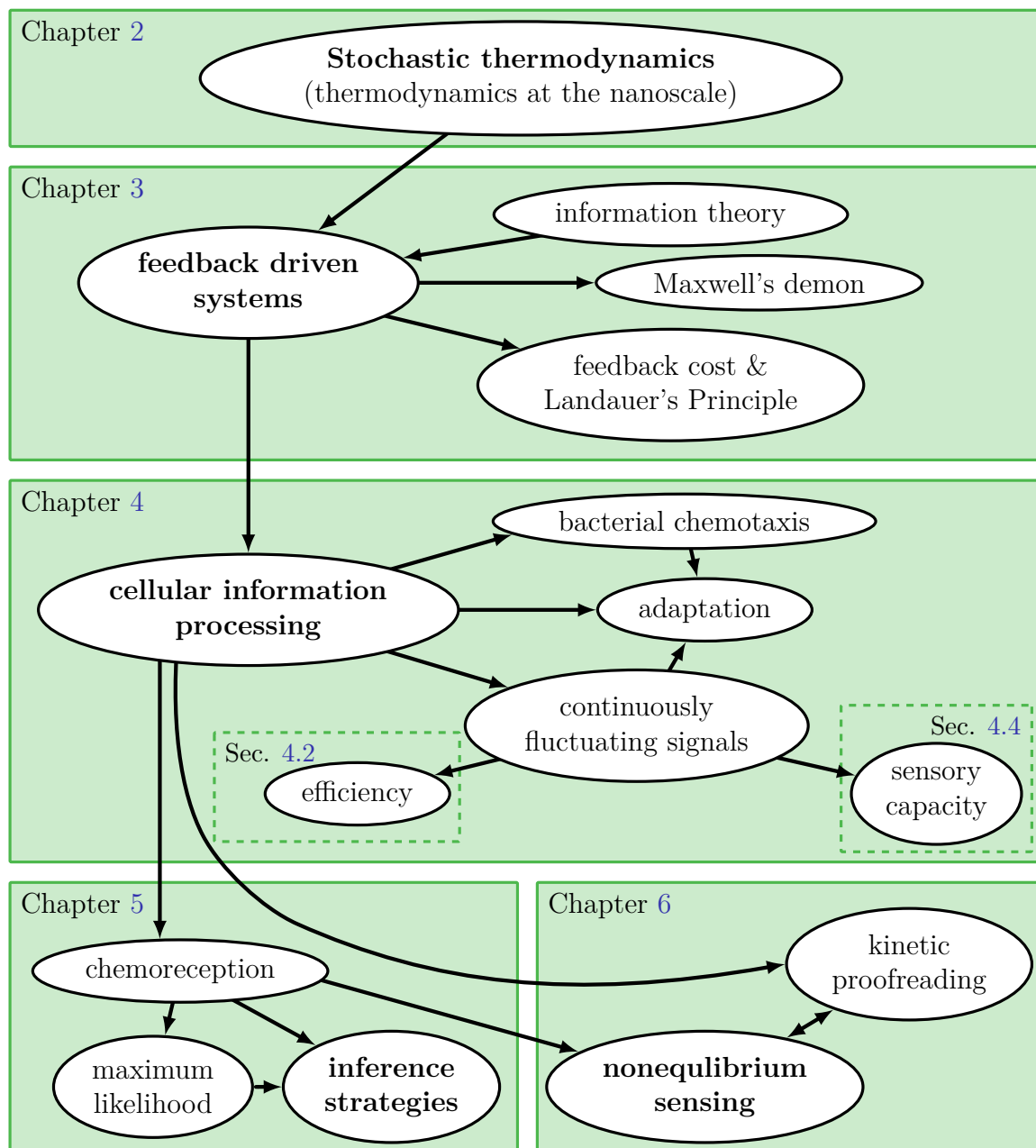


Figure 1.2| Structure of the thesis.

fluctuating signal. We find that the rate at which a sensor acquires information about a continuously fluctuating signal is limited by the rate at which the sensor dissipates energy. From this finding we define in Sec. 4.2 an efficiency that is bounded by one and relates the rate at which a sensor acquires information to the rate at which it dissipates energy. We use several models inspired by the sensory network of the *Escherichia coli* chemotaxis system to illustrate our findings. A model including adaptation is also discussed.

In a second part (Sec. 4.4) we define the sensory capacity that is a purely information theoretic quantity, which relates the information a sensor acquires with its current state to the maximal information that is encoded in the full time history of the sensor. We discuss the role of the sensory capacity for noise filtering techniques. We find a trade-off between the sensory capacity and the efficiency, implying that a sensor cannot be both: an optimal noise filter and energetically efficient. This trade-off is analytically analyzed with a cellular two component network measuring a continuously fluctuating signal.

In chapter 5 we investigate binary sensors that measure a stochastic static signal over some time span. We compare the information loss of a specific class of inference strategy that is solely based on time averaging to a maximum likelihood estimate, which considers the full time history of the sensor. The information loss of time averaging methods is shown to be bounded by 0.5 bit, which can be associated with a signal-to-noise ratio reduced by a factor of 1/2 compared with using the full time history of the sensor. Furthermore, we find implications for the accuracy of the linear noise approximation, which is a powerful tool to approximate the dynamics of a discrete chemical network by a continuous Brownian motion. For example, we find these approximation schemes lose information on the trajectory level, which is up to 0.5 bit.

In chapter 6 we investigate receptor models that are driven out of equilibrium by an ATP hydrolysis reaction. It is shown that the free energy release by hydrolyzing one ATP can be used to increase the sensitivity of a receptor to changes of an external ligand concentration. Furthermore, the increase of the sensitivity integrated over some concentration span is shown to be bounded by the energy of one hydrolyzed ATP. This relation illustrates how nonequilibrium driving forces arising from ATP hydrolysis improve sensing. Remarkably, we find a clear analogy between nonequilibrium sensing and kinetic proofreading, where the increase of the sensitivity due nonequilibrium driving is analogous to the decrease of the error rate in kinetic proofreading. Finally, we conclude in chapter 7.

2 Foundations of stochastic thermodynamics

The following chapter introduces the framework of stochastic thermodynamics. We will show, for example, how one can formulate the first law of thermodynamics at the level of individual trajectories. Moreover, fluctuation theorems are briefly explained.

2.1 Thermodynamic quantities on a single trajectory

It has been shown for stochastic Brownian motion and discrete master equations that heat, work, and energy can be well defined on the level of individual trajectories [1], which are the central ingredients of the first law of thermodynamics. These findings borrow from the calculus of stochastic processes [28], developed over the last century, which we now briefly motivate.

Consider first the Brownian motion of a micro-sized particle with mass m in a fluid. At these scales the dominant friction force is determined through Stokes friction [29], with inverse friction coefficient or mobility μ . For instance, the time needed to reach the maximum speed if a force is applied is about $\tau_{\text{relax}} \equiv m\mu \sim 10^{-7}$ s, which also determines the drift time after removing a force. For such systems it is quite useful to describe the dynamics of the position of the particle x_t at time t by an overdamped Langevin equation

$$\dot{x}_t = \mu F(x_t, t) + \xi_t, \quad (2.1)$$

where $F(x_t, t)$ is a systematic force applied to the particle and ξ_t is stochastic noise that arises from the interaction with the molecules of the medium at temperature T , which does not favor any particular direction $\langle \xi_t \rangle = 0$ and decorrelates very quickly, i.e., $\langle \xi_t \xi_{t'} \rangle = 2D\delta(t - t')$. Thermodynamic consistency enters here via the Einstein relation $D = \mu k_B T$.

There are some issues concerning the stochastic calculus arising from the irregularity of ξ_t , which are important for defining thermodynamic quantities on the level of individual trajectories. To show them we write (2.1) as an Ito differential equation [28]

$$dx_t \equiv x_{t+dt} - x_t = \mu F(x_t, t)dt + d\xi_t \equiv -\mu \frac{\partial V}{\partial x}(x_t, t)dt + d\xi_t, \quad (2.2)$$

where dt is a infinitesimal time increment and $d\xi_t \equiv \int_t^{t+dt} dt' \xi_{t'}$ is normally distributed with zero mean and variance $2Ddt$. For simplicity, we have assumed in the second step that the force stems from a potential. Due to the irregularity of the absolute value of the noise increment $|d\xi_t| \sim \sqrt{dt}$, one can most importantly show that $d\xi_t^2 = 2Ddt$ in

the continuous limit “ $dt \rightarrow 0$ ”, where also $dt^2 = dt d\xi_t = 0$ holds, see [3, 28] for more information. For instance, we have $dx_t^2 = 2Ddt$. Consequently, stochastic differentials of functions of x_t require an expansion up to second order in dx_t , which implies that the change of potential energy of the particle reads

$$dV \equiv V(x_{t+dt}, t+dt) - V(x_t, t) = \frac{\partial V}{\partial t}(x_t, t)dt + \frac{\partial V}{\partial x}(x_t, t)dx_t + \frac{1}{2} \frac{\partial^2 V}{\partial x^2}(x_t, t)dx_t^2. \quad (2.3)$$

The first term in (2.3) can be identified by the work applied to the system [1]

$$dW \equiv \frac{\partial V}{\partial t}(x_t, t)dt \quad (2.4)$$

and the second term as minus the heat dissipated into the environment according to Stokes friction [1]

$$\begin{aligned} dQ &\equiv -\frac{\partial V}{\partial x}(x_t, t)dx_t - \frac{1}{2} \frac{\partial^2 V}{\partial x^2}(x_t, t)dx_t^2 = -\frac{1}{2} \left[\frac{\partial V}{\partial x}(x_t, t) + \frac{\partial V}{\partial x}(x_{t+dt}, t) \right] dx_t \\ &\equiv -\frac{\partial V}{\partial x}(x_t, t) \circ dx_t = F(x_t, t) \circ dx_t, \end{aligned} \quad (2.5)$$

where we have defined the Stratonovich type product “ \circ ” in the second line. In this form the first law on a individual stochastic differential reads $dV = dW - dQ$. Two technical points should be noted. First, the last step determines the exchanged heat $dQ = F \circ dx_t$ even if an additional external force F^{ext} is present such that $F \equiv -\partial_x V + F^{\text{ext}}$. In this case the work exchange becomes $dW = [\partial_t V dt + F^{\text{ext}}] \circ dx_t$ and the heat becomes $dQ = [-\partial_x V + F^{\text{ext}}] \circ dx_t$ [18]. Second, if the potential is changed according to an external control parameter λ_t one has to replace $V(x_t, t) \rightarrow V(x_t, \lambda_t)$ and $\partial_t V dt \rightarrow \partial_\lambda V \circ d\lambda_t$ [1–3]. This identification of the first law of thermodynamics with work and heat defined on single stochastic differentials has firstly been identified by K. Sekimoto in [1], see [2] for an approach based exclusively on Langevin equations.

Chemical reaction networks, conformational states of biomolecules or driven random walks on a lattice are often modeled by discrete states $n(t) = 1, \dots, \Omega$ instead of continuously valued variables that are changing in time t . In this case the systems dynamics is governed by a master equation

$$\frac{\partial}{\partial t} P_t(n) = \sum_{n'=1}^{\Omega} \left[P_t(n') w_{n'n} - P_t(n) w_{nn'} \right], \quad (2.6)$$

where $P_t(n)$ denotes the probability of $n(t) = n$, i.e., the probability of observing state n at time t , and $w_{nn'}$ denotes the rate from state n to n' . An individual stochastic trajectory can numerically be generated from (2.6) by using, for example, the Gillespie algorithm [30]. Specifically, a trajectory $\{n_{\nu'}\}_{0 \leq \nu' \leq t} \equiv (n_0, \tau_0; \dots; n_N, \tau_N)$ consists of a sequence of states n_i in which the system remains for a waiting time τ_i such that $t = \sum_{i=0}^N \tau_i$. Similarly to the Langevin equation, one can evaluate the heat that is dissipated along a single trajectory. The local-detailed balance condition for individual transitions from n to n' reads [18, 31]

$$Q_{nn'} + T(s_{n'}^{\text{int}} - s_n^{\text{int}}) = k_B T \ln \frac{w_{nn'}}{w_{n'n}} = F_n - F_{n'} + W_{nn'}, \quad (2.7)$$

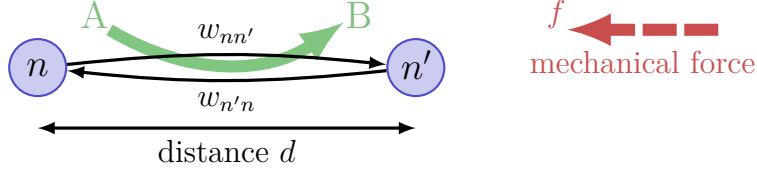


Figure 2.1| Illustration of the local detailed balance relation. Transition from n to n' is driven by a chemical reaction $A \rightarrow B$ transforming chemicals A into chemicals B with a chemical free energy difference $\mu_A - \mu_B \geq 0$. A mechanical force f is pointing in the opposite direction (see dashed arrow) towards the n . A transition $n \rightarrow n'$ along a distance d transforms chemical energy $W_{nn'}^{\text{chem}} = \mu_A - \mu_B$ into extracted mechanical work $-W_{nn'}^{\text{mech}} = fd$. The local detailed balance relation (2.7) reads for this example $k_B T \ln(w_{nn'}/w_{n'n}) = F_n - F_{n'} + \mu_A - \mu_B - df$.

where $Q_{nn'}$ is the heat dissipated into the medium, $W_{nn'}$ is the work performed along the transition, F_n is the free energy of state n and s_n^{int} is its intrinsic entropy, which accounts for the possible degeneracy of state n . If the transition $n \rightarrow n'$ does not change the intrinsic entropy ($s_n^{\text{int}} = s_{n'}^{\text{int}}$), $F_{n'} - F_n$ would correspond to the change of internal energy along the transition $n \rightarrow n'$. In this case the local-detailed balance relation corresponds to the first law of thermodynamics evaluated along a individual stochastic transition. The work may have a contribution due to chemical imbalances $W_{nn'}^{\text{chem}}$ and/or mechanical forces $W_{nn'}^{\text{mech}}$ such that $W_{nn'} = W_{nn'}^{\text{chem}} + W_{nn'}^{\text{mech}}$, which satisfies $W_{nn'} = -W_{n'n}$, see Fig. 2.1 for an example. If no external forces are present, that is, $W_{nn'} = 0$ for all pair of possible transitions $n, n' \in \{1, \dots, \Omega\}$, the system relaxes for $t \rightarrow \infty$ to equilibrium such that each summand in (2.6) vanishes, which for $t \rightarrow \infty$ results in an equilibrium distribution $P_t(n) \rightarrow P^{\text{eq}}(n) \propto \exp(-\beta F_n)$, where $\beta \equiv 1/(k_B T)$ is the inverse temperature. If only a single cycle of states $\tilde{n}_1 \rightarrow \tilde{n}_2 \dots \rightarrow \tilde{n}_\nu \rightarrow \tilde{n}_1$ has a nonzero affinity $\mathcal{A} \equiv W_{\tilde{n}_1 \tilde{n}_2} + \dots + W_{\tilde{n}_\nu \tilde{n}_1} \neq 0$ the system would relax into a non-equilibrium steady state that constantly dissipates energy into the medium. According to the local-detailed balance relation, a forward transition rate is larger than its reverse ($w_{nn'} > w_{n'n}$) if the free energy of the initial state n is larger than the free energy in the final state n' or if it is driven through an external influence $W_{nn'} > 0$ towards the n' state. One should note that if the transition rates $w_{nn'}$ vary in time t , which also implies that F_n becomes a function of time, one has a second contribution to the work arising from lifting or lowering the free energy of individual states, see, e.g., [18, 32] for more information.

For the full individual trajectory $\{n_{t'}\}_{0 \leq t' \leq t} = (n_0, \tau_0; \dots; n_N, \tau_N)$ one obtains the heat that is dissipated along the stochastic path

$$Q[\{n(t')\}_{0 \leq t' \leq t}] = \sum_{i=0}^{N-1} Q_{n_i n_{i+1}} = T [s_{n(0)}^{\text{int}} - s_{n(t)}^{\text{int}}] + k_B T \sum_{i=0}^{N-1} \ln \frac{w_{n_i n_{i+1}}}{w_{n_{i+1} n_i}}, \quad (2.8)$$

where the last identity has been deduced from (2.7). Similarly one obtains from (2.5) the heat dissipated along a path of a Brownian particle $\{x_{t'}\}_{0 \leq t' \leq t}$, which is given by

$$Q[\{x_{t'}\}_{0 \leq t' \leq t}] = \int_0^t \mathrm{d}Q = \int_0^t F(x_{t'}, t') \circ \mathrm{d}x_{t'}, \quad (2.9)$$

i.e., the friction force integrated along the path. For the following discussion, however, we mainly focus on the discrete state description, since one can mathematically turn a

continuous Brownian motion to a biased random walk on a infinitesimal lattice (cf., low noise approximation [33, 34]).

2.2 Stochastic entropy and Fluctuation theorems

The Jarzynski relation, one of the most prominent integral fluctuation theorem [4, 5], is an exact relation that allows one to infer equilibrium free energy changes directly from non-equilibrium finite time work measurements. We will sketch a fluctuation theorem that is related to this remarkable result. For convenience we set $k_B \equiv 1$ from now on, which renders entropy dimensionless and turns temperature into a thermal energy ($k_B T \rightarrow T$).

Similarly to the heat and work evaluated along a single trajectory, it has been found that the Shannon entropy of systems can be defined on the level of individual trajectories. For a system labeled by discrete states one can define the stochastic entropy $s[n(t), t] \equiv -\ln P_t(n(t))$ [6, 8], where P_t is the solution of the master equation (2.6). Taking the ensemble average leads to the familiar Gibbs or Shannon entropy [35–37]

$$S(t) \equiv \langle s[n(t), t] \rangle = -\langle \ln P_t(n(t)) \rangle = -\sum_{n=1}^{\Omega} P_t(n) \ln P_t(n). \quad (2.10)$$

Summarizing all entropic changes along the trajectory, namely, the change of systems entropy $\Delta s \equiv s[n(t), t] - s[n(0), 0] = \ln[P_0(n(0))/P_t(n(t))]$, the change of intrinsic entropy $\Delta s^{\text{int}} \equiv s_{n(t)}^{\text{int}} - s_{n(0)}^{\text{int}}$ and the medium entropy $\Delta s^{\text{m}} \equiv Q[\{x_{t'}\}_{0 \leq t' \leq t}]/T$, results in the total entropy along a trajectory $\Delta s^{\text{tot}} = \Delta s + \Delta s^{\text{int}} + \Delta s^{\text{m}}$ [18]. Most remarkably, it has been found that the stochastic entropy can be expressed by comparing probability $P[\{x_{t'}\}_{0 \leq t' \leq t}]$ of the path with its reverse path weight $P^{\text{R}}[\{x_{t'}\}_{0 \leq t' \leq t}]$ through $\Delta s^{\text{tot}} = \ln(P[\{x_{t'}\}_{0 \leq t' \leq t}]/P^{\text{R}}[\{x_{t'}\}_{0 \leq t' \leq t}])$ such that Δs^{tot} is odd under time reversal and obeys a integral fluctuation theorem [6, 8, 18, 32, 38]

$$\langle e^{-\Delta s^{\text{tot}}} \rangle = \sum_{\{x_{t'}\}_{0 \leq t' \leq t}} P[\{x_{t'}\}_{0 \leq t' \leq t}] \frac{P^{\text{R}}[\{x_{t'}\}_{0 \leq t' \leq t}]}{P[\{x_{t'}\}_{0 \leq t' \leq t}]} = 1. \quad (2.11)$$

Using Jensen's inequality one can derive for such a stochastic dynamics the second law of thermodynamics

$$\Delta S^{\text{tot}} \equiv \langle \Delta s^{\text{tot}} \rangle = \sum_{\{x_{t'}\}_{0 \leq t' \leq t}} P[\{x_{t'}\}_{0 \leq t' \leq t}] \ln \frac{P[\{x_{t'}\}_{0 \leq t' \leq t}]}{P^{\text{R}}[\{x_{t'}\}_{0 \leq t' \leq t}]} \geq 0. \quad (2.12)$$

As a technical side remark it should be noted that the third expression can be identified by the Kullback-Leibler distance between the forward path weight and its reverse $\Delta S^{\text{tot}} = D_{\text{KL}}(P[\{x_{t'}\}_{0 \leq t' \leq t}] || P^{\text{R}}[\{x_{t'}\}_{0 \leq t' \leq t}]) \geq 0$, which according to log-sum-inequality is positive and quantifies the “relative distance” between two probability distributions [36]. Specifically, the rate of the average total entropy production for the master equation (2.6) reads [8, 39, 40]

$$\dot{S}^{\text{tot}}(t) \equiv \frac{d}{dt} \Delta S^{\text{tot}} = \sum_{n, n'} P_t(n) w_{nn'} \ln \frac{P_t(n) w_{nn'}}{P_t(n') w_{n'n}} \geq 0. \quad (2.13)$$

If the system is driven between two equilibrium states, separated by an equilibrium free energy difference $\Delta\mathcal{F}$, one obtains with $\Delta s^{\text{tot}} \equiv \beta(W[\{n(t')\}_{0 \leq t' \leq t}] - \Delta\mathcal{F})$ the celebrated Jarzynski integral fluctuation theorem

$$\langle e^{-\beta W} \rangle = e^{-\beta \Delta\mathcal{F}}, \quad (2.14)$$

which allows to infer an equilibrium free energy difference from repeated experiments by using a nonlinear average of the work. The experiment can, in principle, be performed arbitrary away from equilibrium as long as the statistics is sufficient.

3 Stochastic thermodynamics of bipartite systems with feedback

This chapter introduces into stochastic thermodynamics of bipartite systems. We focus on the scenario where the first subsystem is used to extract work from a heat bath while being controlled by the second subsystem. We show that the second subsystem allows for a particularly transparent interpretation of a Maxwell’s demon, which is a feedback-driven engine. For example, the work that can be extracted from the first subsystem is bounded by the heat dissipated by the second subsystem, which represents the demon. A thermodynamic consistent quantity is derived, which we call the learning rate, that quantifies the rate at which the uncertainty of the controlled subsystem is reduced due to the coupling to the demon. The learning rate is shown to bound the extracted work from the first subsystem, while being itself bounded by the heat that is dissipated by the second subsystem. Compared to a second information theoretic measure called the transfer entropy, the learning rate is shown to be the tightest bound on the extracted work. From a simple example involving a four state system, we show that transfer entropy rate and the heat that is dissipated by the demon are not related through an inequality, which reveals the transfer entropy to be a thermodynamically inconsistent measure for the performance of a feedback controller. Moreover, the presented framework introduces ideas that will be relevant to cellular information processing, which goes beyond the realm of feedback-driven engines and is presented in chapter 4. This chapter is based on Ref. [41].

3.1 Introduction

3.1.1 Historical overview: Maxwell’s demon and Landauer principle

As we have briefly sketched in the introduction, thermodynamics of information processing originated a long time ago from thought experiments which seemingly violate the second law of thermodynamics. In the original proposal J. C. Maxwell invented an agent, “whose faculties are so sharpened that he can follow every molecule in its course” [25]. With such an agent, nowadays called Maxwell’s demon, it is possible to produce a difference in temperature without the expenditure of work, which is a direct violation of the second law of thermodynamics [25]. The idea is as follows: a box at uniform temperature is separated into two parts (left and right), where particles can only be exchanged through a small hole in the middle. The demon only opens the hole if a molecule with higher kinetic energy is coming from the right or a particle with lower kinetic energy is coming from the left, see Fig. 3.1. Otherwise the hole remains closed to reflect molecules with higher kinetic energy to the left or molecules with lower kinetic energy to the right, see lower panel of Fig. 3.1. After a certain time, the left side of the box becomes hotter and

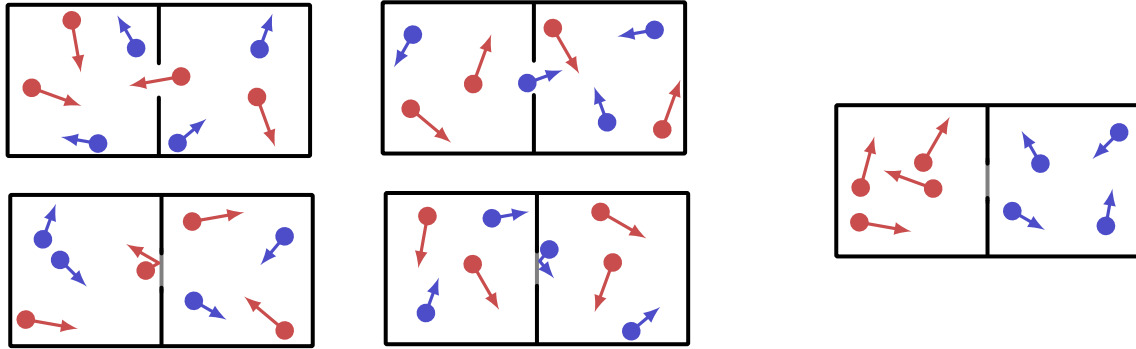


Figure 3.1 | Original Maxwell's demon setup. Faster molecules are characterized by elongated red arrows and slower molecules by shortened blue arrows. On the left are shown the four possible events with the corresponding open hole (upper panel) and closed hole (lower panel) configuration. Eventually, the system reaches a state with the right half being cooler than the left half (see right part of the figure).

the right side of the box cooler, as shown on the right in Fig. 3.1. With the information about the velocity and position of individual molecules a demon can apply feedback to run such a cooling process without the expenditure of work.

The first step towards a quantitative understanding of the connection between this paradox of Maxwell's demon and information theory has been done by L. Szilard [26]. He simplified the thought experiment to a single molecule in a box, which is in contact with a heat bath at temperature T . At the ensemble level one assumes an ideal gas with a single molecule in which the pressure is given by $p = k_B T/V$, where V is the volume of the box and k_B Boltzmann's constant. The experiment with the assistance of Maxwell's demon is shown in Fig. 3.2, which includes the following steps. A barrier is inserted in the middle of the box without the expenditure of work. There are two distinct cases that may occur, either the molecule is in the left half of the box ($x = L$) or in the right half ($x = R$). The demon then measures, whether the particle is left or right without error, i.e., the measurement outcome y satisfies $y = x$. Depending on the measurement outcome $y = L, R$, it moves the barrier to expand the volume, in which it has detected the particle, from $V_{\text{ini}} = V/2$ to $V_{\text{fin}} = V$. If the expansion is performed isothermally one is able to extract the maximum amount of work $W_{\text{ext}} = k_B T \ln(V_{\text{fin}}/V_{\text{ini}}) = k_B T \ln 2$. Finally, the barrier is removed to restore the initial state. In the complete cycle one has extracted an amount of heat $k_B T \ln 2$ from a single heat bath that has been completely converted into work, according to the first law of thermodynamics.

Note that this work extraction is not possible without the measurement y , since one cannot know, whether the barrier has to be moved to the left or to the right to expand the gas. Specifically, if the demon measures the particle in the wrong side of the box $y \neq x$, one would perform a compression of the gas, which requires work. In Fig. 3.2 an error would correspond to moving the barrier to the left in state (iii.a) or to the right in state (iii.b). One can confirm that the maximum work $W = k_B T \ln 2$ can only be extracted if the binary measurement $y = L, R$ is performed perfectly ($y = x$). To restore the second law of thermodynamics, L. Szilard believed that somehow an entropy increase due to the

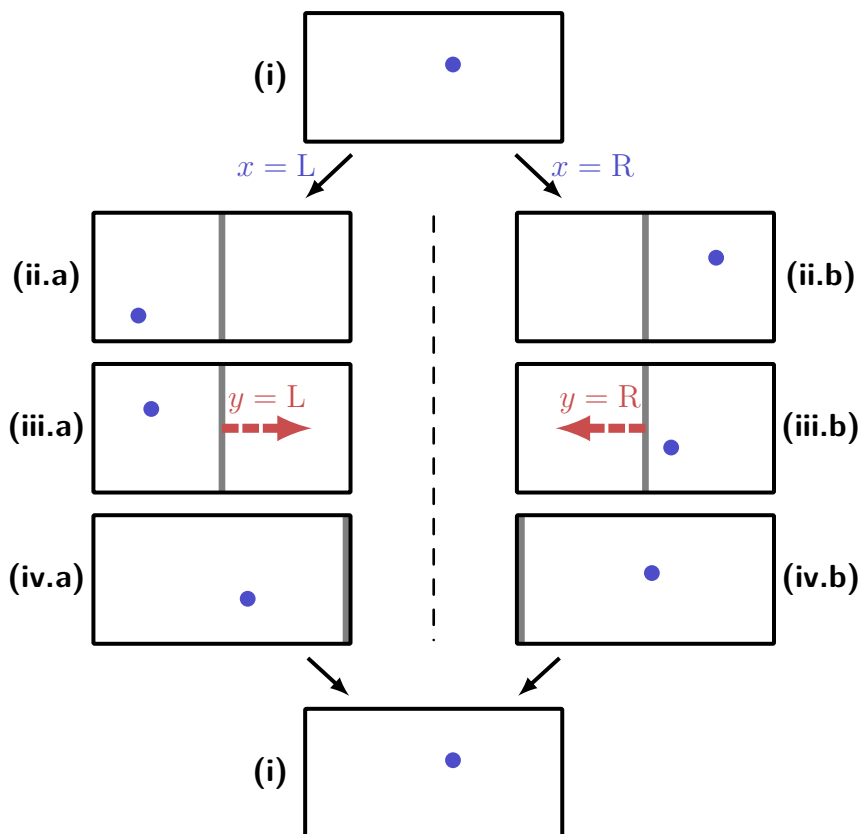


Figure 3.2| Szilard engine with error free measurement. From (i) to (ii) the barrier is inserted. Step (ii) to (iii), the demon measures the position of the particle $x = R, L$, depending on the measurement outcome $y = R, L$ ($y = x$ for perfect measurement), the demon moves the barrier away from y (see red dashed arrow). After the barrier reaches the end of the box (iv) it is removed to restore the original state (i).

demon's measurement had to compensate for the entropy decrease in the heat bath [26].

This paradox about Maxwell's demon could be resolved with the result of R. Landauer, who found that logical irreversible computations, for example the erasure of a bit $0, 1 \rightarrow 1$, which do not have a single-valued inverse, are inevitably associated with a certain minimum amount of heat dissipated into the environment [22]. This important insight constitutes Landauer's principle, which for the first time provides a convincing quantitative theoretical limit on the energy consumption of computation. Specifically, the erasure of a single bit requires $k_B T \ln 2$ of heat to be dissipated. Consequently, the demon from the Szilard engine (Fig. 3.2) has to dissipate a minimum amount of energy $k_B T \ln 2$ to overwrite (or erase) the measurement outcome from the previous cycle [42]. Assuming the engine is operating cyclically and the demon has only a finite data storage available, it is inevitable to erase some part of the memory to measure the position of the particle in the following cycle.

C. H. Bennett has used Landauer's principle to resolve the paradox of Maxwell's demon in the seminal work on the thermodynamics of computation [42], where he also stressed the difference between logical irreversibility and thermodynamic irreversibility. The latter

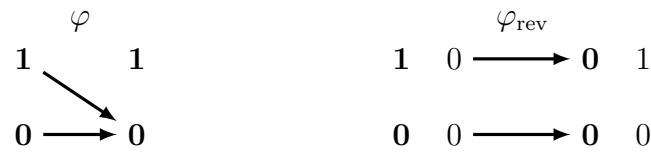


Figure 3.3 | Logical irreversible erasure operation φ turned reversible φ_{rev} . The reversible operation requires an auxiliary bit at state 0.

cannot be circumvented, whereas logical irreversibility can be made reversible, as shown in Fig. 3.3, which requires an auxiliary blank state “0” that has to be prepared. If one would use a tape of auxiliary blank states one could, in principle, render any computational program reversible [42]. Such a program, however, has to store “the input in some corner of the machine”, which will finally “clutter up our machine bit positions with unnecessary information about intermediate results” [22]. Moreover, it requires a prepared blank tape, with only zero’s, for instance, see [42] for more detailed information.

Summarizing, the paradox of the demon, firstly proposed by J. C. Maxwell, which shows the “limitations of the second law of thermodynamics” [25], can be resolved with Landauer’s principle which “exorcises” Maxwell’s demon. Any work (or heat) that the demon extracts from a heat bath in a cyclic operating engine via measurement and feedback must be compensated by the thermodynamic costs of overwriting or erasing its memory. For more information on the developments of Maxwell’s demon the reader is referred to [43–46]. For further information on Landauer’s principle and on fundamental limits to computation, see [42, 47] or [48] for a broader more recent review.

3.1.2 Recent experimental advances for feedback systems

The reason why Maxwell’s demon has attracted renewed interest, recently, is due to the fact that experimental as well as theoretical progress has been made, which allows to perform and analyze single molecule experiments. Thereby, one has to control individual particles and measure energy exchanges of the order of $1 k_{\text{B}}T$ (e.g., $k_{\text{B}}T \simeq 4 \times 10^{-21}$ J at room temperature).

Experiments that mimic a Szilard engine have firstly been realized with colloidal systems. In the first experiment a dimeric colloidal particle was attached to a glass surface [27]. A potential was generated by a rotating electric field that was under feedback control. By employing measurement and feedback, the particle effectively moved up a spiral-staircase-like potential and heat was thereby effectively converted into useful work [27]. In another experiment a colloidal particle has been trapped by two optical tweezers with an additional static electric field, which allowed to study the energetics of a micro-sized Szilard engine [49]. These colloidal particle experiments are typically performed at room temperature.

Information powered engines have also been realized with single electron experiments at low temperatures [50–52]. By controlling a gate voltage of a single electron transistor, one can build an information-driven engine that extracts work from a single heat bath [50, 51]. It has been demonstrated that information can also be used to power a refrigerator by applying feedback to a single electron transistor, which achieved a cooling power of

about 6×10^{-18} W [52]. This information powered refrigerator is closely related to the original proposal of Maxwell’s demon, shown in Fig. 3.1.

Landauer’s principle on the other side has been experimentally verified with colloidal systems in a double well potential [23, 24]. The erasure was performed by tilting the potential with an external applied flow [23] or with a virtual potential, which was created by a feedback loop [24]. Both experiments confirmed that the average work, necessary to erase a single bit, is above Landauer’s limit $k_B T \ln 2$. Moreover, it has been observed that Landauer’s limit can only be reached if the erasure process is performed quasi-statically; see [53] for a more detailed experimental view.

3.1.3 Second law and fluctuation theorems with feedback

Alongside the experimental advances discussed above, considerable theoretical progress has been made, which involves the derivation of second law inequalities [54–59] and integral fluctuation relations [60–68] for feedback-driven engines.

Moreover, simple models have been investigated that provide interesting implications or further insight [69–90]. More precisely, these models involve feedback-driven Brownian particles in a ratchet-like potential [69] or in a harmonic potential [76–79], where information of a measurement is used to extract work or to reduce fluctuations and, thereby, effectively cool down the system. A Kalman filter has been shown to “optimally” reduce fluctuations in a linear systems [71, 87, 88] such as colloidal systems or electrical circuits. Two or multilevel systems were investigated [72, 74, 80, 85, 86, 89], where individual energy levels are under control by some external agent. Among them were models for single electron transistors [85] and information-driven engines that mimic the kinetics of a molecular motor [74], which will be of particular importance for this thesis. Furthermore, correlations between measurements have been shown to cause an interesting phase behavior [86, 89], where above a critical measurement error the current measurement outcome becomes less trustworthy than the sequence of previous measurements. Protocols that optimize the conversion of information to work were investigated in [73]. Specific models are used to discuss Landauer’s principle with continuous double well potentials [70, 81] or discrete two level systems [82], the latter allowed that the ultimate limit proposed by Landauer can only be attained with a quasi-static protocol. A study on the measurement cost can be found in [75]. Finally, a critique on the relevance of Landauer’s principle to feedback-driven engines can be found in [91]. For example, the thermodynamic cost for realizing a time dependent protocol as it is used for the Szilard engine from Fig. 3.2 is at least five times the amount predicted by using Landauer’s principle.

Despite these theoretical efforts a unifying framework for feedback-driven engines that includes the dynamics of both controlled system and a continuously coupled feedback controller, had not been investigated in these previous studies. The only exception I am aware of is Ref. [57], which considered two jointly coupled colloidal particles performing Brownian motion.

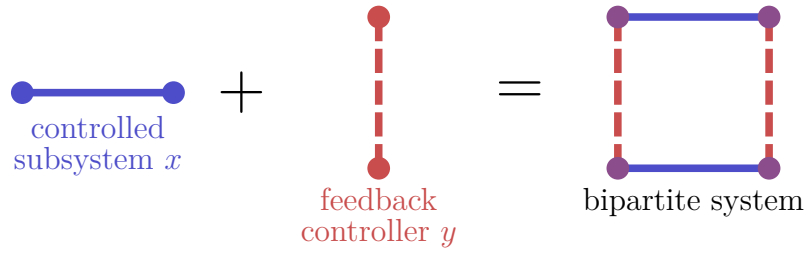


Figure 3.4 | Bipartite Markov process, where x labels a subsystem that is under control by another subsystem y . The bipartite system, which is labeled by variable (x, y) , includes the dynamics of both parts.

3.2 Bipartite systems and entropy production

3.2.1 Basic definitions and Shannon entropy

We assume a system is separated into two subsystems that are coupled to each other. The first subsystem “x” is labeled by states $x \in \{1, \dots, \Omega_x\} \equiv \mathcal{X}$ and the second subsystem “y” is labeled by states $y \in \{1, \dots, \Omega_y\} \equiv \mathcal{Y}$. The joint system of “x” and “y” is then labeled by a pair of variables $\mathbf{z} \equiv (x, y)$, where $x \in \mathcal{X}$ and $y \in \mathcal{Y}$, i.e., $\mathbf{z} \in \mathcal{Z} \equiv \mathcal{X} \times \mathcal{Y}$. We restrict our discussion to a class of bipartite Markov processes [92, 93], for which the transition rates from (x, y) to (x', y') satisfy

$$w_{yy'}^{xx'} \equiv \begin{cases} w_y^{xx'} & \text{if } x \neq x' \text{ and } y = y', \\ w_{yy'}^x & \text{if } x = x' \text{ and } y \neq y', \\ 0 & \text{otherwise.} \end{cases} \quad (3.1)$$

A transition, where the variables x and y changes simultaneously is not allowed, which is the central feature of bipartite systems. In this chapter we focus on feedback-driven systems, where x labels the state of a controlled system and y labels the state of the feedback controller, see Fig. 3.4. The bipartite system joins the dynamics of both the controlled subsystem “x” and the feedback controller “y”. Other examples for such systems can be found in cellular sensing [92, 94, 95], where one variable could represent the state of a receptor and the second variable a concentration of phosphorylated internal protein or the degree of methylation of a receptor, which is important for cellular adaptation [95]. Another example are quantum-dots exchanging particles with two particle reservoirs [85, 96]. Moreover, two interacting colloids [97] provide a continuous example for a bipartite system. Understanding the thermodynamics of such bipartite systems is, therefore, of particular importance.

The dynamics associated with the transition rates (3.1) is governed by the master equation

$$\dot{P}_t(x, y) \equiv \sum_{x' \in \mathcal{X}} [P_t(x', y)w_y^{xx'} - P_t(x, y)w_y^{xx'}] + \sum_{y' \in \mathcal{Y}} [P_t(x, y')w_{yy'}^x - P_t(x, y)w_{yy'}^x], \quad (3.2)$$

where $P_t(x, y)$ is the probability of finding the joint system in state $(x_t, y_t) = (x, y)$ at time t . After a certain time the joint system reaches a steady state distribution, which

we denote by $P(x, y)$, where the right hand side of (3.2) vanishes. The marginals of this steady state joint distribution are denoted by $P(x) \equiv \sum_y P(x, y)$ and $P(y) \equiv \sum_x P(x, y)$. The conditional steady state distributions are defined by $P(x|y) \equiv P(x, y)/P(y)$ and $P(y|x) \equiv P(x, y)/P(x)$. Moreover, we assume here and in the following that each sum containing the summation variable x and y runs over all elements of \mathcal{X} and \mathcal{Y} , respectively.

The key information theoretic quantities are the Shannon entropy and the mutual information [35–37]. The Shannon entropy of a random variable A is

$$H[A] \equiv - \sum_a \mathcal{P}(A = a) \ln \mathcal{P}(A = a), \quad (3.3)$$

where a is a specific possible value of A and $\mathcal{P}(A = a)$ is the probability of the event $A = a$. We generally use “ \mathcal{P} ” as a probability measure. The Shannon entropy $H[A]$ quantifies the uncertainty of the random variable A . If A is the instantaneous state of the system, i.e., $A = (x_t, y_t)$ with possible events $a = (x, y) \in \mathcal{Z}$, the Shannon entropy of the system reads, explicitly,

$$H[x_t, y_t] = - \sum_{x,y} P_t(x, y) \ln P_t(x, y). \quad (3.4)$$

As a short remark, from Eq. (3.4) and $n(t) = (x_t, y_t)$ we find $S(t) = H[x_t, y_t]$. The random variable A can also represent a full time series x_0^t of subsystem “x” or a full time series y_0^t of subsystem “y”. In this latter case the sum over all possible realizations in (3.3) corresponds to a functional integral over all possible trajectories. The conditional Shannon entropy of A given another random variable B is given by

$$H[A|B] \equiv - \sum_{a,b} \mathcal{P}(A = a, B = b) \ln \mathcal{P}(A = a|B = b), \quad (3.5)$$

where $\mathcal{P}(A = a|B = b) \equiv \mathcal{P}(A = a, B = b)/\mathcal{P}(B = b)$. The conditional entropy quantifies the uncertainty of random variable A if the random variable B is known. Since side information always leads to decreased uncertainty, that is, $H[A] \geq H[A|B]$, one can define the positive mutual information

$$I[A:B] \equiv H[A] - H[A|B] = H[B] - H[B|A] \geq 0, \quad (3.6)$$

where the second equality indicates that the mutual information is symmetric in the variables A and B , i.e., $I[A:B] = I[B:A]$. Most importantly, the mutual information can be interpreted as the reduction of uncertainty of A due to the side information contained in B . Similarly, the conditional mutual information reads

$$I[A:B|C] \equiv H[A|C] - H[A|B, C] \geq 0, \quad (3.7)$$

where C is a third random variable. For more details the reader is referred to [36].

3.2.2 Entropy production of the subsystem

The systems Shannon entropy is given by (3.4). Taking the time derivative and inserting the master equation (3.2) yields a rate of Shannon entropy change

$$\frac{d}{dt} H[x_t, y_t] = \sum_{x,x',y} P_t(x, y) w_y^{xx'} \ln \frac{P_t(x, y)}{P_t(x', y)} + \sum_{x,y,y'} P_t(x, y) w_{yy'}^x \ln \frac{P_t(x, y)}{P_t(x, y')}, \quad (3.8)$$

where the first term corresponds to the Shannon entropy change due to jumps in the subsystem “x” and the second term to the Shannon entropy change due to jumps in the subsystem “y”. In the steady state the probability distribution is constant and, hence, the rate of systems entropy change (3.8) vanishes, whereas the individual contributions are not zero. For instance, the change in Shannon entropy due to the dynamics of subsystem “x” reads

$$h_x \equiv \sum_{x,x',y} P(x,y) w_y^{xx'} \ln \frac{P(x,y)}{P(x',y)}. \quad (3.9)$$

Similarly, the change in the Shannon entropy due to jumps of the subsystem “y” is

$$h_y \equiv \sum_{x,y,y'} P(x,y) w_{yy'}^x \ln \frac{P(x,y)}{P(x,y')}. \quad (3.10)$$

Since the joint Shannon entropy $H[x_t, y_t]$ remains constant in the steady state, one can find $h_x + h_y = 0$, which implies that an increase of Shannon entropy h_x due to dynamics of subsystem “x” must be compensated by a decrease of Shannon entropy $-h_y$ due to the dynamics of subsystem “y”, i.e., $h_x = -h_y$.

Similar to the change in the Shannon entropy the entropy production in the external medium [18] for bipartite systems can be expressed by the following two contributions. The first contribution is the entropy production in the environment due to transitions in subsystem “x”, which is given by

$$\sigma_x \equiv \sum_{x,x',y} P(x,y) w_y^{xx'} \ln \frac{w_y^{xx'}}{w_y^{x'x}}, \quad (3.11)$$

where $P(x,y)$ is the steady state distribution of (3.2). The second contribution is caused by transitions in the subsystems “y”

$$\sigma_y \equiv \sum_{x,y,y'} P(x,y) w_{yy'}^x \ln \frac{w_{yy'}^x}{w_{y'y}^x}. \quad (3.12)$$

These two contributions together satisfy the standard second law of thermodynamics [18]

$$\sigma \equiv \sigma_x + \sigma_y \geq 0. \quad (3.13)$$

As a technical side remark it should be noted that σ_x (σ_y) is not related to a coarse-grained entropy production as for example discussed in [97–106] since it requires the detailed dynamics of both parts of the system. For instance, the coarse-grained trajectory of the “x”-process is not sufficient to calculate σ_x .

Besides the second law for the full system (3.13), we find the total entropy production caused by transitions of the subsystem “x” using (3.9) and (3.11)

$$\sigma_x + h_x = \sum_{x,x',y} P(x,y) w_y^{xx'} \ln \frac{P(x,y) w_y^{xx'}}{P(x',y) w_y^{x'x}} \geq 0. \quad (3.14)$$

This inequality is direct consequence of the log sum inequality and is explicitly considered in [57] for a Brownian motion and in [107] for a Markov jump process.

The same inequality as (3.14) is also valid for the subsystem “y”

$$\sigma_y + h_y = \sum_{x,y,y'} P(x,y) w_{yy'}^x \ln \frac{P(x,y) w_{yy'}^x}{P(x,y') w_{y'y}^x} \geq 0. \quad (3.15)$$

3.2.3 Interpretation of subsystem “y” as a Maxwell’s demon

Let us now consider the case where subsystem “x” is controlled by subsystem “y”. For example, subsystem “y” plays the role of a Maxwell’s demon, which implies that the entropy in the external medium decreases at a rate $-\sigma_x$ due to dynamics of the subsystem “x”. From (3.14), (3.15) and $h_x = -h_y$ follow the inequalities

$$-\sigma_x \leq h_x \leq \sigma_y. \quad (3.16)$$

For the scenario of a Maxwell’s demon setup $-\sigma_x$ becomes positive, the first inequality states that the entropy reduction in the external medium is bounded by the rate $h_x = -h_y$ at which the subsystems entropy is reduced due to its coupling to the Maxwell’s demon (subsystem “y”). We will discuss this in more detail below, when we introduce the learning rate. The second inequality involves σ_y , which gives the thermodynamic costs the demon has to invest.

For a more specific interpretation we focus on an isothermal process with the following local detailed balance relation involving the first law

$$\ln \frac{w_y^{xx'}}{w_y^{x'x}} = E(x,y) - E(x',y) + W_y^{xx'}, \quad (3.17)$$

where $E(x,y)$ is the internal energy of state (x,y) and $W_y^{xx'}$ is the work applied to the system along the transition $(x,y) \rightarrow (x',y)$; the left hand side constitutes the heat that is dissipated along the transition [see, e.g., (2.7)]. Note that $W_y^{x'x} = -W_y^{xx'}$. We have set here and throughout the chapter $k_B T \equiv 1$, i.e., all energies are expressed in units of $k_B T$. In the stationary state we obtain a rate of energy change due to dynamics of subsystem “x”

$$\dot{E}_x \equiv \sum_{x,x',y} P(x,y) w_y^{xx'} [E(x',y) - E(x,y)] \quad (3.18)$$

and the rate of extracted work

$$\dot{W}^{\text{out}} \equiv - \sum_{x,x',y} P(x,y) w_y^{xx'} W_y^{xx'}. \quad (3.19)$$

Using the first law we can identify $\sigma_x = -\dot{E}_x - \dot{W}^{\text{out}}$ as the dissipated heat due to transitions of variable x . For the specific case $\dot{E}_x = 0$ we find $-\sigma_x = \dot{W}^{\text{out}}$ implying with (3.16) that the extracted work is bounded by h_x . Furthermore, the average energy $E \equiv \sum_{x,y} P(x,y) E(x,y)$ remains constant in the stationary state, which allow to identify $\sigma_y = \dot{W}^{\text{in}}$, where \dot{W}^{in} is the rate at which the Maxwell’s demon (subsystem “y”) invests

work. The standard second law $\sigma_x + \sigma_y \geq 0$ then states $\dot{W}^{\text{in}} \geq \dot{W}^{\text{out}}$. From this example one can see that inequalities (3.16) for this scenario imply $\dot{W}^{\text{out}} \leq h_x \leq \dot{W}^{\text{in}}$, which refines the standard second law of thermodynamics.

Similar ideas have been proposed, where information has been considered as a reservoir. For example, Mandal and Jarzynski has introduced a minimal model that constitutes an autonomous Maxwell's demon [108]. The conceived device is supposed to “convert heat into work” while simultaneously randomizing a memory register. By increasing the Shannon entropy of the register the system is able to deliver work. Conversely, work is required to reduce the randomness in a memory register, which can be quantified by its Shannon entropy [108], see [109] for a model that includes reversible transitions. This model allows to discuss an autonomous Maxwell demon engine and Landauer's principle on the same footing, simultaneously. In the above description the delivered work corresponds to $-\sigma_x$ and the work cost to restore the memory register corresponds to σ_y , i.e., subsystem “y” constitutes the memory register. This idea which was proposed by Bennett [42] has triggered the idea of information reservoirs [68, 109–117]. Similarly, a memory register or tape that randomizes itself can also be used to let heat flow from cold to hot reservoirs [118].

Summarizing, these bipartite systems allow for a transparent interpretation of a Maxwell's demon, where the full thermodynamic cost is easily accessible via the standard second law of thermodynamics (3.13). In the following we interpret h_x as the rate at which subsystem “y” learns about the subsystem “x”, which allows us to explain the importance of thermodynamic consistency as well as its relation to an information theoretic measure called “transfer entropy” that is important to detect causal influence within a time series analysis.

3.2.4 Learning rate and thermodynamic consistency

The learning rate is defined as [119, 120]

$$l_y \equiv \frac{H[x_t|y_t] - H[x_t|y_{t+dt}]}{dt}, \quad (3.20)$$

where here and in the following we assume $dt \rightarrow 0$ for all expression with dt in the denominator. The learning rate quantifies the rate at which subsystem “y” reduces the uncertainty about the subsystem “x” that is under control. Note that if system “y” undergoes a transition $y_t \rightarrow y_{t+dt}$ it forgets its previous state, which is due to the Markovian character of the dynamics of the full bipartite system. For example, the learning rate (3.20) accounts for this “physical forgetting”, since the definition (3.20) does not contain a conditional uncertainty that involves y_t and y_{t+dt} , simultaneously. In Sec 3.3 we will discuss an information theoretic measure called transfer entropy that can be used to detect causal influence between two random processes and contains more than a single time step of the process.

Using the relations

$$\begin{aligned} \mathcal{P}(x_{t+dt} = x' | x_t = x, y_t = y) &= w_y^{xx'} dt + O(dt)^2 \quad \text{for } x \neq x' \\ \mathcal{P}(y_{t+dt} = y' | x_t = x, y_t = y) &= w_{yy'}^x dt + O(dt)^2 \quad \text{for } y \neq y' \end{aligned} \quad (3.21)$$

the learning rate (3.20) becomes

$$l_y = \sum_{x,y,y'} P(x,y) w_{yy'}^x \ln \frac{P(x|y')}{P(x|y)} \quad (3.22)$$

in the steady state. Most importantly we find $l_y = h_x$ in the stationary state, which can be understood as follows. Using (3.9) we find

$$h_x = \sum_{x,x',y} P(x,y) w_y^{xx'} \ln \frac{P(x|y)}{P(x'|y)} = \frac{H[x_{t+dt}|y_t] - H[x_t|y_t]}{dt}. \quad (3.23)$$

Since the conditional Shannon entropy remains constant, that is, $\frac{d}{dt}H[x_t|y_t] = h_x - l_y = 0$, we can interpret h_x as the new randomness that enters due to the dynamics of variable x and l_y as the reduction of uncertainty due to the coupling with subsystem “y”. Therefore, l_y quantifies the rate at which variable y learns due to its dynamics about a second variable x . Identifying $h_x = l_y$ we can rewrite (3.16) to

$$-\sigma_x \leq l_y \leq \sigma_y. \quad (3.24)$$

This replacement has the following main advantages. Eq. (3.20) provides more direct interpretation than (3.9): The first inequality in (3.24) implies that the entropy decrease in the medium due to subsystem “x”, which is $-\sigma_x$, is bounded by the rate at which subsystem “y” learns about the subsystem “x” under control. The second inequality in (3.24) underlines the thermodynamic consistency since the learning rate l_y is bounded by the (additional) thermodynamic cost σ_y that arises from the variable y . For this second relation it is important to note that after a transition $y_t \rightarrow y_{t+dt}$ the state y_t has been “erased” and replaced by y_{t+dt} . Therefore, the second inequality constitutes Landauer’s principle [22] for bipartite systems and guarantees thermodynamic consistency, which is important to assure that there is no additional “hidden third” part involved. Second and more importantly, we are now able to discuss the link between l_y and the transfer entropy, which is useful to detect directed information transfer between two random processes. We will discuss the transfer entropy in the following section after making some remarks on the current state of research.

Using (3.6) one can easily find that the learning rate (3.20) can be written as the time derivative of a time delayed mutual information

$$l_y = \frac{I[x_t:y_{t+dt}] - I[x_t:y_t]}{dt}, \quad (3.25)$$

which has been used under the term “information flow” [57, 88, 96]. Therefore, “information flow” and learning rate are equivalent quantities, which describe the increase of a mutual information between feedback controller “y” and the other subsystem “x”. One can explicitly verify this statement by comparing \dot{I}^Y from [96] with l_y defined here in (3.22).

Similarly, for the steady state, where $l_y = h_x$ holds, we obtain

$$l_y = h_x = \frac{I[x_t:y_t] - I[x_{t+dt}:y_t]}{dt}. \quad (3.26)$$

This expression has been used in [59], where $I[x_{t+dt}:y_t]$ has been considered as “predictive power” of subsystem “y” about subsystem “x”. Moreover the difference $I[x_t:y_t] - I[x_{t+dt}:y_t]$ has been called “(useless) nostalgia”. Here it should be stressed that in [59] an erasure process without feedback was assumed. We will later see in chapter 4 that the learning rate l_y can also be used to describe the sensory performance of a sensor “y” that is influenced by a signal “x” in the absence of feedback, which is a different physical scenario.

3.3 Transfer entropy in bipartite systems

3.3.1 Causal influence between two random processes

The transfer entropy is a information theoretical measure that has been proposed to detect causal dependencies between two random processes [121]. It is particularly important for the relation between information and thermodynamics for causal networks [67], feedback-driven systems [65] and computation [122, 123]. The transfer entropy from subsystem “x” to subsystem “y” is defined by [121]

$$\mathcal{T}_{x \rightarrow y} \equiv \frac{H[y_{t+dt}|y_0^t] - H[y_{t+dt}|y_0^t, x_0^t]}{dt} = \frac{H[y_{t+dt}|y_0^t] - H[y_{t+dt}|x_t, y_t]}{dt}, \quad (3.27)$$

where y_0^t denotes the history of visited states of subsystem “y” along the time interval $[0, t]$. The second equality in (3.27) follows from the Markov property of the full process. For simplicity we assume here and in the following $t \rightarrow \infty$, i.e., the system is in the stationary state at time t . From the definition of the transfer entropy one can verify that $\mathcal{T}_{x \rightarrow y}$ is nonzero if and only if variable y is influenced by variable x . For example if variable y were not affected by x both conditional entropies would become equal, i.e., $H[y_{t+dt}|y_0^t] = H[y_{t+dt}|y_0^t, x_0^t]$ leading to a vanishing transfer entropy ($\mathcal{T}_{x \rightarrow y} = 0$). This sensitivity for causal influence “x \rightarrow y” is important to distinguish a driven system from a feedback-driven system. If subsystem “x” were just driven by subsystem “y”, then σ_x could not be negative as in the scenario of Maxwell’s demon. The following discussion clarifies this issue.

Using (3.27) the transfer entropy can be written as

$$\mathcal{T}_{x \rightarrow y} = \frac{H[y_{t+dt}|y_0^t] - H[y_{t+dt}|x_t, y_0^t]}{dt} = \frac{I[y_{t+dt}:x_t|y_0^t]}{dt} = \frac{H[x_t|y_0^t] - H[x_t|y_0^{t+dt}]}{dt}, \quad (3.28)$$

where we have used $H[y_{t+dt}|x_t, y_t] = H[y_{t+dt}|x_t, y_0^t]$ in the first step. The second step shows the transfer entropy rate as a mutual information (3.7) that underlines its positivity $\mathcal{T}_{x \rightarrow y} \geq 0$. The last step formally relates the transfer entropy to the learning rate (3.20). The difference between the transfer entropy and the learning rate is that the transfer entropy accounts for the entropy reduction due to the full time history instead of the instantaneous state. Specifically, the formal replacement $l_y \rightarrow \mathcal{T}_{x \rightarrow y}$ by comparing (3.20) and (3.28) reads $y_t \rightarrow y_0^t$ and $y_{t+dt} \rightarrow y_0^{t+dt}$, which is also illustrated in Fig. 3.5. Most remarkably, one can show that

$$l_y \leq \mathcal{T}_{x \rightarrow y}, \quad (3.29)$$

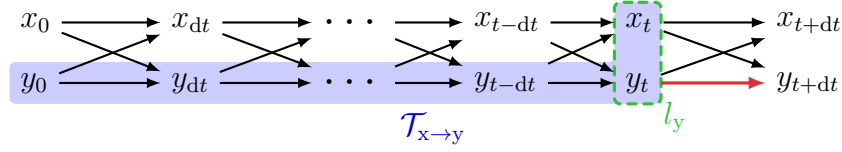


Figure 3.5| Illustration of transfer entropy $\mathcal{T}_{x \rightarrow y}$ and learning rate l_y . Bayesian network representation from [67, 124], where arrows demonstrate their causal relations, for example x_{t+dt} and y_{t+dt} evolves from x_t, y_t independently, which is due to the bipartite structure. The learning rate l_y accounts for the reduction of uncertainty due to the instantaneous state (dashed green box) and the transfer entropy $\mathcal{T}_{x \rightarrow y}$ accounts for the reduction of uncertainty due to the full time history (blue shaded region).

see [41] or Sec. 3.A for a proof, which requires further preparations. This relation (3.29) constitutes one of the main results of this thesis, which states that the full time history of subsystem “y” learns more about subsystem “x” than its memoryless instantaneous state. This was shown for the first time in [41] and provides an important link between bipartite systems, which interact autonomically, and feedback-driven engines. For instance using (3.24) and (3.29) yields $-\sigma_x \leq l_y \leq \mathcal{T}_{x \rightarrow y}$. From the relation one can immediately see that $-\sigma_x \leq \mathcal{T}_{x \rightarrow y}$ implying a negative entropy production σ_x in the medium due to subsystem “x”, or equivalently $-\sigma_x > 0$ requires a nonzero transfer entropy ($\mathcal{T}_{x \rightarrow y} > 0$). On the other hand a vanishing transfer entropy $\mathcal{T}_{x \rightarrow y} = 0$ implies that subsystem “y” just drives subsystem “x” without any feedback, which in turn implies $\sigma_x \geq 0$, as mentioned at the end of the previous paragraph.

In feedback-driven engines the transfer entropy is useful if the state of a system is controlled by using repeated correlated measurements. To my knowledge, the first appearances of transfer entropy in the context of feedback-driven engines can be found in [56, 62], although the quantity was not used under this term. Shortly afterward, fluctuation theorems for feedback-driven engines involving transfer entropy, explicitly, have been found that account for correlations between repeated measurements in a more general context [65]. In [67] one can find a powerful framework called “information thermodynamics on causal networks”, which amongst other things, discusses bipartite colloidal systems. Interestingly, it has been found that repeated measurements show a phase transition, where above a critical measurement error the history of measurements allows to extract more information than just the current measurement outcome [86, 89]. The reason why the transfer entropy appears now for bipartite systems is that these systems consist of two parts, which continuously interact with one another. These interactions introduce time correlations that can be seen as correlated measurements of each subsystem, which are immediately fed back to the other subsystem.

Summarizing, the relation (3.29) advances the field in the following way. With the thermodynamic learning rate that obeys (3.24) we can now relate the transfer entropy to a thermodynamic consistent quantity quantifying the performance of a feedback device. Information theoretic efficiencies that involve transfer entropy and thermodynamic costs (e.g., $-\sigma_x/\mathcal{T}_{x \rightarrow y}$) can underestimate the thermodynamic efficiency ($-\sigma_x/\sigma_y$), where we assume $-\sigma_x$ to be positive. We will return to this point, explicitly, when discussing the examples in Sec. 3.4.

Similar to Eq. (3.27) the transfer entropy rate from subsystem “y” to subsystem “x”

can be written as

$$\mathcal{T}_{y \rightarrow x} \equiv \frac{H[x_{t+dt}|x_0^t] - H[x_{t+dt}|x_0^t, y_0^t]}{dt} = \frac{H[x_{t+dt}|x_0^t] - H[x_{t+dt}|x_t, y_t]}{dt}. \quad (3.30)$$

At this point it should be noted that determining the transfer entropy, explicitly, is generally difficult, since no closed analytical formula is known. An exception can be found for simple linear systems, see, e.g., [88]. The reason why the transfer entropy introduces such difficulties is the conditional Shannon entropy that involves the full time history of the coarse grained process x_0^t or y_0^t , which concerns $H[x_{t+dt}|x_0^t]$ from (3.30) and $H[y_{t+dt}|y_0^t]$ from (3.27). Fortunately, as we show in the following subsection one can find an analytical bound of the transfer entropy, which can be quite useful in particular if the dynamics of the two subsystems obey a certain time scale separation. We explain the numerical method to determine the transfer entropy by using random matrices to Appendix 3.B, which involves Shannon entropy rates that are explained shortly (subsection 3.3.3).

3.3.2 Analytic upper bound on transfer entropy rate

One important feature of Shannon entropy is that conditioning reduces entropy, i.e., $H[y_{t+dt}|y_t] \geq H[y_{t+dt}|y_0^t]$ holds [36], see also [92, 93]. Based on this inequality one can define the upper bound on the transfer entropy

$$\bar{\mathcal{T}}_{x \rightarrow y} \equiv \frac{H[y_{t+dt}|y_t] - H[y_{t+dt}|x_t, y_t]}{dt} \geq \frac{H[y_{t+dt}|y_0^t] - H[y_{t+dt}|x_t, y_t]}{dt} = \mathcal{T}_{x \rightarrow y}, \quad (3.31)$$

where we have identified the transfer entropy (3.27) in the last step. In other words, the upper bound $\bar{\mathcal{T}}_{x \rightarrow y}$ overestimates the randomness of the coarse-grained y -process. Inserting Eq. (3.21) and

$$\mathcal{P}(y_{t+dt} = y' | y_t = y) = \bar{w}_{yy'} dt + O(dt)^2 \quad \text{for } y \neq y', \quad (3.32)$$

where the coarse-grained transition rates are given by

$$\bar{w}_{yy'} \equiv \sum_x P(x|y) w_{yy'}^x, \quad (3.33)$$

into (3.31) yields

$$\bar{\mathcal{T}}_{x \rightarrow y} = \sum_{\substack{x, y, y' \\ y \neq y'}} P(x, y) w_{yy'}^x \ln \frac{w_{yy'}^x}{\bar{w}_{yy'}}. \quad (3.34)$$

Therefore, the upper bound $\bar{\mathcal{T}}_{x \rightarrow y}$ on the transfer entropy rate $\mathcal{T}_{x \rightarrow y}$ can be written in terms of the stationary distribution $P(x, y)$ and the transition rates $w_{yy'}^x$.

There are three important properties, that $\bar{\mathcal{T}}_{x \rightarrow y}$ adopts from $\mathcal{T}_{x \rightarrow y}$. First, its sensitivity for causal influence “ $x \rightarrow y$ ”. The bound of the transfer entropy is zero ($\bar{\mathcal{T}}_{x \rightarrow y} = 0$) if and only if $w_{yy'}^x = \bar{w}_{yy'}$, i.e., subsystem “ y ” is completely unaffected by subsystem “ x ”. This can be shown by using log-sum-inequality [36]. Second, the relation $l_y \leq \bar{\mathcal{T}}_{x \rightarrow y}$, which is

weaker than (3.29) but much simpler to show. For example, using (3.22) and (3.34) one obtains

$$\overline{\mathcal{T}}_{x \rightarrow y} - l_y = \sum_{\substack{x, y, y' \\ y \neq y'}} P(x, y) w_{yy'}^x \ln \frac{P(x|y) w_{yy'}^x}{P(x|y') \overline{w}_{yy'}} \geq 0, \quad (3.35)$$

where the last inequality follows from log-sum-inequality (summation over variable x) and Eq. (3.33). This inequality ($\overline{\mathcal{T}}_{x \rightarrow y} - l_y \geq 0$) has been shown in [57] for two coupled Brownian particles. Third, we expect $\overline{\mathcal{T}}_{x \rightarrow y} \simeq \mathcal{T}_{x \rightarrow y}$ if subsystem “ x ” evolves on a much faster time scale than subsystem “ y ” ($w_y^{xx'} \gg w_{yy'}^x$). In this case the coarse-grained y -process becomes approximately Markovian, since on the time scale of subsystem “ y ” the x -process effectively visits all its possible states resulting in a dynamic that is governed by transition rates (3.33), i.e., $H[y_{t+dt}|y_t] \simeq H[y_{t+dt}|y_0^t]$. Examples that underline this statement can be found in [93] and Fig. 3.10 from Sec. 3.4.4.

Similarly, with

$$\overline{w}^{xx'} \equiv \sum_y P(y|x) w_y^{xx'} \quad (3.36)$$

we obtain

$$\overline{\mathcal{T}}_{y \rightarrow x} = \sum_{\substack{x, x', y \\ x \neq x'}} P(x, y) w_y^{xx'} \ln \frac{w_y^{xx'}}{\overline{w}^{xx'}}, \quad (3.37)$$

which satisfies $\overline{\mathcal{T}}_{y \rightarrow x} \geq \mathcal{T}_{y \rightarrow x}$.

3.3.3 Rate of mutual information and Shannon entropy rates

Even though we have now found important bounds on the transfer entropy, $l_y \leq \mathcal{T}_{x \rightarrow y} \leq \overline{\mathcal{T}}_{x \rightarrow y}$, the transfer entropy $\mathcal{T}_{x \rightarrow y}$ can still be hard to determine, numerically. There are some recent advances involving the rate of mutual information [92, 93] and random matrices that can be applied here to numerically calculate the transfer entropy.

The rate of mutual information between two random processes x_0^t and y_0^t is defined by

$$\dot{\mathcal{I}} \equiv \lim_{t \rightarrow \infty} \frac{I[x_0^t : y_0^t]}{t} = \lim_{t \rightarrow \infty} \left(\frac{H[x_0^t]}{t} + \frac{H[y_0^t]}{t} - \frac{H[x_0^t, y_0^t]}{t} \right) \quad (3.38)$$

and quantifies the mutual information between two processes per time interval in the long time limit ($t \rightarrow \infty$). For notational convenience we assume from now on for all expressions involving time t the limit $t \rightarrow \infty$, without explicitly displaying “ $\lim_{t \rightarrow \infty}$ ”. Using the chain rule for probabilities we obtain [36, 92, 93]

$$\dot{\mathcal{I}} = \frac{H[x_{t+dt}|x_0^t] + H[y_{t+dt}|y_0^t] - H[x_{t+dt}, y_{t+dt}|x_t, y_t]}{dt}, \quad (3.39)$$

where we have used the Markov property of the full process $H[x_{t+dt}, y_{t+dt}|x_0^t, y_0^t] = H[x_{t+dt}, y_{t+dt}|x_t, y_t]$. The rate of mutual information is symmetric with respect to subsystem “ x ” and “ y ”, i.e., exchanging $x_0^t \leftrightarrow y_0^t$ does not vary $\dot{\mathcal{I}}$. Therefore, $\dot{\mathcal{I}}$ does not

distinguish between correlations that result from subsystem “x” influencing subsystem “y” and correlations that result from subsystem “y” influencing subsystem “x”. For bipartite processes, however, it is possible to split the rate of mutual information in two such contributions.

To see this we use (3.21) to verify the relation

$$\begin{aligned} \mathcal{P}(x_{t+dt} = x', y_{t+dt} = y' | x_t = x, y_t = y) \\ = \mathcal{P}(x_{t+dt} = x' | x_t = x, y_t = y) \mathcal{P}(y_{t+dt} = y' | x_t = x, y_t = y) + O(dt)^2, \end{aligned} \quad (3.40)$$

i.e., $H[x_{t+dt}, y_{t+dt} | x_t, y_t] = H[x_{t+dt} | x_t, y_t] + H[y_{t+dt} | x_t, y_t] + O(dt)^2$. With this finding one can rewrite the rate of mutual information as follows [41]

$$\begin{aligned} \dot{\mathcal{I}} &= \frac{H[x_{t+dt} | x_0^t] + H[y_{t+dt} | y_0^t] - H[x_{t+dt} | x_t, y_t] - H[y_{t+dt} | x_t, y_t]}{dt} \\ &= \mathcal{T}_{x \rightarrow y} + \mathcal{T}_{y \rightarrow x}. \end{aligned} \quad (3.41)$$

From the first to the second line we have identified the transfer entropy rates (3.27) and (3.30). Therefore, we can separate the correlations between two coarse-grained processes x_0^t and y_0^t into two causal contributions “x → y” and “y → x”.

There are discrete time methods for calculating Shannon entropy rates, which can be identified by the individual terms in the numerator of Eq. (3.39). The discrete time Shannon entropy rate of the full process reads [36]

$$\begin{aligned} H_{x,y}(dt) &\equiv H[x_{t+dt}, y_{t+dt} | x_0^t, y_0^t] = H[x_{t+dt} | x_t, y_t] + H[y_{t+dt} | x_t, y_t] + O(dt)^2 \\ &= - \sum_{\substack{x, x', y \\ x \neq x'}} P(x, y) dt w_{yy'}^x \left[\ln(dt w_y^{xx'}) - 1 \right] - \sum_{\substack{x, y, y' \\ y \neq y'}} P(x, y) dt w_{yy'}^x \left[\ln(dt w_{yy'}^x) - 1 \right] + O(dt)^2. \end{aligned} \quad (3.42)$$

One can associate the logarithm terms $\ln(dt w_y^{xx'})$ and $\ln(dt w_{yy'}^x)$ with jump events of variable x and y , respectively. The remaining terms that represent “−1” in the first and second bracket arise from remaining in state (x, y) for time dt , where we used that $(1 - dt\Sigma) \ln(1 - dt\Sigma) = -dt\Sigma + O(dt)^2$ holds. For $dt \rightarrow 0$ one can verify that $H_{x,y}(dt)/dt \rightarrow \infty$. The Shannon entropy rate for the continuous time process [93, 125, 126] can formally be obtained by setting $dt = 1$ in the leading term of (3.42)

$$\begin{aligned} \mathcal{H}_{x,y} &= - \sum_{\substack{x, x', y \\ x \neq x'}} P(x, y) w_y^{xx'} \left(\ln w_y^{xx'} - 1 \right) - \sum_{\substack{x, y, y' \\ y \neq y'}} P(x, y) w_{yy'}^x \left(\ln w_{yy'}^x - 1 \right) \\ &\equiv \mathcal{H}_{x,y}^{(1)} + \mathcal{H}_{x,y}^{(2)}, \end{aligned} \quad (3.43)$$

where we have identified $\mathcal{H}_{x,y}^{(1)}$ as the first sum and $\mathcal{H}_{x,y}^{(2)}$ as the second sum. See Appendix 3.B for a more detailed derivation.

Similarly, from the coarse-grained Shannon entropy rates

$$\begin{aligned} H_x(dt) &\equiv H[x_{t+dt} | x_0^t] \\ H_y(dt) &\equiv H[y_{t+dt} | y_0^t] \end{aligned} \quad (3.44)$$

one can define the continuous time Shannon entropy rates [41, 93]

$$\begin{aligned}\mathcal{H}_x &\equiv \frac{1}{dt} \left[H_x(dt) + \sum_{\substack{x,x',y \\ x \neq x'}} P(x,y) dt w_y^{xx'} \ln dt \right] \\ \mathcal{H}_y &\equiv \frac{1}{dt} \left[H_y(dt) + \sum_{\substack{x,y,y' \\ y \neq y'}} P(x,y) dt w_{yy'}^x \ln dt \right].\end{aligned}\tag{3.45}$$

We show in Appendix 3.B how to calculate these Shannon entropy rates directly in continuous time [93], see [92, 93, 127–129] for discrete time methods.

With the explicit analytical formula (3.43) as well as the method for calculating (3.45) presented in Sec. 3.B we are now able to calculate numerically the transfer entropies

$$\begin{aligned}\mathcal{T}_{x \rightarrow y} &= \mathcal{H}_y - \mathcal{H}_{x,y}^{(2)}, \\ \mathcal{T}_{y \rightarrow x} &= \mathcal{H}_x - \mathcal{H}_{x,y}^{(1)}.\end{aligned}\tag{3.46}$$

More information on Shannon entropy rates in discrete time can be found in [92, 127–129], on continuous time Shannon entropy rates for Markovian processes [125, 126], and more generally, coarse-grained non-Markovian processes, as relevant for Eq. (3.45), can be found in [93].

3.4 Main results and Examples

3.4.1 Summary of important inequalities

The main results from Eqs. (3.24), (3.29) and (3.31) can be summarized by

$$-\sigma_x \leq l_y \leq \begin{cases} \sigma_y, \\ \mathcal{T}_{x \rightarrow y} \leq \bar{\mathcal{T}}_{x \rightarrow y}, \end{cases}\tag{3.47}$$

which provides a clear interpretation of a Maxwell’s demon system, where subsystem “x” is measured and controlled by subsystem “y”. Thereby, $-\sigma_x$ is the rate at which subsystem “x” reduces the entropy of the external medium. For example, if there were no feedback, the second law would imply $\sigma_x \geq 0$, i.e., $-\sigma_x$ could not be positive. With the learning rate l_y we have found a thermodynamically consistent measure for feedback-driven engines that bounds on the one hand the entropy reduction due to the controlled system part “x” ($-\sigma_x \leq l_y$) and on the other hand is bounded by the thermodynamic cost σ_y of the feedback controller ($l_y \leq \sigma_y$).

The second line of (3.47) involves the transfer entropy, which is a conditional mutual information between feedback controller “y” and system $\mathcal{T}_{x \rightarrow y} = I[x_t : y_{t+dt} | y_0^t] / dt$ (note that $\bar{\mathcal{T}}_{x \rightarrow y} = I[x_t : y_{t+dt} | y_t] / dt$). The transfer entropy accounts for correlations between current “measurement” y_{t+dt} and “measurements” in the past y_0^t . For bipartite systems the transfer entropy can be considered as the tightest bound of $-\sigma_x$ involving a mutual information term as discussed in [54–56, 58, 60–65, 71–77, 86] for feedback systems, where [56, 62, 65, 67, 86] consider a transfer entropy term. However, no relation can be found

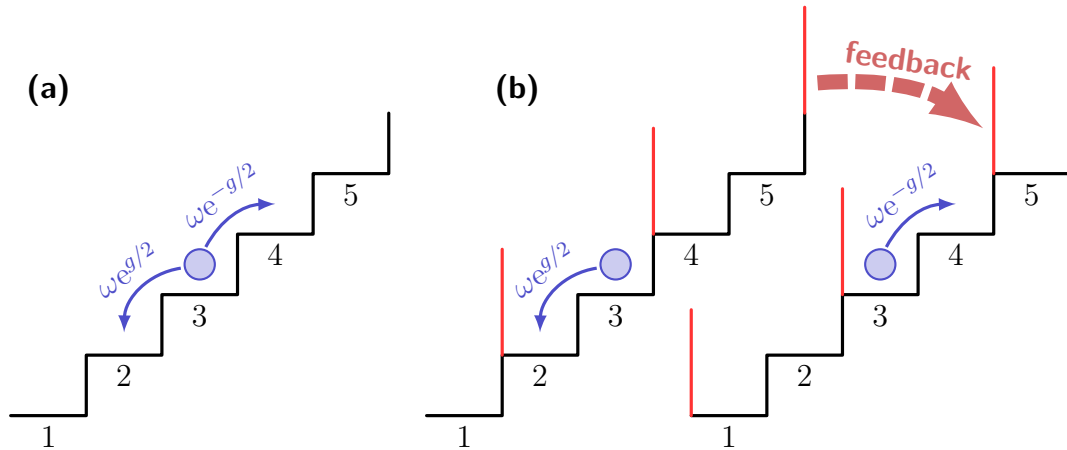


Figure 3.6| Biased random walk. (a) Random walk without feedback. (b) Random walk with feedback, where a barrier (shown in red) hinders the particle to pass. The feedback mechanism, which moves the barriers dependent on the position of the particle, allows to create a mean velocity upwards.

between the transfer entropy rate $\mathcal{T}_{x \rightarrow y}$ and the thermodynamic cost of the feedback device σ_y .

Summarizing, the learning rate l_y is the tightest bound on $-\sigma_x$. In contrast to the transfer entropy, the learning rate allows for a fully thermodynamic consistent view on each part of a bipartite system, since $-\sigma_x \leq l_y$ and $l_y \leq \sigma_y$ hold. From a technical point of view one should note that the learning rate l_y and $\overline{\mathcal{T}}_{x \rightarrow y}$ are generally much simpler to calculate than the full transfer entropy rate $\mathcal{T}_{x \rightarrow y}$. In the following, we illustrate our main results.

3.4.2 Biased random walk with stochastic feedback control

For our examples we consider the easiest conceivable system, which is related to the experiment from [27]. As shown in Fig. 3.6(a) we consider a simple biased random walk in a staircase-like potential. The “potential” arises from a load force $g > 0$ pointing to the left, such that one step to the right (left) delivers an amount of g ($-g$) work, where we have set $T \equiv 1$ for the examples. This load force implies that the rate for jumping up the potential ($\omega e^{-g/2}$) is smaller than the rate for jumping down the potential ($\omega e^{g/2}$), i.e., without any feedback the particle will move with mean velocity $\omega(e^{g/2} - e^{-g/2})$ down the potential (to the left) while dissipating potential energy.

We now introduce barriers behind every second step as illustrated in Fig. 3.6(b), which cannot be passed by the particle. The goal of the feedback mechanism is to alter the barrier positions according to the particle position. For example, as illustrated in Fig. 3.6(b), if the particle is at position “3” (odd numbered), the barriers will have to be shifted to an odd numbered position (see thick dashed arrow), such that the barrier is behind the particle to block the motion downwards.

Labeling the particle position by “even” and “odd” according to its position, one obtains four possible states that determine the particle position and barrier position, where each position can be either “odd” or “even”. In Fig. 3.7 all four possible states are shown,

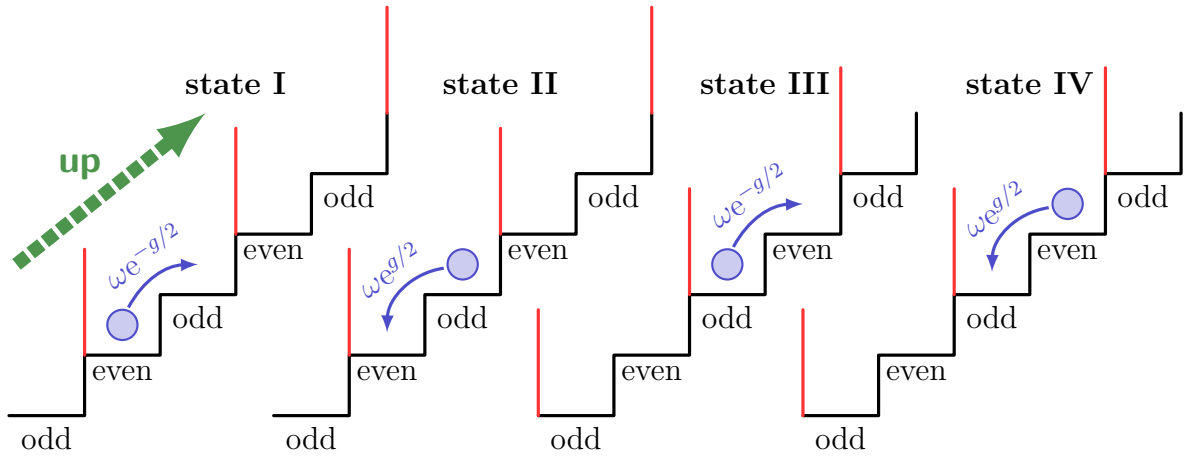


Figure 3.7| All four possible configurations for the feedback-driven system from Fig. 3.6(b). State II and state III is shown in 3.6(b). From left to right the particle jumps up the potential along transition from state I to state II and from state III to state IV. The thick dashed green arrow points along the “up” direction, which is used in Fig. 3.8.

which have labels I,II, III and IV, where states II and III are displayed in Fig. 3.6(b). Along transitions $I \rightarrow II$ and $III \rightarrow IV$ the particle moves one step up the potential, where in each transition an amount of work g is delivered from the system. A transition between states I and II as well as between states IV and I changes the barrier positions without altering the particle position (blue circle). Along a full cycle $I \rightarrow II \rightarrow III \rightarrow IV \rightarrow I$ the particle has moved up two steps in potential (one period), which corresponds to a delivered work $W_{\text{cycle}}^{\text{out}} \equiv 2g$.

The dynamics of the feedback mechanism that changes the positions of the barriers is assumed to underlie the same thermodynamic rules as the particle performing the random walk in the tilted potential. More precisely, if the system is in state II the barrier position alter with a rate $\gamma(1 - \varepsilon)$, whereas the reverse transition from state III occurs with a rate $\gamma\varepsilon$. This corresponds mathematically to barrier change with constant rate γ , where ε can be interpreted as the probability of an erroneous action, which can be a switch from state III to state II or no change of the barriers in state II. Physically, we assume an “odd” particle position forces the barriers to an “odd” position with a “force” $f_+^{\text{fb}} = [\ln(1 - \varepsilon)/\varepsilon]$, whereas an “even” particle position forces the barriers in the opposite direction $f_-^{\text{fb}} = -f_+^{\text{fb}}$, see Fig. 3.8. The feedback force $f_{\pm}^{\text{fb}} = \pm \ln[(1 - \varepsilon)/\varepsilon]$ can stem from a mechanical or chemical force. Along the full cycle $I \rightarrow II \rightarrow III \rightarrow IV \rightarrow I$ the feedback mechanism introduces two barrier switches along this force, which corresponds to a invested work $W_{\text{cycle}}^{\text{in}} = f_+^{\text{fb}} - f_-^{\text{fb}} = 2 \ln[(1 - \varepsilon)/\varepsilon]$, where $W_{\text{cycle}}^{\text{out}} = 2g$ is the extracted work due to particle jumps. A biased motion towards the “up” direction, see Figs. 3.7 and 3.8, requires the error ε to be small enough $\varepsilon < 1/(1 + e^g) < 1/2$ such that $W_{\text{cycle}}^{\text{out}} < W_{\text{cycle}}^{\text{in}}$ holds.

3.4.3 Bipartite four state system

In the following we discuss our main results from (3.47) for the four state system from Fig. 3.8, which we have derived in the previous subsection. We assume a feedback-driven

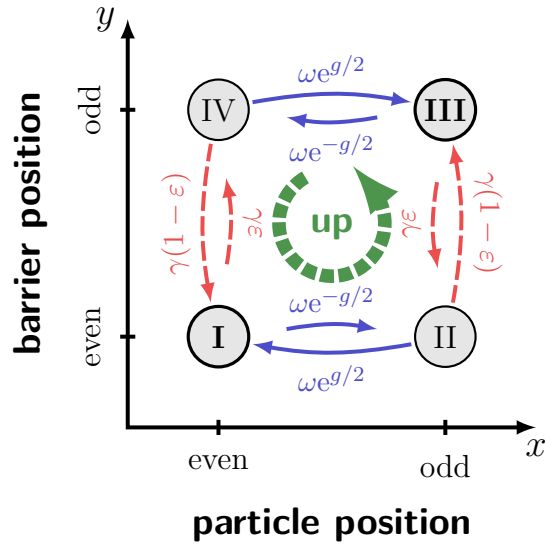


Figure 3.8 | Biased random with feedback controller from Fig. 3.6 as bipartite system. Transitions of the particle are shown as solid blue arrows and transitions barrier position by dashed red arrows. A particle leaves state I or III performs a jump upwards the potential, see thick dashed green arrow labeled by “up”.

engine, which corresponds to $g > 0$ and $\varepsilon < 1/(1 + e^g)$. Calculating the steady state probabilities P_z of states $z = \text{I, II, III, IV}$ yield

$$P_{\text{I}} = P_{\text{III}} = \frac{\gamma(1 - \varepsilon) + \omega e^{g/2}}{2\gamma + 2\omega(e^{g/2} + e^{-g/2})} \quad \text{and} \quad P_{\text{II}} = P_{\text{IV}} = \frac{\gamma\varepsilon + \omega e^{-g/2}}{2\gamma + 2\omega(e^{g/2} + e^{-g/2})}, \quad (3.48)$$

where states I and III are more probable than state II and IV, i.e., $P_{\text{I}} = P_{\text{III}} \geq P_{\text{II}} = P_{\text{IV}}$. Moreover the steady state current in “up” direction

$$J_{\text{up}} = P_{\text{I}}\omega e^{-g/2} - P_{\text{II}}\omega e^{g/2} = \frac{\gamma}{2} \left[\frac{(1 - \varepsilon)\omega e^{-g/2} - \varepsilon\omega e^{g/2}}{\gamma + \omega(e^{g/2} + e^{-g/2})} \right], \quad (3.49)$$

quantifies the average rate for completing a cycle $\text{I} \rightarrow \text{II} \rightarrow \text{III} \rightarrow \text{IV} \rightarrow \text{I}$ which corresponds to two steps of the particle in the staircase potential from Fig. 3.7. Note that $g > 0$ and $\varepsilon < 1/(1 + e^g)$ implies $J_{\text{up}} > 0$.

The thermodynamic entropy production rates in the medium due to the subsystems read

$$\sigma_x = -2J_{\text{up}}g \quad \text{and} \quad \sigma_y = 2J_{\text{up}} \ln \frac{1 - \varepsilon}{\varepsilon}, \quad (3.50)$$

where $-\sigma_x \equiv \dot{W}^{\text{out}}$ is the delivered work (power) by the particle and $\sigma_y \equiv \dot{W}^{\text{in}}$ the consumed work (power) by the feedback mechanism. The standard second law

$$\sigma = \sigma_x + \sigma_y = 2J_{\text{up}} \left(\ln \frac{1 - \varepsilon}{\varepsilon} - g \right) \geq 0, \quad (3.51)$$

implies $\dot{W}^{\text{in}} \geq \dot{W}^{\text{out}}$. The learning rate is given by

$$l_y = h_x = J_{\text{up}} \ln \frac{P_{\text{I}}P_{\text{III}}}{P_{\text{II}}P_{\text{IV}}} = 2J_{\text{up}} \ln \left[\frac{\gamma(1 - \varepsilon) + \omega e^{g/2}}{\gamma\varepsilon + \omega e^{-g/2}} \right] \quad (3.52)$$

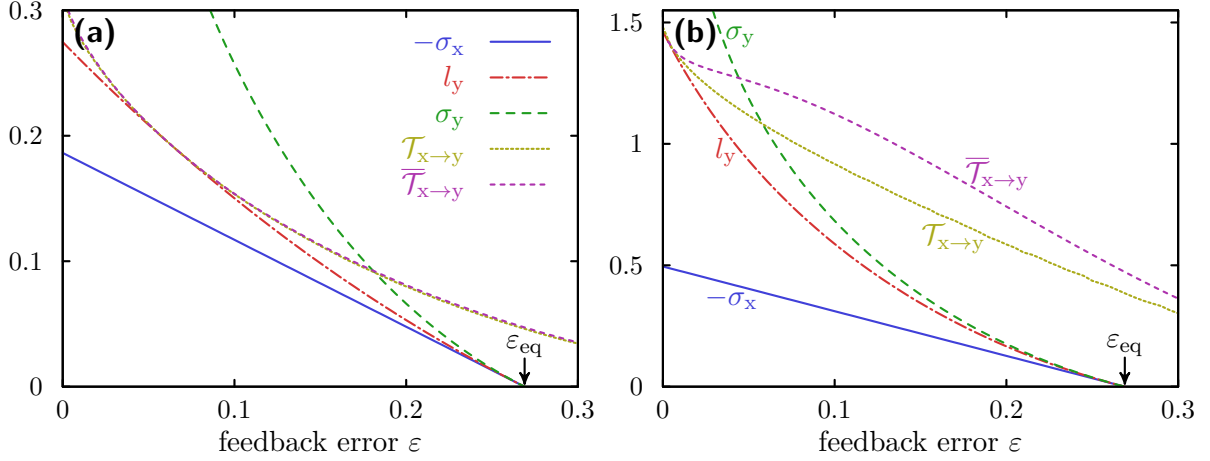


Figure 3.9 | Performance of four state system from Fig. 3.8. (a) No time scale separation $\omega = \gamma = 1$. (b) Feedback controller faster than system dynamics $\gamma \gg \omega$ ($\gamma = 10$ and $\omega = 1$). Parameters: Potential step $g = 1$, hopping frequency of particle $\omega = 1$ and feedback rate (a) $\gamma = 1$, (b) $\gamma = 10$. Each value of the transfer entropy rate $\mathcal{T}_{x \rightarrow y}$ is estimated from a single trajectory with $N = 10^8$ jump events.

and quantifies the reduction of uncertainty of subsystem “x” due to the dynamics of subsystem “y”. The learning rate is positive since the feedback mechanism drives the system to states I and III, implying $P_I P_{III} > P_{II} P_{IV}$. The upper bound on the transfer entropy rate is

$$\bar{\mathcal{T}}_{x \rightarrow y} = 2P_I \gamma \varepsilon \ln \frac{\gamma \varepsilon}{\bar{w}_y} + 2P_{II} \gamma (1 - \varepsilon) \ln \frac{\gamma (1 - \varepsilon)}{\bar{w}_y}, \quad (3.53)$$

where $\bar{w}_y = 2P_I \gamma \varepsilon + 2P_{II} \gamma (1 - \varepsilon)$. An analytical expression for the transfer entropy rate $\mathcal{T}_{x \rightarrow y}$ is not known but can be calculated with the numerical method explained in Appendix 3.B.

In figure 3.9 we show different bounds on the extracted work $-\sigma_x$ from our main result (3.47). We confirm the learning rate l_y to be the tightest bound on $-\sigma_x$, which also vanishes at equilibrium $\varepsilon_{\text{eq}} = 1/(1 + e^g) \simeq 0.27$. Most remarkably, there is a clear crossing between the transfer entropy $\mathcal{T}_{x \rightarrow y}$ and the invested work from the feedback controller σ_y . The transfer entropy rate $\mathcal{T}_{x \rightarrow y}$ is nonzero even at equilibrium $\varepsilon_{\text{eq}} = 1/(1 + e^g) \simeq 0.27$ and remains finite for infinite driving ($\varepsilon \rightarrow 0$), where σ_y diverges. In Fig. 3.9(a) we find $\mathcal{T}_{x \rightarrow y} \simeq \bar{\mathcal{T}}_{x \rightarrow y}$ even for $\gamma = \omega = 1$, which we generally expect for slow feedback dynamics “ $\gamma \ll \omega$ ” as mentioned in Sec. 3.3.2. The following subsection will briefly discuss the limit $\gamma \ll \omega$ in more detail.

3.4.4 Four state system with time scale separation

In the following we consider the system from Fig. 3.8 in the slow feedback regime, where $\gamma \ll \omega$. All approximations “ \approx ” are exact “=” for the limit $\omega \rightarrow \infty$. For the upper bound on the transfer entropy rate (3.53) we obtain

$$\bar{\mathcal{T}}_{x \rightarrow y} \approx \gamma \varepsilon \frac{e^g}{1 + e^g} \ln \left[\frac{\varepsilon (e^g + 1)}{\varepsilon e^g + 1 - \varepsilon} \right] + \gamma (1 - \varepsilon) \frac{1}{1 + e^g} \ln \left[\frac{(1 - \varepsilon)(e^g + 1)}{\varepsilon e^g + 1 - \varepsilon} \right] \equiv \bar{\mathcal{T}}_{x \rightarrow y}^\infty. \quad (3.54)$$

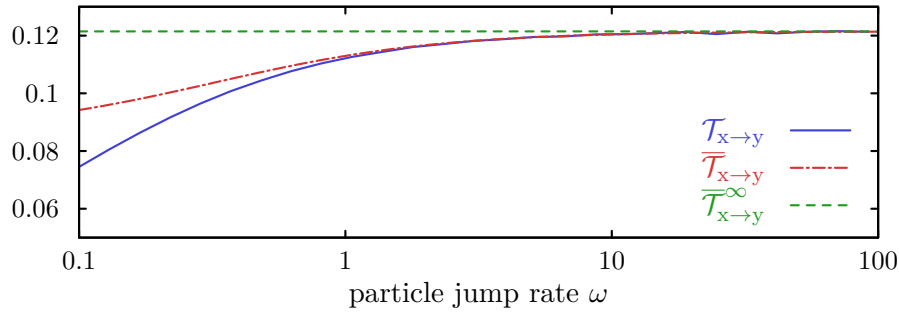


Figure 3.10 | Time scale separation $\gamma \ll \omega$ implies $\mathcal{T}_{x \rightarrow y} \approx \bar{\mathcal{T}}_{x \rightarrow y}$, where $\bar{\mathcal{T}}_{x \rightarrow y}^\infty$ is the transfer entropy in the limit $\omega \rightarrow \infty$ from (3.54). Model from Fig. 3.8 with parameters $\gamma = 1$, $\varepsilon = 0.15$ and $g = 1$. Each value of the transfer entropy $\mathcal{T}_{x \rightarrow y}$ is estimated from a single trajectory with $N = 10^8$ jump events.

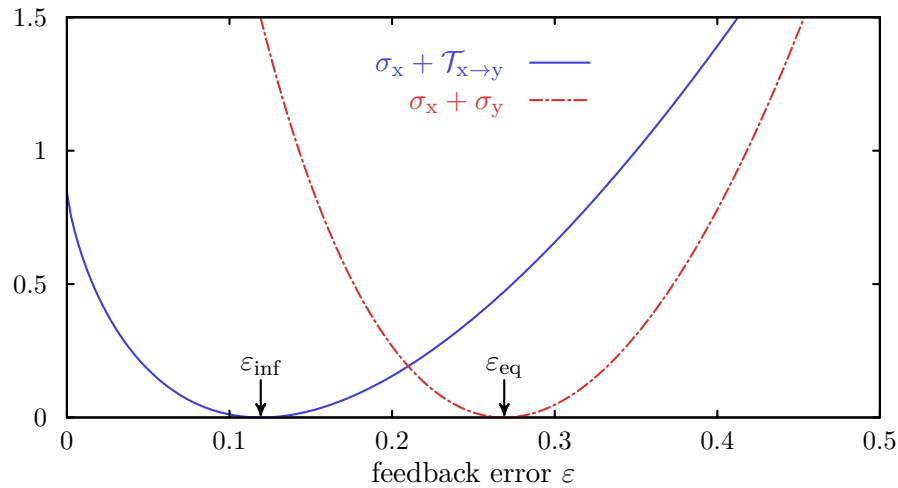


Figure 3.11 | Transfer entropy versus thermodynamic cost in the slow feedback regime “ $\gamma \ll \omega$ ”. Parameters: $\gamma = g = 1$ and formally $\omega = \infty$. The transfer entropy is calculated from (3.54).

A slow y -process cannot track a much faster x -process, which effectively, renders the slow y -process Markovian for any relevant “slow” time scale γ^{-1} , which leads to $\mathcal{T}_{x \rightarrow y} \approx \bar{\mathcal{T}}_{x \rightarrow y}$ as discussed in Sec. 3.3.2. We confirm in Fig. 3.10 that the transfer entropy rate $\mathcal{T}_{x \rightarrow y}$ indeed approaches its upper bound $\bar{\mathcal{T}}_{x \rightarrow y}$ for $\omega \rightarrow \infty$ (happens also for $\gamma \rightarrow 0$). Moreover, the learning rate of the feedback controller from (3.52) becomes $l_y \approx -\sigma_x$.

We now discuss the two remaining inequalities involving the second law $-\sigma_x \leq \sigma_y$ and transfer entropy $-\sigma_x \leq \mathcal{T}_{x \rightarrow y}$, which are equivalent to $\sigma_x + \sigma_y \geq 0$ and $\sigma_x + \mathcal{T}_{x \rightarrow y} \geq 0$, respectively. Fig. 3.11 shows both inequalities, which saturate at two different values of the feedback error $\varepsilon_{\text{inf}} = 1/(1 + e^{2g}) \simeq 0.12$ and $\varepsilon_{\text{eq}} = 1/(1 + e^g) \simeq 0.27$. Note $\varepsilon \leq \varepsilon_{\text{eq}}$ corresponds to the feedback-driven case. The full engine reaches highest efficiency $-\sigma_x/\sigma_y \leq 1$ for $\varepsilon \rightarrow \varepsilon_{\text{eq}}$, whereas $-\sigma_x/\mathcal{T}_{x \rightarrow y}$ vanishes and, therefore does not characterize the efficiency of a feedback-driven engine.

Such an effect has, firstly, been found in [74], where an information-driven engine was compared with a molecular motor with the same kinetics, i.e., two different physical

systems with same dynamics. Here we can identify the same discrepancy for a single system, where the positive rate $\sigma_x + \mathcal{T}_{x \rightarrow y} \geq 0$ is analogous to the “entropy production a information-driven engine” from [74], and the entropy production $\sigma_x + \sigma_y \geq 0$, which are not related as illustrated in Fig. 3.11.

3.4.5 Further related research

The results presented in this chapter reveal further similarities with the following research. Refs. [108] contain a model, where the entropy of a tape can be changed while extracting (or delivering work) from (or to) a work reservoir. For example, one can “extract work” from a single heat bath while increasing the entropy of the tape. Among a series of inequalities [68] the Shannon entropy difference between initial and final tape configuration provides the tightest bound on the work that can be extracted in such a process. Conversely, thermodynamic cost to restore the initial state of that tape are higher than the amount of work that has been extracted in the randomization process, see [68] for a detailed discussion. More studies in this field involving “information reservoirs” can be found in [68, 108–118].

For causal networks the transfer entropy has been shown to be useful to detect causal dependencies in feedback-driven engines [67], which amongst other things, involves a quite general integral fluctuation theorem involving the transfer entropy and entropy reduction in the medium. Furthermore, a so-called time reversed transfer entropy rate has been investigated for thermodynamics and gambling [130–132]. We postpone further discussion on transfer entropy and biological systems to the following chapter.

Moreover, it turned out that the learning rate and the rate of dissipation vanish if a feedback-system approaches equilibrium. This feature has just recently been used to derive a linear response theory for information-driven engines [133]. A generalization of this framework from bipartite to multipartite systems, which contain more than two system parts can be found in [134]. Further, refined studies [135, 136] consider individual transitions rather than different parts of a system; a concrete example involves the thermodynamics of resetting [137]. Further studies on continuously interacting systems considering the same quantities from Fig. 3.9 can be found in [88, 96, 138–140]. We note that the learning rate discussed in this chapter has been used under the term information flow in, for instance, [57, 88, 96, 134, 138], which also involve processes of continuous valued variables.

An instruction to calculate the analytical expressions for the the quantities showing up in (3.47) for continuous valued processes with a Fokker-Planck dynamics is presented in [120], see also Appendix 3.C. Finally, the first experimental test of the first line of our main result (3.47) is presented in [52], where a feedback-driven refrigerator has been realized with two single electron boxes that are capacitively coupled.

3.5 Conclusion

For two continuously interacting systems we have derived a set of inequalities (3.47) that can be used to characterize the performance of feedback-driven engines. This framework of stochastic thermodynamics of bipartite systems allows for a particular transparent

interpretation of a Maxwell's demon, where thermodynamic cost involving the feedback controller (demon) are fully accessible. The rate at which the controlled subsystem reduces the entropy in the medium $-\sigma_x$ is shown to be bounded by the learning rate of the feedback controller l_y , which in turn is bounded by the thermodynamic cost to maintain the feedback σ_y . Among a second information theoretic quantity, the transfer entropy $\mathcal{T}_{x \rightarrow y}$, the learning rate l_y is shown to be the tightest bound on $-\sigma_x$.

Using a simple four state system we could show that the transfer entropy is *not* bounded by the thermodynamic cost to maintain the feedback, which can explicitly deduced from the crossing between $\mathcal{T}_{x \rightarrow y}$ and σ_y in Fig. 3.9. This feature has allowed us to show that the transfer entropy is not a thermodynamic consistent quantity to characterize the performance of a feedback-driven systems. For example, the transfer entropy accounts for memorizing the time history of the feedback controller, which can only be physically realized if one adds an additional "memory". We will show in the following chapter on cellular information processing that the addition of a memory is accompanied with thermodynamic costs.

Appendices to chapter 3

3.A Transfer entropy versus learning rate

In this Appendix we prove $l_y \leq \mathcal{T}_{x \rightarrow y}$, which is (3.29).

3.A.1 Rewriting transfer entropy rate

After a sufficiently long time t ($t \rightarrow \infty$) the conditional Shannon entropy $H[x_t|y_0^t]$ saturates to a constant value, i.e., $\frac{d}{dt}H[x_t|y_0^t] = 0$. Now calculating the time derivative yields

$$\begin{aligned} \frac{d}{dt}H[x_t|y_0^t] &\equiv \frac{H[x_{t+dt}|y_0^{t+dt}] - H[x_t|y_0^t]}{dt} \\ &= \underbrace{\frac{H[x_{t+dt}|y_0^t] - H[x_t|y_0^t]}{dt}}_{\equiv \mathcal{R}_{x \rightarrow y}} + \underbrace{\frac{H[x_t|y_0^{t+dt}] - H[x_t|y_0^t]}{dt}}_{= -\mathcal{T}_{x \rightarrow y}} = 0. \end{aligned} \quad (3.55)$$

From the first to the second line we have used the bipartite property (x_t and y_t cannot change simultaneously), which allows us to apply the chain rule for the time derivative. Furthermore, we have defined the first term by $\mathcal{R}_{x \rightarrow y}$ and identified the second term by $-\mathcal{T}_{x \rightarrow y}$ using (3.28). Thereby, $\mathcal{R}_{x \rightarrow y}$ is a randomness function which equals precisely $\mathcal{T}_{x \rightarrow y}$ in the steady state, which is analogous to $\frac{d}{dt}H[x_t|y_t] = h_x - l_y = 0$ from Sec. 3.2.4.

Using (3.5) we can write

$$\mathcal{R}_{x \rightarrow y} = \frac{H[x_{t+dt}|y_0^t] - H[x_t|y_0^t]}{dt} = \frac{1}{dt} \left\langle \ln \frac{\mathcal{P}(x_t|y_0^t)}{\mathcal{P}(x_{t+dt}|y_0^t)} \right\rangle. \quad (3.56)$$

3.A.2 Finishing the proof

We will now show $\mathcal{T}_{x \rightarrow y} = \mathcal{R}_{x \rightarrow y} \geq h_x = l_y$. Specifically, we will prove (3.29) by showing $\sigma_x + \mathcal{R}_{x \rightarrow y} \geq \sigma_x + h_x$. We begin by rewriting σ_x from (3.11) as follows. We define the fixed function

$$W(x'|x, y) \equiv \mathcal{P}(x_{t+dt} = x' | x_t = x, y_t = y), \quad (3.57)$$

where (3.21) is satisfied for $x \neq x'$, which states $W(x'|x, y) = w_y^{xx'} dt + \mathcal{O}(dt)^2$ for $x \neq x'$. Moreover, normalization of W implies $\sum_{x'} W(x'|x, y) = 1$. Note that (3.57) is equivalent to $W(x_{t+dt}|x_t, y_t) = \mathcal{P}(x_{t+dt}|x_t, y_t)$, whereas in general $W(x_t|x_{t+dt}, y_t) \neq \mathcal{P}(x_t|x_{t+dt}, y_t)$. Using (3.57) we find

$$\sigma_x = \sum_{x, x', y} P(x, y) w_y^{xx'} \ln \frac{w_y^{xx'}}{w_y^{x'x}} = \frac{1}{dt} \left\langle \ln \frac{W(x_{t+dt}|x_t, y_t)}{W(x_t|x_{t+dt}, y_t)} \right\rangle. \quad (3.58)$$

In order to see this one has to use (3.21) and to verify that for $dt \rightarrow 0$ all terms related to $x_{t+dt} = x_t$ (“ $x = x'$ ”) cancel out.

With this result we are able to show

$$\begin{aligned} \sigma_x + \mathcal{T}_{x \rightarrow y} &= \sigma_x + \mathcal{R}_{x \rightarrow y} = \frac{1}{dt} \left\langle \ln \frac{W(x_{t+dt}|x_t, y_t) \mathcal{P}(x_t|y_0^t)}{W(x_t|x_{t+dt}, y_t) \mathcal{P}(x_{t+dt}|y_0^t)} \right\rangle \\ &= \frac{1}{dt} \left\langle \ln \frac{W(x_{t+dt}|x_t, y_t) \mathcal{P}(x_t, y_0^t)}{W(x_t|x_{t+dt}, y_t) \mathcal{P}(x_{t+dt}, y_0^t)} \right\rangle \\ &= \frac{1}{dt} \left\langle \ln \frac{\mathcal{P}(x_{t+dt}, x_t, y_0^t)}{W(x_t|x_{t+dt}, y_t) \mathcal{P}(x_{t+dt}, y_0^t)} \right\rangle. \end{aligned} \quad (3.59)$$

Since the numerator contains the weight $\mathcal{P}(x_{t+dt}, x_t, y_0^t)$ associated with $\langle \dots \rangle$ we are able to apply the log-sum-inequality [36] by integrating out y_0^{t-dt} , which leads to

$$\begin{aligned} \sigma_x + \mathcal{T}_{x \rightarrow y} &\geq \left\langle \ln \frac{\mathcal{P}(x_{t+dt}, x_t, y_t)}{W(x_t|x_{t+dt}, y_t) \mathcal{P}(x_{t+dt}, y_t)} \right\rangle = \left\langle \ln \frac{W(x_{t+dt}|x_t, y_t) \mathcal{P}(x_t, y_t)}{W(x_t|x_{t+dt}, y_t) \mathcal{P}(x_{t+dt}, y_t)} \right\rangle \\ &= \sum_{\substack{x, x', y \\ x \neq x'}} P(x, y) w_y^{xx'} \ln \frac{P(x, y) w_y^{xx'}}{P(x, y) w_y^{x'x}} = \sigma_x + h_x = \sigma_x + l_y. \end{aligned} \quad (3.60)$$

From the first to the second line we have used (3.21) and $\mathcal{P}(x_t, y_t) = P(x_t, y_t)$ as well as $\mathcal{P}(x_{t+dt}, y_t) = P(x_{t+dt}, y_t) + O(dt)$, where $P(x, y)$ is the steady state probability of $(x_t, y_t) = (x, y)$. In the last two steps we have used (3.14) and $h_x = l_y$ from (3.23), which completes the proof of (3.29).

3.A.3 Comments on the proof

The presented proof contains the following crucial ideas. First, identifying, $\mathcal{R}_{x \rightarrow y} = \mathcal{T}_{x \rightarrow y}$ in (3.55). Second, using σ_x as auxiliary quantity to be able to show $\sigma_x + \mathcal{R}_{x \rightarrow y} \geq \sigma_x + h_x$, where $h_x = l_y$. More details about this proof can be seen in [41]. The derivation presented there is more technical and starts with the discrete time picture, using following notational changes: $dt \rightarrow \tau$ and $\mathcal{R}_{x \rightarrow y} \rightarrow \hat{T}_{x \rightarrow y}$.

3.B Calculating Shannon entropy rates

3.B.1 Path weight and continuous time Shannon entropy rates

The full trajectory of the joint process is denoted by $\mathbf{z}_0^t \equiv (\mathbf{z}_0, \tau_0; \mathbf{z}_1, \tau_1; \dots; \mathbf{z}_N, \tau_N)$, where N is the number of jumps along the trajectory and τ_n denotes the waiting time in state \mathbf{z}_n ($n = 0, 1, \dots, N$), which satisfy $\tau_0 + \tau_1 + \dots + \tau_N = t$. Note that the sequence of visited states is $\mathbf{z}_0 \rightarrow \mathbf{z}_1 \rightarrow \dots \rightarrow \mathbf{z}_N$. The probability of this trajectory \mathbf{z}_0^t is given by (e.g., see [18])

$$P(\mathbf{z}_0^t) = P_0(\mathbf{z}_0) \prod_{n=0}^{N-1} w_{\mathbf{z}_n \mathbf{z}_{n+1}} \prod_{n=0}^N \exp(-r_{\mathbf{z}_n} \tau_n), \quad (3.61)$$

where $r_z \equiv \sum_{z'} w_{zz'} = \sum_{x'} w_y^{xx'} + \sum_{y'} w_{yy'}$ is the total rate for leaving the state $z = (x, y)$. The continuous time Shannon entropy rate then reads [125]

$$\mathcal{H}_z = \mathcal{H}_{x,y} \equiv \lim_{t \rightarrow \infty} \frac{1}{t} \langle \ln \mathcal{P}(z_0^t) \rangle. \quad (3.62)$$

The central limit theorem implies that the number of jumps $\hat{n}_{zz'}$ from state z to state z' satisfy $\lim_{t \rightarrow \infty} \hat{n}_{zz'}/t = P(z)w_{zz'}$ and the total time $\hat{\tau}_z$ spend in state z satisfies $\lim_{t \rightarrow \infty} \hat{\tau}_z/t = P(z)$. Identifying the introduced functionals as $\hat{n}_{zz'} = \sum_{n=0}^{N-1} \delta_{z,z_n} \delta_{z,z_{n+1}}$ and $\hat{\tau}_z = \sum_{n=0}^{N-1} \delta_{z,z_n} \tau_n$ from (3.61) and inserting them into (3.62) yields [125]

$$\mathcal{H}_z = - \sum_{z,z'} P(z)w_{zz'} \ln w_{zz'} + \sum_z P(z)r_z, \quad (3.63)$$

which is equivalent to Eq. (3.43).

Let us now make a comment on two individual contributions of \mathcal{H}_z . Since the long time limit $t \rightarrow \infty$ renders the initial preparation of the system irrelevant, we consider for convenience the case $P_t(z)|_{t=0} = P_0(z) \equiv P(x)P(y)$. Using the individual exit rates

$$r_z^{(1)} = r_{x,y}^{(1)} \equiv \sum_{x'|x' \neq x} w_y^{xx'} \quad \text{and} \quad r_z^{(2)} = r_{x,y}^{(2)} \equiv \sum_{y'|y' \neq y} w_{yy'}^x, \quad (3.64)$$

which satisfy $r_z = r_{x,y} = r_{x,y}^{(1)} + r_{x,y}^{(2)}$, we can write the path weight (3.61) as a product of two modified path probabilities

$$\hat{\mathcal{P}}_{y_0^t}(x_0^t) \equiv P(x) \prod_{\substack{n=0 \\ x_n \neq x_{n+1}}}^{N-1} w_{y_n}^{x_n x_{n+1}} \exp(-r_{z_n}^{(1)} \tau_n) \quad (3.65)$$

and

$$\hat{\mathcal{P}}_{x_0^t}(y_0^t) \equiv P(y) \prod_{\substack{n=0 \\ y_n \neq y_{n+1}}}^{N-1} w_{y_n y_{n+1}}^{x_n} \exp(-r_{z_n}^{(2)} \tau_n), \quad (3.66)$$

such that

$$\mathcal{P}(z_0^t) = \mathcal{P}(x_0^t, y_0^t) = \hat{\mathcal{P}}_{y_0^t}(x_0^t) \hat{\mathcal{P}}_{x_0^t}(y_0^t). \quad (3.67)$$

Note that $\hat{\mathcal{P}}_{y_0^t}(x_0^t)$ contains only transition rates of subsystem “x” ($w_y^{xx'}$) and $\hat{\mathcal{P}}_{x_0^t}(y_0^t)$ contains only transition rates of subsystem “y” ($w_{yy'}^x$).

Let us motivate a short interpretation of the quantity $\hat{\mathcal{P}}_{y_0^t}(x_0^t)$. Suppose subsystem “x” were a Markov process with time dependent rates $w^{xx'}(t) \equiv w_{y_t}^{xx'}$ for jumping from state x to state x' , which assumes y_t is a deterministic control parameter that influences the system labeled by variable x as a function of time t' ($0 \leq t' \leq t$). If the assumption of the previous sentence were true one would interpret $\hat{\mathcal{P}}_{y_0^t}(x_0^t)$ as the probability of process x_0^t influenced by a time dependent “deterministic” control parameter y_t with full time protocol y_0^t . Similarly, one can interpret $\hat{\mathcal{P}}_{x_0^t}(y_0^t)$ as the probability of the stochastic process y_0^t influenced by the deterministic parameter x_0^t .

n	0	1	2	3	4	5	6	7	8
x_n	1	3	2	1	2	3	1	-	-
y_n	2	1	2	-	-	-	-	-	-
\mathbf{z}_n	$\begin{pmatrix} x_0 \\ y_0 \end{pmatrix}$	$\begin{pmatrix} x_1 \\ y_0 \end{pmatrix}$	$\begin{pmatrix} x_2 \\ y_0 \end{pmatrix}$	$\begin{pmatrix} x_2 \\ y_1 \end{pmatrix}$	$\begin{pmatrix} x_3 \\ y_1 \end{pmatrix}$	$\begin{pmatrix} x_4 \\ y_1 \end{pmatrix}$	$\begin{pmatrix} x_5 \\ y_1 \end{pmatrix}$	$\begin{pmatrix} x_6 \\ y_1 \end{pmatrix}$	$\begin{pmatrix} x_6 \\ y_2 \end{pmatrix}$
τ_n	τ_0^x	τ_1^x	$\tau_0^y - \tau_0^x - \tau_1^x$	$\tau_2^x - \tau_2$	τ_3^x	τ_4^x	τ_5^x	$\tau_6^x - \tau_2^y$	τ_2^y

Table 3.1 | Detailed list of visited states of the process illustrated in Fig. 3.12. The full process $\mathbf{z}_0^t = (\mathbf{z}_0, \tau_0; \dots; \mathbf{z}_N, \tau_N)$ with specific waiting times τ_n , where n count the number of transitions accumulated along the trajectory. For completeness: The waiting time for $n = 3$ is $\tau_3 = \tau_2^x - \tau_2 = \tau_2^x - \tau_0^y + \tau_0^x + \tau_1^x$.

Using (3.65) and (3.64) we obtain [41, 93]

$$\mathcal{H}_{x,y}^{(1)} \equiv \lim_{t \rightarrow \infty} \frac{1}{t} \langle \ln \hat{\mathcal{P}}_{y_0^t}(x_0^t) \rangle = - \sum_{\substack{x,x',y \\ x \neq x'}} P(x,y) w_y^{xx'} (\ln w_y^{xx'} - 1) \quad (3.68)$$

Similarly, from (3.66) and (3.64) follows [41, 93]

$$\mathcal{H}_{x,y}^{(2)} \equiv \lim_{t \rightarrow \infty} \frac{1}{t} \langle \ln \hat{\mathcal{P}}_{x_0^t}(y_0^t) \rangle = - \sum_{\substack{x,y,y' \\ y \neq y'}} P(x,y) w_{yy'}^x (\ln w_{yy'}^x - 1). \quad (3.69)$$

Note that $\mathcal{H}_z = \mathcal{H}_{x,y} = \mathcal{H}_{x,y}^{(1)} + \mathcal{H}_{x,y}^{(2)}$ holds.

3.B.2 Random matrices and path weight of coarse-grained processes

Our goal is to find an expression for the path weights $\mathcal{P}(x_0^t)$ and $\mathcal{P}(y_0^t)$ of the coarse-grained processes x_0^t and y_0^t , respectively. Before deriving such an expression we have to introduce the following notation.

We now label the coarse-grained processes by $x_0^t = (x_0, \tau_0^x; x_1, \tau_1^x; \dots; x_{N_x}, \tau_{N_x}^x)$ and $y_0^t = (y_0, \tau_0^y; y_1, \tau_1^y; \dots; y_{N_y}, \tau_{N_y}^y)$, where N_x (N_y) is the total number of jumps of variable x (y), which satisfies $N_x + N_y = N$, see Fig. 3.12 for an example trajectory. The x -process (y -process) visit the states in the following order $x_0 \rightarrow x_1 \rightarrow \dots \rightarrow x_{N_x}$ ($y_0 \rightarrow y_1 \rightarrow \dots \rightarrow y_{N_y}$), where the n -th visited state x_n (y_n) is kept for a waiting time τ_n^x (τ_n^y) with $n = 0, 1, \dots, N_x$ ($n = 0, 1, \dots, N_y$). The sum of all waiting times satisfies $\tau_0^x + \tau_1^x + \dots + \tau_{N_x}^x = \tau_0^y + \tau_1^y + \dots + \tau_{N_y}^y = t$. Figure 3.12 and table 3.1 shows a sample trajectory, which compares the coarse-grained processes (x_0^t or y_0^t) with the full process $\mathbf{z}_0^t = (x_0^t, y_0^t)$.

With this notation we write the coarse-grained path weights as matrix products, which read [93]

$$\begin{aligned} \mathcal{P}(x_0^t) &= \left\| e^{\tau_{N_x}^x \mathbf{M}^x(x_{N_x}|x_{N_x})} \mathbf{M}^x(x_{N_x}|x_{N_x-1}) \dots e^{\tau_1^x \mathbf{M}^x(x_1|x_1)} \mathbf{M}^x(x_1|x_0) e^{\tau_0^x \mathbf{M}^x(x_0|x_0)} \mathbf{p}^x(x_0) \right\|_1 \\ &\equiv \left\| e^{\tau_{N_x}^x \mathbf{M}^x(x_{N_x}|x_{N_x})} \left[\prod_{n=0}^{N_x-1} \mathbf{M}^x(x_{n+1}|x_n) e^{\tau_n^x \mathbf{M}^x(x_n|x_n)} \right] \mathbf{p}^x(x_0) \right\|_1 \end{aligned} \quad (3.70)$$

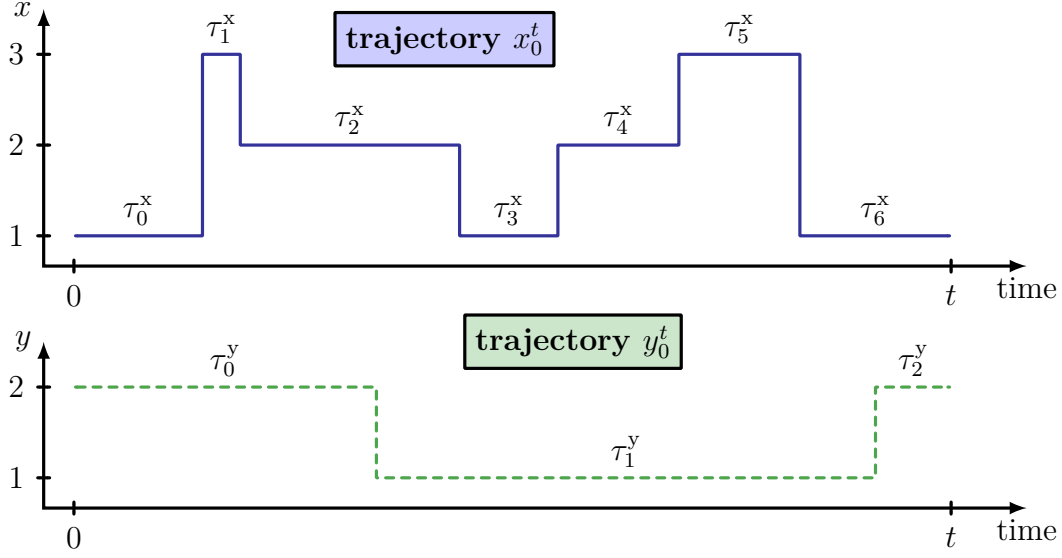


Figure 3.12 | Illustration of coarse-grained processes with possible states $x = 1, 2, 3$ and $y = 1, 2$. The process x_0^t (solid blue line) contains here $N_x = 6$ jumps and the process y_0^t (dashed green line) contains here $N_y = 2$ jumps. The total number of transition is $N = N_x + N_y$. More details can be found in table 3.1.

and

$$\begin{aligned} \mathcal{P}(y_0^t) &= \left\| e^{\tau_{N_y}^y \mathbf{M}^y(y_{N_y}|y_{N_y})} \mathbf{M}^y(y_{N_y}|y_{N_y-1}) \dots e^{\tau_1^y \mathbf{M}^y(y_1|y_1)} \mathbf{M}^y(y_1|y_0) e^{\tau_0^y \mathbf{M}^y(y_0|y_0)} \mathbf{p}^y(y_0) \right\|_1 \\ &\equiv \left\| e^{\tau_{N_y}^y \mathbf{M}^y(y_{N_y}|y_{N_y})} \left[\prod_{n=0}^{N_y-1} \mathbf{M}^y(y_{n+1}|y_n) e^{\tau_n^y \mathbf{M}^y(y_n|y_n)} \right] \mathbf{p}^y(y_0) \right\|_1, \end{aligned} \quad (3.71)$$

where $\mathbf{M}^x, \mathbf{M}^y$ are matrices and $\mathbf{p}^x, \mathbf{p}^y$ vectors that will be explained shortly. Furthermore, $\|\mathbf{v}\|_1$ is the sum norm of a vector \mathbf{v} , which is also used under the term l_1 -norm or taxicab norm. Note that the exponentials in the product represent matrix exponentials.

To explain the remaining quantities that appear in (3.70) and (3.71), we have to introduce the following matrix notation of the master equation (2.6), which is equivalent to

$$\dot{P}_t(x, y) = \sum_{x', y'} L_{yy'}^{xx'} P_t(x, y), \quad (3.72)$$

where we have identified

$$L_{yy'}^{xx'} = \begin{cases} w_y^{x'x} & \text{if } x \neq x' \text{ and } y = y', \\ w_{y'y}^x & \text{if } x = x' \text{ and } y \neq y', \\ -\sum_{\tilde{x}} w_y^{x\tilde{x}} - \sum_{\tilde{y}} w_{y\tilde{y}}^x & \text{if } x = x' \text{ and } y = y', \\ 0 & \text{otherwise.} \end{cases} \quad (3.73)$$

Note that $L_{yy}^{xx} = -r_{x,y} = -r_z$ holds. Using the elements $L_{yy'}^{xx'}$, we can define two sets of matrices $\mathbf{M}^x(x|x')$ and $\mathbf{M}^y(y|y')$ that appeared in the above expressions (3.70) and (3.71),

where \mathbf{M}^x is a $\Omega_y \times \Omega_y$ -matrix and \mathbf{M}^y is a $\Omega_x \times \Omega_x$ -matrix with elements defined as

$$[\mathbf{M}^x(x|x')]_{yy'} \equiv [\mathbf{M}^y(y|y')]_{xx'} \equiv L_{yy'}^{xx'}. \quad (3.74)$$

Moreover, $\mathbf{p}^x(x)$ ($\mathbf{p}^y(y)$) is a vector with Ω_y (Ω_x) components that are defined by

$$[\mathbf{p}^x(x)]_y \equiv [\mathbf{p}^y(y)]_x \equiv P_0(x, y), \quad (3.75)$$

where $P_0(x, y)$ is the probability of $(x_0, y_0) = (x, y)$ at time $t = 0$ and $x \in \{1, \dots, \Omega_x\}$ and $y \in \{1, \dots, \Omega_y\}$.

With the definitions (3.74) and (3.75) one can interpret the matrix product from (3.70) as the partial sum of the full path weight (3.61) over all possible paths y_0^t . Similarly, the matrix product in (3.71) represents the full path weight (3.61) integrated over all possible paths x_0^t .

3.B.3 Shannon entropy rates of coarse-grained processes

The Shannon entropy rates of the coarse-grained processes read

$$\begin{aligned} \mathcal{H}_x &\equiv \lim_{t \rightarrow \infty} \frac{1}{t} \langle \ln \mathcal{P}(x_0^t) \rangle, \\ \mathcal{H}_y &\equiv \lim_{t \rightarrow \infty} \frac{1}{t} \langle \ln \mathcal{P}(y_0^t) \rangle. \end{aligned} \quad (3.76)$$

Using the central limit theorem or more precisely the Shannon-Macmillan-Breiman theorem [141] yields

$$\begin{aligned} \mathcal{H}_x &= \lim_{t \rightarrow \infty} \frac{1}{t} \ln \mathcal{P}(x_0^t), \\ \mathcal{H}_y &= \lim_{t \rightarrow \infty} \frac{1}{t} \ln \mathcal{P}(y_0^t), \end{aligned} \quad (3.77)$$

which simplifies the determination of the Shannon entropy rates remarkably. To determine the Shannon entropy rates \mathcal{H}_x and \mathcal{H}_y numerically, we just have to generate a single long trajectory $\mathbf{z}_0^t = (x_0^t, y_0^t)$ evaluate $t^{-1} \ln \mathcal{P}(x_0^t)$ and $t^{-1} \ln \mathcal{P}(y_0^t)$ by using (3.70) and (3.71). The Shannon entropy rate “reduces” to the determination of the maximum Lyapunov exponent for the random matrix products (3.70) and (3.71), where the matrices are defined in (3.74). The transfer entropy rates (3.46) finally read $\mathcal{T}_{x \rightarrow y} = \mathcal{H}_y - \mathcal{H}_{x,y}^{(2)}$ and $\mathcal{T}_{y \rightarrow x} = \mathcal{H}_x - \mathcal{H}_{x,y}^{(1)}$, where analytical expressions for $\mathcal{H}_{x,y}^{(1)}$ and $\mathcal{H}_{x,y}^{(2)}$ can be found in Eqs. (3.68) and (3.69), respectively.

Further numerical details on continuous time Shannon entropy rates can be found in [93], which involves a trick from [142] to avoid numerical precision problems (note that $\mathcal{T}^{(x)}$ and $\mathcal{T}^{(y)}$ therein represents \mathbf{M}^x and \mathbf{M}^y from here). More information about Shannon entropy rates for discrete time processes can be found in [127–129]. References [125, 126] discusses continuous time Shannon entropy rates for Markov processes.

3.C Continuous variables

For continuous valued bipartite systems the dynamics will be governed by a Fokker-Planck equation

$$\dot{\rho}_t(x, y) = -\nabla \cdot \mathbf{J}_t(x, y), \quad (3.78)$$

where $\rho_t(x, y)$ is the probability density to find state (x, y) at time t , $\nabla \equiv (\partial_x, \partial_y)$ and $\mathbf{J}_t(x, y)$ the current density function. For notational convenience, we consider the steady state $\dot{\rho}_t(x, y) = 0$ by dropping the subscript t ($\rho_t \rightarrow \rho$, $\mathbf{J}_t \rightarrow \mathbf{J}$). The steady state current reads

$$\mathbf{J}(x, y) \equiv \begin{pmatrix} J_x(x, y) \\ J_y(x, y) \end{pmatrix} = \begin{pmatrix} \mu_x F_x(x, y) \rho(x) - D_x \partial_x \rho(x, y) \\ \mu_y F_y(x, y) \rho(x) - D_y \partial_y \rho(x, y) \end{pmatrix}, \quad (3.79)$$

where $F_i(x, y)$ is a local force, μ_i is the mobility and D_i the diffusion coefficient of component $i = x, y$. Note that Einstein relation reads $D_i = T\mu_i$, where Boltzmann's constant is set to $k_B \equiv 1$. The bipartite property of the system requires that the diffusion separates into a “x” part and a “y” part [134], which has already been used, since there is no ∂_y in the first line of (3.79) and no ∂_x in the second line of (3.79).

For the Fokker-Planck dynamics, one can deduce [120] (see also [134])

$$\begin{aligned} h_x &= \int dx \int dy \partial_x J_x(x, y) \ln \rho(x, y) = - \int dx \int dy J_x(x, y) \partial_x \ln \rho(x, y), \\ h_y &= \int dx \int dy \partial_y J_y(x, y) \ln \rho(x, y) = - \int dx \int dy J_y(x, y) \partial_y \ln \rho(x, y) \end{aligned} \quad (3.80)$$

from (3.9) and (3.10), where $h_x + h_y = 0$. Note that the learning rate satisfies $l_y = -h_y = h_x$. Moreover, the entropy production in the medium due to the dynamics of the subsystems read [120]

$$\begin{aligned} \sigma_x &\equiv \frac{1}{T} \int dx \int dy J_x(x, y) F_x(x, y) = \int dx \int dy J_x(x, y) D_x^{-1} \mu_x F_x(x, y) \\ \sigma_y &= \frac{1}{T} \int dx \int dy J_y(x, y) F_y(x, y) = \int dx \int dy J_y(x, y) D_y^{-1} \mu_y F_y(x, y), \end{aligned} \quad (3.81)$$

which obey the second law inequalities for the individual subsystems

$$\begin{aligned} \sigma_x + h_x &= \int dx \int dy \frac{J_x(x, y)^2}{D_x \rho(x, y)} \geq 0, \\ \sigma_y + h_y &= \int dx \int dy \frac{J_y(x, y)^2}{D_y \rho(x, y)} \geq 0; \end{aligned} \quad (3.82)$$

see also [57] for a similar result, where h_x and h_y has been termed information flow.

Finally, the upper bound on the transfer entropy reads [120]

$$\begin{aligned} \bar{\mathcal{T}}_{x \rightarrow y} &= \frac{D_y}{4T^2} \int dx \int dy \rho(x, y) [F_y(x, y) - \tilde{F}_y(y)]^2 \\ &= \frac{D_y}{4T^2} \int dx \int dy \rho(x, y) [F_y(x, y)^2 - \tilde{F}_y(y)^2] \end{aligned} \quad (3.83)$$

where

$$\tilde{F}_y(y) = \int dx F_y(x, y) \rho(x|y) \equiv \int dx F_y(x, y) \frac{\rho(x, y)}{\int dx' \rho(x', y)}. \quad (3.84)$$

To show that $\bar{\mathcal{T}}_{x \rightarrow y} \geq l_y$, we first rewrite the learning rate by using (3.10) as

$$l_y = \int dx \int dy \left[\mu_y F_y(x, y) \rho(x, y) - D_y \rho(y) \partial_y \rho(x|y) \right] \partial_y \ln \rho(x|y), \quad (3.85)$$

which can also be used for non-stationary systems [replace $\rho(x, y) \rightarrow \rho_t(x, y)$ for the dynamic case $\dot{\rho}_t(x, y) \neq 0$]. Note we have used the marginal density $\rho(y) \equiv \int dx \rho(x, y)$ and $\rho(x|y) \equiv \rho(x, y)/\rho(y)$. From (3.83) and (3.85) we get

$$\bar{\mathcal{T}}_{x \rightarrow y} - l_y = \int dx \int dy \frac{\rho(x, y)}{4D_y} \left\{ \left[\mu_y F_y(x, y) - 2D_y \frac{\partial_y \rho(x|y)}{\rho(x|y)} \right]^2 - \mu_y^2 \tilde{F}_y(y)^2 \right\} \geq 0, \quad (3.86)$$

where we have used the conditional average

$$\int dx \rho(x|y) \left[F_y(x, y) - 2D_y \frac{\partial_y \rho(x|y)}{\rho(x|y)} \right] = \int dx \rho(x|y) F_y(x, y) = \tilde{F}_y(y) \quad (3.87)$$

to identify $4D_y(\bar{\mathcal{T}}_{x \rightarrow y} - l_y)$ by the conditional variance of $F_y(x, y) - 2D_y \rho(x|y)^{-1} \partial_y \rho(x|y)$ to obtain the inequality in (3.86).

4 Cellular information processing in bipartite systems

In this chapter we show that stochastic thermodynamics of bipartite systems is a powerful framework, which can be used beyond the realm of feedback-driven engines discussed in the previous chapter. Here we consider a different problem: sensing. More precisely, we assume a stochastic, time dependent external signal, which is measured by a sensor. We show the reduction of uncertainty about an external signal due to the sensor dynamics characterized by the learning rate is bounded by the thermodynamic cost for maintaining the sensory network, which allows us to define an efficiency that relates the acquired information to the thermodynamic costs [119]. Specific models with increasing complexity inspired by the *Escherichia coli* sensory network are used to identify the entropy production by the chemical work that is consumed inside the cell and work that is delivered by the signal. The models involve activation/deactivation of proteins, classical Monod-Wyman-Changeux models for receptor complexes and/or adaptation mechanisms.

In a complementary part we introduce the sensory capacity from [120]. It is a purely information theoretic quantity that characterizes the performance of a sensor: the sensory capacity is maximal if the instantaneous state of the sensor has as much information about a signal as the whole time history of the sensor state. We show the sensory capacity can be raised by a memory, where the increase of the sensory capacity characterizes the performance of the memory. Most importantly, we find a trade-off between sensory capacity and efficiency. A sensor that reaches the maximal sensory capacity 1 has a thermodynamic efficiency below $1/2$. A cellular two-component network is used as a physical realization of a sensor, which estimates a fluctuating ligand concentration that constitutes the signal. We obtain coupled linear Langevin equations that can be solved analytically.

4.1 Introduction to cellular information processing

Cellular organisms (e.g., bacteria) must sense their fluctuating environment to survive. They measure concentrations of food or poison to bias their motion along a food gradient or away from poison, which is known as chemotaxis. A classical example of cells measuring a ligand concentration via time-averaging can be found in [143]. Our goal is to gain deeper insight into the thermodynamics of cellular information processing, which has attracted much interest recently. For example, the role of energy dissipation has been investigated for *E. coli* [95] and eukaryotic [144] adaptation, two-component systems computing an external ligand concentration [94], the switching behavior of flagellar motors [145], biochemical sensing [92, 146–153] and kinetic proofreading [83, 154–161], see also

[20, 21, 162, 163] for classical works. In these studies, energy dissipation is characterized by the thermodynamic entropy production of an isothermal system.

An entropic rate that quantifies the performance of a sensory system and is bounded by the thermodynamic entropy production through an inequality had not been found in these previous works. In related work [92], it had been shown that the rate of mutual information between the time series of an external signal process and an internal sensor process is *not* bounded by the thermodynamic entropy production.

Furthermore, the relation between information and thermodynamics has attracted much interest recently, see, for example, Ref. [46] for a recent review. Most relevant to this chapter will be the recent advances in stochastic thermodynamics of bipartite systems [41], which are presented in chapter 3, where we introduced the learning rate. There, the learning rate is used to quantify the reduction of the Shannon entropy of the system due to the dynamics of a feedback controller. This entropic rate was studied for the first time by Allahverdyan *et al.* [57] for Brownian particles coupled to different heat baths, where it was interpreted as an information flow. The information flow was calculated from the time derivative of a time-delayed mutual information. Extensions for the applications of information flow to bipartite Markov jump processes can be found in [96], see [88, 134, 138] for similar work on feedback-driven engines.

In contrast to feedback-driven engines, where information is converted into useful energy, a sensor that measures a stochastic signal dissipates energy to obtain information about the signal. In related work, Still *et al.* [59] have investigated the minimum energetic cost to memorize and/or predict a stochastic driving signal. It has been shown that the difference between memorized information and predictive information is bounded by the dissipated energy.

In this chapter we show the learning rate we have introduced for feedback-driven system can be used to characterize the performance of a sensor measuring a stochastic time dependent signal. Thereby, the learning rate quantifies the reduction of uncertainty of a signal due to the dynamics of the sensor dynamics (Sec. 4.2). The fact that the learning rate is bounded by the dissipation rate of the sensor allows us to define a thermodynamic efficiency that can be used for biological systems. In Sec. 4.3 we present three sensor models, which are related to the chemotaxis network of *E. coli* [19, 164–168], one of which includes adaptation (see Sec. 4.3.3). For simplicity, we restrict our discussion in Sec. 4.3 to a stochastic time dependent binary signal, where a ligand concentration jumps between two values.

In Sec. 4.4 we introduce the sensory capacity, which is a purely information theoretic quantity that characterizes the performance of a sensor. The sensory capacity can formally be written as the ratio between learning rate and transfer entropy rate, the latter of which quantifies by how much the time history of the sensor reduces the uncertainty about the signal. The sensory capacity is generally bounded between 0 and 1. A sensor reaches the maximal sensor capacity 1 if the instantaneous state of the sensor contains the same amount of information about the signal as its full time history.

The sensory capacity can be raised with additional physical degrees of freedom that serve as a memory. Such an increase of the sensory capacity is related to the information from the time series of the sensor that is stored in the instantaneous state of the memory. We illustrate our findings with a cellular two-component network, where one degree of

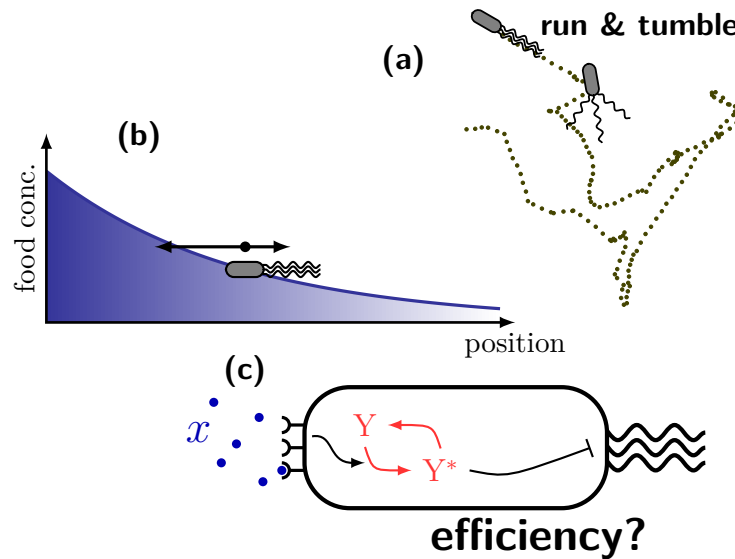


Figure 4.1| Schematic illustration of *E. coli* chemotaxis. (a) Run and tumble motion. (b) Bacteria want to bias their motion along gradients of food concentration (to the left). The motion to the right is prevented by an increase of the tumbling rate. (c) Central parts of the signaling network. Food molecules (blue dots) can bind to receptors. Unoccupied receptors activate the “tumbling proteins” ($Y \rightarrow Y^*$), where an active protein Y^* can bind to the flagellar motor to trigger a tumbling event.

freedom represents receptors that directly measure a ligand concentration and a second internal degree of freedom represents proteins which average the receptor signal over some time span and constitute the memory [94, 150, 151, 169, 170]. From the two-component network we derive coupled linear Langevin equations that can be solved analytically. We find that a sensor that represents an optimal Kalman-Bucy filter maximizes the sensory capacity.

Remarkably, we find an intriguing trade-off between sensory and thermodynamic efficiency, which is discussed in Sec. 4.6. If a sensor reaches the maximal sensory capacity 1, it will dissipate at least the twice amount of free energy as it learns, i.e., the thermodynamic efficiency must be below $1/2$. This trade-off, which holds for arbitrary bipartite systems, is illustrated for the coupled linear Langevin equations derived from the cellular two-component network.

4.2 Efficiency of cellular information processing

4.2.1 Processing time dependent signals for bacterial chemotaxis

A beautiful example for cellular information processing is the chemotaxis signaling network of *E. coli*, which we will now briefly explain; see Fig. 4.1 for a schematic overview. This signaling network will also play an important role for our examples.

Quite a long time ago the bacteria’s motion, which is characterized by a “run and tumble walk” was experimentally measured in three dimension by Berg and Brown [171],

as illustrated in Fig. 4.1(a). It has been found that the motion consists of “run” events, where the bacterium swims in a direction with constant velocity, and “tumble” events which interrupt the motion. During a tumble event the bacterium chooses randomly a new direction for the next run. If nutrient resources are limited the cell must find a way to bias its motion along directions of higher food concentration, see Fig. 4.1(b). In order to realize this bias, the bacterium has to measure a gradient of the external nutrient concentration, which is performed by transmembrane receptors. Remarkably, the cell is too small to detect such a concentration gradient directly. It uses a rather indirect approach, namely, it monitors the concentration as a function of time while it is swimming. For example, if the bacterium is heading in the “wrong” direction, the receptors will detect a decrease of concentration, which then trigger a tumble event earlier. More precisely, as illustrated Fig. 4.1(c), receptors that are not occupied by a ligand will preferably activate an internal protein ($Y \rightarrow Y^*$), which in turn can bind to the flagellar motor to initiate a tumble event. This strategy allows the bacterium from Fig. 4.1(b) to shorten its runs to the right and elongate runs to the left, which lead to a mean bias of its motion along the food gradient. Summarizing, successful chemotaxis requires to measure an external time dependent signal (e.g., ligand concentration) by internal degrees of freedom (e.g., receptors, proteins).

We will show that such a setup can be studied within the framework of stochastic thermodynamics of bipartite systems [41, 92, 93], which we have introduced in Sec. 3. For a sensor measuring a stochastic time dependent signal, we will show that the sensory performance of the sensor can be characterized by a learning rate quantifying the reduction of uncertainty of a signal due to the dynamics of the sensor. Remarkably, this learning rate is positive and bounded by the thermodynamic cost for maintaining the network, which will allow us to introduce an efficiency that can be used for biological systems. Three models inspired by the chemotaxis sensory system (Fig. 4.1) are studied in detail.

4.2.2 Bipartite process: Signal and Sensor

We assume a stochastic Markovian signal which constitutes an external process is labeled by x . The signal is measured by a chemical network denoted by y that represents the sensor. More precisely, we consider a bipartite Markov process [92, 93] with transition rates from the discrete state (x, y) to state (x', y') given by

$$w_{yy'}^{xx'} \equiv \begin{cases} w^{xx'} & \text{if } x \neq x' \text{ and } y = y', \\ w_{yy'}^x & \text{if } x = x' \text{ and } y \neq y', \\ 0 & \text{otherwise,} \end{cases} \quad (4.1)$$

where x, x' label states of the signal and y, y' states of the sensor, see Fig. 4.2. The transition rates are similar to the transition rates from (3.1), where only the first line differs. The transition rates of the signal $w^{xx'}$ are assumed not to be affected by the sensor state y , i.e., there is no feedback from sensor to the signal. Imperative is the influence of the signal dynamics on the sensor dynamics ($w_{yy'}^x$), which allows the sensor to establish correlations with the signal. In Fig. 4.3 we show two examples for bipartite Markov processes generated by the dynamics (4.1) as a function of time t . Thereby, the sensor process y_t (dotted green line) establishes correlations with the signal x_t (blue

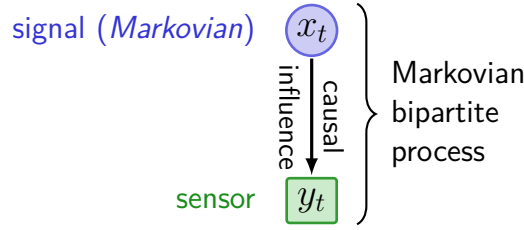


Figure 4.2| General setup. The signal x_t fluctuates as function of time t . The the dynamics of the sensor state y_t is influenced by the signal, whereas the sensor does not influence the signal. The state of the full bipartite system at time t is given by (x_t, y_t) .

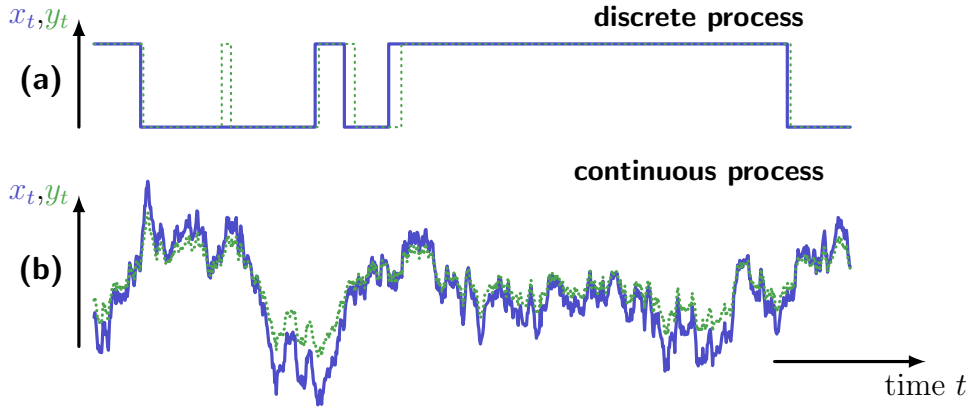


Figure 4.3| Examples for bipartite Markov processes of signal x_t (solid blue line) and sensor y_t (dotted green line) from Fig. 4.2. (a) Bipartite process with discrete valued states. (b) Bipartite process with continuous valued states (Brownian motion). A definition for a general continuous valued bipartite processes can be found in Sec. 3.C, where a setup of a signal and sensor process implies here $F_x(x, y) \equiv F_x(x)$.

solid line). Fig. 4.3(b) displays a bipartite Markov process labeled by continuously valued states, as used in sections 4.4 and 4.6 (see [120, 134] or Appendix 3.C for continuous valued bipartite processes).

In the long time limit, correlations between the sensor variable y and the signal variable x can be found in the steady state distribution $P(x, y)$ for state (x, y) . Borrowing the notation from chapter 3, we denote the marginal distributions by $P(x) \equiv \sum_y P(x, y)$ and $P(y) \equiv \sum_x P(x, y)$. The conditional probability then reads $P(x|y) \equiv P(x, y)/P(y)$, where $P(x|y) \neq P(x)$ indicates that the sensor y contains information about the signal, as we explain in the following paragraph.

The “static” uncertainty of the signal can be quantified by the Shannon entropy $H[x_t]$, which in the steady state is given by (3.3)

$$H[x_t] = - \sum_x P(x) \ln P(x). \quad (4.2)$$

The goal of the sensor is to reduce this uncertainty of the signal. Specifically, the sensor state y_t reduces the “static” uncertainty of the signal to (3.5)

$$H[x_t|y_t] = - \sum_{x,y} P(x, y) \ln P(x|y) \leq H[x_t]. \quad (4.3)$$

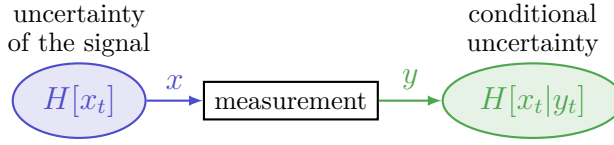


Figure 4.4 | Information of measurement is characterized by the reduction of uncertainty $I[x_t:y_t] = H[x_t] - H[x_t|y_t] \geq 0$.

One can interpret this scenario as communication along a noisy channel [35, 36], see Fig. 4.4 for an illustration. Thereby, the information that y_t receives is quantified by the reduction of uncertainty

$$I[x_t:y_t] = H[x_t] - H[x_t|y_t] = \sum_{x,y} P(x,y) \ln \frac{P(x,y)}{P(x)P(y)} \geq 0, \quad (4.4)$$

which is called mutual information [35, 36], see also Eq. (3.6). The mutual information $I[x_t:y_t]$ quantifies the correlation between the instantaneous state of the sensor y_t and the instantaneous state of the signal x_t .

Such correlations, however, do not come for free. For example, a bipartite system with dynamics (4.1) and steady state distribution $P(x,y)$ continuously dissipates energy. The thermodynamic cost for maintaining this network is quantified by the familiar thermodynamic entropy production [18]

$$\sigma = \sigma_x + \sigma_y \geq 0, \quad (4.5)$$

where

$$\sigma_x \equiv \sum_{x,x',y} P(x,y) w^{xx'} \ln \frac{w^{xx'}}{w^{x'x}} \geq 0 \quad (4.6)$$

is the contribution due to the signal dynamics and

$$\sigma_y \equiv \sum_{x,y,y'} P(x,y) w^{yy'} \ln \frac{w^{yy'}}{w^{y'y}} \geq 0 \quad (4.7)$$

arises from the dynamics of the sensor. In contrast to the feedback-driven case from the previous chapter, both contributions to the entropy production σ_x and σ_y are positive, which is a direct consequence of (4.1).

4.2.3 Learning rate and thermodynamic efficiency of a sensor

The mutual information (4.4) characterizes the “static” reduction of uncertainty due to the sensor. To compare the sensory performance of the sensor to the thermodynamic cost, we are interested in an entropic *rate* that characterizes the performance of the sensor. Fortunately, we have introduced in Sec. 3.2.4 the learning rate for feedback-driven systems to characterize the performance of a feedback controller. We show here the learning rate can also be used to characterize the performance of the sensor, which has nice properties

that are generally not satisfied for systems discussed in the previous chapter. Let us repeat the definition of the learning rate from Sec. 3.2.4,

$$l_y \equiv \frac{H[x_t|y_t] - H[x_t|y_{t+dt}]}{dt} = \sum_{x,y,y'} P(x,y)w_{yy'}^x \ln \frac{P(x|y')}{P(x|y)}, \quad (4.8)$$

where we have used (3.22) in the final step. As in Sec. 3.2.4 we assume here and in the following for all expressions with a time difference “ dt ” in the denominator the limit $dt \rightarrow 0$. The learning rate quantifies the reduction of uncertainty due to the dynamics of the sensor. More precisely, a transition $(x,y) \rightarrow (x,y')$ changes the conditional stochastic entropy [6, 8] (see also Sec. 2.2) from $s(x|y) \equiv -\ln P(x|y)$ to $s(x|y') \equiv -\ln P(x|y')$, which is associated with an entropy change $s(x|y') - s(x|y) = -\ln[P(x|y')/P(x|y)]$ that is exactly minus the last logarithmic term in (4.8). Due to the last-named minus sign the term $\ln[P(x|y')/P(x|y)]$ characterizes the reduction of stochastic entropy along the transition $(x,y) \rightarrow (x,y')$, which in the steady state occurs with the rate $P(x,y)w_{yy'}^x$. Therefore, the learning rate can be interpreted as the average reduction of Shannon entropy of the signal due to the dynamics of the sensor governed by rates $w_{yy'}^x$.

The directed causal influence $x_t \rightarrow y_t$, i.e., the lack of feedback $x_t \leftarrow y_t$ follows from the first line of (4.1). One important consequence from the absence of feedback (4.1) is $l_y \geq 0$. To show that the learning rate is indeed positive, we recall from (3.23) the Shannon entropy increase due to the dynamics of the signal “ x ”

$$h_x = \frac{H[x_{t+dt}|y_t] - H[x_t|y_t]}{dt} = \sum_{x,x',y} P(x,y)w^{xx'} \ln \frac{P(x|y)}{P(x'|y)}. \quad (4.9)$$

In the stationary state the conditional Shannon entropy remains constant

$$\frac{d}{dt}H[x_t|y_t] = h_x - l_y = 0, \quad (4.10)$$

where h_x accounts for the randomness that enters from the dynamics of the signal and l_y accounts for the reduction of uncertainty due to the sensor. Using this feature we obtain

$$l_y = h_x = \sum_{x,x'} P(x)w^{xx'} \sum_y P(y|x) \ln \frac{P(y|x)}{P(y|x')} \geq 0, \quad (4.11)$$

where the second equality follows from $\frac{d}{dt}H[x_t] = \sum_{x,x'} P(x)w^{xx'} \ln[P(x)/P(x')] = 0$, which has been subtracted from h_x ; the inequality is a consequence of the log-sum-inequality [36] for the sum over the variable y .

In the previous chapter we have found the learning rate l_y to be bounded by the entropy production σ_y of the subsystem “ y ” that represents the sensor, i.e., $l_y \leq \sigma_y$. If one integrates out the sensor process the signal process remains a Markov process and, hence, the entropy production due to transitions of the signal variable is positive ($0 \leq \sigma_x$), which is equivalent to $\sigma_y \leq \sigma$. Summarizing, we obtain with (4.11)

$$0 \leq l_y \leq \sigma_y \leq \sigma. \quad (4.12)$$

This chain of inequalities is the main foundation of this section. For a bipartite system with x_t being an external signal process, the rate at which a sensory network y_t learns

about the signal x_t is bounded by the thermodynamic entropy production. Therefore, a sensor must dissipate energy to realize a nonzero learning rate. Using the chain of inequalities (4.12) we define the thermodynamic efficiency [119]

$$\eta \equiv \frac{l_y}{\sigma_y} \leq 1. \quad (4.13)$$

From a technical point of view, it should be noted that if the signal process “ x ” is an equilibrium process ($\sigma_x = 0$), which is true for all examples used in this chapter, one obtains $\sigma = \sigma_y$ and $\eta = l_y/\sigma$.

In the following section 4.3, we will discuss three models inspired by the chemotaxis system of *E. coli* to show that this framework can be useful to study cellular information processing. Before discussing the examples we have to introduce a coarse-grained learning rate that is particularly relevant to the examples presented in Sec. 4.3.2 and Sec. 4.3.3, which involve a Monod-Wyman-Changeux (MWC) model for a receptor [172, 173].

4.2.4 Coarse-grained learning rate

We consider the case where the state of the sensor is characterized by two variables $y_t = (y_1(t), y_2(t))$. At signal state x the transition rate from sensor state $y \equiv (y_1, y_2)$ to sensor state $y' \equiv (y'_1, y'_2)$ is denoted by $w_{yy'}^x = w_{(y_1 y_2)(y'_1 y'_2)}^x$. The first component, labeled by variables y_1, y'_1 , learns about the signal with a coarse-grained rate [119, 120]

$$l_{y_1} = \sum_{y_1, y_2, y'_1, x} P(x, y) w_{(y_1 y_2)(y'_1 y'_2)}^x \ln \frac{P(x|y_1)}{P(x|y'_1)}, \quad (4.14)$$

where $P(x|y_1) \equiv P(x, y_1)/P(y_1)$ is a conditional steady state probability with coarse-grained joint distribution $P(x, y_1) \equiv \sum_{y_2} P(x, y)$ and marginal distribution $P(y_1) \equiv \sum_x P(x, y_1)$. Using effective rates for the coarse-grained process

$$\tilde{w}_{y_1 y'_1}^x \equiv \frac{1}{P(x, y_1)} \sum_{y_2, y'_2} P(x, y) w_{(y_1 y_2)(y'_1 y'_2)}^x \quad (4.15)$$

for $y_1 \neq y'_1$ allows us to write the coarse-grained learning rate in a similar form as shown in Eq. (4.8),

$$l_{y_1} = \sum_{y_1, y'_1, x} P(x, y_1) \tilde{w}_{y_1 y'_1}^x \ln \frac{P(x|y_1)}{P(x|y'_1)}. \quad (4.16)$$

Moreover, the coarse-grained entropy change due to the signal dynamics (4.9) becomes

$$h_x^{(1)} \equiv \sum_{x, x', y_1} P(x, y_1) w^{xx'} \ln \frac{P(x|y_1)}{P(x'|y_1)}, \quad (4.17)$$

where the steady state implies $\frac{d}{dt} H[x_t|y_1(t)] = h_x^{(1)} - l_{y_1} = 0$. Remarkably, the coarse grained learning rate satisfies

$$l_{y_1} = h_x^{(1)} = \sum_{x, x'} P(x) \sum_{y_1} P(y_1|x) w^{xx'} \ln \frac{P(y_1|x)}{P(y_1|x')} \geq 0, \quad (4.18)$$

where we have used the stationary state property in the first and second equality [cf. Eq. (4.11)], and the log-sum-inequality [36] for the sum over variable y_1 in the final step. Comparing the coarse-grained learning rate l_{y_1} from (4.18) with the learning rate l_y from (4.11) we find $l_{y_1} \leq l_y$, which follows directly from the log-sum-inequality [36]. Therefore, a subsystem of the sensor learns less about a signal than the full sensor.

Using effective the transition rates from (4.15) one obtains the coarse-grained entropy production [103]

$$\tilde{\sigma}_{y_1} \equiv \sum_{x, y_1, y'_1} p(x, y_1) \tilde{w}_{y_1 y'_1}^x \ln \frac{\tilde{w}_{y_1 y'_1}^x}{\tilde{w}_{y'_1 y_1}^x}. \quad (4.19)$$

The coarse-grained entropy production $\tilde{\sigma}_{y_1}$ is a lower bound on the entropy production σ_y . Moreover, we find the coarse-grained entropy production bounds the coarse-grained learning rate

$$0 \leq l_{y_1} \leq \tilde{\sigma}_{y_1}. \quad (4.20)$$

The following calculation will show (4.20), which is of particular importance for the models involving the MWC receptor model discussed in sections 4.3.2 and 4.3.3. First, we find

$$\sigma_y - l_y = \sum_{x, y, y'} P(x, y) w_{yy'}^x \ln \frac{P(x, y) w_{yy'}^x}{P(x, y') w_{y'y}^x} \geq \sum_{x, y_1, y'_1} P(x, y_1) \tilde{w}_{y_1 y'_1}^x \ln \frac{P(x, y_1) \tilde{w}_{y_1 y'_1}^x}{P(x, y'_1) \tilde{w}_{y'_1 y_1}^x} = \tilde{\sigma}_{y_1} - l_{y_1}, \quad (4.21)$$

where the first identity is derived from (4.6) and (4.8), while the inequality follows from the log-sum-inequality over the sum of variables y_2, y'_2 and identifying the rates from (4.15). The last equality in (4.21) is obtained with (4.16) and (4.19). Second, using the log-sum-inequality for the sum over variables y_1, y'_1 yields $\tilde{\sigma}_{y_1} - l_{y_1} \geq 0$, which is equivalent to the right hand side of (4.20). Moreover, from (4.21) we find $\tilde{\sigma}_{y_1} \leq \sigma_y + l_{y_1} - l_y \leq \sigma_y$, i.e., the coarse-grained entropy production $\tilde{\sigma}_{y_1}$ systematically underestimates the entropy production σ_y as mentioned before.

Summarizing, integrating out variables $y = (y_1, y_2) \rightarrow y_1$ lead to a decrease of the learning rate and, simultaneously, to a systematic decrease of the apparent entropy production ($l_{y_1} \leq l_y$ and $\tilde{\sigma}_{y_1} \leq \sigma_y$).

4.3 Examples systems from *E. coli* chemotaxis

We use models inspired by the *E. coli* chemotaxis system (Fig. 4.1) to illustrate our results from the previous section. The external signal process x_t is assumed to be a time dependent ligand concentration that switches at random with a constant rate γ_c between two values c_1 and c_2 , see Fig. 4.5. Using Eq. (4.6) one can easily see that such an external process formally satisfies $\sigma_x = 0$, i.e., the total entropy production reads $\sigma = \sigma_y$. We discuss in the following three sensor models labeled by y .

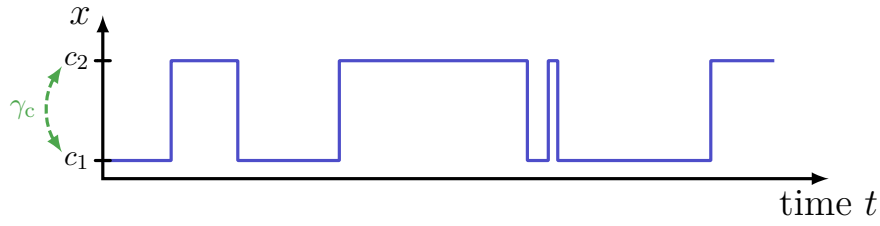


Figure 4.5| Signal external ligand concentration that jumps between two values c_1 and c_2 at a constant rate γ_c .

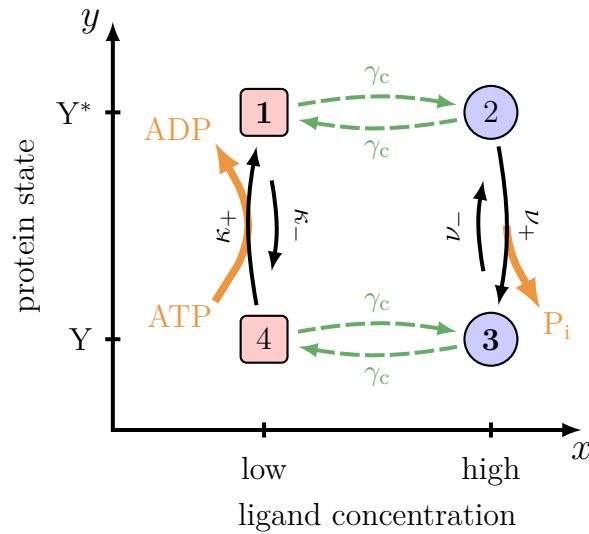


Figure 4.6| Toy Model with four states.

4.3.1 Toy model

We start with a quite simplified model [92] for which inequality (4.12) can be studied, see Fig. 4.6. The internal state is characterized by a protein CheY, which can either be in an active state Y^* or in an inactive state Y . In the *E. coli* chemotaxis system from Fig. 4.1(c), for example, tumbling events, which “stop” the motion, are triggered by proteins in state Y^* . The protein state can be changed by two different reversible chemical reactions. First, the protein can be activated $Y \rightarrow Y^*$ along a phosphorylation reaction



where an adenosine triphosphate (ATP) is turned to an adenosine diphosphate (ADP) with transition rates κ_{\pm} . Second, the protein can be deactivated ($Y^* \rightarrow Y$) along a dephosphorylation reaction



through a release of an inorganic phosphate P_i , where ν_{\pm} are transition rates. Following both reactions (4.22) and (4.23) along the “+”-direction will not change the state of the

protein, whereas it hydrolyzes one ATP ($\text{ATP} \rightarrow \text{ADP} + \text{P}_i$) while consuming the chemical free energy $\Delta\mu \equiv \mu_{\text{ATP}} - \mu_{\text{ADP}} - \mu_{\text{P}_i} \geq 0$, where μ_s is the chemical potential of species $s = \text{ATP}, \text{ADP}, \text{P}_i$. The kinetic rates κ_{\pm} and ν_{\pm} are inherently coupled to this non-equilibrium driving force

$$\Delta\mu = \ln \frac{\kappa_+ \nu_+}{\kappa_- \nu_-}, \quad (4.24)$$

which follows from the local detailed balance relation (2.7), where here and for the remainder of the chapter we have set $k_B T \equiv 1$.

The external process is assumed to be an external concentration of ligands which jumps at random between two extreme values “low” and “high” with a constant rate γ_c , which corresponds to $c_1 \ll c_2$ in Fig. 4.5. If the concentration is low, most receptors on the cell membrane will be empty, which turns the receptors active. Active receptors are assumed to promote phosphorylation of proteins, where we assume here that only reaction (4.22) is allowed to change the state of the protein CheY. If on the other side the concentration is high, most receptors will be occupied by a ligand, and consequently being inactive. We assume in the case of inactive receptors that proteins can only change their state via dephosphorylation (4.23), whereas the phosphorylation reaction (4.22) is completely blocked. This leads to the four state model in Fig. 4.6. Note that a more complete model, as considered in [92], would allow both chemical reactions to happen at both low and high concentrations, which would be represented by two additional vertical links for each state x of the signal in Fig. 4.6. Furthermore, models with more than one CheY protein as discussed in [94, 120] will be discussed in Sec. 4.5 later.

We denote the state distribution of the states $z = 1, 2, 3, 4$ from Fig. 4.6 by P_z . The stationary current then reads

$$J_+ = P_4 \kappa_+ - P_1 \kappa_- = \frac{\gamma_c}{2} \frac{\kappa_+ \nu_+ - \kappa_- \nu_-}{(\kappa_+ + \kappa_-)(\nu_+ + \nu_-) + \gamma_c(\kappa_+ + \kappa_- + \nu_+ + \nu_-)}, \quad (4.25)$$

which is the rate of ATP consumption. According to Kirchhoff’s law J_+ equals the current along each of all four edges in clockwise direction from Fig. 4.6. Consequently, the entropy production (4.5) becomes

$$\sigma = J_+ \Delta\mu. \quad (4.26)$$

Moreover, the learning rate (4.8) is given by

$$l_y = J_+ \ln \left(\frac{P_1 P_3}{P_2 P_4} \right) \equiv J_+ f, \quad (4.27)$$

where $f = \ln[P_1 P_3 / (P_2 P_4)]$ is bounded by the chemical potential difference $\Delta\mu$.

In Fig. 4.7(a) we show the thermodynamic efficiency for the model system from Fig. 4.6. One can deduce two important limiting scenarios regarding the switching frequency of the external signal process γ_c . If the signal process is very slow ($\gamma_c \ll \kappa_+, \nu_+$) the protein will track the signal with highest fidelity $f \rightarrow \Delta\mu$, which corresponds to a adiabatic switching with maximal efficiency $\eta \rightarrow 1$. A slow signal, however, does not contain much information, which results in a very low learning rate l_y on the left in Fig. 4.7(b). At the

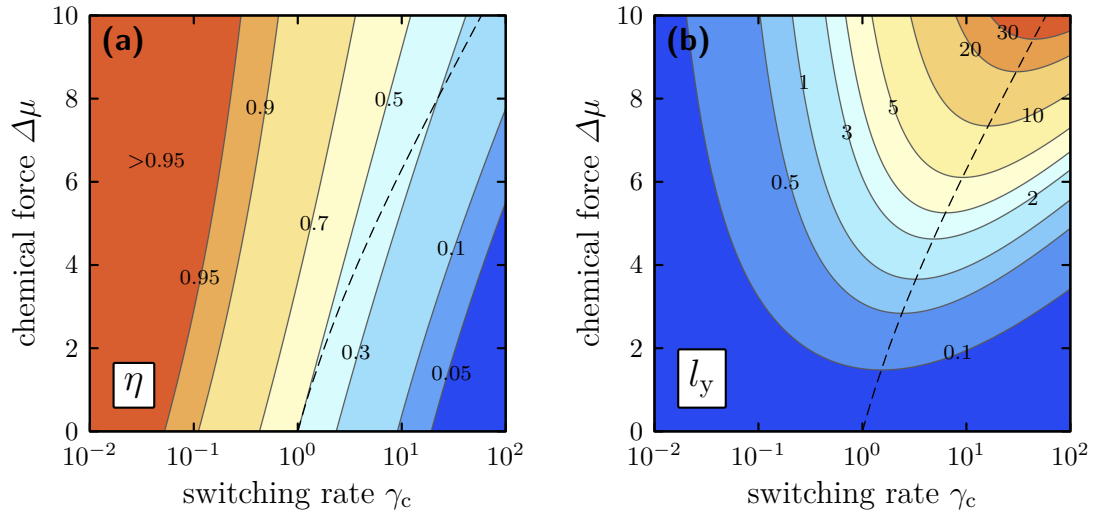


Figure 4.7 | Sensory performance of toy model from Fig. 4.6. **(a)** Thermodynamic efficiency $\eta = l_y/\sigma$. **(b)** Learning rate l_y . Parameters: $\kappa_+ = \nu_+ = e^{\Delta\mu/2}$ and $\kappa_- = \nu_- = 1$.

other extreme, where the signal switches extremely fast ($\gamma_c \gg \kappa_+, \nu_+$), the protein is not able to track the signal $f \rightarrow 0$. In this limit of fast external switching ($\gamma_c \rightarrow \infty$) both learning rate l_y and efficiency η will vanish.

Between these two limits is an intermediate external switching rate $\gamma_c = \gamma_c^*(\Delta\mu)$, where the learning rate is maximal, see the dashed line in Fig. 4.7. As shown in Fig. 4.8, the maximum learning rate $l_y^*(\Delta\mu) \equiv l_y(\Delta\mu, \gamma_c^*)$ increases with the chemical non-equilibrium driving force $\Delta\mu$, which shows that an increase of the energy consumption systematically increases the sensory performance. However, the efficiency at maximum power $\eta^* \equiv l_y^*/\sigma^*$ decreases with the chemical force $\Delta\mu$, where $\eta^*(\Delta\mu) \equiv \eta(\Delta\mu, \gamma_c^*)$; see inset of Fig. 4.8. The efficiency at maximum power approaches $1/2$ close to equilibrium, which allows for an analogy to molecular motors. For example, it is well known for tightly coupled heat engines [174] and molecular motors [175] that the efficiency at maximum power becomes $1/2$ in the linear response regime. In contrast to a molecular motor, where chemical energy is used to perform mechanical work, a sensor, as discussed here, dissipates energy so that a protein can learn about an external signal process at a rate l_y . A more systematic linear response theory for bipartite systems involving the learning rate has recently been derived in [133], where the learning rate has been interpreted as “information flow”.

In this subsection we have shown a model, where the entropy production corresponds to chemical work that is consumed inside the cell, which arises from an internal ATP hydrolysis reaction. In the following we show that the work necessary for a non-zero learning rate can also be delivered by the external process.

4.3.2 Single receptor model

The receptors of *E. coli* are located on the cell surface allowing external ligands to bind. The activity of a kinase CheA is influenced by the binding of ligands to the receptor via a linker protein CheW. If the kinase CheA labeled by variable $a = 0, 1$ is activated ($a = 1$), it acts as an enzyme for the phosphorylation (4.22) of the protein CheY [19], which is

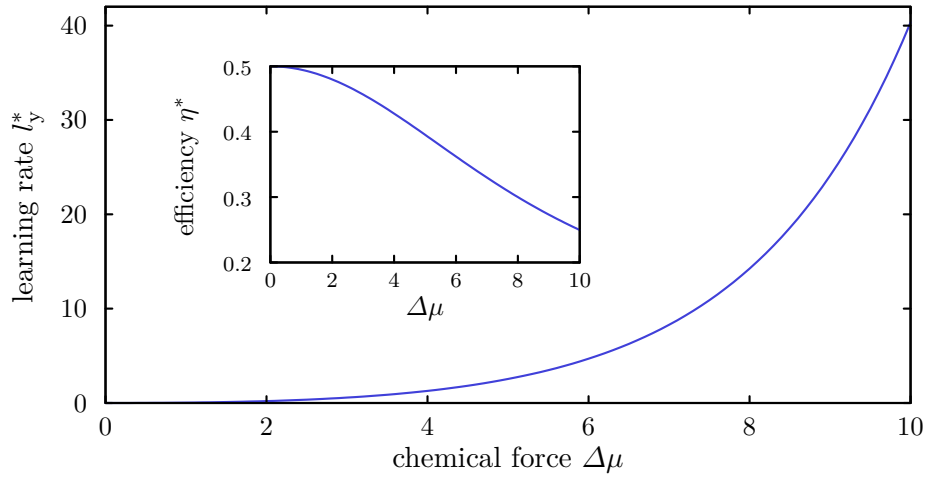


Figure 4.8| Maximum learning rate and efficiency. It is shown the maximum learning rate l_y^* for parameters from Fig. 4.7 as function of the chemical force $\Delta\mu$. The inset shows the corresponding efficiency at maximum power η^* . Parameter: $\kappa_+ = \nu_+ = e^{\Delta\mu/2}$ and $\kappa_- = \nu_- = 1$.

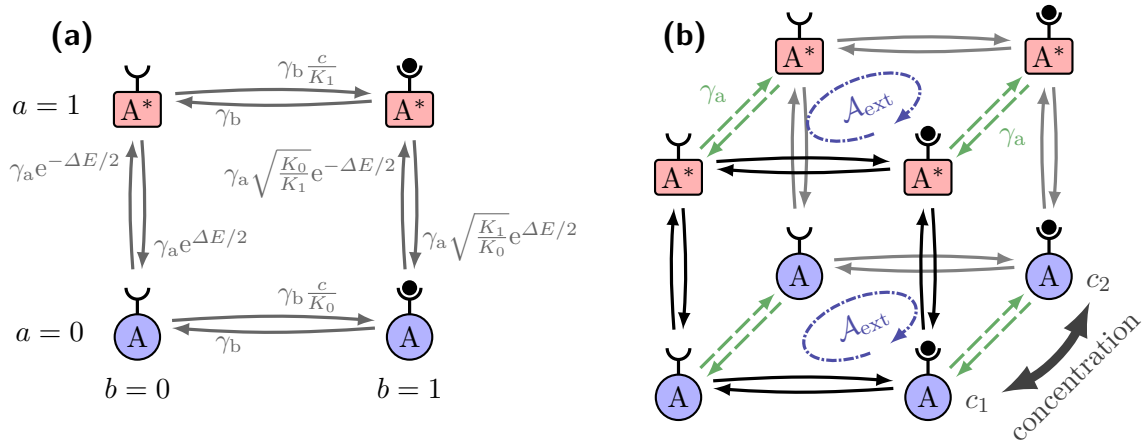


Figure 4.9| Signal receptor model. (a) MWC receptor model with transition rates corresponding to the internal sensor process. (b) Full model including the signal state that corresponds to concentrations c_1 and c_2 . The dash-dotted blue cycle corresponds to the only non-vanishing affinity $\mathcal{A}_{\text{ext}} \equiv \ln(c_2/c_1)$.

responsible for the tumbling motion of the bacterium. We consider an MWC model for a single receptor, where the external ligand binding indirectly regulates the activity of the kinase CheA [148, 176]. For convenience, we consider only a single receptor, i.e., no cooperative interaction between multiple receptors, which is also another important feature of the MWC model [173]. It should be noted that an extension to multiple receptors with cooperative interactions is straightforward.

The single receptor model with four states is shown in Fig. 4.9(a). The states of the receptor are labeled by $y = (a, b)$. The receptor can either be occupied by a ligand, $b = 1$, or be empty, $b = 0$. Moreover, the kinase CheA can be in an active state $a = 1$ or in

an inactive state $a = 0$. The free energy difference between an occupied receptor and an empty receptor is given by $F_{\text{occupied}} - F_{\text{empty}} = \ln(K_a/c)$, where K_a is the dissociation constant for activity state $a = 0, 1$ and c is the external ligand concentration. More precisely, the term $\ln K_a$ can be associated with the bare free energy between occupied receptor and empty receptor for kinase state a and the term $\ln c$ can be associated with the chemical potential of the ligand [31]. The free energy difference between active ($a = 1$) and inactive ($a = 0$) state of an empty receptor is denoted by ΔE . Since a conformational change is assumed to be an equilibrium process the free energy of each internal state (a, b) can be written as

$$F(a, b|c) = a\Delta E - b \ln \frac{c}{K_a}. \quad (4.28)$$

The specific transition rates $w_{(a,b)(a',b')}^c$ from Fig. 4.9(a) are chosen to satisfy the local detailed balance $\ln[w_{(a,b)(a',b')}^c/w_{(a',b')(a,b)}^c] = F(a, b|c) - F(a', b'|c)$. Note that the rate γ_a sets the time-scale of the conformational change and the rate γ_b the time-scale of binding events, where it is assumed that ligand binding and unbinding is faster than conformational changes of the receptor ($\gamma_b \gg \gamma_a$). It should be noted that the four state model from Fig. 4.9(a) has a vanishing cycle affinity which follows from being an equilibrium MWC model.

Let us now add the dynamics of the external signal process, which is a ligand concentration that jumps with a rate γ_c between two values c_1 and c_2 . The full bipartite system becomes an eight-state model as shown in Fig. 4.9(b). Using the steady state probability $P(c; a, b)$ of the full state $(x; y) = (c; a, b)$ and Schnakenberg's formula [39] allows us to write the entropy production as a product of probability current times cycle affinity as explained in the following. First, the only non-vanishing cycle affinity of the "cube" from Fig. 4.9(b) is $\mathcal{A}_{\text{ext}} = \ln(c_2/c_1)$, which is indicated by dash-dotted blue arrows. It corresponds to a ligand binding at $c = c_2$ and releasing the ligand at concentration $c = c_1$, where $\ln(c_2/c_1)$ is difference of the chemical potential of the ligand along these concentration switches. Second, the probability current along this cycle

$$J = \gamma_c \sum_a [P(c_2; a, 1) - P(c_1; a, 1)] \quad (4.29)$$

can be interpreted as the rate at which ligands are taken from concentration c_2 and released at concentration c_1 . Summarizing, the total entropy production (4.5) becomes

$$\sigma = J \ln \frac{c_2}{c_1}. \quad (4.30)$$

Note that the chemical work which compensates for the entropy production is delivered by the external signal, which switches the ligand concentration in a time-dependent manner between two values c_2 and c_1 . In contrast to the previous example, the external process delivers the work necessary for a nonzero learning rate, which for the full sensor labeled by $y = (a, b)$ reads (4.11)

$$l_{\text{ab}} \equiv l_y = \gamma_c \sum_{a,b} [P(c_2; a, b) - P(c_1; a, b)] \ln \frac{P(c_2; a, b)}{P(c_1; a, b)}. \quad (4.31)$$

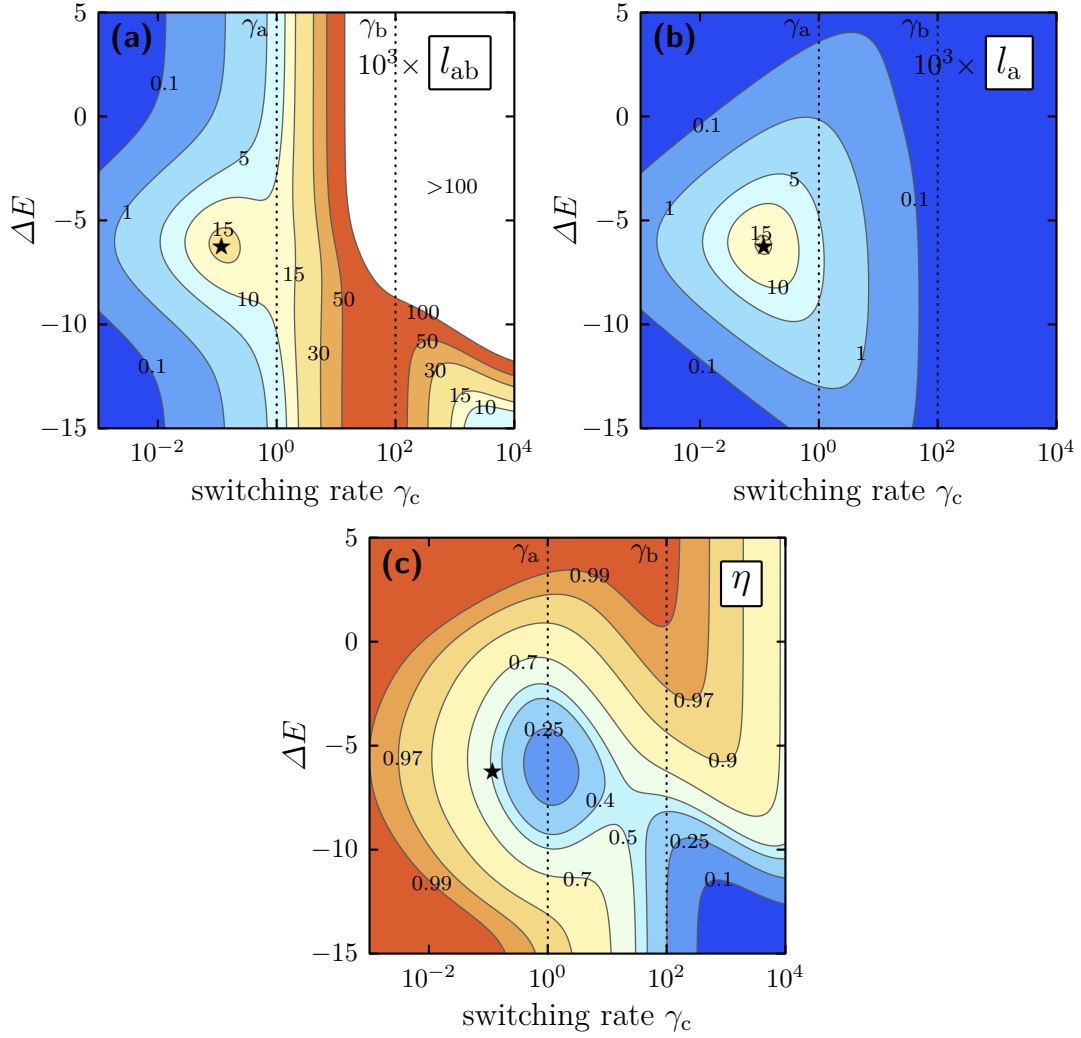


Figure 4.10 | Sensory performance of single receptor MWC model as function of external switching rate γ_c and conformational free energy difference ΔE . **(a)** Learning rate l_{ab} . **(b)** Coarse-grained learning rate l_a . **(c)** Efficiency $\eta = l_{ab}/\sigma$. Parameters from Fig. 4.9 are set to $K_1 = (K_0)^{-1} = 400$ and $c_2 = 1/c_1 = 3$; the rate of conformational change $\gamma_a = 1$ and the rate of binding kinetics $\gamma_b = 100$ are indicated by vertical dotted lines.

Moreover, coarse-grained learning rate of the conformational state of the sensor labeled by variable $y_1 \equiv a$ is given by (4.18)

$$l_a \equiv l_{y_1} = \gamma_c \sum_a \left[P(c_2, a) - P(c_1, a) \right] \ln \frac{P(c_2, a)}{P(c_1, a)}, \quad (4.32)$$

where $P(c, a) \equiv \sum_b P(c; a, b)$.

In Fig. 4.10 is plotted the sensory performance as a function of the conformational free energy difference ΔE and the external switching rate γ_c . Comparing figures 4.10(a) and 4.10(b), we find that for a slowly switching environment ($\gamma_c < \gamma_a$) the coarse-grained conformational state of the sensor a learns as much as the full sensor ($l_a \simeq l_{ab}$), which includes the fast binding-unbinding kinetics of ligands that is labeled by b . Increasing the

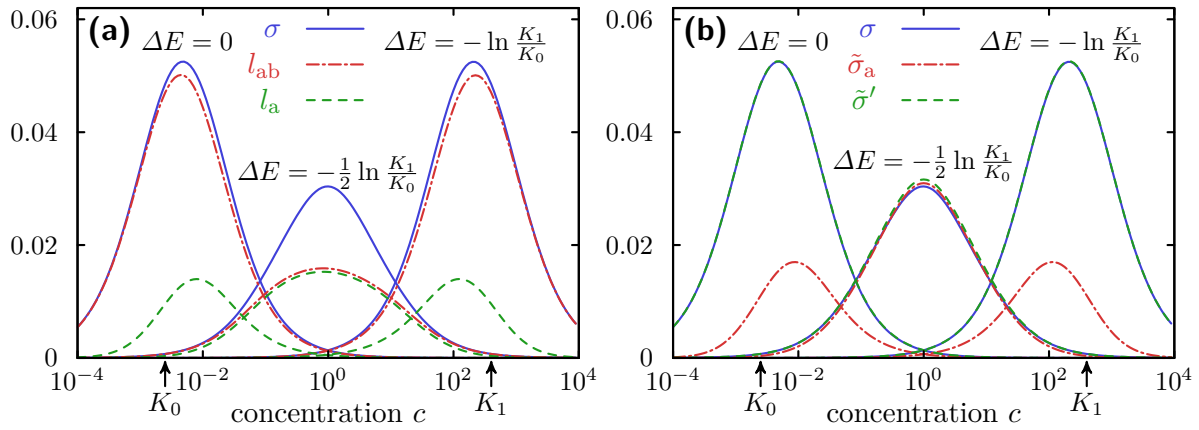


Figure 4.11 | Numerical result for single receptor model for three different conformational free energies. **(a)** Dissipation rate σ , learning rate l_{ab} , and coarse-grained learning rate l_a as function of the ligand concentration. **(b)** Entropy production of full system σ and coarse-grained entropy production $\tilde{\sigma}_a$ and entropy of the full system $\tilde{\sigma}'$ with perfect timescale separation ($\gamma_b \rightarrow \infty$). Parameters as in Fig. 4.10: $K_1 = (K_0)^{-1} = 400$, $\gamma_a = 1$, $\gamma_b = 100$, $c_1 = c/3$ and $c_2 = 3c$.

switching rate, we find the coarse-grained learning rate has a maximum $l_a \simeq 0.015$ at a switching rate $\gamma_c \sim 10^{-1}$. It decays $l_a \rightarrow 0$ as the switching rate increases further, since the conformational state labeled by variable a cannot track the signal any more. It should be noted that the fast binding unbinding kinetics $\gamma_b \gg \gamma_a$ allow the full learning rate l_{ab} to be substantially larger than l_a for $\gamma_c > \gamma_a$, whereas if the switching rate of the external signal becomes much larger the binding unbinding kinetics ($\gamma_c \gg \gamma_b$) we find even the fast binding-unbinding kinetics cannot track the signal any more, which leads to a decay of the full learning rate ($l_{ab} \rightarrow 0$) for $\gamma_c \rightarrow \infty$, which is partially shown the lower right of Fig. 4.10(a).

Considering the thermodynamic efficiency from Fig. 4.10(c), we find the adiabatic limit of slow switching $\gamma_c \rightarrow 0$ maximizes the efficiency $\eta \rightarrow 1$. The star in Fig. 4.10 marks the maximum of the coarse-grained learning rate $l_a \simeq 0.015$, where the efficiency is decreased $\eta \simeq 0.5$. As the switching of the environment becomes faster than the receptor binding kinetics $\gamma_c \gg \gamma_b$, the efficiency drops to zero ($\eta \rightarrow 0$) since the receptor cannot track quickly fluctuating signals.

From the contour plot of l_a , where the concentration switches between $c_1 = 1/3$ and $c_2 = 3$, we find the optimal conformational free energy to be $\Delta E \simeq -\frac{1}{2} \ln(K_1/K_0) \simeq -6$. Interestingly, the optimal conformational free energy ΔE depends on the concentration values of the external signal. To see that, we show the entropy production σ and the learning rates l_{ab} as well as l_a for three different conformational free energies ΔE in Fig. 4.11(a) as functions of the background concentration c , where $c_1 \equiv c/3$ and $c_2 \equiv 3c$. Each individual conformational free energy difference $\Delta E = 0, -\frac{1}{2} \ln(K_1/K_0), \ln(K_1/K_0)$ is “optimal” for a specific concentration range $c \sim 10^{-2}, 1, 10^2$, respectively. The conformational free energy ΔE will later play an important role, for the adaptation mechanism that helps to adopt the receptor to specific background concentrations. We note that for $K_0 \ll c \ll K_1$ and $\Delta E = -\frac{1}{2} \ln(K_1/K_0)$ we find $l_a \simeq l_{ab}$, since the bound (or unbound)

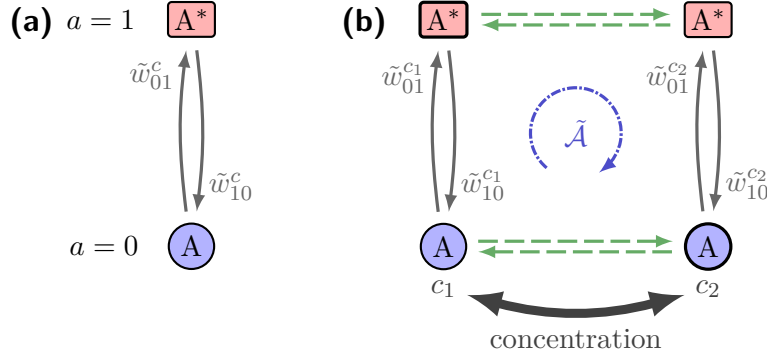


Figure 4.12| Coarse-grained system. (a) Internal state of coarse-grained system from Fig. 4.9(a). (b) Coarse-grained system with external states c_1 and c_2 . The dash-dotted arrow corresponds to the cycle affinity $\tilde{\mathcal{A}}_{\text{ext}}$ from Eq. (4.36).

state of the receptor is highly correlated with the inactive (or active) conformational state.

Since there is a clear time scale separation between the slow kinetics of conformational changes and the fast kinetics of ligand binding ($\gamma_b \gg \gamma_a$), we are able to integrate out the fastest variable b . Thereby, the four internal states from Fig. 4.9(a) become two internal states as shown in Fig. 4.12(a). In the formal limit $\gamma_b \rightarrow \infty$ one can define the coarse-grained transition rates [103]

$$\tilde{w}_{aa'}^c \equiv \sum_b w_{(a,b)(a',b)}^c \frac{(c/K_a)^b}{1 + c/K_a}, \quad (4.33)$$

where $(c/K_a)^b/(1 + c/K_a)$ is the conditional probability $P(b|a, c)$ in the limit $\gamma_b \rightarrow \infty$. Specifically, the transition rates from Fig. 4.9(a) lead to coarse-grained rates

$$\tilde{w}_{01}^c = \gamma_a e^{-\Delta E/2} \left(\frac{1 + c/\sqrt{K_0 K_1}}{1 + c/K_0} \right) \quad \text{and} \quad \tilde{w}_{10}^c = \gamma_a e^{\Delta E/2} \left(\frac{1 + c/\sqrt{K_0 K_1}}{1 + c/K_1} \right). \quad (4.34)$$

Therefore, the conformational free energy difference between active state of the receptor and inactive state of the receptor

$$\Delta F(c) = \ln \frac{\tilde{w}_{10}^c}{\tilde{w}_{01}^c} = \Delta E + \ln \left(\frac{1 + \frac{c}{K_0}}{1 + \frac{c}{K_1}} \right) \quad (4.35)$$

is a function of the external concentration. Fig. 4.12(b) shows the coarse-grained model including the environmental switches between concentration c_1 and c_2 , where the coarse-grained affinity

$$\tilde{\mathcal{A}}_{\text{ext}} \equiv -\Delta F(c_1) + \Delta F(c_2) = \ln \frac{\tilde{w}_{01}^{c_1} \tilde{w}_{10}^{c_2}}{\tilde{w}_{10}^{c_1} \tilde{w}_{01}^{c_2}} = \ln \left[\left(\frac{1 + \frac{c_1}{K_1}}{1 + \frac{c_1}{K_0}} \right) \left(\frac{1 + \frac{c_2}{K_0}}{1 + \frac{c_2}{K_1}} \right) \right] \quad (4.36)$$

arises from the external switches. Denoting the coarse-grained probability of (c, a) by $\tilde{P}(c, a)$ allows us to write the coarse-grained entropy production (4.19) as

$$\tilde{\sigma}_a = \tilde{J} \tilde{\mathcal{A}}_{\text{ext}}, \quad (4.37)$$

where the current reads

$$\tilde{J} = \gamma_c [\tilde{P}(1, c_1) - \tilde{P}(1, c_2)]. \quad (4.38)$$

Note that $\tilde{\sigma}_a$ is a lower bound on the total entropy production (4.30) which can be associated with the chemical work delivered by the external signal. Using (4.29) one can deduce the current

$$\tilde{J}' = \gamma_c \sum_a \left[\tilde{P}(c_2, a) \frac{c_2}{K_a + c_2} - \tilde{P}(c_1, a) \frac{c_1}{K_a + c_1} \right], \quad (4.39)$$

which satisfies $\tilde{J}' \simeq J$ for $\gamma_a \ll \gamma_b$, which allows to infer the total entropy production (4.30) via the formula

$$\tilde{\sigma}' \equiv \tilde{J}' \ln \frac{c_2}{c_1}, \quad (4.40)$$

which satisfies $\tilde{\sigma}' = \sigma$ for $\gamma_b \rightarrow \infty$. In Fig. 4.11(b) we compare the entropy production rates. We confirm that for $\gamma_b/\gamma_a = 100 \gg 1$ the total entropy production can be well approximated by $\sigma \simeq \tilde{\sigma}'$. Moreover, the coarse-grained entropy production $\tilde{\sigma}_a$ is a lower bound on the total entropy production.

More generally, the conformational change labeled by a could involve ATP consumption [148, 177], which leads to an entropy production which has two contributions; see also chapter 6 for a nonequilibrium receptor model. One contribution would be the chemical work that is consumed inside the cell and the second contribution would be the work that is delivered by the signal. In the following we discuss the adaptation mechanism that allows to dynamically adjust the conformational free energy difference ΔE to the background concentration c as illustrated in Fig. 4.11. Such an adaptation mechanism requires additional chemical energy to be consumed inside the cell.

4.3.3 Model with adaptation

In this subsection we add an adaptation mechanism to the system which changes the conformational free energy difference ΔE between the active ($a = 1$) and the inactive state ($a = 0$). It allows us to obtain a more complete model, where the conformational change of the receptor is adopted from the coarse-grained model (Fig. 4.12). In addition to the kinase activity a , the receptor includes a methylation level m that changes the conformational free energy difference ΔE [95]. Up to four methyl groups can bind to the receptor, which correspond to levels $m = 0, 1, \dots, 4$. The internal state of the receptor network is labeled by $y = (a, m)$, see Fig. 4.13(a). The goal of the adaptation mechanism is to keep the mean value of kinase activity around 1/2, where the kinase activity is most sensitive for an external stimuli.

The free energy difference between an active receptor ($a = 1$) and an inactive receptor ($a = 0$) depends on the methylation level such that (4.35) becomes

$$\Delta F(m|c) = \Delta E(m) + \ln \left(\frac{1 + \frac{c}{K_0}}{1 + \frac{c}{K_1}} \right), \quad (4.41)$$

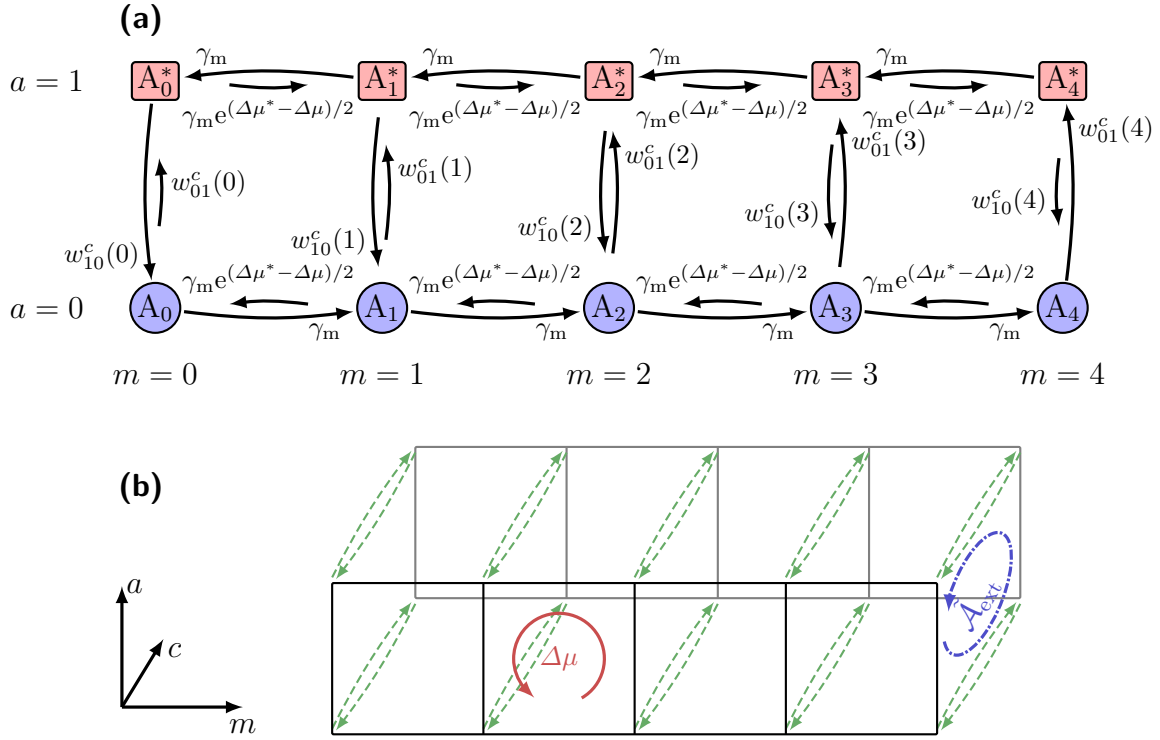


Figure 4.13| Model with adaptation. (a) Internal states of the system with specific transition rates $w_{(1,m)(1,m+1)}^c \equiv w_{(0,m+1)(0,m)}^c \equiv \gamma_m$ and $w_{(0,m)(0,m+1)}^c \equiv w_{(1,m+1)(1,m)}^c \equiv \gamma_m e^{(\Delta\mu^* - \Delta\mu)/2}$. (b) Schematic view of the full system including the external states c_1 and c_2 . A cycle in as indicated by the dash-dotted blue arrow contributes to an amount of work \mathcal{A}_{ext} delivered by the signal to the system. The solid red arrow contributes to an amount of work $\Delta\mu$ that is consumed inside the cell.

where we assume a linear dependence on m

$$\Delta E(m) \equiv -\frac{m}{4} \ln \frac{K_1}{K_0}. \quad (4.42)$$

The definition of $\Delta E(m)$ is chosen such that $\Delta F = 0$ for $(m = 4, c \rightarrow \infty)$ and $(m = 0, c = 0)$. We adopt the vertical transition rates in Fig. 4.13(a) from (4.34)

$$w_{01}^c(m) \equiv \gamma_a e^{-\Delta E(m)/2} \left(\frac{1 + c/\sqrt{K_0 K_1}}{1 + c/K_0} \right) \quad \text{and} \quad w_{10}^c = \gamma_a e^{\Delta E(m)/2} \left(\frac{1 + c/\sqrt{K_0 K_1}}{1 + c/K_1} \right), \quad (4.43)$$

which satisfy the local detailed balance relation $\ln[w_{10}^c(m)/w_{01}^c(m)] = \Delta F(m|c)$. Moreover, we set the free energy of each state in Fig. 4.13(a) to

$$F(a, m|c) \equiv a\Delta F(m|c). \quad (4.44)$$

The degree of methylation of the receptor is mediated by two enzymes the methyltransferase CheR and the methylesterase CheB, which add or remove methyl groups to or from

specific sites of the receptor [178]. More precisely, if the receptor is in the inactive state $a = 0$ the enzyme CheR allows the receptor to be methylated by the reaction



where a S-adenosyl methionine (SAM) molecule has turned to a S-adenosyl-L-homocysteine (SAH) molecule, while having transferred a methyl group to the receptor ($A_m \rightarrow A_{m+1}$). The individual transition rates $w_{(0,m+1)(0,m)}^c$ and $w_{(0,m)(0,m+1)}^c$ must satisfy local detailed balance

$$\ln \frac{w_{(0,m)(0,m+1)}^c}{w_{(0,m+1)(0,m)}^c} = F(0, m|c) - F(0, m+1|c) + \mu_{\text{SAM}} - \mu_{\text{SAH}} = \mu_{\text{SAM}} - \mu_{\text{SAH}}, \quad (4.46)$$

where μ_X is the chemical potential of species $X = \text{SAM}, \text{SAH}$. Note we have used (4.44) in the final step. If the receptor is in its active state $a = 1$ it will be demethylated by the reaction



which is catalyzed by the enzyme CheB, where a water molecule H_2O takes a methyl group from the receptor. Similarly, the local detailed balance reads

$$\ln \frac{w_{(1,m+1)(1,m)}^c}{w_{(1,m)(1,m+1)}^c} = F(1, m+1|c) - F(1, m|c) + \mu_{\text{H}_2\text{O}} - \mu_{\text{CH}_3\text{OH}} = \mu_{\text{H}_2\text{O}} - \mu_{\text{CH}_3\text{OH}} - \frac{1}{4} \ln \frac{K_1}{K_0}, \quad (4.48)$$

where μ_X is the chemical potential of species $X = \text{H}_2\text{O}, \text{CH}_3\text{OH}$. Moreover, we have used (4.44) in the last step. Summarizing, the chemical force

$$\Delta\mu \equiv \mu_{\text{SAM}} + \mu_{\text{H}_2\text{O}} - \mu_{\text{SAH}} - \mu_{\text{CH}_3\text{OH}} \quad (4.49)$$

drives internal process out of equilibrium, which corresponds to a cycle as indicated in Fig. 4.13. For $\Delta\mu = 0$ the internal process is in equilibrium. Moreover, there is a critical chemical potential difference

$$\Delta\mu^* \equiv \ln \frac{w_{10}^c(m)w_{01}^c(m+1)}{w_{01}^c(m)w_{10}^c(m+1)} = \Delta F(m|c) - \Delta F(m+1|c) = \frac{1}{4} \ln \frac{K_1}{K_0}, \quad (4.50)$$

which the chemical potential $\Delta\mu$ must exceed to allow the adaptation machinery to work properly for two reasons. First, if $0 < \Delta\mu < \Delta\mu^*$ the system is internally driven out of equilibrium but will also be pushed away from the adaptation level m that corresponds to a receptor being most sensitive for a change of concentration. Second, to recover a mean kinase activity of $1/2$ requires the chemical force $\Delta\mu$ to be larger than the bias of the conformational free energy $\Delta\mu^*$. For example, only if $\Delta\mu > \Delta\mu^*$ will a receptor in state $a = 0$ increase its methylation level to “push” the receptor more to the $a = 1$ state such that the mean activity of the receptor is mediated around $1/2$.

We now add the external process c , which is assumed to switch between two values $c = c_1$ and $c = c_2$ such that the full system becomes a 20 state system as illustrated in Fig. 4.13(b). The internal state is labeled by variables $y = (a, m)$. We denote the steady state probability of the full state (c, a, m) by $P(c; a, m)$ and its corresponding coarse-grained distribution by $P(c, a) \equiv \sum_{m=0}^4 P(c; a, m)$. Calculating the entropy production yields

$$\sigma = \sum_{c,a,a',m} P(a; c, m) w_{aa'}^c(m) \ln \frac{w_{aa'}^c(m)}{w_{a'a}^c(m)} + \sum_{c,a,m,m'} P(a; c, m) w_{(a,m)(a,m')}^c \ln \frac{w_{(a,m)(a,m')}^c}{w_{(a,m')(a,m)}^c}. \quad (4.51)$$

We find the entropy production can be split into two contributions

$$\sigma = \sigma_{\text{int}} + \sigma_{\text{ext}}, \quad (4.52)$$

where σ_{int} contributes to chemical work that is consumed inside the cell and σ_{ext} can be associated with chemical work that is delivered by the external signal.

Specifically, the rate at which SAM is consumed inside the cell is determined by

$$J_{\text{int}} \equiv \sum_{m=0}^3 \sum_c \left[P(c; 0, m) w_{(0,m)(0,m+1)}^c - P(c; 0, m) w_{(0,m)(0,m+1)}^c \right]. \quad (4.53)$$

Any SAM that is consumed inside the cell can be associated with a chemical work $\Delta\mu$ that is consumed inside the cell, as defined in (4.49). Consequently, the entropy production due to internally consumed chemicals reads

$$\sigma_{\text{int}} = J_{\text{int}} \Delta\mu. \quad (4.54)$$

Moreover, the free energy of the internal states depends on the external concentration. A concentration switch from c_1 to c_2 in the active state ($a = 1$) corresponds to a free energy change

$$\mathcal{A}_{\text{ext}} \equiv F(1, m|c_2) - F(1, m|c_1) = \ln \left[\left(\frac{1 + \frac{c_2}{K_0}}{1 + \frac{c_2}{K_1}} \right) \left(\frac{1 + \frac{c_1}{K_1}}{1 + \frac{c_1}{K_0}} \right) \right], \quad (4.55)$$

where we have used (4.41) and (4.44). The change of the free energy \mathcal{A}_{ext} is delivered by the signal such that

$$\sigma_{\text{ext}} = \gamma_c \left[P(c_1, 1) - P(c_2, 1) \right] \ln \left[\left(\frac{1 + \frac{c_2}{K_0}}{1 + \frac{c_2}{K_1}} \right) \left(\frac{1 + \frac{c_1}{K_1}}{1 + \frac{c_1}{K_0}} \right) \right] \quad (4.56)$$

contributes to the rate at which the signal delivers work to the system. Formally, a systematic derivation of the above expressions for $\sigma = \sigma_{\text{int}} + \sigma_{\text{ext}}$ can also be obtained by using Schnakenberg's network theory [39]. It should be noted that σ_{ext} is a lower bound on the chemical work that is delivered by the system through binding of ligands at varying concentration. Using a similar idea as in (4.40) allows us to write the full chemical work that is delivered by the signal in the following form

$$\sigma'_{\text{ext}} = \gamma_c \sum_a \left[P(c_2; a) \frac{c_2}{c_2 + K_a} - P(c_1; a) \frac{c_1}{c_1 + K_a} \right] \ln \frac{c_2}{c_1}. \quad (4.57)$$

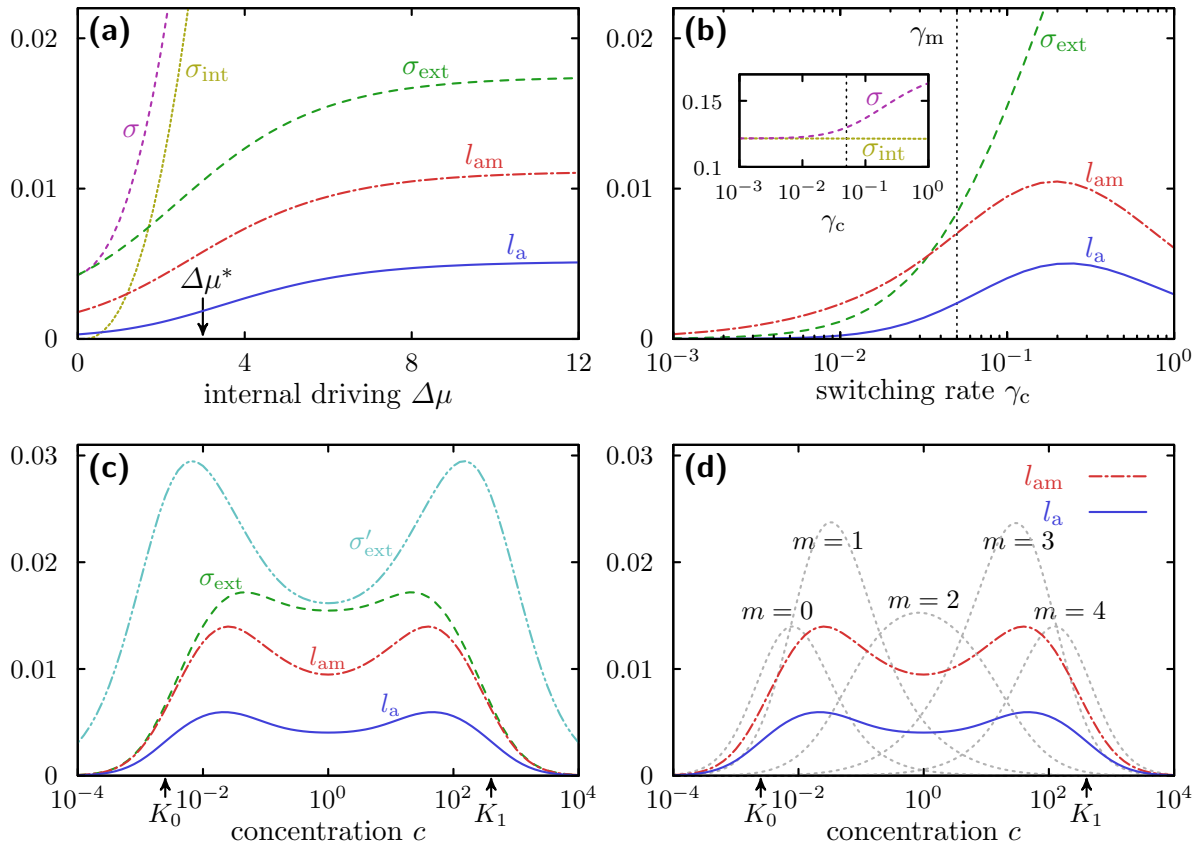


Figure 4.14 | Numerical results for system with adaptation from Fig. 4.13. Sensory performances (l_a, l_{am}) and energy consumptions ($\sigma_{ext}, \sigma_{int}, \sigma = \sigma_{ext} + \sigma_{int}$) as function of (a) chemical potential difference $\Delta\mu$, (b) the external switching rate γ_c , and (c) the concentration c , where $c_1 = c/3$ and $c_2 = 3c$. (d) Learning rates l_a and l_{am} of the system with adaptation versus the learning rate l_a for the MWC systems without adaptation as illustrated in Fig. 4.11(a) (dotted gray lines) for different conformational free energy differences ΔE . The methylation level $m = 0, 1, \dots, 4$ correspond to conformational free energy differences $\Delta E(m)$ defined in (4.42). Parameters: $K_1 = (K_0)^{-1} = 400$, $\Delta\mu^* = \frac{1}{4} \ln(K_1/K_0)$, $\gamma_a = 1$, $\gamma_m = 1/20$. (a), (c), (d) $\Delta\mu = 6$. (a), (b) $c_1 = 1/3$, $c_2 = 3$. (b)-(d) $\gamma_c = 0.1$.

Moreover, the learning rate of the full process labeled by $y = (a, m)$ reads (4.11)

$$l_{am} \equiv l_y = \gamma_c \sum_{a,m} [P(c_2; a, m) - P(c_1; a, m)] \ln \frac{P(c_2; a, m)}{P(c_1; a, m)}. \quad (4.58)$$

The learning rate of coarse-grained variable $y_1 \equiv a$ is given by (4.18)

$$l_a \equiv l_{y_1} = \gamma_c \sum_a [P(c_2, a) - P(c_1, a)] \ln \frac{P(c_2, a)}{P(c_1, a)}, \quad (4.59)$$

where $P(c, a) \equiv \sum_m P(c, a, m)$ denotes the marginal distribution of (c, a) .

The numerical results for the system are shown in Fig. 4.14. In Fig. 4.14(a) we find the sensory performance quantified by the learning rates l_{am}, l_a to grow substantially if

the chemical potential difference exceeds $\Delta\mu > \Delta\mu^*$, which lead to a high rate of internal energy consumption σ_{int} . Since successful adaptation requires the chemical potential difference to satisfy $\Delta\mu > \Delta\mu^*$ we have chosen $\Delta\mu$ accordingly in figures 4.14(b-c). In Fig. 4.14(b) we vary the external switching rate γ_c . As shown in the inset, the internal dissipated energy σ_{int} , which can be related to the consumption of SAM inside the cell, is much larger than the learning rates and does virtually not depend on the external switching rate. Interestingly, at slow switching rate we find the learning rate l_{am} to be larger than the work that is delivered by the external signal σ_{ext} , see Fig. 4.14(b). Therefore, a cell can learn more than the driving of the external process σ_{ext} if the internal process provides additional energetic input.

Changing the concentration c which parametrizes the values of the external concentrations via $c_1 = c/3$ and $c_2 = 3c$ we find in Fig. 4.14(c) the learning rates l_a and l_{am} to be substantial for concentration between the values of the dissociation constants $K_0 < c < K_1$. Moreover, we find $\sigma_{\text{ext}} \simeq \sigma'_{\text{ext}}$ for $K_0 \ll c \ll K_1$. Fig. 4.14(d) compares the coarse-grained learning rate l_a from the adaptive system (solid blue line) with the learning rate of the kinase activity l_a without adaptation dynamics from Fig. 4.11 (dotted gray lines), where the methylation level $m = 0, 1, \dots, 4$ correspond to conformational free energy differences $\Delta E = \Delta E(m)$. Comparing the solid blue lines and the dotted gray lines in Fig. 4.14(d), we find the coarse-grained learning rate l_a to be large over a broader range of concentration values c . Similarly, it has been found that the adaptation mechanism allows the sensitivity to concentration changes to be high over a wide range of concentration [176]. More importantly, we find the full learning rate l_{am} that includes the methylation level receptor to be much larger than l_a , which is a signature for a more complex response when including the methylation level m . For example, it has been found that chemotaxis systems with simple response without adaptation will lead to paradoxical compromise between long and short time behavior [179, 180], i.e., to a failing of chemotaxis. Therefore, the adaptation mechanism is essential for *E. coli* chemotaxis, see [179, 180] for more information.

A closely related study to this example can be found in [181], which discusses the same *E. coli* adaptation system from Fig. 4.13(a). In contrast to our model they used a single stochastic concentration change from an initial value to a stochastically chosen final value. Their mutual information between the full internal system (a, m) and the final concentration is analogous to our learning rate l_{am} . They found that after a long time $t \gg \gamma_a^{-1}$ most of the information about the final concentration is encoded in the methylation level. Similarly, we find for extremely slow external switching rate $\gamma_c \ll \gamma_m$, see Fig. 4.14(b), the coarse-grained learning rate l_a to be negligible compared to l_{am} , i.e., $l_{\text{am}} \simeq l_{\text{am}} - l_a$ for $\gamma_c \ll \gamma_m$.

In [182] Ito and Sagawa show that the transfer entropy rate can be used to characterize the performance of an adaptation mechanism; the transfer entropy limits the accuracy and the speed to adapt. Similarly, we will discuss in the following section the role of the transfer entropy for the ability of a sensor to filter out noise, which will lead to a new purely information theoretic quantity that characterizes the performance of a sensor.

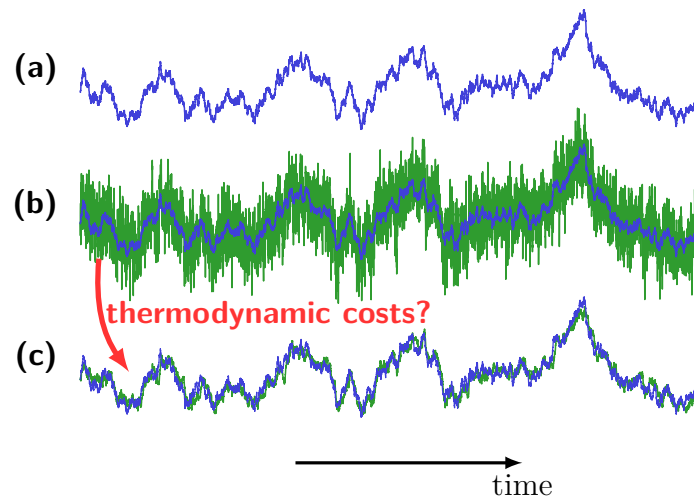


Figure 4.15 | Example for signal inference. The signal is represented in blue and the state of the sensor is shown in green. **(a)** Stochastic time dependent signal. **(b)** Bare sensor state with signal from (a) as function of time. **(c)** Measurement of sensor with optimal noise filtering (Kalman-Bucy filter) with signal from (a).

4.4 Sensory capacity

Until now we have discussed the sensory performance of the sensor that is characterized by the learning rate that takes into account the dynamics of the *state* of a sensor. We will now shift our focus to the *time history* of the visited states of a sensor along a trajectory. The following subsection on noise filtering will give a short motivation.

4.4.1 Optimal noise filtering

Noise filtering or suppression of noise does play an important role in feedback cooling [87, 88], hidden Markov processes [89], adaptation [182, 183], and gene regulatory networks [184] to name but a few examples. A prominent example we are going to discuss involves optimal filters for Gaussian processes known as Kalman-Bucy filters [88, 185, 186], see Fig. 4.15. Fig. 4.15(a) displays a stochastic time dependent signal (blue line), which can be considered to be a continuous valued concentration of ligands that is randomly fluctuating in time. Fig. 4.15(b) shows the same signal (thin blue line) with the time history of the sensor (noisy green line) which measures the signal and is corrupted by thermal noise. Using the time history of the state of the bare sensor one is able to increase the signal-to-noise ratio. We show in Fig. 4.15(c) the result of an optimal Kalman-Bucy filter, where the bare state of the sensor from Fig. 4.15(b) is exponentially averaged over a finite time span. Note that the correlations between the time histories of the signal and the sensor quantified by their mutual information does not change with noise filtering techniques, since Fig. 4.15(c) is derived from Fig. 4.15(b).

In the following we introduce the sensory capacity as a purely information theoretic measure which is bounded between 0 and 1. For example, the sensory capacity reaches its maximum value 1 if the instantaneous state of the sensor knows as much about the signal as its full time history, which corresponds to the scenario shown in Fig. 4.15(c).

The sensory capacity can be raised with the addition of a memory that stores information from the time history of the sensor in the instantaneous state of the memory. Thereby, the increase of the sensory capacity characterizes the improvement of the sensory performance with the addition of a memory.

4.4.2 Transfer entropy rate and sensory capacity

The maximal rate of information that can be transferred from the signal to the sensor is quantified by the mutual information between the time series of the signal x_0^t and the time series of the sensor y_0^t divided by the total time t . More precisely, the rate of mutual information is defined by [92, 93]

$$\dot{I} \equiv \lim_{t \rightarrow \infty} \frac{I[x_0^t : y_0^t]}{t}, \quad (4.60)$$

where I is the mutual information (3.6), see Sec. 3.3.3. In the following the steady state limit $t \rightarrow \infty$ is assumed for all expressions involving time t . For bipartite processes we have found in Eq. (3.41) that the rate of mutual information does have two causal contributions

$$\dot{I} = \mathcal{T}_{x \rightarrow y} + \mathcal{T}_{y \rightarrow x} = \mathcal{T}_{x \rightarrow y}, \quad (4.61)$$

where $\mathcal{T}_{x \rightarrow y}$ is the transfer entropy rate from signal “x” to sensor “y” and $\mathcal{T}_{y \rightarrow x}$ is the transfer entropy rate from sensor “y” to signal “x”, see (3.27) and (3.30) for definition of the transfer entropies. Note in the last step we have used $\mathcal{T}_{y \rightarrow x} = 0$, which is a consequence of the signal being *not* affected by the sensor, see Eq. (4.1). Therefore, the transfer entropy from signal to sensor $\mathcal{T}_{x \rightarrow y}$ characterizes the maximal performance of the sensor that can be derived from the time history of visited sensor states. We repeat the definition of the transfer entropy from (3.28)

$$\mathcal{T}_{x \rightarrow y} \equiv \frac{H[y_{t+dt} | y_0^t] - H[y_{t+dt} | y_0^t, x_t]}{dt} = \frac{I[x_t : y_{t+dt} | y_0^t]}{dt} = \frac{H[x_t | y_0^t] - H[x_t | y_0^{t+dt}]}{dt}, \quad (4.62)$$

where the last expression can be used to compare it with the learning rate from (4.8). The transfer entropy characterizes the rate at which the uncertainty of the signal is reduced due the *time history* of the sensor y_0^t , whereas the learning rate characterizes the reduction of uncertainty due to the dynamics of the instantaneous *state* of the sensor y_t , see Fig. 4.16 for an illustration.

We have shown in the previous chapter that the learning rate is bounded by the transfer entropy rate $l_y \leq \mathcal{T}_{x \rightarrow y}$, see also [41], which simply means that the time history of the sensor y_0^t contains more information about the signal state x_t than the instantaneous state of the sensor y_t . On the basis of this inequality we define the positive sensory capacity [120]

$$C \equiv \frac{l_y}{\mathcal{T}_{x \rightarrow y}} \leq 1. \quad (4.63)$$

The sensory capacity is a purely information theoretic quantity characterizing the performance of a sensor. A sensor reaches its information theoretic limit $C = 1$ if the

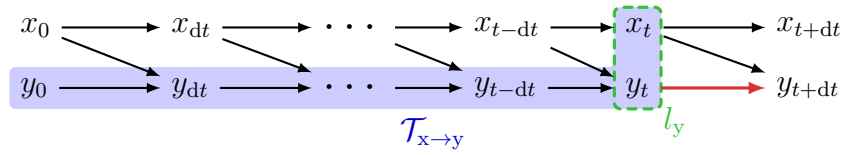


Figure 4.16 | Presentation of transfer entropy versus learning rate as in Fig. 3.5 with single directed causal influence from signal to sensor. The time history of the bipartite process (x_0^t, y_0^t) is shown with discrete time spacing dt . The learning rate takes into account only the instantaneous state y_t (dashed green box) to infer the signal x_t , whereas the transfer entropy considers the full time history y_0^t (blue shaded region).

instantaneous state of the sensor has the maximum information, which is the information contained in the full time history of the sensor. As a side note, it has been similarly shown that information driven engines, which use the information from a history of measurements, can extract more work than engines, which use only the single last measurement [86, 89]. Thereby, the increase of work extraction can be characterized by a gain or discord parameter that is bounded between 0 and 1, like the sensory capacity discussed here.

We note that the sensory capacity should not be confused with the familiar channel capacity in information theory [36]. The sensory capacity quantifies the sensory performance of a sensor for specific time dependent signals, whereas the channel capacity is defined for a different setup, where two static random variables constituting the input and the output are considered, similar to the example from Fig. 4.4. For a predefined conditional probability of the output given the input, the channel capacity is the maximum mutual information between input and output, where the maximization is performed over the probability distribution of the input [36].

4.4.3 Sensor with a memory

Suppose the sensor is composed of two degrees of freedom $y = (r, m)$, where r labels the first degree of freedom directly sensing the signal and m labels the memory acquiring information from the time history r_0^t from the first degree of freedom (see [170] for a similar setup). The coarse-grained learning rate of the first degree of freedom is given by (4.14) (see also [119])

$$l_r \equiv \frac{H[x_t|r_t] - H[x_t|r_{t+dt}]}{dt} = \sum_{x,r,r',m} P(x,r,m) w_{(r,m)(r',m)}^x \ln \frac{P(x|r')}{P(x|r)}, \quad (4.64)$$

where $w_{(r,m)(r',m)}^x$ is the transition rate from state (x, r, m) to state (x, r', m) , and $P(x, r, m)$ is the joint steady state probability of the variable (x, r, m) . Moreover, the coarse-grained learning rate satisfies $l_r \leq l_y$, see Sec. 4.2.4 or [119, 120]. The full dynamics of the signal and the sensor with memory is determined by a master equation with transition rates

$$w_{yy'}^{xx'} \equiv \begin{cases} w^{xx'} & \text{if } x \neq x' \text{ and } y = y', \\ w_{rr'}^x & \text{if } x = x', r \neq r', \text{ and } m = m', \\ w_{(r,m)(r',m')} & \text{if } x = x', r = r' \text{ and } m \neq m', \\ 0 & \text{otherwise,} \end{cases} \quad (4.65)$$

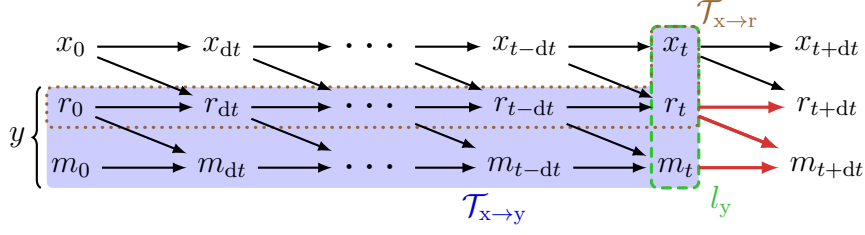


Figure 4.17 | Presentation of transfer entropy versus learning rate as in Fig. 3.5 with single directed causal influence from signal to sensor.

where $y' = (r', m')$. These transition rates imply the causal relation $x \rightarrow r \rightarrow m$ as illustrated in Fig. 4.17. A system with three variables, where only one variable can change in a single jump, as in (4.65), forms a tripartite system, which constitutes a specific example of a multipartite Markov process [134]. Inserting the transition rates (4.65) in the expression for the coarse-grained learning rate (4.64) yields

$$l_r = \sum_{x, r, r'} P(x, r) w_{rr'}^x \ln \frac{P(x|r')}{P(x|r)}. \quad (4.66)$$

Importantly, the transfer entropy from the signal x to the first layer of the sensor r , which is defined by

$$\mathcal{T}_{x \rightarrow r} \equiv \frac{H[r_{t+dt}|r_0^t] - H[r_{t+dt}|r_0^t, x_t]}{dt}, \quad (4.67)$$

equals the transfer entropy from the signal x to full sensor $y = (r, m)$, i.e.,

$$\mathcal{T}_{x \rightarrow r} = \mathcal{T}_{x \rightarrow y}. \quad (4.68)$$

This relation (4.68) follows from the causal relation $x \rightarrow r \rightarrow m$ as we show in the following paragraph, see also [120].

We define $\mathbf{z}_t \equiv (x_t, r_t, m_t)$ such that the conditional probability $\mathcal{P}(\mathbf{z}_{t+dt}|\mathbf{z}_t)$ can be written in the form

$$\mathcal{P}(\mathbf{z}_{t+dt}|\mathbf{z}_t) = \mathcal{P}(x_{t+dt}|x_t)\mathcal{P}(r_{t+dt}|x_t, r_t)\mathcal{P}(m_{t+dt}|r_t, m_t) + O(dt)^2, \quad (4.69)$$

where we have used the structure of the rates (4.65), see also (3.40) for a similar calculation. Using (4.69) and the definition of the conditional Shannon entropy (3.5) allows us to derive the relations

$$H[\mathbf{z}_{t+dt}|\mathbf{z}_t] = H[x_{t+dt}|x_t] + H[r_{t+dt}|x_t, r_t] + H[m_t|r_t, m_t] + O(dt)^2 \quad (4.70)$$

and

$$H[y_{t+dt}|\mathbf{z}_t] \equiv H[r_{t+dt}, m_{t+dt}|x_t, r_t, m_t] = H[r_{t+dt}|x_t, r_t] + H[m_t|r_t, m_t] + O(dt)^2. \quad (4.71)$$

Moreover, using the Markov property $\mathcal{P}(\mathbf{z}_{t+dt}|\mathbf{z}_t) = \mathcal{P}(\mathbf{z}_{t+dt}|\mathbf{z}_0^t)$, Eq. (4.69), and taking the limit $t \rightarrow \infty$ yields

$$H[y_{t+dt}|y_0^t] \equiv H[r_{t+dt}, m_{t+dt}|r_0^t, m_0^t] = H[r_{t+dt}|r_0^t] + H[m_{t+dt}|m_t, r_t] + O(dt)^2. \quad (4.72)$$

Therefore, we obtain the relation for the transfer entropy rate

$$\mathcal{T}_{x \rightarrow y} \equiv \frac{H[y_{t+dt}|y_0^t] - H[y_{t+dt}|x_t, y_t]}{dt} = \frac{H[r_{t+dt}|r_0^t] - H[r_{t+dt}|x_t, r_t]}{dt} = \mathcal{T}_{x \rightarrow r}, \quad (4.73)$$

where we have used the definition of the transfer entropy from (3.27) in the first step, inserted Eqs. (4.71),(4.72) in the second step, and finally identified the expression with the transfer entropy rate $\mathcal{T}_{x \rightarrow r}$ from (4.67) by using the Markov property $H[r_{t+dt}|x_t, r_t] = H[r_{t+dt}|x_t, r_0^t]$. Note we use the convention $dt \rightarrow 0$ whenever dt appears in a denominator.

The addition of a memory does have an interesting effect on the analytic upper bound on the transfer entropy rate. To see this we rewrite the analytic bound

$$\bar{\mathcal{T}}_{x \rightarrow y} = \frac{H[y_{t+dt}|y_t] - H[y_{t+dt}|x_t, y_t]}{dt} = \frac{H[r_{t+dt}|r_t, m_t] - H[r_{t+dt}|x_t, r_t]}{dt}, \quad (4.74)$$

where we have used in the first step the definition of the upper bound on the transfer from (3.31), and then inserted (4.69) in the last step. From $H[r_{t+dt}|r_t, m_t] \leq H[r_{t+dt}|r_t]$ we can derive the inequality

$$\bar{\mathcal{T}}_{x \rightarrow y} \leq \bar{\mathcal{T}}_{x \rightarrow r}, \quad (4.75)$$

where

$$\bar{\mathcal{T}}_{x \rightarrow r} = \frac{H[r_{t+dt}|r_t] - H[r_{t+dt}|x_t, r_t]}{dt} \quad (4.76)$$

is the upper bound on the transfer entropy rate corresponding to the first layer of the sensor. Importantly, inequality (4.75) is contrary to what we have found for the coarse-grained learning rate, which satisfies $l_r \leq l_y$. We can summarize the inequalities derived in this subsection by the following chain of inequalities

$$l_r \leq l_y \leq \mathcal{T}_{x \rightarrow r} = \mathcal{T}_{x \rightarrow y} \leq \bar{\mathcal{T}}_{x \rightarrow y} \leq \bar{\mathcal{T}}_{x \rightarrow r}. \quad (4.77)$$

4.5 Cellular two-component network

4.5.1 Model definition with memory and fluctuating signal

For our examples we consider the following cellular two-component network as realization of a sensor that measures a time dependent fluctuating ligand concentration as shown in Fig. 4.18, see [170] for a similar setup. The signal x_t at time t is related to an external ligand concentration via $x = \ln(c_t/c_{\text{ref}})$, where c_t is the ligand concentration at time t and c_{ref} is some reference concentration value, i.e., the signal x_t characterizes the change of the chemical potential of the external ligands, where we have set $k_B T \equiv 1$. The first layer of the cellular two-component network consists of N_r receptors, which directly sense the external concentration. Thereby, the i -th receptor can either be occupied by a ligand ($b_i = 1$) or be empty ($b_i = 0$), where $i = 1, \dots, N_r$. The total number of receptors being bound by a ligand is then given by $n_b \equiv \sum_{i=1}^{N_r} b_i$ with possible values $n_b = 0, 1, \dots, N_r$. The second layer of the network, which constitutes the memory, is composed of internal

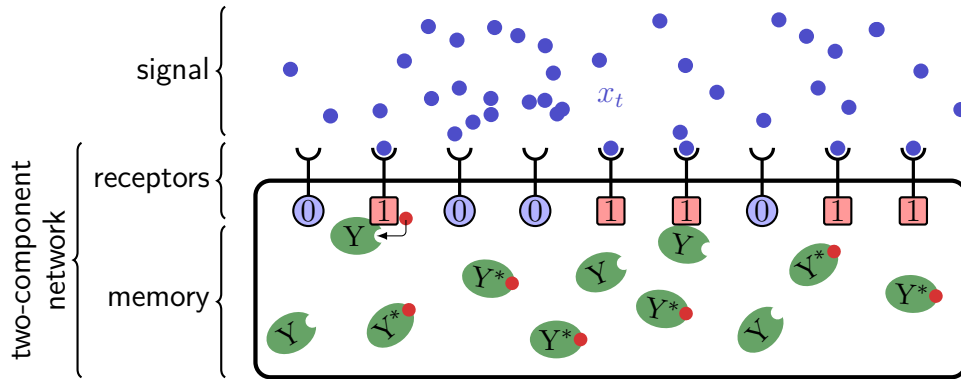


Figure 4.18 | Cellular two-component network measuring a fluctuating external concentration. The total number of receptors is $N_r = 9$, where $n_b = 5$ of them are being occupied by a ligand. The number of memory proteins is $N_m = 11$, where $n_y = 6$ of them are in the phosphorylated state Y^* . In contrast to the examples for the *E. coli* chemotaxis systems from Sec. 4.3 the ligands here should formally considered to be repellent (poison) instead of attractants (food).

proteins Y that can be in a phosphorylated state Y^* . We denote the total number of phosphorylated proteins by n_y , where $n_y = 0, 1, \dots, N_m$, with N_m being the total number of proteins. The second degree of freedom, which is the memory, does not affect the dynamics of the occupancy of the receptor n_b , whereas the state of the receptors n_b influences the variable n_y , i.e., the phosphorylation and dephosphorylation reaction of the proteins. Summarizing, the full sensor state is labeled by $y = (n_b, n_y)$.

The signal is assumed to be a continuous valued stochastic process that can be described by the Langevin equation

$$\dot{x}_t = -\omega_x x_t + \xi_t, \quad (4.78)$$

where ω_x is the rate at which the signal changes and ξ_t is stochastic noise with zero mean and covariance

$$\langle \xi_t \xi_{t'} \rangle = 2D_x \delta(t - t'). \quad (4.79)$$

The process shown in Fig. 4.15(a) is generated the Langevin equation from (4.78). We note a Langevin equation (4.78) can also be approximated by discrete process as follows. Using discrete signal values x that are multiples of dx , the transition rates become

$$w_x^\pm(x) = \frac{D_x}{dx^2} \exp\left(\mp \frac{\omega_x x}{2D_x} dx\right), \quad (4.80)$$

where “ \pm ” indicates a signal change $x \rightarrow x \pm dx$. In the limit $dx \rightarrow 0$ the discrete dynamics of the signal becomes equivalent to the continuous Langevin equation (4.78), see also [120].

The number of occupied receptors n_b changes with rates

$$\begin{aligned} w_r^+(x, n_b) &= \omega_b^+(x)(N_r - n_b), \\ w_r^-(x, n_b) &= \omega_b^-(x)n_b, \end{aligned} \quad (4.81)$$

where $\omega_b^+(x)$ is the rate for the binding of a ligand to an individual receptor and $\omega_b^-(x)$ is the rate for a release of a ligand from a receptor. These rates satisfy the local detailed balance relation $\ln[\omega_b^+(x)/\omega_b^-(x)] = \Delta F(x)$, where $\Delta F(x)$ is the free energy difference between the empty receptor state and the occupied receptor state. It is assumed that the number of external ligands is large compared to the number of receptors such that ligand binding events to receptors and unbinding events from receptors do not alter the external ligand concentration.

Similarly to the system from Sec. 4.3.1, the internal memory changes its state through two chemical reactions. First, a single memory protein can be activated along the phosphorylation



where $n_b\kappa_{\pm}$ are the individual transition rates for a single protein, which are assumed to be proportional to the number of occupied receptors n_b . The second chemical reaction involving changes of the memory is the dephosphorylation reaction



where the transition rates ν_{\pm} are assumed to be independent of n_b . Thermodynamic consistency requires the transition rates to satisfy $\ln[\kappa_+\nu_+/(\kappa_-\nu_-)] = \Delta\mu$, where $\Delta\mu = \mu_{\text{ATP}} - \mu_{\text{ADP}} - \mu_{\text{P}_i}$ is the free energy release from hydrolyzing on ATP molecule. The total transition rates for an individual protein then read

$$\begin{aligned} \omega_y^+(n_b) &\equiv n_b\kappa_+ + \nu_-, \\ \omega_y^-(n_b) &\equiv n_b\kappa_- + \nu_+, \end{aligned} \quad (4.84)$$

such that the overall number of phosphorylated proteins changes with total rates

$$\begin{aligned} w_m^+(n_b, n_y) &\equiv \omega_y^+(n_b)(N_m - n_y), \\ w_m^-(n_b, n_y) &\equiv \omega_y^-(n_b)n_y, \end{aligned} \quad (4.85)$$

where $w_m^{\pm}(n_b, n_y)$ is the rate for a transition from n_y to $n_y \pm 1$ at constant occupancy level n_b . See Fig. 4.19 for an illustration of the rates (4.81) and (4.85).

The entropy production of the cellular two-component network has the following two contributions. First, ligand binding and unbinding events to or from receptors contribute to the entropy production

$$\sigma_r = \sum_{x, n_b} J_r(x, n_b) \ln \frac{w_r^+(x, n_b)}{w_r^-(x, n_b + 1)} \quad (4.86)$$

where

$$J_r(x, n_b) \equiv P(x, n_b)w_r^+(x, n_b) - P(x, n_b + 1)w_r^-(x, n_b + 1) \quad (4.87)$$

is the steady state probability current with $P(x, n_y)$ being the steady state probability distribution of (x, n_b) . Second, the entropy production due to transitions of the memory proteins can be estimated by

$$\sigma_m \equiv \sum_{n_b, n_y} J_m(n_b, n_y) \ln \frac{w_m^+(x, n_b)}{w_m^-(x, n_b + 1)}, \quad (4.88)$$

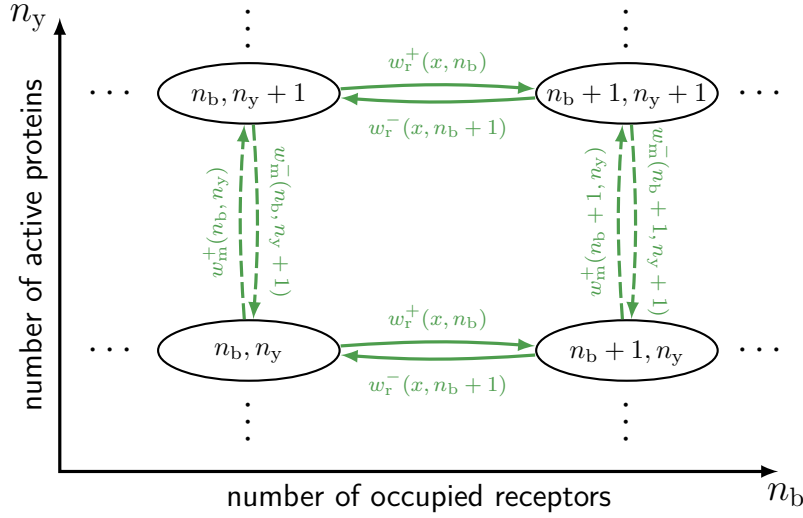


Figure 4.19 | Transition rates of internal states $y = (n_b, n_y)$.

where

$$J_m(n_b, n_y) \equiv P(n_b, n_y)w_m^+(x, n_b) - P(x, n_b + 1)w_m^-(x, n_b + 1) \quad (4.89)$$

is the total steady state probability current for transitions of the memory with $P(n_b, n_y)$ being the stationary probability of state (n_b, n_y) . The quantity σ_m provides a lower bound on the free energy that is dissipated due to internal chemical reactions. For convenience we will use σ_m in the following.

For the sake of completeness, we introduce the full expression for the entropy production σ'_m due to the chemical reactions (4.82) and (4.83), which is slightly more involved than σ_m . First, we split the transition rates from (4.85) into

$$\begin{aligned} w_m^{+, \text{phos}}(n_b, n_y) &\equiv n_b \kappa_+ (N_m - n_y), & w_m^{+, \text{dephos}}(n_b, n_y) &\equiv \nu_- (N_m - n_y), \\ w_m^{-, \text{phos}}(n_b, n_y) &\equiv n_b \kappa_- n_y, & w_m^{-, \text{dephos}}(n_b, n_y) &\equiv \nu_+ n_y, \end{aligned} \quad (4.90)$$

which satisfy $w_m^\pm(n_b, n_y) = w_m^{\pm, \text{phos}}(n_b, n_y) + w_m^{\pm, \text{dephos}}(n_b, n_y)$. Using the transition rates (4.90) the full expression for entropy production due to memory transitions becomes

$$\sigma'_m = \sum_{n_b, n_y, i} J_m^{(i)}(n_b, n_y) \ln \frac{w_m^{+, i}(x, n_b)}{w_m^{-, i}(x, n_b + 1)}, \quad (4.91)$$

where

$$J_m^{(i)}(n_b, n_y) \equiv P(n_b, n_y)w_m^{+, i}(x, n_b) - P(x, n_b + 1)w_m^{-, i}(x, n_b + 1) \quad (4.92)$$

and $i = \text{phos, dephos}$. In the following we stick with the estimate σ_m that satisfies $\sigma_m \leq \sigma'_m$.

For this cellular two-component network $\sigma_y \equiv \sigma_r + \sigma_m \geq 0$ is rate at which the network dissipates energy. The term σ_r arises from ligand binding and unbinding events at different concentration values and, therefore, is compensated by the work that is delivered by the

external signal. The term σ_m is compensated by the chemical work that is consumed inside the cell along ATP hydrolysis reactions. As mentioned in the previous paragraph σ_m is only a lower bound on the free energy that is dissipated inside the cell. We note that a similar splitting into externally delivered work and internally consumed work that allows a nonzero learning rate is discussed in Sec. 4.3.3 and [119], where the adaptation mechanism of *E. coli* is discussed.

For a small fluctuating signal, we show in Appendix 4.A that the linear noise approximation can be used to transform the dynamics associated with Eqs. (4.78), (4.81) and (4.85) into a set of coupled Langevin equations

$$\begin{aligned}\dot{x}_t &= -\omega_x x_t + \xi_t^x && \text{(signal),} \\ \dot{r}_t &= -\omega_r (r_t - x_t) + \xi_t^r && \text{(bare sensor),} \\ \dot{m}_t &= -\omega_m (m_t - r_t) + \xi_t^m && \text{(memory),}\end{aligned}\tag{4.93}$$

where the noise terms ξ_t^i have zero mean and covariance

$$\langle \xi_t^i \xi_{t'}^j \rangle = 2D_i \delta_{ij} \delta(t - t'),\tag{4.94}$$

for $i, j = x, r, m$. The variable r_t characterizes the state of the bare sensor and is related to the number of receptors that are occupied by a ligand at time t , see Eq. (4.136) from Appendix 4.A. Moreover, the memory variable m_t is related to the number of phosphorylated proteins inside the cell, see Eq. (4.136). The noise amplitudes D_r, D_m are given in Eq. (4.138) from Appendix 4.A, where one can identify the following three important features. First, without internal energy consumption ($\Delta\mu = 0$) the memory becomes uncorrelated with the state of the receptors, which formally leads to a divergent noise amplitude of the memory $D_m \rightarrow \infty$, as can be deduced from Eq. (4.138) in Appendix 4.A. Second, the noise amplitude of the memory D_m decreases with increasing number of proteins N_m , where $D_m \sim N_m^{-1}$. Third, the noise amplitude of the bare sensor D_r is inversely proportional to the number of receptors N_r .

4.5.2 Bare sensor

We begin with the bare sensor, where the evolution of the system is ruled by just the first two Langevin equations from (4.93), i.e., the memory that is labeled by variable m_t is excluded for this subsection. In this subsection we add the subscript ‘‘r’’ to differentiate quantities expressed for the bare sensor that is characterized by variable r_t from quantities expressed for the full sensor with the memory that is characterized by variable $y_t = (r_t, m_t)$ and will be discussed in the next subsection. Specifically, the sensory capacity of the bare sensor is denoted by C_r , whereas for the efficiency we use η_r . The coupled dynamics of signal and sensor is a Gaussian process. Thereby, the covariance matrix

$$\Sigma = \begin{pmatrix} \Sigma_{xx} & \Sigma_{xr} \\ \Sigma_{rx} & \Sigma_{rr} \end{pmatrix} \equiv \begin{pmatrix} \langle x_t^2 \rangle - \langle x_t \rangle^2 & \langle x_t r_t \rangle - \langle x_t \rangle \langle r_t \rangle \\ \langle r_t x_t \rangle - \langle r_t \rangle \langle x_t \rangle & \langle r_t^2 \rangle - \langle r_t \rangle^2 \end{pmatrix}\tag{4.95}$$

must satisfy the Lyapunov equation [28, 34]

$$\dot{\Sigma} = -\mathbf{A}\Sigma - \Sigma\mathbf{A}^\top + 2\mathbf{D},\tag{4.96}$$

where

$$\mathbf{A} \equiv \begin{pmatrix} \omega_x & 0 \\ -\omega_r & \omega_r \end{pmatrix} \quad \text{and} \quad \mathbf{D} \equiv \begin{pmatrix} D_x & 0 \\ 0 & D_r \end{pmatrix}. \quad (4.97)$$

The stationary distribution of (x_t, r_t) is a normal distribution with zero mean and covariance

$$\Sigma = \mathcal{E}_x^2 \begin{pmatrix} 1 & \frac{\nu_r}{\nu_r+1} \\ \frac{\nu_r}{\nu_r+1} & [\frac{\nu_r}{\nu_r+1} + \frac{B_r}{\nu_r}] \end{pmatrix}, \quad (4.98)$$

which is the stationary solution ($\dot{\Sigma} = 0$) of the Lyapunov equation (4.96), where we have defined $\mathcal{E}_x^2 \equiv D_x/\omega_x$ (signal variance), $\nu_r \equiv \omega_r/\omega_x$ (ratio of the relaxation rate), and $B_r \equiv D_r/D_x$ (noise ratio). As shown in Appendix 4.B, the learning rate is given by (4.150)

$$l_r = \omega_x \left[\frac{\nu_r^3}{\nu_r^2 + B_r(1 + \nu_r)^2} \right], \quad (4.99)$$

the transfer entropy adopted from [88] reads

$$\mathcal{T}_{x \rightarrow r} = \frac{\omega_r}{2} \left(\sqrt{1 + \frac{\nu_r^2}{B_r}} - 1 \right), \quad (4.100)$$

and the entropy production due to the bare sensor dynamics is given by (4.144)

$$\sigma_r = \omega_x \frac{\nu_r^2}{B_r(1 + \nu_r)}. \quad (4.101)$$

The quantities are shown in Fig. 4.20(a). All three quantities are getting larger as the sensor noise is getting smaller. At an intermediate noise level $B_r = \nu_r^2/(\nu_r^2 - 1)$ the learning rate equals the transfer entropy $l_r = \mathcal{T}_{x \rightarrow r}$, implying the sensory capacity saturates at $C_r = 1$ as shown in Fig. 4.20(b). As sensor noise decreases further the learning rate saturates to $l_r \approx 10$, whereas the transfer entropy $\mathcal{T}_{x \rightarrow r}$ and the entropy rate σ_r both diverge $\sim B_r^{-1}$. Thereby, a decrease of the noise amplitude can be realized by an increase in the number of receptors, see Eq. (4.138) from Appendix 4.A, which accounts for a larger rate of energy dissipation. Since the bare sensor is not assumed to consume chemicals inside the cell, the entropy production is equal to the rate at which the signal delivers work to the sensor.

An interesting feature can be found in Fig. 4.20(b). At maximal sensory capacity $C_r = 1$ the efficiency is $\eta_r = 1/2$, i.e., the sensor dissipates energy at twice the rate at which it learns ($\sigma_r = 2l_r$). More generally, we show in Sec. 4.6 a trade-off between sensory capacity and efficiency which states that $C = 1 \Rightarrow \eta \leq 1/2$. A further useful relation involves the upper bound on the transfer entropy rate. Calculating the upper bound on the transfer entropy rate as shown in the Appendix 4.B yields (4.154)

$$\bar{\mathcal{T}}_{x \rightarrow r} = \frac{\omega_x \nu_r^2}{4B_r} \left[\frac{\nu_r^2 + B_r(1 + \nu_r)^2}{\nu_r^2(1 + \nu_r) + B_r(1 + \nu_r)^2} \right]. \quad (4.102)$$

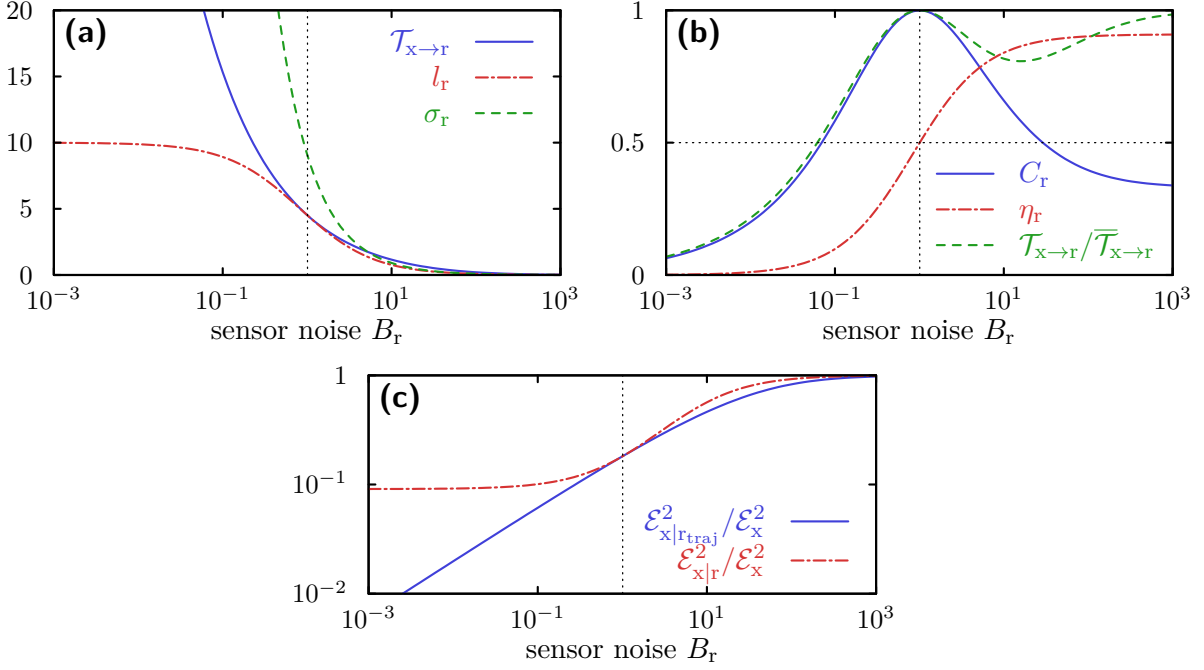


Figure 4.20 | Sensory performance of the bare sensor model as function of the sensor noise $B_r = D_r/D_x$. **(a)** Transfer entropy rate $\mathcal{T}_{x \rightarrow r}$, learning rate l_r , and entropy production σ_r . The vertical dotted line at $B_r = \nu_r^2/(\nu_r^2 - 1)$ indicates the point for which $l_r = \mathcal{T}_{x \rightarrow r}$, i.e., the capacity saturates ($C_r = 1$). **(b)** Sensory capacity ($C_r = l_r/\sigma_r$) and thermodynamic efficiency ($\eta_r = l_r/\sigma_r$) of the bare sensor. At maximal sensory capacity $C_r = 1$ the efficiency is $\eta_r = 1/2$ as well as $\mathcal{T}_{x \rightarrow r} = \bar{\mathcal{T}}_{x \rightarrow r}$. **(c)** Comparison to conditional variances. For $C_r = 1$ the inequality $\mathcal{E}_{x|r_{\text{traj}}} \leq \mathcal{E}_{x|r}$ saturates. Parameters: $\omega_x = 1$, $\nu_r = \omega_r/\omega_x = 10$, and $\mathcal{E}_x^2 = D_x/\omega_x = 0.1$.

This quantity has also been derived in [182]. Comparing the transfer entropy with its upper bound we find $\mathcal{T}_{x \rightarrow r} = \bar{\mathcal{T}}_{x \rightarrow r}$ at maximal sensory capacity $C_r = 1$; see Fig. 4.20(b). This feature “ $\mathcal{T}_{x \rightarrow y} = \bar{\mathcal{T}}_{x \rightarrow y}$ at $C = 1$ ” will be useful later in Sec. 4.6, where we show the trade-off between sensory capacity and efficiency.

We compare two conditional signal variances in Fig. 4.20(c). The conditional variance of the signal x_t given the state of the sensor r_t is denoted by $\mathcal{E}_{x|r}^2 \equiv \langle (x_t - \langle x_t \rangle_{r_t})^2 \rangle$, whereas $\mathcal{E}_{x|r_{\text{traj}}}^2$ is the conditional variance of $x_t | r_0^t$, which generally satisfies $\mathcal{E}_{x|r_{\text{traj}}}^2 \leq \mathcal{E}_{x|r}^2$, since the time history r_0^t reduces the variance of the signal more than just the instantaneous state r_t . Note the conditional variance $\mathcal{E}_{x|r_{\text{traj}}}^2$ is derived in Appendix 4.C. At maximal sensory capacity $C_r = 1$ both uncertainties become equal $\mathcal{E}_{x|r_{\text{traj}}}^2 = \mathcal{E}_{x|r}^2$, implying a memory that stores the information from the time history r_0^t cannot further reduce the uncertainty of the signal. We note $\mathcal{E}_x^2/\mathcal{E}_{x|r}^2 \geq 1$ is the signal-to-noise ratio, which is the inverse to the quantity plotted in Fig. 4.20(c), where $\mathcal{E}_x^2/\mathcal{E}_{x|r_{\text{traj}}}^2$ is the maximal signal-to-noise ratio that can be attained with the addition of a memory. As a side note we have shown in the Appendices 4.B and 4.C that the transfer entropy rates can be expressed as $\bar{\mathcal{T}}_{x \rightarrow r} = (4B_r)^{-1} \omega_x \nu_r^2 \mathcal{E}_{x|r}^2/\mathcal{E}_x^2$ and $\mathcal{T}_{x \rightarrow r} = (4B_r)^{-1} \omega_x \nu_r^2 \mathcal{E}_{x|r_{\text{traj}}}^2/\mathcal{E}_x^2$, see Eqs. (4.154) and (4.163).

4.5.3 Memory increases sensory capacity

If the bare sensor does not reach a sensory capacity close to 1, it is possible to increase the sensory capacity with the addition of a memory. We add the memory by considering the third line of Eq. (4.93), where the Lyapunov equation (4.96) involves the 3×3 matrices

$$\mathbf{A} \equiv \begin{pmatrix} \omega_x & 0 & 0 \\ -\omega_r & \omega_r & 0 \\ 0 & -\omega_m & \omega_m \end{pmatrix} \quad \text{and} \quad \mathbf{D} = \begin{pmatrix} D_x & 0 & 0 \\ 0 & D_r & 0 \\ 0 & 0 & D_m \end{pmatrix} \quad (4.103)$$

where Σ becomes a 3×3 matrix with elements Σ_{ij} , where $i, j = x, r, m$. The expression for the steady state solution of the covariance matrix Σ is too long to be displayed here.

The exact expression for learning rate l_y is shown in Eq. (4.151) of Appendix 4.B. We have shown in Eq. (4.68) that the transfer entropy rate does not change with the addition of a memory $\mathcal{T}_{x \rightarrow r} = \mathcal{T}_{x \rightarrow y}$, which implies that Eq. (4.100) remains the expression for the transfer entropy from signal to the sensor with memory. Moreover, the expression for the coarse-grained learning rate l_r is still given by (4.99). For this subsection, we adopt the sensor parameters of the bare sensor from Fig. 4.20 with $B_r = 10^{-2}$. This set of parameters corresponds to a low sensory capacity of the bare sensor $C_r \simeq 0.2$, see Fig. 4.20(b), which is similar to the case presented in Fig. 4.15(b). In this case the sensory performance can be improved with the addition of a memory. In Fig. 4.21(a) we show the learning rate l_y as a function of the memory noise $B_m \equiv D_m/D_x$. At low amplitude of the memory noise the learning rate approaches the transfer entropy $l_y \approx \mathcal{T}_{x \rightarrow r}$, where the instantaneous state of the memory includes the maximal information from the time history of the bare sensor, i.e., the sensory capacity approaches $C \approx 1$ as shown in Fig. 4.21(b). As the memory noise increases the learning rate decreases, where the limit $B_m \rightarrow \infty$ renders the memory useless, since the sensor capacity approaches the sensory capacity of the bare sensor without memory ($C \rightarrow C_r$).

The addition of the memory, which increases the sensory capacity, is accompanied by additional internal dissipation of chemical energy due to the consumption of ATP molecules. More precisely, the sensor with memory dissipates free energy at a rate $\sigma_y = \sigma_r + \sigma_m$, where σ_r given by (4.101) contributes to the work that is delivered by the external signal and σ_m contributes to chemical work that is consumed inside the cell. As shown in the Appendix 4.B the rate at which the memory dissipates energy is related to (4.145)

$$\sigma_m = \omega_x \frac{\nu_m^2 [\nu_r^2 + B_r(1 + \nu_m)(1 + \nu_r)]}{B_m(1 + \nu_m)(1 + \nu_r)(\nu_m + \nu_r)}, \quad (4.104)$$

where we have defined the relaxation rate of the memory $\nu_m \equiv \omega_m/\omega_x$ and the memory noise $B_m \equiv D_m/D_x$. The entropy production due to the memory σ_m increases as the memory noise B_m decreases, which according to (4.138) can be realized by increasing the number of memory proteins and/or the chemical potential difference $\Delta\mu$. As shown in Fig. 4.21(b) the efficiency $\eta = l_y/\sigma_y$ decays as the sensory capacity approaches its maximal value 1, which follows from the ATP consumption due to the memory inside the cell.

In the contour plot from Fig. 4.22 we present the sensory capacity as a function of both memory parameters ν_m and B_m , from which we can deduce the following important

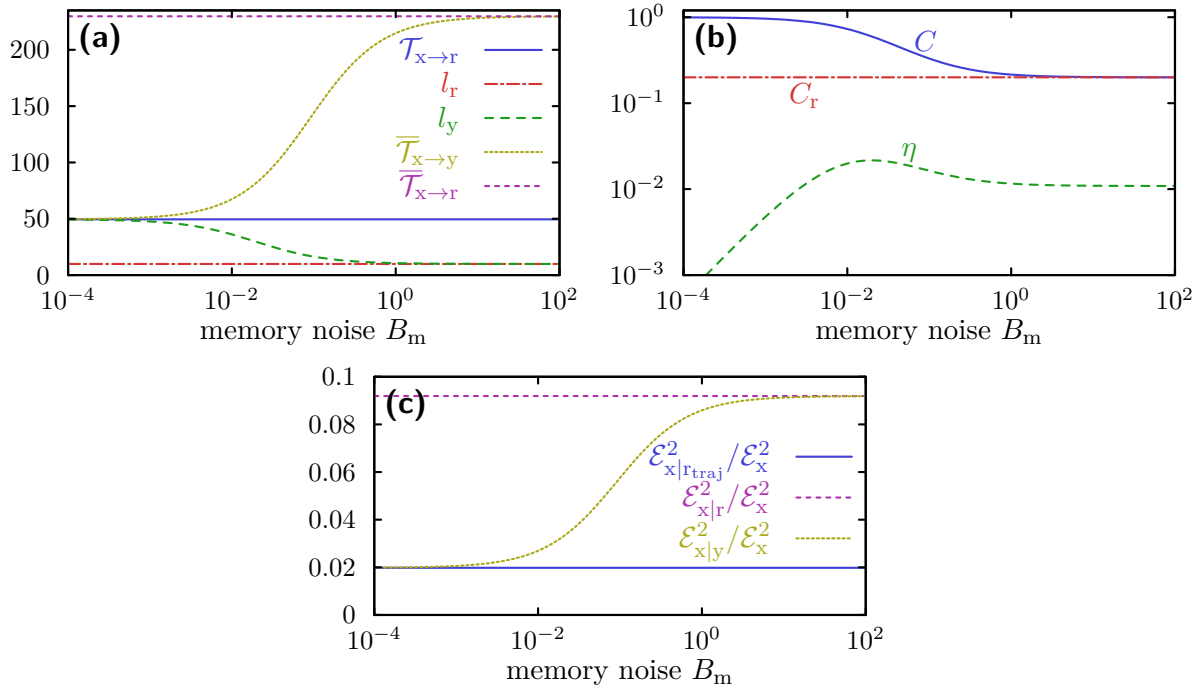


Figure 4.21 | Numerical results for the sensor model with memory. **(a)** Transfer entropy $\mathcal{T}_{x \rightarrow r}$, coarse-grained learning rate l_r , learning rate l_y (including the memory), and both upper bounds on the transfer entropy $\overline{\mathcal{T}}_{x \rightarrow y}$, $\overline{\mathcal{T}}_{x \rightarrow r}$ as function of the memory noise $B_m \equiv D_m/D_x$. Both the upper bound on the transfer entropy $\overline{\mathcal{T}}_{x \rightarrow y}$ and the learning rate l_y approach the transfer entropy $\mathcal{T}_{x \rightarrow y}$ as $B_m \rightarrow 0$. **(b)** Sensory capacity $C = l_y/\mathcal{T}_{x \rightarrow r}$ (with memory), $C_r = l_y/\mathcal{T}_{x \rightarrow r}$ (without memory) and efficiency η . **(c)** Conditional variances of the signal. The conditional variances of $x_t|r_0^t$, $x_t|r_t$, $x_t|y_t$ are denoted by $\mathcal{E}_{x|r_{\text{traj}}}^2$, $\mathcal{E}_{x|r}^2$, $\mathcal{E}_{x|y}^2$, respectively. The addition of a memory with low noise amplitude allows to reduce the variance $\mathcal{E}_{x|y}^2$ to its minimal possible value $\mathcal{E}_{x|r_{\text{traj}}}^2$. Parameters: $\omega_x = 1$, $\nu_r = \omega_r/\omega_x = 10$, $\mathcal{E}_x^2 = D_x/\omega_x = 0.1$, $B_r = 10^{-2}$ and $\nu_m = \sqrt{1 + \nu_r^2/B_r} \simeq 100$.

conditions to realize a large sensory capacity. First, the noise amplitude B_r must be small. Second, the relaxation rate of the memory ν_m must be chosen carefully. If the memory is too fast, it will effectively average over just the instantaneous state of the bare sensor r_t , i.e., the memory state m_t does not store additional information from the time history r_0^t of the bare sensor implying $C \simeq C_r$. If the memory is too slow, it averages the sensor state r_t for too long such that it filters out any noise but also the signal. The maximal sensory performance can be attained at an intermediate value $\nu_m = \sqrt{1 + \nu_r^2/B_r} \equiv \nu^*$ (see dotted line in Fig. 4.22), which is a compromise between time resolution and noise canceling through averaging, allowing the sensory capacity to approach its maximal value 1. The efficiency of the sensory network is quite low for this scenario. For example, the maximal efficiency $\eta^* \simeq 0.024$ is achieved for memory parameters as marked by the star in Fig. 4.22. In this regime the thermodynamic efficiency does not seem to be the relevant quantity to characterize the performance of the sensor.

In Fig. 4.21(c) we show the conditional variances of $x_t|r_t$, $x_t|y_t$, $x_t|r_0^t$ denoted by $\mathcal{E}_{x|r}^2$, $\mathcal{E}_{x|y}^2$, $\mathcal{E}_{x|r_{\text{traj}}}^2$, respectively. As shown in Appendices 4.B and 4.C the uncertainties are

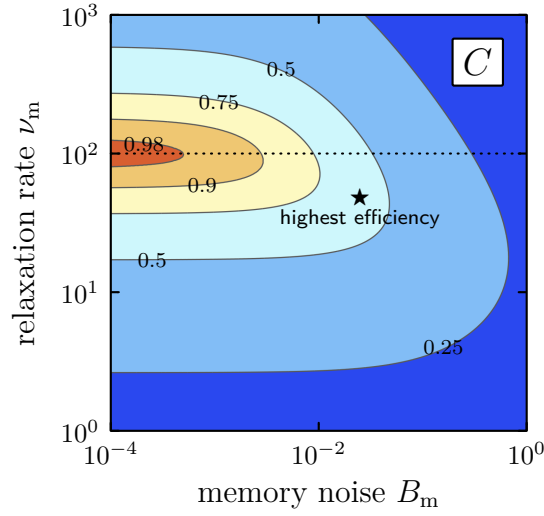


Figure 4.22 | Sensory capacity of the sensor with memory as function of the memory parameters ν_m and B_m . The dashed line indicates the relaxation rate $\nu_m = \sqrt{1 + \nu_r^2/B_r}$, which has been used for the plot of C in Fig. 4.21(b). The star (\star) marks the memory point (B_m^\star, ν_m^\star) for which the efficiency is maximal (here $\eta^\star \simeq 0.024$). Parameters: $\nu_r = 10$ and $B_r = 10^{-2}$ (as in Fig. 4.21).

proportional to the transfer entropy rate or the upper bounds on the transfer entropy rate such that

$$\overline{\mathcal{T}}_{x \rightarrow r} = \frac{\omega_x \nu_r^2 \mathcal{E}_{x|r}^2}{4B_r \mathcal{E}_x^2}, \quad \overline{\mathcal{T}}_{x \rightarrow y} = \frac{\omega_x \nu_r^2 \mathcal{E}_{x|y}^2}{4B_r \mathcal{E}_x^2}, \quad \mathcal{T}_{x \rightarrow r} = \frac{\omega_x \nu_r^2 \mathcal{E}_{x|r_{\text{traj}}}^2}{4B_r \mathcal{E}_x^2} = \mathcal{T}_{x \rightarrow y} \quad (4.105)$$

holds [cf. Eqs. (4.154), (4.156) and (4.163)]. Moreover, the relation $\mathcal{E}_{x|r_{\text{traj}}} \leq \mathcal{E}_{x|y} \leq \mathcal{E}_{x|r}$ implies $\mathcal{T}_{x \rightarrow r} \leq \overline{\mathcal{T}}_{x \rightarrow y} \leq \overline{\mathcal{T}}_{x \rightarrow r}$. With the addition of a memory the upper bound on the transfer entropy decreases ($\overline{\mathcal{T}}_{x \rightarrow y} \leq \overline{\mathcal{T}}_{x \rightarrow r}$), whereas the the learning rate increases ($l_r \leq l_y$). Thereby, the chain of inequalities (4.77) is satisfied as illustrated in Fig. 4.21(a), which also shows that if the sensory capacity approaches its maximal value one, the learning rate, transfer entropy and the upper bound on the transfer entropy will coincide, i.e., $l_y = \mathcal{T}_{x \rightarrow r} = \overline{\mathcal{T}}_{x \rightarrow y}$ at $C = 1$. The simultaneous saturation of both inequalities $l_y \leq \mathcal{T}_{x \rightarrow r} \leq \overline{\mathcal{T}}_{x \rightarrow y}$ at $C = 1$ plays an important role in the following subsection, since it allows us to derive a trade-off between sensory capacity and thermodynamic efficiency.

4.6 Trade-off between sensory capacity and efficiency

4.6.1 Trade-off for linear two-component network

From the linear two-component system we were able to identify two scenarios where the capacity reaches its maximum $C = 1$. First, the kinetic parameters, which characterize the dynamics of signal and the first layer of the network, are chosen in such a way that the time history r_0^t does not provide further information about the signal compared to the instantaneous state r_t . Second, a dissipative memory is added which stores information

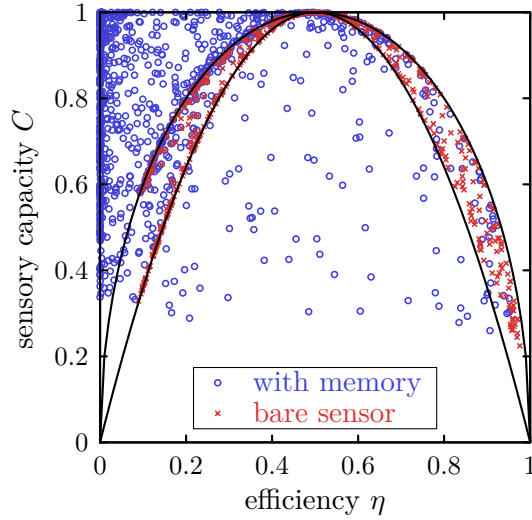


Figure 4.23 | Trade-off between sensory capacity and efficiency. The parameters are chosen at random with $10^{-1} \leq \nu_r, B_r, \nu_m, B_m \leq 10^2$. The bare sensor involves the parameters ν_r, B_r . The solid lines represent the bounds $4\eta(1-\eta) \leq C \leq 2\sqrt{\eta(1-\eta)}$ for the bare sensor. The bound $C \leq 2\sqrt{\eta(1-\eta)}$ is also valid for the sensor with memory for $\eta \geq 1/2$.

from the time history r_0^t in the instantaneous state of the memory m_t . In the first case, we have found that the efficiency is $\eta = 1/2$ for $C = 1$, whereas in the second case we have found $\eta < 1/2$ due to additional dissipation inside the cell.

The trade-off between sensory capacity and efficiency for the linear two-component network with dynamics from (4.93) is shown in Fig. 4.23. For the bare sensor we obtain

$$4\eta_r(1-\eta_r) \leq C_r \leq 2\sqrt{\eta_r(1-\eta_r)}, \quad (4.106)$$

which can be demonstrated as follows. Using (4.99) and (4.101) the efficiency of the bare sensor reads

$$\eta_r = \frac{l_r}{\sigma_r} = \frac{B_r \nu_r (1 + \nu_r)}{\nu_r^2 + B_r (1 + \nu_r)^2}, \quad (4.107)$$

moreover, using (4.99) and (4.100) the sensory capacity of the bare sensor reads

$$C_r = \frac{l_r}{\mathcal{T}_{x \rightarrow r}} = \frac{2\nu_r^3}{[\nu_r^2 + B_r(1 + \nu_r^2)][\sqrt{1 + \nu_r^2/B_r} - 1]}. \quad (4.108)$$

The bounds on the sensory capacity (4.106) are obtained by minimizing or maximizing (4.108) while keeping (4.107) fixed and satisfying $\nu_r, B_r \geq 0$. Most importantly, the upper bound (4.106) holds also for the sensor with memory for $\eta \geq 1/2$, which is responsible for the empty region in the upper right corner of the scatter plot in Fig. 4.23.

4.6.2 General trade-off

We now prove a general trade-off between sensory capacity and efficiency: a sensor with maximal sensory capacity $C = 1$ implies $\eta \leq 1/2$ as we have shown in [120]. The proof

depends on the reasonable assumption that for any sensor one can add a fictitious memory that stores all information from the time history of the sensor in the instantaneous state of the fictitious memory. We use the example from Sec. 4.5 involving the Langevin equations (4.93) to verify that such a fictitious memory indeed could be constructed. First, the memory must be precise, i.e., must not be noisy, which corresponds to $D_m = 0$ in (4.93). Second, the memory maybe composed of different subunits, where each subunit is sensitive for a different frequency ω_m , i.e., storing a different time frame of the time series of the sensor. For the Gaussian process from (4.93) we have seen that a single frequency $\omega_m = \omega_x \sqrt{1 + \nu_r^2/B_r}$ suffices to reach the maximal sensory capacity $C = 1$.

The chain of inequalities that has been derived in Eq. (4.77) demonstrates that the addition of a memory leads to an increase of the learning rate and a decrease of the upper bound on the transfer entropy rate. In a first step we show the trade-off by assuming that (i) maximal sensory capacity is reached $C = 1$ and (ii) the upper bound on transfer entropy rate equals the transfer entropy rate, i.e., $l_y = \mathcal{T}_{x \rightarrow y} = \bar{\mathcal{T}}_{x \rightarrow y}$ holds. From Eq. (3.35), we obtain

$$\bar{\mathcal{T}}_{x \rightarrow y} - l_y = \sum_{y, y'} P(y) \sum_x P(x|y) w_{yy'}^x \ln \frac{P(x|y) w_{yy'}^x}{P(x|y') \bar{w}_{yy'}} \geq 0, \quad (4.109)$$

where the inequality follows from the log-sum-inequality [36]. Note this inequality saturates if and only if the logarithm term is constant one for all values of x [36], i.e.,

$$P(x|y') = \frac{P(x, y) w_{yy'}^x}{P(y) \bar{w}_{yy'}} \equiv P(x|y \rightarrow y'), \quad (4.110)$$

must be satisfied, where $P(x|y) = P(x, y)/P(y)$ has been used and $P(x|y \rightarrow y')$ has been defined as the right hand side of the equation. Eq. (4.110) has a clear physical explanation: $P(x|y')$ is the probability distribution of signal if the sensor state y' is known and $P(x|y \rightarrow y')$ is the probability distribution of the signal if the current sensor state y' and its previous state y is known, more precisely, the transition $y \rightarrow y'$. The fact $P(x|y') = P(x|y \rightarrow y')$ suggests that the time history of the sensor which involves the transition $y \rightarrow y'$ does not provide more information about the signal x than the instantaneous state of the sensor. A more thorough discussion will follow below. By solving Eq. (4.110) for $w_{yy'}^x$ and inserting the expression for the rate of dissipation (4.7) yields

$$\sigma_y = \sum_{x, y, y'} P(x, y) w_{yy'}^x \ln \left[\frac{P(x|y') \bar{w}_{yy'}}{P(x|y) \bar{w}_{yy'}} \right] = 2l_y + \tilde{\sigma}_y, \quad (4.111)$$

where we have identified the learning rate l_y from (4.8) and defined the coarse-grained entropy production [103]

$$\tilde{\sigma}_y \equiv \sum_{y, y'} P(y) \bar{w}_{yy'} \ln \frac{\bar{w}_{yy'}}{\bar{w}_{y'y}} \geq 0, \quad (4.112)$$

which generally fulfills $\tilde{\sigma}_y \leq \sigma_y$. Hence, at maximal sensory capacity $C = 1$ the thermodynamic efficiency reads

$$\eta = \frac{l_y}{\sigma_y} = \frac{l_y}{2l_y + \tilde{\sigma}_y} \leq \frac{1}{2}. \quad (4.113)$$

In the following paragraph we show that $C = 1$ indeed implies $\mathcal{T}_{x \rightarrow y} = \overline{\mathcal{T}}_{x \rightarrow y}$, which completes the proof of the trade-off. We now add a fictitious memory m^f to the sensor y . Consider the transition rates from (4.65), where the sensor variable y replaces the variable r and the fictitious memory m^f replaces m . The learning rate of this fictitious sensor is given by (4.10)

$$l_z = \sum_{x, x'} P(x) w^{xx'} \sum_{y, m^f} P(y, m^f | x) \ln \frac{P(y, m^f | x)}{P(y, m^f | x')} \geq 0 \quad (4.114)$$

where the state of the fictitious sensor is characterized by $z = (y, m^f)$ and $P(y, m^f | x)$ is the conditional distribution of (y, m^f) given x . Within this fictitious sensor l_y is considered to be a coarse-grained learning rate which is smaller than l_z , i.e.,

$$l_z - l_y = \sum_{x, x', y} P(x, y) w^{xx'} \sum_{m^f} P(m^f | x, y) \ln \frac{P(m^f | x, y)}{P(m^f | x', y)} \geq 0. \quad (4.115)$$

At maximal sensory capacity $C = 1$ the fictitious memory cannot raise the learning rate such that $l_z - l_y = 0$ must hold. The inequality (4.115) can only saturate if $P(m^f | x, y) = P(m^f | x', y) = P(m^f | y)$ holds, which implies $P(x | y, m^f) = \frac{P(y)P(x|y)P(m^f|x,y)}{P(y)P(m^f|y)} = P(x|y)$, i.e.,

$$H[x_t | y_t, m_t^f] = H[x_t | y_t]. \quad (4.116)$$

Our key assumption is that it is always possible to find a fictitious memory that stores all information from the time history of the sensor in the instantaneous state of the memory

$$H[x_t | y_t, m_t^f] = H[x_t | y_0^t]. \quad (4.117)$$

Since the fictitious memory is unspecified, we can choose such a fictitious memory to obtain

$$H[x_t | y_t] = H[x_t | y_0^t], \quad (4.118)$$

from Eqs. (4.116) and (4.117). Therefore, maximal sensory capacity $C = 1$ implies (4.118). Furthermore, Eq. (4.118) implies $I[x_t : y_0^t] = I[x_t : y_t, y_{t-dt}] = I[x_t : y_t]$, which can be used to write the learning rate in the form

$$l_y = \frac{I[x_t : y_t] - I[x_{t+dt} : y_t]}{dt} = \frac{I[x_t : y_t, y_{t-dt}] - I[x_{t+dt} : y_t]}{dt} = \frac{I[x_{t+dt} : y_{t+dt}, y_t] - I[x_{t+dt} : y_t]}{dt}, \quad (4.119)$$

where we have used (3.26) in the first step, $I[x_t : y_t, y_{t-dt}] = I[x_t : y_t]$ in the second step, and finally used the steady state property $I[x_t : y_t, y_{t-dt}] = I[x_{t+dt} : y_{t+dt}, y_t]$. Inserting the conditional distributions from (3.21) and (3.32) into (4.119) yields

$$l_y = \sum_{x, y, y'} P(x, y) w_{yy'}^x \ln \frac{w_{yy'}^x}{\overline{w}_{yy'}} = \overline{\mathcal{T}}_{x \rightarrow y}, \quad (4.120)$$

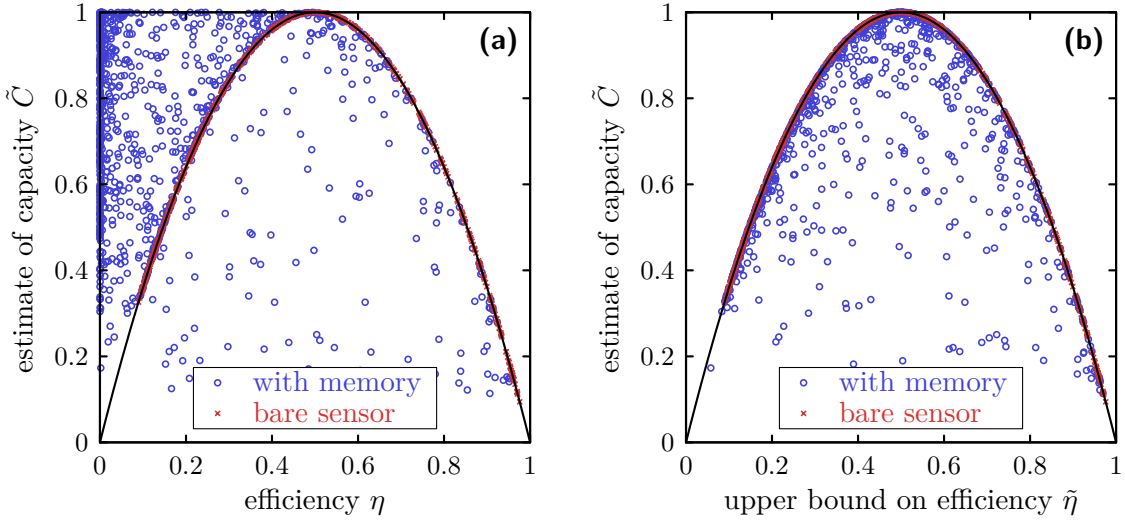


Figure 4.24| Estimate of the sensory capacity \tilde{C} versus efficiency. (a) Results from Fig. 4.23, where C is replaced by $\tilde{C} = l_y/\overline{\mathcal{T}}_{x \rightarrow y}$. Black line indicates $\tilde{C} = 4\eta(1 - \eta)$. (b) Estimate of sensory capacity $\tilde{C} \equiv l_y/\overline{\mathcal{T}}_{x \rightarrow y}$ versus lower bound on efficiency $\tilde{\eta} \equiv l_r/(\sigma_y - \tilde{\sigma}_y)$. For the bare sensor we use $\tilde{C}_r \equiv l_r/\overline{\mathcal{T}}_{x \rightarrow r}$ and $\tilde{\eta}_r \equiv l_r/(\sigma_r - \tilde{\sigma}_r)$, where $\tilde{\sigma}_r = 0$. The estimate of the sensory capacity of the bare sensor satisfies $\tilde{C}_r = 4\tilde{\eta}_r(1 - \tilde{\eta}_r)$, see solid black line in (a) and (b). Parameters ν_r, B_r, ν_m, B_m are chosen as in Fig. 4.23.

where we have identified the expression by the upper bound on the transfer entropy rate from (3.34) in the final step. Summarizing, we have shown that $C = 1 \Rightarrow H[x_t|y_t] = H[x_t|y_0^t] \Rightarrow l_y = \overline{\mathcal{T}}_{x \rightarrow y} \Rightarrow C = 1$. Therefore, whenever the sensory capacity saturates $C = 1$ we will find $l_y = \overline{\mathcal{T}}_{x \rightarrow y} = \overline{\mathcal{T}}_{x \rightarrow y}$.

We note for the bare sensor from Sec. 4.5.2 the coarse-grained entropy production (4.112) vanishes, which with (4.113) implies $\eta = 1/2$ for $C = 1$. The sensory network with memory from Sec. 4.5.3 includes internal dissipation, which also implies $\tilde{\sigma}_y > 0$. In accordance with (4.113), we obtained $\eta \geq 1/2$ for $C = 1$.

4.6.3 Estimate of sensory capacity and refined efficiency

It is generally much simpler to calculate the upper bound on the transfer entropy rate $\overline{\mathcal{T}}_{x \rightarrow y}$ from (3.34), rather than $\mathcal{T}_{x \rightarrow y}$, which usually does not have an analytical expression. Using the upper bound on the transfer entropy, we define the estimate for the sensory capacity

$$\tilde{C} \equiv \frac{l_y}{\overline{\mathcal{T}}_{x \rightarrow y}} \leq C \leq 1, \quad (4.121)$$

where the first inequality follows from $\mathcal{T}_{x \rightarrow y} \leq \overline{\mathcal{T}}_{x \rightarrow y}$. We note that in Sec. 4.6.2 is shown that $C = 1$ implies $l_y = \overline{\mathcal{T}}_{x \rightarrow y}$, i.e., $C = 1 \Rightarrow \tilde{C} = 1$. If the transfer entropy rate is not accessible one may fall back to this estimate \tilde{C} . In Fig. 4.24(a) we show the scatter plot from Fig. 4.23, where the sensory capacity C has been replaced by \tilde{C} from (4.121). For the bare sensor, which does not involve internal dissipation of chemical energy, we use $\tilde{C}_r = l_r/\overline{\mathcal{T}}_{x \rightarrow r}$, where l_r is given by (4.99) and $\overline{\mathcal{T}}_{x \rightarrow r}$ is given by (4.102). Comparing the

estimate of the sensory capacity for the bare sensor with (4.107) yields $\tilde{C}_r = 4\eta_r(1 - \eta_r)$. We note that there is an analogy to periodically driven engines [187, 188], where the estimate of the sensory capacity \tilde{C} is similar to the ratio of maximum power at given efficiency and global maximum power; compare Fig. 4 from Ref. [188] and Fig. 4.24(a). First, the bare sensor, where $\tilde{\sigma}_y$ vanishes, corresponds to the case in which the figure of merit diverges [188]. Second, the decrease of the efficiency at maximum power below 1/2 due to the idle heat current [188] is similar to the reduction of efficiency below 1/2 from (4.113), where l_y corresponds to the power output and $\tilde{\sigma}_y$ to the idle heat current. This analogy should clearly be distinguished from the discussion in Sec. 4.3.1 involving Fig. 4.8 as well as the linear response theory for information driven engines from [133], since these discussions do not involve the transfer entropy rate.

The coarse-grained entropy production $\tilde{\sigma}_y$ that appeared in the derivation for the trade-off between sensory capacity and efficiency in Eq. (4.112) allows us to refine one of our main inequalities from (4.12) involving the thermodynamic cost. More precisely, it follows from the log-sum-inequality [36] and (4.112) that

$$\sigma_y - l_y = \sum_{y,y'} P(y) \sum_x P(x|y) w_{yy'}^x \ln \frac{P(x|y) w_{yy'}^x}{P(x|y') w_{y'y}^x} \geq \tilde{\sigma}_y. \quad (4.122)$$

Based on this inequality we can define the refined efficiency

$$\tilde{\eta} \equiv \frac{l_y}{\sigma_y - \tilde{\sigma}_y} \leq 1, \quad (4.123)$$

which satisfies $\eta \leq \tilde{\eta}$. Importantly, one can show that $\eta = 1$ implies $\tilde{\eta} = 1$, which in turn after some extended algebra generally yields $\tilde{C} = 0$. This result implies that a sensor with maximal efficiency $\eta = 1$ has vanishing sensory capacity estimate $\tilde{C} = 0$, i.e., an energetically efficient sensor is a lousy noise filter. This is analogous to a heat engine reaching Carnot efficiency only at zero power [187, 188]. For completeness, we show the specific trade-off between \tilde{C} and $\tilde{\eta}$ for the cellular two-component network in Fig. 4.24(b). For future work it would be worthwhile to investigate whether this trade-off holds for arbitrary nonlinear networks.

4.7 Conclusion

In this chapter, we have shown that the performance of a sensor can be characterized by an entropic rate which we call learning rate [119, 120]. The fact that the learning rate l_y is bounded by the thermodynamic cost σ_y to maintain the sensory network has allowed us to define an efficiency $\eta = l_y/\sigma_y$ that relates the acquired information of a sensor to the energy, which is dissipated by the sensor. We have analyzed three models inspired by the *E. coli* sensory network. With these specific models, we were able to relate the entropy production σ_y to chemical work that is consumed inside the cell and/or to work that is delivered by the signal. In particular, the learning rate of a sensor can exceed the rate at which the external signal delivers energy to the sensor if an internal mechanism provides additional energetic input; see, e.g., Fig. 4.14(b), where $l_{\text{am}} > \sigma_{\text{ext}}$ at slow switching rates γ_c .

In a second part we have introduced a purely information theoretic measure, the sensory capacity, that characterizes the performance of a sensor. The sensory capacity relates the information that a sensor acquires about a signal with its state to the maximal information that can be inferred from the time history of a sensor. The sensory capacity is formally the ratio between the learning rate l_y and transfer entropy rate $\mathcal{T}_{x \rightarrow y}$ ($C = l_y / \mathcal{T}_{x \rightarrow y}$). A sensor reaches the maximal sensory capacity $C = 1$ if the instantaneous state of the sensor contains as much information about a fluctuating signal as its full time history. We have shown the sensory capacity can be increased with the addition of a memory.

A cellular two-component network has been used to show that the sensory capacity can indeed saturate ($C = 1$), allowing the instantaneous state of the sensor to carry the same amount of information about a signal as the full time history of the sensor. For a sensor with low sensory capacity ($C \ll 1$) an additional dissipative memory can increase the sensory capacity to its maximum $C = 1$, where the instantaneous state of the memory stores information from the time history of the sensor.

Most prominently, a trade-off between the sensory capacity C and thermodynamic efficiency η has been identified, implying that a sensor with maximal sensory capacity $C = 1$ cannot be efficient ($\eta \leq 1/2$). This trade-off, which holds for arbitrary sensory networks, allows a sensor either to be energetically efficient or to be a good noise filter, but not to be both. The trade-off has been analyzed in detail for the specific cellular two-component network. Moreover, a dissipative memory with low noise amplitude can increase the sensory capacity from a very low value to its maximum. For this specific linear model we could show a more detailed trade-off between sensory capacity and efficiency, as illustrated in Figs. 4.23 and 4.24.

In Sec. 4.6.3 we have introduced an analytical estimate of the sensory capacity \tilde{C} , which lower bounds the precise value $\tilde{C} \leq C$. Most prominently, the estimate of the sensory capacity \tilde{C} is shown to vanish for sensors which are energetically efficient $\eta = 1$, i.e., $\eta = 1 \Rightarrow \tilde{C} = 0$. This finding goes beyond what has been found in [120]. It would be interesting to investigate whether the full trade-off from Fig. 4.24 [$\tilde{C} \leq 4\eta(1 - \eta)$ for $\eta \geq 1/2$] hold for arbitrary nonlinear networks.

Appendices to chapter 4

4.A Linear noise approximation for cellular two-component network

4.A.1 Diffusion approximation

We denote the probability of (x, n_b, n_y) at time t by $P_t(x, n_b, n_y)$, where x is continuous and n_b, n_y take discrete values $n_b = 0, 1, \dots, N_r$ and $n_y = 0, 1, \dots, N_m$, respectively. In the following, we introduce a diffusion approximation which is quite accurate if the number of individual components is large $N_r, N_m \gg 1$ [33, 34]. The dynamics is given by the following partial differential equation

$$\begin{aligned} \dot{P}_t(x, n_b, n_y) = & \omega_x \frac{\partial}{\partial x} x P_t(x, n_b, n_y) + D_x \frac{\partial^2}{\partial x^2} P_t(x, n_b, n_y) \\ & + w_r^+(x, n_b - 1) P_t(x, n_b - 1, n_y) - w_r^+(x, n_b) P_t(x, n_b, n_y) \\ & + w_r^-(x, n_b + 1) P_t(x, n_b + 1, n_y) - w_r^-(x, n_b) P_t(x, n_b, n_y) \\ & + w_m^+(n_b, n_y - 1) P_t(x, n_b, n_y - 1) - w_m^+(n_b, n_y) P_t(x, n_b, n_y) \\ & + w_m^-(n_b, n_y + 1) P_t(x, n_b, n_y + 1) - w_m^-(n_b, n_y) P_t(x, n_b, n_y), \end{aligned} \quad (4.124)$$

where the first line follows from the Langevin equation (4.78), see [28, 34] for the inter-conversion of Langevin equations into Fokker-Planck equations; the second and the third line correspond to transitions involving ligand binding and unbinding; the fourth and fifth line take into account the transition of the memory protein. Using the Taylor series approximations

$$\begin{aligned} w_r^\pm(x, n_b \mp 1) P_t(x, n_b \mp 1, n_y) \approx & w_r^\pm(x, n_b) P_t(x, n_b, n_y) \mp \frac{\partial}{\partial n_b} w_r^\pm(x, n_b) P_t(x, n_b, n_y) \\ & + \frac{1}{2} \frac{\partial^2}{\partial n_b^2} w_r^\pm(x, n_b) P_t(x, n_b, n_y) \end{aligned} \quad (4.125)$$

and

$$\begin{aligned} w_m^\pm(n_b, n_y \mp 1) P_t(x, n_b, n_y \mp 1) \approx & w_m^\pm(n_b, n_y) P_t(x, n_b, n_y) \mp \frac{\partial}{\partial n_y} w_m^\pm(n_b, n_y) P_t(x, n_b, n_y) \\ & + \frac{1}{2} \frac{\partial^2}{\partial n_y^2} w_m^\pm(n_b, n_y) P_t(x, n_b, n_y) \end{aligned} \quad (4.126)$$

allow us to approximate (4.124) by the Fokker-Planck equation

$$\begin{aligned} \dot{P}_t(x, n_b, n_y) = & \omega_x \frac{\partial}{\partial x} x P_t(x, n_b, n_y) + D_x \frac{\partial^2}{\partial x^2} P_t(x, n_b, n_y) \\ & - \frac{\partial}{\partial n_b} \left[F_b(x, n_b) + \frac{\partial}{\partial n_b} D_b(x, n_b) \right] P_t(x, n_b, n_y) \\ & - \frac{\partial}{\partial n_y} \left[F_y(n_b, n_y) + \frac{\partial}{\partial n_y} D_y(n_b, n_y) \right] P_t(x, n_b, n_y), \end{aligned} \quad (4.127)$$

where

$$F_b(x, n_b) \equiv w_r^+(x, n_b) - w_r^-(x, n_b), \quad (4.128a)$$

$$D_b(x, n_b) \equiv \frac{1}{2} \left[w_r^+(x, n_b) + w_r^-(x, n_b) \right], \quad (4.128b)$$

$$F_y(n_b, n_y) \equiv w_m^+(n_b, n_y) - w_m^-(n_b, n_y), \quad (4.128c)$$

$$D_y(n_b, n_y) \equiv \frac{1}{2} \left[w_m^+(n_b, n_y) + w_m^-(n_b, n_y) \right]. \quad (4.128d)$$

Thereby, the variables n_b and n_y become continuous. Inserting the transition rates from (4.81) and (4.85) in (4.128) yields

$$F_b(x, n_b) = \omega_r(x) [\bar{n}_b(x) - n_b], \quad (4.129a)$$

$$D_b(x, n_b) \equiv \frac{\omega_r(x) \bar{n}_b(x) [N_r - \bar{n}_b(x)]}{N_r}, \quad (4.129b)$$

$$F_y(n_b, n_y) = \omega_m(n_b) [\bar{n}_y(n_b) - n_y], \quad (4.129c)$$

$$D_y(n_b, n_y) = \frac{\omega_m(n_b) \bar{n}_y(n_b) [N_m - \bar{n}_y(n_b)]}{N_m}, \quad (4.129d)$$

where $\omega_r(x) \equiv \omega_r^+(x) + \omega_r^-(x)$, $\bar{n}_b(x) \equiv N_r \omega_r^+(x) / [\omega_r^+(x) + \omega_r^-(x)]$, $\omega_m(n_b) \equiv \omega_m^+(n_b) + \omega_m^-(n_b)$, and $\bar{n}_y(n_b) \equiv N_m \omega_y^+(n_b) / [\omega_m^+(n_b) + \omega_m^-(n_b)]$. We note the Fokker-Planck equation (4.127) is equivalent to the Langevin equations [28, 34]

$$\begin{aligned} \dot{x}_t = & -\omega_x x_t + \xi_t^x, \\ \dot{n}_b(t) = & F_b(x_t, n_b(t)) + \xi_t^b, \\ \dot{n}_y(t) = & F_y(n_b(t), n_y(t)) + \xi_t^y, \end{aligned} \quad (4.130)$$

where the stochastic terms ξ_t^b, ξ_t^y are white noise terms that similarly to (4.79) have noise amplitudes, which are defined in (4.129b) and (4.129d), respectively. Note all stochastic differential equations are interpreted as Ito stochastic differential equations [28, 34] throughout this thesis.

4.A.2 Small signal variation and linear noise approximation

In the following, we derive an analytically solvable approximation of (4.130) for a weak fluctuating signal x_t , which is assumed to fluctuate around zero, see also [34]. Therefore, we expand the expressions from (4.129) around $x = 0$, which yields

$$F_b(x, n_b) \approx \omega_r [n_b^* + \alpha_1 x - n_b] \quad \text{and} \quad D_b(x, n_b) \approx \frac{\omega_r \bar{n}_b^* [N_r - \bar{n}_b^*]}{N_r} \equiv D_b^*, \quad (4.131)$$

where $\omega_r \equiv \omega_r(0)$, $n_b^* \equiv \bar{n}_b(0)$ and $\alpha_1 \equiv \partial_x \bar{n}_b(x)|_{x=0}$. Moreover, expanding n_b around n_b^* yields

$$F_y(n_b) \approx \omega_m [n_y^* + \alpha_2(n_b - n_b^*) - n_y] \quad \text{and} \quad D_y(n_b, n_y) \approx \frac{\omega_r \bar{n}_y^* [N_m - \bar{n}_y^*]}{N_m} \equiv D_y^*, \quad (4.132)$$

where $\omega_m \equiv \omega_m(0)$, $n_y^* \equiv \bar{n}_y(n_b^*)$ and $\alpha_2 \equiv \partial_{n_b} \bar{n}_y(n_b)|_{n_b=n_b^*}$. With the above approximations the Langevin equations (4.130) become

$$\begin{aligned} \dot{x}_t &= -\omega_x x_t + \xi_t^x, \\ \dot{n}_b(t) &= -\omega_r [n_b(t) - n_b^* - \alpha_1 x] + \xi_t^b, \\ \dot{n}_y(t) &= -\omega_m [n_y(t) - n_y^* - \alpha_2(n_b(t) - n_b^*)] + \xi_t^y, \end{aligned} \quad (4.133)$$

where the noise terms ξ_t^b, ξ_t^y have zero mean and covariances $\langle \xi_t^b \xi_{t'}^b \rangle = 2D_b^* \delta(t - t')$ and $\langle \xi_t^y \xi_{t'}^y \rangle = 2D_y^* \delta(t - t')$. We note the explicit form of the parameter α_1 from (4.131) is

$$\alpha_1 = \frac{n_b^* (N_r - n_b^*)}{N_r} \frac{\partial \Delta F(x)}{\partial x} \quad (4.134)$$

and α_2 from (4.132) is

$$\alpha_2 = \frac{n_y^* (N_m - n_y^*)}{N_m} \left[\frac{\kappa_+ \nu_+ - \kappa_- \nu_-}{(n_b^* \kappa_+ + \nu_-)(n_b^* \kappa_- + \nu_+)} \right]. \quad (4.135)$$

Importantly, if the internal ATP hydrolysis reaction were in equilibrium, i.e., $\Delta\mu = \ln[\kappa_+ \nu_+ / (\kappa_- \nu_-)] = 0$, the parameter α_2 would vanish. Thus internal energy consumption is necessary to establish correlations between the memory state n_y and the occupancy level of the receptors n_b .

Finally, the Langevin equations (4.133) can further be simplified to Eq. (4.93) by using the transformations

$$r_t \equiv \frac{n_b(t) - n_b^*}{\alpha_1} \quad \text{and} \quad m_t \equiv \frac{n_y(t) - n_y^*}{\alpha_1 \alpha_2}, \quad (4.136)$$

where the noise amplitudes become

$$D_r = D_b^* / \alpha_1^2 \quad \text{and} \quad D_m = D_y^* / (\alpha_1 \alpha_2)^2. \quad (4.137)$$

Using Eqs. (4.131)-(4.135), the noise amplitudes explicitly read

$$\begin{aligned} D_r &= \frac{\omega_r N_r}{n_b^* (N_r - n_b^*)} \left[\frac{\partial \Delta F(x)}{\partial x} \right]^{-2}, \\ D_m &= \left[\frac{\omega_r N_r}{n_b^* (N_r - n_b^*)} \right]^2 \left[\frac{\partial \Delta F(x)}{\partial x} \right]^{-2} \frac{\omega_m N_m}{n_y^* (N_m - n_y^*)} \left[\frac{(n_b^* \kappa_+ + \nu_-)(n_b^* \kappa_- + \nu_+)}{\kappa_+ \nu_+ - \kappa_- \nu_-} \right]^2, \end{aligned} \quad (4.138)$$

where $n_b^* \sim N_r$ and $n_y^* \sim N_m$. Therefore, the noise amplitude of the receptor variable D_r is inversely proportional to the number of receptors N_r , i.e., $D_r \sim N_r^{-1}$. Moreover, the noise amplitude of the memory D_m decreases with increasing number of proteins N_m and/or with increasing chemical potential $\Delta\mu = \ln[\kappa_+ \nu_+ / (\kappa_- \nu_-)]$.

4.B Entropic rates for Gaussian linear process

In this Appendix we calculate the entropy production and the learning rate for a sensor with dynamics from Eq. (4.93). We start by rewriting the the linear Langevin equations from (4.93) in the form

$$\begin{pmatrix} \dot{x}_t \\ \dot{y}_t \end{pmatrix} = -\mathbf{A} \begin{pmatrix} x_t \\ y_t \end{pmatrix} + \boldsymbol{\xi}_t, \quad (4.139)$$

where $\langle \boldsymbol{\xi}_t \boldsymbol{\xi}_{t'}^\top \rangle = 2\mathbf{D}\delta(t-t')$. Thereby, for the bare sensor $y_t = r_t$ holds and the matrices \mathbf{A} , \mathbf{D} are given by (4.97), whereas for the full sensor $y_t = (r_t, m_t)$ the matrices \mathbf{A} and \mathbf{D} are given by (4.103). The stationary probability density $\rho(x, y)$ of $(x_t, y_t) = (x, y)$ is a normal distribution with zero mean and covariance $\boldsymbol{\Sigma}$, which is the stationary solution of the Lyapunov equation (4.96). Identifying the first term in (4.139) as ‘‘mobility times force’’ motivates the definition

$$\beta \mathbf{F}(x, y) \equiv -\mathbf{D}^{-1} \mathbf{A} \begin{pmatrix} x \\ y \end{pmatrix}, \quad (4.140)$$

where $\beta \equiv 1/T$ is the inverse temperature and \mathbf{F} is the force. Note we have used the Einstein relation $\beta = \mu_i/D_i$, where μ_i is the mobility of the i -th component and $i = x, r, m$. The probability current, see (3.79) from Appendix 3.C, is in this case given by

$$\mathbf{J}(x, y) = -[\mathbf{A} - \mathbf{D}\boldsymbol{\Sigma}^{-1}] \begin{pmatrix} x \\ y \end{pmatrix} \rho(x, y) \quad (4.141)$$

where $\boldsymbol{\Sigma}^{-1}$ is the inverse of $\boldsymbol{\Sigma}$, which arises from taking the gradient of the Gaussian density distribution function. We denote the i -th component of the force from (4.140) by F_i and the i -th component of the current from (4.141) by J_i , where $i = x, r$ for the bare sensor and $i = x, r, m$ for the sensor with memory.

In order to simplify the following calculations considerably, we define the matrix

$$\boldsymbol{\Phi} \equiv \int dx \int dy \mathbf{J}(x, y) \beta \mathbf{F}(x, y)^\top, \quad (4.142)$$

which by using Eqs. (4.140), (4.141) and the fact that $\rho(x, y)$ is a normal distribution with covariance $\boldsymbol{\Sigma}$, becomes

$$\boldsymbol{\Phi} = [\mathbf{A} - \mathbf{D}\boldsymbol{\Sigma}^{-1}] \boldsymbol{\Sigma} \mathbf{A}^\top \mathbf{D}^{-1} = \mathbf{A} \boldsymbol{\Sigma} \mathbf{A}^\top \mathbf{D}^{-1} - \mathbf{D} \mathbf{A}^\top \mathbf{D}^{-1}. \quad (4.143)$$

Using Eq. (3.81) from Appendix 3.C, the entropy production due to subsystem ‘‘r’’ becomes

$$\sigma_r \equiv \int dx \int dy J_r(x, y) \beta F_r(x, y) = \Phi_{rr} = \omega_x \frac{\nu_r^2}{B_r(1 + \nu_r)}, \quad (4.144)$$

where we have identified σ_r by the second diagonal element of (4.142) in the second step, and finally inserted Eqs. (4.98), (4.143) with $\nu_r \equiv \omega_r/\omega_x$, $B_r \equiv D_r/D_x$ (as defined in

Sec. 4.5.2). This expression for σ_r is shown in (4.101). Similarly, the entropy production due to subsystem “m” is given by

$$\sigma_m \equiv \int dx \int dy J_m(x, y) \beta F_m(x, y) = \Phi_{mm} = \omega_x \frac{\nu_m^2 [\nu_r^2 + B_r(1 + \nu_m)(1 + \nu_r)]}{B_m(1 + \nu_m)(1 + \nu_r)(\nu_m + \nu_r)}, \quad (4.145)$$

where $\nu_m \equiv \omega_m/\omega_x$ and $B_m \equiv D_m/D_x$ (as defined in Sec. 4.5.3). Note the covariance Σ , which appears in (4.143), must be considered to be the 3×3 matrix that solves the steady state Lyapunov equation (4.96), whereas the matrices \mathbf{A} , \mathbf{D} are defined in (4.103). This expression for σ_m is shown in Eq. (4.104) of the main text.

We use a similar trick to calculate the learning rates l_r and l_y . First, we have shown in (4.10) that $l_y = h_x$ holds. Therefore, the learning rate is given by

$$l_y = h_x = - \int dx \int dy J_x(x, y) \frac{\partial}{\partial x} \ln \rho(x, y), \quad (4.146)$$

where we have used Eq. (3.80) from Appendix 3.C in the last step. The gradient of the logarithm of the probability is given by

$$\mathbf{a} \equiv - \begin{pmatrix} \partial_x \\ \partial_y \end{pmatrix} \ln \rho(x, y) = \Sigma^{-1} \begin{pmatrix} x \\ y \end{pmatrix}. \quad (4.147)$$

We define the matrix

$$\mathbf{L} \equiv \int dx \int dy \mathbf{J}(x, y) \mathbf{a}(x, y)^\top = -(\mathbf{A} - \mathbf{D}\Sigma^{-1})\Sigma\Sigma^{-1} = \mathbf{D}\Sigma^{-1} - \mathbf{A}, \quad (4.148)$$

where we have used (4.141) and (4.147). The learning rate can then be identified by the first element of the matrix

$$l_y = (\mathbf{L})_{xx} = D_x(\Sigma^{-1})_{xx} - (\mathbf{A})_{xx}. \quad (4.149)$$

For learning rate of the bare sensor we use the 2×2 covariance matrix of (x_t, r_t) from (4.98) and (4.149) to get

$$l_r = \frac{\omega_x \nu_r^3}{\nu_r^2 + B_r(1 + \nu_r)^2}. \quad (4.150)$$

Note we use the subscript “r” to distinguish the learning rate of the bare sensor l_r from the learning rate of the sensor with memory l_y . Using the 3×3 covariance matrix of (x_t, r_t, m_t) and (4.149) we obtain

$$l_y = \frac{\omega_x \nu_r^2 (\nu_m + \nu_r) \{ B_r \nu_m^2 (\nu_m \nu_r + 1) + \nu_r [B_m (\nu_m + 1)^2 (\nu_m + \nu_r) + \nu_m^2 \nu_r] \}}{\nu_m^2 \{ B_r \nu_r^2 [\nu_m^2 + \nu_m (4\nu_r + 2) + \nu_r^2 + 2\nu_r + 2] + B_r^2 (\nu_m + 1)^2 (\nu_r + 1)^2 + \nu_r^4 \} + B_m (\nu_m + 1)^2 [B_r (\nu_r + 1)^2 + \nu_r^2] (\nu_m + \nu_r)^2}. \quad (4.151)$$

In the following we denote conditional averages by

$$\langle \cdots \rangle_y \equiv \int \rho(x|y) (\cdots) dx, \quad (4.152)$$

where the subscript “ y ” indicates the condition and $\rho(x|y)$ is the conditional density, whereas we use $\langle \cdots \rangle_r$ for the bare sensor. Using Eq. (3.83) of Appendix 3.C the upper bound on the transfer entropy rate becomes [120]

$$\overline{\mathcal{T}}_{x \rightarrow r} = \frac{1}{4D_r} \left\langle [F_r(x, r) - \langle F_r(x, r) \rangle_r]^2 \right\rangle = \frac{\omega_r^2}{4D_r} \left\langle [x - \langle x \rangle_r]^2 \right\rangle \equiv \frac{\omega_r^2}{4D_r} \mathcal{E}_{x|r}^2, \quad (4.153)$$

where we have used $F_r(x, r) = -\omega_r(r - x)$ from (4.93) in the second step and defined the conditional variance of x given r by $\mathcal{E}_{x|r}^2$ in the last step, see also [41]. Note in contrast to (3.83), where F_y is a force, here we use $F_r(x, r)$ as drift velocity which has led to a change of the prefactor in front of the integral in (4.153). With $\mathcal{E}_x = D_x/\omega_x$, $\nu_r = \omega_r/\omega_x$ and $B_r = D_r/D_x$ the upper bound on the transfer entropy becomes

$$\overline{\mathcal{T}}_{x \rightarrow r} = \frac{\omega_x \nu_r^2 \mathcal{E}_{x|r}^2}{4B_r \mathcal{E}_x^2}, \quad (4.154)$$

where

$$\frac{\mathcal{E}_{x|r}^2}{\mathcal{E}_x^2} = \frac{\nu_r^2 + B_r(1 + \nu_r)^2}{\nu_r^2(1 + \nu_r) + B_r(1 + \nu_r)^2} \quad (4.155)$$

is derived from the covariance matrix (4.98) by using the Schur complement [189, 190] (see also [120]). For the sensor with memory, the upper bound on the transfer entropy rate analogously to (4.154) is given by [120]

$$\overline{\mathcal{T}}_{x \rightarrow y} = \frac{\omega_r^2}{4D_r} \left\langle [x - \langle x \rangle_y]^2 \right\rangle \equiv \frac{\omega_x \nu_r^2 \mathcal{E}_{x|y}^2}{4B_r \mathcal{E}_x^2}, \quad (4.156)$$

where the conditional variance satisfies

$$\frac{\mathcal{E}_{x|y}^2}{\mathcal{E}_x^2} = \frac{B_m(1+\nu_m)^2(\nu_m+\nu_r)^2[\nu_r^2+B_r(1+\nu_r)^2]+\nu_m^2\{\nu_r^4+B_r^2(1+\nu_m)^2(1+\nu_r)^2+B_r\nu_r^2[(1+\nu_m)^2+(1+\nu_r)^2+4\nu_m\nu_r]\}}{B_m(1+\nu_m)^2(1+\nu_r)(\nu_m+\nu_r)^2[\nu_r^2+B_r(1+\nu_r)]+\nu_m^2[\nu_r^2+B_r(1+\nu_m)(1+\nu_r)][B_r(1+\nu_m)(1+\nu_r)+\nu_r^2(1+\nu_m+\nu_r)]}. \quad (4.157)$$

The conditional variance of $x|r_0^t$, which is denoted by $\mathcal{E}_{x|r_{\text{traj}}}^2$, will be calculated in the following appendix by using a Kalman-Bucy filter.

4.C Uncertainty from time series

The conditional variances $\mathcal{E}_{x|r}^2$ and $\mathcal{E}_{x|y}^2$ are generally simple to calculate if the covariance matrix Σ is known, since it can be expressed as Schur complement of Σ [189], see also [190]. In the following we show how to calculate the conditional variance of $x_t|r_0^t$ by using a Kalman-Bucy filter, see, e.g., [88, 185]. Following [185] we determine the conditional average $\hat{x}_t \equiv \langle x_t \rangle_{y_0^t}$, as defined in (4.152), and the conditional variance

$$\mathcal{E}^2(t) \equiv \langle (x_t - \hat{x}_t)^2 \rangle, \quad (4.158)$$

which saturates $\mathcal{E}(t) \rightarrow \mathcal{E}_{x|r_{\text{traj}}}$ in the steady state limit $t \rightarrow \infty$.

First, we note that \hat{x}_t is a function of r_0^t , which minimizes the variation (4.158), i.e., replacing \hat{x}_t by any other function $f(r_0^t)$ in (4.158) will increase $\mathcal{E}^2(t)$. As shown in, e.g., [185], the function \hat{x}_t is a linear projection of x_t on r_0^t , where $\langle x_t r_{t'} \rangle = \langle \hat{x}_t r_{t'} \rangle$ must be satisfied for all $t' \leq t$, which also implies $\langle \hat{x}_t (x_t - \hat{x}_t) \rangle = 0$. We rewrite the first two lines from (4.93) as stochastic Ito differential equations

$$\begin{aligned} dx_t &= -\omega_x x_t dt + d\xi_t^x, \\ dr_t &= -\omega_r (r_t - \phi x_t) dt + d\xi_t^r = -\omega_r (r_t - \phi \hat{x}_t) dt + \omega_r (\phi x_t - \phi \hat{x}_t) dt + d\xi_t^r, \end{aligned} \quad (4.159)$$

where we have generalized the differential equation with a parameter ϕ , which in case of Eq. (4.93) is $\phi = 1$, and used independent Wiener increments $d\xi_t^i$ with zero mean and $(d\xi_t^i)^2 = 2D_i dt$ ($i = x, r$); the second step introduces \hat{x}_t as the linear projection of x_t on r_0^t , which allows us to define $dr_t^{\parallel} \equiv -\omega_r (r_t - \phi \hat{x}_t) dt$ and $dr_t^{\perp} \equiv dr_t - dr_t^{\parallel}$ that satisfy $\langle r_{t'} dr_t \rangle = \langle r_{t'} dr_t^{\parallel} \rangle$ as well as $\langle r_{t'} dr_t^{\perp} \rangle = 0$ for all $t' \leq t$. We note that the increment $dr_t^{\perp} \equiv r_{t+dt} - r_t$ contains new information about x_t from r_0^{t+dt} that is not in r_0^t [185]. Using the dr_t^{\perp} we can derive a stochastic differential equation for the linear projection of the signal

$$\begin{aligned} d\hat{x}_t &= -\omega_x \hat{x}_t dt + \frac{\langle x_t dr_t^{\perp} \rangle}{\langle (dr_t^{\perp})^2 \rangle} dr_t^{\perp} = -\omega_x \hat{x}_t dt + \frac{\omega_r \phi \langle x_t (x_t - \hat{x}_t) \rangle}{2D_r} \left[\omega_r \phi (x_t - \hat{x}_t) dt + d\xi_t^r \right] \\ &= -\omega_x \hat{x}_t dt + \frac{\omega_r \phi \mathcal{E}^2(t)}{2D_r} \left[\omega_r \phi (x_t - \hat{x}_t) dt + d\xi_t^r \right], \end{aligned} \quad (4.160)$$

involving the following calculations. The first step in (4.160) contains two terms, where one accounts for the update of \hat{x}_t due to the signal dynamics [see first line of (4.159)] and second term arises from the Gram-Schmidt procedure by considering dr_t^{\perp} as a base vector for the new observation that is orthogonal to r_0^t , i.e., $\langle r_{t'} dr_t^{\perp} \rangle = 0$ for all $t' \leq t$. In the second step of Eq. (4.160) we have inserted dr_t^{\perp} . From the first to the second line in Eq. (4.160) we have used $\langle \hat{x}_t (x_t - \hat{x}_t) \rangle = 0$ and (4.158).

From the stochastic differential equation of the projection \hat{x}_t we can derive the so-called Riccati equation [88, 120, 185]

$$\begin{aligned} \frac{d}{dt} \mathcal{E}^2(t) &= \frac{2\langle (x_t - \hat{x}_t)(dx_t - d\hat{x}_t) \rangle}{dt} + \frac{\langle (dx_t - d\hat{x}_t)^2 \rangle}{dt} \\ &= -2\omega_x \mathcal{E}^2(t) - \frac{\omega_r^2 \phi^2}{D_r} [\mathcal{E}^2(t)]^2 + 2D_x + \frac{\omega_r^2 \phi^2}{4D_r^2} [\mathcal{E}^2(t)]^2 (2D_r) \\ &= -\frac{\omega_r^2 \phi^2}{2D_r} [\mathcal{E}^2(t)]^2 - 2\omega_x \mathcal{E}^2(t) + 2D_x, \end{aligned} \quad (4.161)$$

where from the first to the second line (4.160) and (4.159) have been used. Note that $dx_t^2 = 2D_x dt$, $d\hat{x}_t^2 = \omega_r^2 \phi^2 [\mathcal{E}^2(t)]^2 / (4D_r^2) (d\xi_t^r)^2$, and $(d\xi_t^r)^2 = 2D_r dt$.

Setting the left hand side of (4.161) to zero yields

$$\mathcal{E}_{x|r_{\text{traj}}}^2 = \mathcal{E}_x^2 \left(\frac{2}{1 + \sqrt{1 + \frac{\nu_x^2}{B_r}}} \right), \quad (4.162)$$

where $\mathcal{E}_x = D_x/\omega_x$, $\nu_r = \omega_r/\omega_x$ and $B_r = D_r/D_x$. Moreover, comparing (4.162) with the transfer entropy from (4.100) yields

$$\mathcal{T}_{x \rightarrow r} = \frac{\omega_x \nu_r^2}{4B_r} \frac{\mathcal{E}_{x|_{\text{traj}}}^2}{\mathcal{E}_x^2}, \quad (4.163)$$

which is quite analogous to what we have found for the upper bounds on the transfer entropy rates $\overline{\mathcal{T}}_{x \rightarrow r}$ from (4.154) and $\overline{\mathcal{T}}_{x \rightarrow y}$ from (4.156).

5 Optimal inference strategies and approximation schemes

For an array of independent binary sensors (e.g., receptors, single electron transistors) measuring a stochastic signal (e.g., ligand concentration, gate voltage), we investigate the information loss of inference strategies that are solely based on the time averaging of the sensor state. It is shown that these inference strategies lose up to $1/2$ bit of information compared with the full time history of the sensor. Moreover, it turns out that this information loss is independent of the number of binary sensors. Using the local detailed balance relation, we derive a condition that determines whether or not such a loss of information occurs. For example, if the free energy difference arising from the signal, influences the both forward and backward rate in a symmetric manner, time integration will capture the full information about the signal. More broadly, for the long time limit we derive an analytical expression for the hidden information that cannot be accessed by using simple time averaging mechanisms, which is intimately linked to an asymmetry parameter that determines the load distribution of the free energy difference on forward and backward rates of the sensor. As an implication we find a connection between this hidden information and the information loss of approximation schemes for chemical networks. For example, the linear noise approximation loses information compared to the original system dynamics that is precisely the hidden information that cannot be accessed with simple time averaging mechanisms. Thereby, the information loss arises from the simplification of the dynamics. This chapter is based on [190].

5.1 Introduction to chemoreception

In 1977 Berg and Purcell (BP) have studied in their seminal work [143] the physics of chemoreception, where they determined the physical limits to the precision with which a cellular organism can perform concentration measurements with receptor proteins. For a single receptor using the mean occupancy level, which is obtained from time averaging, they have derived an explicit expression for the limit to the precision of such a measurement. Interestingly, it has later been found that using a maximum likelihood (ML) estimate can reduce the uncertainty of the concentration measurement even further by a factor of two [191]. In an information theoretic language the ML estimate “uses” 0.5 bit more information from the time history of the receptor occupancy level than the BP estimate. The ML estimate has been investigated for concentration ramps [169, 192], spatial gradients [193], and competing signals [194] (see [153, 195] for recent reviews). Importantly, it has been shown that this additional information is not accessible with linear networks [94, 196], which illustrate the characteristic information loss for this class of models.

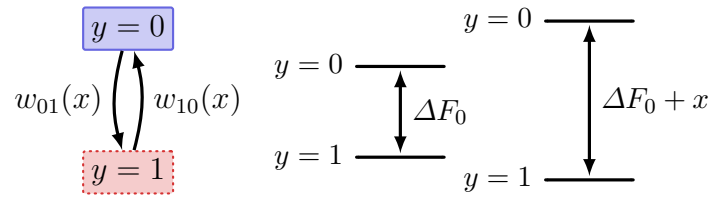


Figure 5.1| Binary sensor model with transition rates on the left. The change x of the free energy difference is shown on the right.

More broadly, the relation between energy consumption and the information acquisition of biological networks has attracted much interest recently. For example, the expenditure of chemical energy can lead to ultra-sensitive response to external stimuli [145, 148, 177]. Furthermore, trade-offs between energy consumption, accuracy and speed has been discovered for bacterial adaptation [95, 178, 182] (see [144] for a different perspective). The role of energy consumption has been studied for cellular computation [94, 181, 197], cellular sensing [92, 119, 149–151, 153, 170, 198] and learning [199]. Specifically, the maximal sensory performance can only be reached at diverging energetic cost [94, 149–151]. To be able to come close to such bounds, it is, therefore, essential to use the optimal inference strategy.

In the following, we investigate inference strategies that allow to reach maximum sensory performance. Thereby, two classes of inference strategies can be identified, which involve time-averaging of the sensor state and counting transitions [198]; we study their joint correlations. For binary sensors responding to a stochastic signal we obtain an analytical expression for the hidden information that cannot be attained with inference strategies that are solely based on time-averaging. For example, this information loss is up to 1/2 bit. The same loss of information can also be identified in the linear noise approximation, which is a useful tool to approximate chemical networks with an effective Brownian motion [33, 34, 200–202]. In this case the information loss arises from the simplification the original system dynamics, which is assumed to be governed by a chemical master equation. We show under which circumstances these approximation schemes are surprisingly accurate on the trajectory level and when they lose up to about 1/2 bit of information .

5.2 Sensor measuring a stochastic concentration

5.2.1 Model for binary sensor

We assume the sensor at time t can be in one of two binary states $y_t = 0, 1$, where $y_t = 0$ corresponds to the “empty” state and $y_t = 1$ corresponds to the “occupied” state. Initially, the two states are equilibrated to a free energy difference ΔF_0 between $y = 0$ and $y = 1$. At time $t = 0$ the signal changes the free energy difference to a new value $\Delta F_0 + x$, where a positive signal ($x > 0$) favors the occupied state. More precisely, the transition rates $w_{yy'}(x)$ from state $y_t = y$ to state $y_t = y'$, as illustrated in Fig. 5.1, must satisfy the local detailed balance relation

$$\ln \frac{w_{01}(x)}{w_{10}(x)} \equiv \Delta F_0 + x, \quad (5.1)$$

where we have set here and in the following the thermal energy to $k_B T \equiv 1$. In equilibrium, the probability for being in the occupied state $y = 1$ at signal value x then reads $P^{\text{eq}}(1|x) = e^{\Delta F_0 + x} / (1 + e^{\Delta F_0 + x})$. For an illustration, let us consider a single receptor which can either be occupied by a ligand ($y = 1$) or be empty ($y = 0$). At concentration c ligands bind to the receptor with a rate $w_{01} \equiv kc$ and unbind with the rate $w_{10} \equiv r$. Denoting the initial concentration by c_0 , the initial free energy difference becomes $\Delta F_0 = \ln(kc_0/r)$ and the change of the ligand concentration $c_0 \rightarrow c$ corresponds to $x = \ln(c/c_0)$, i.e., the signal x corresponds a change of the chemical potential. The mean occupancy level of the receptor then reads $P^{\text{eq}}(1|x) = kc/(kc + r)$, where $c = c_0 e^x$. This example for a receptor measuring an external ligand concentration will be useful to compare our findings with the work from Refs. [94, 191, 192, 196]. A non-biological example is a single electron transistor [50–52], where the signal x can be associated with a change of the gate voltage [50].

Since the local detailed balance relation (5.1) provides only one constraint for two rates, it does not determine both rates $w_{01}(x)$ and $w_{10}(x)$ individually. The asymmetry parameter, which is a central quantity in this chapter, defined through

$$\alpha \equiv -\partial_x \ln w_{10}(x) = 1 - \partial_x \ln w_{01}(x), \quad (5.2)$$

accounts for this freedom of choice, where the second identity follows directly from (5.1). For “natural” values $0 \leq \alpha \leq 1$ the free energy change x influences the rates in such a way that one rate increases while the corresponding reverse rate decreases. For $\alpha = 0$ (or $\alpha = 1$) only one rate is affected by the signal x . The before mentioned receptor model, where $w_{01}(x) = kc_0 e^x$ and $w_{10}(x) = r$, corresponds to $\alpha = 0$. A two level system with fermionic rates $w_{01}(x) = \gamma P^{\text{eq}}(1|x)$ and $w_{10}(x) = \gamma P^{\text{eq}}(0|x)$ (see, e.g., [85]), where γ is a constant rate, has an asymmetry parameter $\alpha = P^{\text{eq}}(1|x)$. For example, the experiment involving a single-electron box with the mean number of electrons of about 1/2 from Ref. [51], corresponds to a system for which $\alpha \simeq 1/2$ holds, which can be deduced from the supporting information (Fig. S1) of Ref. [51].

5.2.2 Main result

Let us first introduce the measurement of a stochastic signal as illustrated in Fig. 5.1. The sensor is initially equilibrated with a free-energy difference ΔF_0 at time $t < 0$. At time $t = 0$ the free-energy difference changes stochastically to a new value $\Delta F_0 + x$, where we assume the change x to be normally distributed with zero mean and variance \mathcal{E}_x^2 , i.e., $P(x) \equiv (2\pi\mathcal{E}_x^2)^{-1/2} \exp[-x^2/(2\mathcal{E}_x^2)]$. For weak signals the condition $\mathcal{E}_x^2 \ll 1$ holds. We are interested in the mutual information between the stochastic signal x and time history of the sensor $y_0^t \equiv \{y_{t'}\}_{0 \leq t' \leq t}$, since mutual information and the minimal estimation error are intimately related with one another [36]; see also [190]. The mutual information is given by (3.6)

$$\mathcal{I} \equiv I[x:y_0^t] \equiv \left\langle \ln \frac{P(y_0^t|x)}{P(y_0^t)} \right\rangle, \quad (5.3)$$

where $P(y_0^t|x)$ is the conditional probability of the sensor time history y_0^t given the signal value x and $P(y_0^t) \equiv \int P(y_0^t|x)P(x)dx$ is the marginal distribution. The brackets $\langle \dots \rangle$

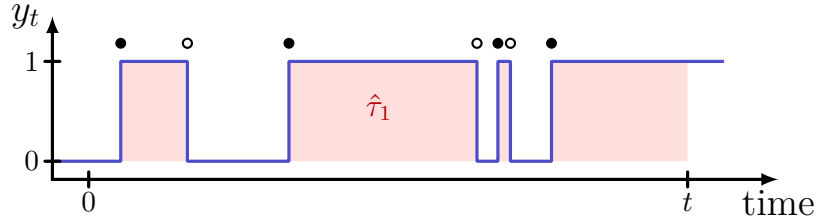


Figure 5.2| Time history of a single binary sensor. The initial state is $y_0 = 0$. The red-shaded region illustrates the functional $\hat{\tau}_1$. The other persistence time reads $\hat{\tau}_0 = t - \hat{\tau}_1$. The dots indicate jump events, where the closed (open) circles indicate transitions of the sensor $0 \rightarrow 1$ ($1 \rightarrow 0$), respectively. The total number of jump events is $\hat{n}_{\text{tot}} = 7$, where the individual number of transitions are $\hat{n}_{01} \equiv \#(\bullet) = 4$ and $\hat{n}_{10} \equiv \#(\circ) = 3$.

denote the average over all possible realizations y_0^t and x , weighted by the joint distribution $P(y_0^t|x)P(x)$. We will later use $\langle \dots \rangle_x$ for the average over all sensor trajectories y_0^t at a given signal value x weighted by the conditional probability $P(y_0^t|x)$. Note that $\langle \langle \dots \rangle_x \rangle = \langle \dots \rangle$ holds. A discrete state Markov process consists of a sequence of visited states, where each state decays exponentially by triggering a transition to a new state. Therefore, the path probability can be written in the form (see, e.g., Refs. [18, 191])

$$P(y_0^t|x) = P(y_0)w_{01}(x)^{\hat{n}_{01}}w_{10}(x)^{\hat{n}_{10}} \exp[-w_{01}(x)\hat{\tau}_0 - w_{10}(x)\hat{\tau}_1], \quad (5.4)$$

where $\hat{n}_{yy'}$ is the number of transitions from state y to state y' and $\hat{\tau}_y$ is the time spent in state y along the time history of the sensor y_0^t . The functionals $\hat{n}_{yy'}$ and $\hat{\tau}_y$ of the trajectory y_0^t are illustrated in Fig. 5.2. Since $\hat{\tau}_0 = t - \hat{\tau}_1$ and, since each transition $0 \rightarrow 1$ must be followed by a transition $1 \rightarrow 0$, the path weight (5.4) is fully characterized by the functionals $y_0, \hat{n}_{\text{tot}} \equiv \hat{n}_{01} + \hat{n}_{10}$, and $\hat{\tau}_1$, implying $\mathcal{I} = I[x:y_0, \hat{n}_{01}, \hat{n}_{10}, \hat{\tau}_0, \hat{\tau}_1] = I[x:y_0, \hat{\tau}_1, \hat{n}_{\text{tot}}]$.

Let us now highlight the important role of the asymmetry parameter α from (5.2) for this inference problem in the long time limit. Using the fact that each forward transition must be followed by the reverse transition, we obtain for $t \rightarrow \infty$ the relations $\hat{n}_{01} \simeq \hat{n}_{10} \simeq \hat{n}_{\text{tot}}/2 \gg 1$. Importantly, for $\alpha = 1/2$ the first terms in the path probability (5.4) do not depend on the value of the signal x , since $w_{01}(x)^{\hat{n}_{01}}w_{10}(x)^{\hat{n}_{10}} \simeq [w_{01}(0)w_{10}(0)]^{\hat{n}_{\text{tot}}/2}$ holds. In this case, where $\alpha = 1/2$, the number of jump events \hat{n}_{tot} does not contain additional information about the signal. More precisely, the coarse-grained variables $(y_0, \hat{\tau}_1)$ contains generally less information than the full time history of the sensor

$$\tilde{\mathcal{I}} \equiv I[x:y_0, \hat{\tau}_1] \leq \mathcal{I}, \quad (5.5)$$

whereas for $\alpha \neq 1/2$ the inequality must saturate, i.e., $\tilde{\mathcal{I}} = \mathcal{I}$. In Figs. 5.3(a) and 5.3(b), we compare the full information from the trajectory \mathcal{I} (blue open circles) with the information $\tilde{\mathcal{I}}$, which excludes the information from the number of jump events (solid red line). For the symmetric weight $\alpha = 1/2$ we confirm $\mathcal{I} = \tilde{\mathcal{I}}$, which implies that the number of jump events \hat{n}_{tot} does not provide additional information about the signal. For asymmetric weight $\alpha \neq 1/2$ as it applies to the aforementioned receptor model, where $\alpha = 0$, the number of jump events \hat{n}_{tot} contribute to a gain of information of about up to $\frac{1}{2} \ln 2 = 1/2$ bit. The same result is obtained for an array of $N = 100$ sensors [see

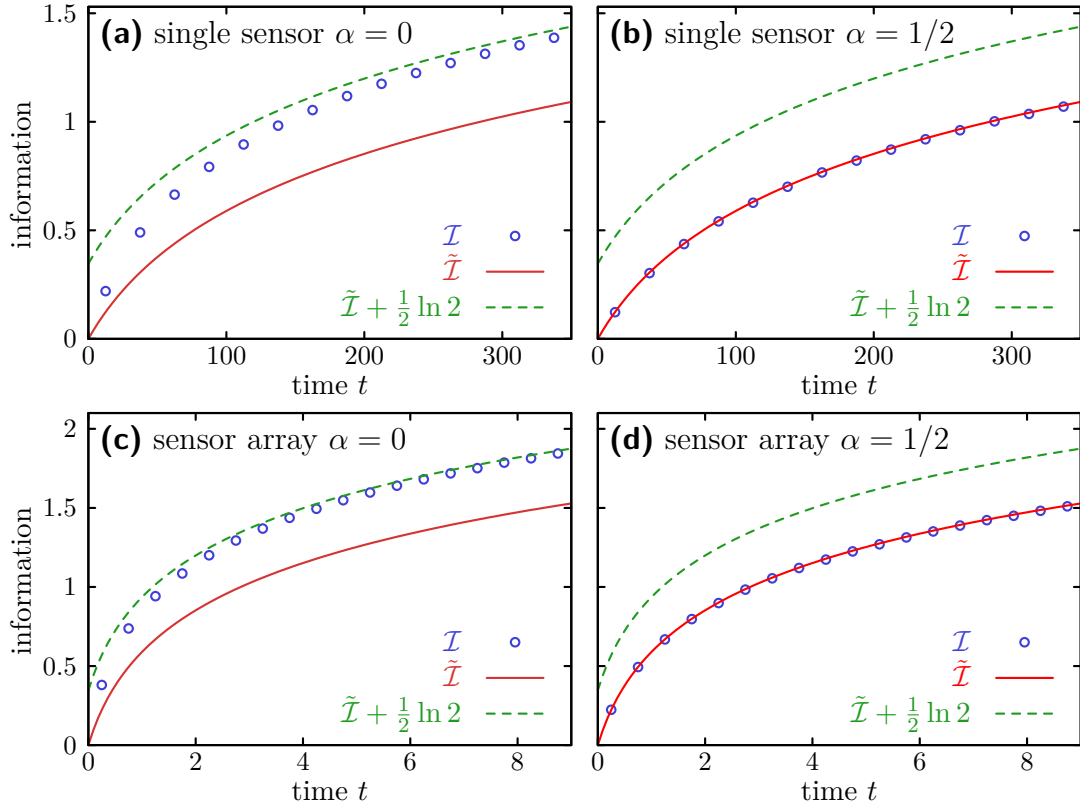


Figure 5.3 | Full information from the time history of the sensors \mathcal{I} (blue open circles) and coarse-grained information $\tilde{\mathcal{I}}$ (solid red line) as function of time. The results are displayed for four different sensory systems, for which the rates are either asymmetrically $\alpha = 0$ (a, c) or symmetrically (b, d) influenced by the signal. The results for a single sensor ($N = 1$) is shown in the upper panel (a, b). The results for the sensor array with $N = 100$ are shown in the lower panel (c, d), where we set $\mathcal{I} \equiv \mathcal{I}_N$ and $\tilde{\mathcal{I}} \equiv \tilde{\mathcal{I}}_N$. The full mutual information \mathcal{I} is obtained from 10^6 individual trajectories y_0^t each with a different stochastic signal x , where we used Eqs. (5.4) and (5.3) for the single sensor case ($N = 1$), and Eqs. (5.7) and (5.8) for the sensor array with $N = 100$ sensors. For the coarse-grained mutual information, we use the approximation from Eq. (5.12). Parameters: Rates $w_{01}(x) \equiv e^{(1-\alpha)x}$ and $w_{10}(x) \equiv e^{-\alpha x}$; asymmetry parameter $\alpha = 0$ (left panel) and $\alpha = 1/2$ (right panel); number of sensors $N \equiv 1$ (upper panel) and $N \equiv 100$ (lower panel); signal standard deviation $\mathcal{E}_x \equiv 0.3$ ($\mathcal{E}_x^2 = 0.09 \ll 1$); $\omega_y \equiv w_{01}(0) + w_{10}(0) = 2$, and $p_0 \equiv w_{01}(0)/\omega_y = 1/2$.

Figs. 5.3(c) and 5.3(d)]. Since the reduction of the signal variance due to the measurement is proportional to $e^{-2\mathcal{I}}$ (see, e.g., [36, 190]) this additional information corresponds to a decrease of the measurement variance (error) by a factor of 2. This enhanced accuracy for ML estimators has been firstly been found in [191] for aforementioned receptor model, where $\alpha = 0$ holds. We note that for binary sensors measuring a stochastic signal such a gain of information from the number of jump events occurs whenever the signal influences forward and backward rate asymmetrically ($\alpha \neq 1/2$).

Using the method of generating function, see the following section 5.3, we obtain more generally

$$\Delta\mathcal{I} \equiv \lim_{t \rightarrow \infty} (\mathcal{I} - \tilde{\mathcal{I}}) = \frac{1}{2} \ln(4\alpha^2 - 4\alpha + 2), \quad (5.6)$$

which is our main result of this chapter. A simple derivation of this formula for narrow-width Gaussian signals ($\mathcal{E}_x^2 \ll 1$) is shown in Sec. 5.3.2. We show in Sec. 5.3.3 that Eq. (5.6) holds even for broadly distributed and/or non-Gaussian signals. Importantly, the relation (5.6) implies that the asymmetry parameter α determines the additional information content of the number of jump events. Under natural conditions, where $0 \leq \alpha \leq 1$ holds, the number of jump events contribute to a gain of information (5.6) up to 1/2 bit. The gain of information can qualitatively be understood as follows. If the transition rates are symmetrically influenced by the signal ($\alpha = 1/2$), a signal change will increase one rate by the same amount as it decreases the corresponding reverse transition rate. Therefore, the total number of transition along both directions $\hat{n}_{\text{tot}} = \hat{n}_{01} + \hat{n}_{10}$ will not expected to be altered by the signal x . Hence, the total number of jump events \hat{n}_{tot} does not provide additional information about x , where $\Delta\mathcal{I} = 0$. However, in the extreme case $\alpha = 0$, only the transition rate $w_{01}(x)$ is influenced by the signal, which leads to a monotonic correlation between the signal x and the number of jump events \hat{n}_{tot} .

We note from a technical point of view that the derivation of the main result, Eq. (5.6), used the method of generating function, which we will present in Sec. 5.3.1. Thereby, the generating function allows to determine in finite time the joint dispersion of different classes of random variables, for example, jump variables $\hat{n}_{yy'}$ and persistence time $\hat{\tau}_y$ [198]. For networks where each component consist of more than two states it might be difficult to calculate the generating function analytically. We show a in Sec. 5.3.4 (see also [190]) a method that allows to determine the joint dispersion of such random variables in the long time limit, which does not require the generating function. A similar method has been derived in [198, 203, 204], whereas we extent this method to correlated dispersion of random variables.

Our main result for the information gain $\Delta\mathcal{I}$ (5.6) holds even for an array of N sensors measuring the same signal x . To see that we first generalize the path weight (5.4) to an arbitrary number of sensors. We label each sensor by a variable $i = 1, \dots, N$, where the i -th sensor is in state $y_t^{(i)} = 0, 1$ at time t . Hence the state of the sensor array at time t is characterized by $\mathbf{y}_t = (y_t^{(1)}, \dots, y_t^{(N)})$ and $\mathbf{y}_0^t \equiv \{\mathbf{y}_{t'}\}_{0 \leq t' \leq t}$ denotes the full trajectory of the sensor array. Denoting for the i -th sensor the time spent in state y by $\hat{\tau}_y^{(i)}$ and the number of transitions from y to y' by $\hat{n}_{yy'}^{(i)}$ the conditional path weight of the sensor array becomes

$$P(\mathbf{y}_0^t | x) \equiv p_0^{Y_0} (1 - p_0)^{N - Y_0} w_{01}(x)^{\hat{n}_{01}} w_{10}(x)^{\hat{n}_{10}} \exp[-w_{01}(x)\hat{\tau}_0 - w_{10}(x)\hat{\tau}_1], \quad (5.7)$$

where we have defined $p_0 \equiv e^{\Delta F_0}/(1+e^{\Delta F_0})$, $Y_0 \equiv \sum_{i=1}^N y_t^{(i)}|_{t=0}$, $\hat{\tau}_1 \equiv \sum_{i=1}^N \hat{\tau}_1^{(i)}$, $\hat{\tau}_0 = Nt - \hat{\tau}_1$, and $\hat{n}_{yy'} \equiv \sum_{i=1}^N \hat{n}_{yy'}^{(i)}$. With the marginal path weight $P(\mathbf{y}_0^t) = \int dx P(\mathbf{y}_0^t|x)P(x)$ the mutual information between the time history of the sensor array and the signal becomes

$$\mathcal{I}_N \equiv \left\langle \ln \frac{P(\mathbf{y}_0^t|x)}{P(\mathbf{y}_0^t)} \right\rangle = I[x:Y_0, \hat{n}_{01}, \hat{n}_{10}, \hat{\tau}_1], \quad (5.8)$$

where the second identity follows from the functional form of path weight (5.7), which is fully characterized by the variables $Y_0, \hat{\tau}_1, \hat{n}_{01}, \hat{n}_{10}$. Note for a sensor array with N sensors holds generally $0 \leq \hat{\tau}_1 \leq Nt$. We define the coarse-grained mutual information for the sensor array

$$\tilde{\mathcal{I}}_N \equiv I[x:Y_0, \hat{\tau}_1], \quad (5.9)$$

which generally satisfies $\tilde{\mathcal{I}}_N \leq \mathcal{I}_N$. Analogously to the derivation of the main result (5.6) we obtain for the sensor array

$$\Delta \mathcal{I}_N \equiv \lim_{t \rightarrow \infty} (\mathcal{I}_N - \tilde{\mathcal{I}}_N) = \frac{1}{2} \ln (4\alpha^2 - 4\alpha + 2), \quad (5.10)$$

i.e., the information gain from the number of jump events for the sensor array with N sensors equals the result for the single sensor case (5.6). A detailed proof of this formula can be found in Sec. 5.3, where Sec. 5.3.2 contains a simple proof, assuming a narrow-width Gaussian signal ($\mathcal{E}_x^2 \ll 1$), and Sec. 5.3.3 shows the (5.10) for arbitrarily distributed signals. A brief summary of the proof for weakly changing signals is shown in the next paragraph. We note that this result (5.10) agrees with Fig. 5.3, where we have observed the same information gain from the number of jump events for the single sensor ($N = 1$) and the sensor array with $N = 100$ sensors; see Figs. 5.3(a) and 5.3(c), where $\alpha = 0$ and $\Delta \mathcal{I}_N = \frac{1}{2} \ln 2$ in both cases, or see Figs. 5.3(b) and 5.3(d), where $\alpha = 1/2$ and $\Delta \mathcal{I}_N = 0$ in both cases.

We briefly outline the proof of the main result (5.10) for weak signals, where $\mathcal{E}_x^2 \ll 1$ holds. As we will show in Sec. 5.3.2 for weak Gaussian distributed signal (\mathcal{E}_x^2) mutual information can be approximated by (5.37)

$$\mathcal{I}_N \approx \frac{1}{2} \ln \left[1 + (2\alpha^2 - 2\alpha + 1)p_0(1-p_0)\mathcal{E}_x^2 N\omega_y t \right] \quad (5.11)$$

and coarse-grained mutual information by (5.38)

$$\tilde{\mathcal{I}}_N \approx \frac{1}{2} \ln \left[1 + \frac{1}{2}p_0(1-p_0)\mathcal{E}_x^2 N\omega_y t \right], \quad (5.12)$$

where we have defined $\omega_y \equiv w_{01}(0) + w_{10}(0)$. These approximations are fairly accurate for $\mathcal{E}_x = 0.3$ as can be confirmed with Figs. 5.3(b) and 5.3(d); see also Fig. 5.5(a) for $\alpha \neq 1/2$. From (5.11) and (5.12) one immediately obtains (5.10) in the limit $t \rightarrow \infty$.

5.3 Dispersion of random variables

In this section, we will introduce the method of generating function that can be used to calculate the dispersion of functionals of the sensor trajectory y_0^t . Note we use two different averages, where $\langle \dots \rangle_x$ is the average over all stochastic trajectories y_0^t at given signal value x and the total average is denoted by $\langle \dots \rangle \equiv \int dx P(x) \langle \dots \rangle_x$.

5.3.1 Generating function and first two moments

For a binary sensor system with states $y = 0, 1$ the master equation at given signal value x reads

$$\begin{aligned}\frac{\partial}{\partial t}P_t(0) &= P_t(1)w_{10}(x) - P_t(0)w_{01}(x), \\ \frac{\partial}{\partial t}P_t(1) &= P_t(0)w_{01}(x) - P_t(1)w_{10}(x),\end{aligned}\tag{5.13}$$

where $P_t(y)$ is the probability for $y_t = y$ at given signal x . Note that $P_t(1) = \langle y_t \rangle_x$. It will be convenient to write the master equation in matrix form

$$\frac{d}{dt}\mathbf{P}_t = \mathbf{L}\mathbf{P}_t\tag{5.14}$$

where

$$\begin{pmatrix} -w_{01}(x) & w_{10}(x) \\ w_{01}(x) & -w_{10}(x) \end{pmatrix} \quad \text{and} \quad \begin{pmatrix} P_t(0) \\ P_t(1) \end{pmatrix}.\tag{5.15}$$

We have dropped here and in the following for notationally convenience the dependence of the generator \mathbf{L} on the signal value x . The time dependent solution \mathbf{P}_t can then be written as a matrix exponential $\mathbf{P}_t = \exp(\mathbf{L}t)\mathbf{P}_0$, where \mathbf{P}_0 is the initial configuration of the sensor. Moreover, the path probability from (5.4) can then be written in the form

$$P(y_0^t|x) = P_0(y_0)(L_{01})^{\hat{n}_{10}}(L_{10})^{\hat{n}_{01}}e^{L_{00}\hat{\tau}_0+L_{11}\hat{\tau}_1} = P_0(y_0)\left[\prod_{\substack{y,y' \\ y \neq y'}}(L_{y'y})^{\hat{n}_{yy'}}\right]\left[\prod_y e^{L_{yy}\hat{\tau}_y}\right].\tag{5.16}$$

The second expression is also valid if the sensor would have more than two states, where the matrix \mathbf{L} would become larger than a 2×2 matrix. Our goal will be to calculate the moments of the functionals $\hat{n}_{yy'}$ and $\hat{\tau}_y$, as well as their joint correlations. We define the generating function as

$$\mathcal{G}(\mathbf{s}, t) \equiv \mathbf{V}^\top \exp[\mathcal{L}(\mathbf{s})t]\mathbf{P}_0,\tag{5.17}$$

where we have used $\mathbf{V}^\top \equiv (1, \dots, 1)$ and defined the elements of the modified generator $\mathcal{L}(\mathbf{s})_{yy'} \equiv L_{yy'}s_{y'y}$. The modified generator of the binary sensor system thus reads

$$\mathcal{L}(\mathbf{s}) = \begin{pmatrix} -w_{01}(x)s_{00} & w_{10}(x)s_{10} \\ w_{01}(x)s_{01} & -w_{10}(x)s_{11} \end{pmatrix}.\tag{5.18}$$

In this matrix notation $\mathbf{V}^\top \mathbf{P}_t = 1$ accounts for the normalization and $\mathbf{V}^\top \mathbf{L}$ is the conservation of probability. From now on we use “ $\mathbf{s} = 1$ ” as a shorthand form for “ $s_{yy'} = 1$ for all pair of states y, y' ”. For example, $\mathcal{L}(\mathbf{s})|_{\mathbf{s}=1} = \mathbf{L}$ holds, which allows us to identify $\mathcal{G}(\mathbf{s}, t)|_{\mathbf{s}=1} = \mathcal{G}(\mathbf{s}, 0) = 1$. Inserting the modified generator $\mathcal{L}(\mathbf{s})$ into the path weight (5.16) allows us to write the generating function as

$$\mathcal{G}(\mathbf{s}, t) = \int d[y_0^t]P_0(y_0)\left[\prod_{\substack{y,y' \\ y \neq y'}}(L_{y'y}s_{yy'})^{\hat{n}_{yy'}}\right]\left[\prod_y e^{L_{yy}\hat{\tau}_y s_{yy}}\right] \equiv \int d[y_0^t]\tilde{P}(y_0^t|x, \mathbf{s}),\tag{5.19}$$

where $\int d[y_0^t]$ is the path integral over all realizations y_0^t ; in the second step we have defined the modified path weight $\tilde{P}(y_0^t|x, \mathbf{s})$, which satisfies $\tilde{P}(y_0^t|x, \mathbf{s})|_{s=1} = P(y_0^t|x)$. From (5.16) and (5.19) it is straight forward to show that the first moments can be calculated with

$$\begin{aligned} \langle \hat{\tau} \rangle_x &= \frac{1}{L_{yy}} \frac{\partial \mathcal{G}(\mathbf{s}, t)}{\partial s_{yy}} \Big|_{s=1}, \\ \langle \hat{n}_{yy'} \rangle_x &= \frac{\partial \mathcal{G}(\mathbf{s}, t)}{\partial s_{yy'}} \Big|_{s=1} \end{aligned} \quad (5.20)$$

and the second moments with

$$\begin{aligned} \langle \hat{\tau}_y^2 \rangle_x &= \frac{1}{L_{yy}^2} \frac{\partial^2 \mathcal{G}(\mathbf{s}, t)}{\partial s_{yy}^2} \Big|_{s=1}, \\ \langle \hat{n}_{yy'} \hat{\tau}_{\tilde{y}} \rangle_x &= \frac{1}{L_{\tilde{y}\tilde{y}}} \frac{\partial^2 \mathcal{G}(\mathbf{s}, t)}{\partial s_{yy'} \partial s_{\tilde{y}\tilde{y}}} \Big|_{s=1}, \\ \langle \hat{n}_{yy'}^2 \rangle_x &= \frac{\partial^2 \mathcal{G}(\mathbf{s}, t)}{\partial s_{yy'}^2} \Big|_{s=1} + \frac{\partial \mathcal{G}(\mathbf{s}, t)}{\partial s_{yy'}} \Big|_{s=1}, \end{aligned} \quad (5.21)$$

where y, y', \tilde{y} are sensor states with $y \neq y'$. Note the last term in the third line of (5.21) corrects the negative term in $\partial_{s_{yy'}}(s_{yy'})^{\hat{n}_{yy'}} = (\hat{n}_{yy'}^2 - \hat{n}_{yy'}) (s_{yy'})^{\hat{n}_{yy'}-2}$; it appears whenever calculating second moments of the *same* jump variable $n_{yy'}$, for example, such a term does not appear for $y \neq y', \tilde{y} \neq \tilde{y}'$ and $y \neq \tilde{y}$, where

$$\langle \hat{n}_{yy'} \hat{n}_{\tilde{y}\tilde{y}'} \rangle = \frac{\partial^2 \mathcal{G}(\mathbf{s}, t)}{\partial s_{yy'} \partial s_{\tilde{y}\tilde{y}'}} \Big|_{s=1} \quad (5.22)$$

holds.

In the limit $t \gg 1/[w_{01} + w_{10}]$, the generating function is dominated by the maximum eigenvalue (maximum real part) of the modified generator (5.18), which is

$$\lambda_{\max}(\mathbf{s}) = -\frac{w_{01}(x)s_{00} + w_{10}(x)s_{11}}{2} + \sqrt{w_{01}(x)w_{10}(x)s_{01}s_{10} + \frac{[w_{01}(x)s_{00} - w_{10}(x)s_{11}]^2}{4}}. \quad (5.23)$$

In this limit, the first moments become

$$\boldsymbol{\mu}(x) \equiv \begin{pmatrix} \langle \hat{\tau}_1 \rangle_x \\ \langle \hat{n}_{\text{tot}} \rangle_x \end{pmatrix} = \begin{pmatrix} \langle \hat{\tau}_1 \rangle_x \\ \langle \hat{n}_{01} \rangle_x + \langle \hat{n}_{10} \rangle_x \end{pmatrix} \approx \frac{w_{01}(x)t}{w_{01}(x) + w_{10}(x)} \begin{pmatrix} 1 \\ 2w_{10}(x) \end{pmatrix} \quad (5.24)$$

Analogously, the signal-dependent covariance becomes

$$\begin{aligned} \boldsymbol{\Sigma}_{\mathbf{m}|x}(x) &\equiv \begin{pmatrix} \langle \hat{\tau}_1^2 \rangle_x - \langle \hat{\tau}_1 \rangle_x^2 & \langle \hat{\tau}_1 \hat{n}_{\text{tot}} \rangle_x - \langle \hat{\tau}_1 \rangle_x \langle \hat{n}_{\text{tot}} \rangle_x \\ \langle \hat{\tau}_1 \hat{n}_{\text{tot}} \rangle_x - \langle \hat{\tau}_1 \rangle_x \langle \hat{n}_{\text{tot}} \rangle_x & \langle \hat{n}_{\text{tot}}^2 \rangle_x - \langle \hat{n}_{\text{tot}} \rangle_x^2 \end{pmatrix} \\ &\approx \frac{2w_{01}(x)w_{10}(x)t}{[w_{01}(x) + w_{10}(x)]^3} \begin{pmatrix} 1 & w_{10}(x) - w_{01}(x) \\ w_{10}(x) - w_{01}(x) & 2[w_{01}(x)^2 + w_{10}(x)^2] \end{pmatrix}. \end{aligned} \quad (5.25)$$

5.3.2 Mutual information for weak Gaussian signals

For Gaussian distributed signals $P(x) = (2\pi\mathcal{E}_x^2)^{-1/2} \exp[-x^2/(2\mathcal{E}_x^2)]$, with small amplitude $\mathcal{E}_x^2 \ll 1$, the joint distribution of $\mathbf{z} \equiv (x, \mathbf{m})$, where $\mathbf{m} \equiv (\hat{\tau}_1, \hat{n}_{\text{tot}})$, is approximatively Gaussian as well. Denoting the covariance matrix by

$$\Sigma \equiv \langle \mathbf{z}\mathbf{z}^\top \rangle - \langle \mathbf{z} \rangle \langle \mathbf{z}^\top \rangle \equiv \begin{pmatrix} \mathcal{E}_x^2 & \mathbf{b}^\top \\ \mathbf{b} & \Sigma_{\mathbf{m}} \end{pmatrix}. \quad (5.26)$$

the mutual information becomes [36] (see also [190])

$$I[x:\mathbf{m}] = \frac{1}{2} \ln \frac{\mathcal{E}_x^2}{\mathcal{E}_{x|\mathbf{m}}^2} = \frac{1}{2} \ln \frac{\det(\Sigma_{\mathbf{m}})}{\det(\Sigma_{\mathbf{m}|x})}, \quad (5.27)$$

where $\mathcal{E}_{x|\mathbf{m}}^2$ and $\Sigma_{\mathbf{m}|x}$ are conditional covariances that can be obtained from the Schur complements of the covariance matrix (5.26), which read [189]

$$\begin{aligned} \mathcal{E}_{x|\mathbf{m}}^2 &= \mathcal{E}_x^2 - \mathbf{b}^\top \Sigma_{\mathbf{m}}^{-1} \mathbf{b}, \\ \Sigma_{\mathbf{m}|x} &= \Sigma_{\mathbf{m}} - \mathbf{b} \frac{1}{\mathcal{E}_x^2} \mathbf{b}^\top. \end{aligned} \quad (5.28)$$

Using (5.27) and the second line of (5.28), the mutual information becomes

$$\begin{aligned} I[x:\mathbf{m}] &= \frac{1}{2} \ln \left[\frac{\det(\Sigma_{\mathbf{m}|x} + \mathbf{b} \frac{1}{\mathcal{E}_x^2} \mathbf{b}^\top)}{\det(\Sigma_{\mathbf{m}})} \right] = \frac{1}{2} \ln \left[\det \left(\mathbf{1} + \Sigma_{\mathbf{m}|x}^{-1} \mathbf{b} \frac{1}{\mathcal{E}_x^2} \mathbf{b}^\top \right) \right] \\ &= \frac{1}{2} \ln \left(1 + \frac{\mathbf{b}^\top \Sigma_{\mathbf{m}|x}^{-1} \mathbf{b}}{\mathcal{E}_x^2} \right), \end{aligned} \quad (5.29)$$

where we have used in the last step the matrix determinant lemma, which states that the determinant of the identity matrix plus a dyadic product can be written as a scalar product.

We use (5.24) and (5.25) to calculate \mathbf{b} and $\Sigma_{\mathbf{m}|x}$, which are necessary for the mutual information (5.29). From the expressions of the first moments we obtain

$$\mathbf{b} \equiv \begin{pmatrix} \langle x\hat{\tau}_1 \rangle - \langle x \rangle \langle \hat{\tau}_1 \rangle \\ \langle x\hat{n}_{\text{tot}} \rangle - \langle x \rangle \langle \hat{n}_{\text{tot}} \rangle \end{pmatrix} = \begin{pmatrix} \langle x\hat{\tau}_1 \rangle \\ \langle x\hat{n}_{\text{tot}} \rangle \end{pmatrix} = \int dx P(x) x \boldsymbol{\mu}(x) \approx \mathcal{E}_x^2 \boldsymbol{\mu}'(0), \quad (5.30)$$

where we have used $\langle x \rangle = 0$ in the second step, Eq. (5.24) in the third step. The final approximation involves the derivative of the first moments with respect to the signal, i.e., $\boldsymbol{\mu}'(x) \equiv \partial_x \boldsymbol{\mu}(x)$. The approximation $\mathbf{b} \approx \mathcal{E}_x^2 \boldsymbol{\mu}'(0)$ is fairly accurate for weakly changing signals $\mathcal{E}_x^2 \ll 1$. Using the definition of the asymmetry parameter (5.2) and (5.24), the vector (5.30) becomes

$$\mathbf{b} \approx \frac{\mathcal{E}_x^2 w_{01}(0) w_{10}(0) t}{[w_{01}(0) + w_{10}(0)]^2} \begin{pmatrix} 1 \\ 2(1 - \alpha)w_{10}(0) - 2\alpha w_{10}(0) \end{pmatrix}. \quad (5.31)$$

Similarly, using (5.25) the conditional covariance reads

$$\Sigma_{\mathbf{m}|x} \equiv \int dx P(x) \Sigma_{\mathbf{m}|x}(x) \approx \Sigma_{\mathbf{m}|x}(0). \quad (5.32)$$

Inserting (5.31) and (5.32) into (5.29) yields

$$\begin{aligned}\mathcal{I} &\approx I[x:\hat{\tau}_1, \hat{n}_{\text{tot}}] = I[x:\mathbf{m}] = \frac{1}{2} \ln \left(1 + \frac{\mathbf{b}^\top \Sigma_{\mathbf{m}|x}(0)^{-1} \mathbf{b}}{\mathcal{E}_x^2} \right) \\ &= \frac{1}{2} \ln \left[1 + (2\alpha^2 - 2\alpha + 1) \frac{\mathcal{E}_x^2 w_{01}(0) w_{10}(0) t}{w_{01}(0) + w_{10}(0)} \right].\end{aligned}\quad (5.33)$$

Similarly for coarse-grained mutual information, where $\mathbf{m} = \hat{\tau}_1$, one obtains from first component of the upper-right component of (5.25) and the first component of (5.31)

$$\tilde{\mathcal{I}} = I[x:\hat{\tau}_1] \approx \frac{1}{2} \ln \left[1 + \frac{(\mathbf{b})_1^2}{[\Sigma_{\mathbf{m}|x}]_{11} \mathcal{E}_x^2} \right] = \frac{1}{2} \ln \left[1 + \frac{1}{2} \frac{\mathcal{E}_x^2 w_{01}(0) w_{10}(0) t}{w_{01}(0) + w_{10}(0)} \right].\quad (5.34)$$

Calculating the difference $\mathcal{I} - \tilde{\mathcal{I}}$ with Eqs. (5.33) and (5.34) yields immediately to the main result (5.6) for the long time limit ($t \rightarrow \infty$). This calculation constitutes the proof of the main result (5.6) for narrow-width Gaussian distributed signals. We note that (5.33) and (5.34) are fairly accurate even for finite time t . Before we turn to arbitrarily distributed signal we make a short comment on the effect of multiple sensors.

The calculations for N independent sensors are quite similar. A more detailed discussion can be found in [190]. We use subscript N to differentiate the deterministic quantities for the sensor array with N sensors from the single sensor case. First, the measurement becomes $\mathbf{m} = (\hat{\tau}_1, \hat{n}_{01} + \hat{n}_{10})$, where $\hat{\tau}_1 \equiv \sum_{i=1}^N \hat{\tau}_1$ and $\hat{\tau}_{yy'} = \sum_{i=1}^N \hat{n}_{yy'}$; see also (5.7) from Sec. 5.2.2. Second, for N sensors the mean becomes

$$\boldsymbol{\mu}_N(x) \equiv \sum_{i=1}^N \left(\begin{array}{c} \langle \hat{\tau}_1^{(i)} \rangle_x \\ \langle \hat{n}_{01}^{(i)} \rangle_x + \langle \hat{n}_{10}^{(i)} \rangle_x \end{array} \right) = N \boldsymbol{\mu}(x),\quad (5.35)$$

where we used $\langle \hat{\tau}_1^{(i)} \rangle_x = \langle \hat{\tau}_1^{(1)} \rangle_x$ and $\langle \hat{n}_{yy'}^{(i)} \rangle_x = \langle \hat{n}_{yy'}^{(1)} \rangle_x$ as well as the first moments of a single sensor (5.24). Therefore, $\mathbf{b}_N = N \mathbf{b}$ holds. Analogously, the signal-dependent covariance matrix

$$\Sigma_{\mathbf{m}|x,N}(x) = \langle \mathbf{m} \mathbf{m}^\top \rangle_x - \langle \mathbf{m} \rangle_x \langle \mathbf{m} \rangle_x^\top = N \Sigma_{\mathbf{m}|x}(x).\quad (5.36)$$

is proportional to the number of receptors. Substituting $\mathbf{b} \rightarrow \mathbf{b}_N$ and $\Sigma_{\mathbf{m}|x}(x) \rightarrow \Sigma_{\mathbf{m}|x,N}(x)$ in (5.33) and (5.34) yields

$$\mathcal{I}_N \approx I[x:\hat{\tau}_1, \hat{n}_{01} + \hat{n}_{10}] \approx \frac{1}{2} \ln \left[1 + (2\alpha^2 - 2\alpha + 1) \frac{N \mathcal{E}_x^2 w_{01}(0) w_{10}(0) t}{w_{01}(0) + w_{10}(0)} \right]\quad (5.37)$$

and

$$\tilde{\mathcal{I}}_N \approx I[x:\hat{\tau}_1] \approx \frac{1}{2} \ln \left[1 + \frac{1}{2} \frac{N \mathcal{E}_x^2 w_{01}(0) w_{10}(0) t}{w_{01}(0) + w_{10}(0)} \right],\quad (5.38)$$

which are equivalent to Eqs. (5.11) and (5.12), respectively. Moreover, the difference $\mathcal{I}_N - \tilde{\mathcal{I}}_N$ approaches $\frac{1}{2} \ln(4\alpha^2 - 4\alpha + 1)$ in the long time limit, which proofs (5.10) for N independent sensors measuring a weakly fluctuating signal.

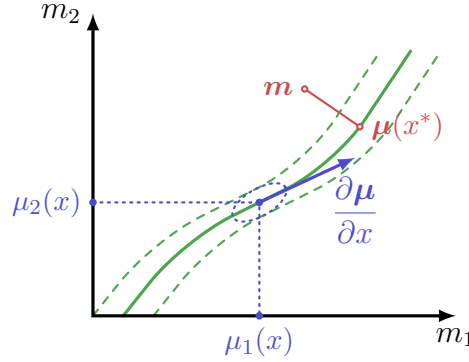


Figure 5.4| Illustration of saddle-point approximation in $d = 2$ dimensions, where $\mathbf{m} = (m_1, m_2)$ and $\boldsymbol{\mu}(x) = (\mu_1(x), \mu_2(x))$. The solid green line indicates all possible points, where $\mathbf{m} = \boldsymbol{\mu}(x)$ is satisfied ($x \in \mathbb{R}$). The dashed green line indicates the width of the marginal distribution $P(\mathbf{m})$, which approach the solid line for $t \rightarrow \infty$. The closest point to \mathbf{m} on the solid green line is $\boldsymbol{\mu}(x^*)$, where $x^* = x^*(\mathbf{m})$ is a function of \mathbf{m} ; see open red points, which are connected via a solid red line. The blue dotted ellipse illustrates the width of the conditional distribution $P(\mathbf{m}|x)$ for a specific signal value x .

5.3.3 Long time limit for arbitrary signal distribution

In this section we show that the main result still holds for if the signal x is broadly distributed with probability $P(x)$. Thereby, $P(x)$ may not be a Gaussian distribution, as it has been used in the previous subsection. We derive an approximation \mathcal{I}^∞ for the mutual information \mathcal{I} from (5.3), which becomes exact in the long time limit $t \rightarrow \infty$ and can be used also for strong signals (e.g., $\mathcal{E}_x^2 > 1$) and/or non-Gaussian distributed signals. We note all approximations that involve “ \approx ” become exact in the limit $t \rightarrow \infty$. The following proof is based on a saddle-point approximation.

We denote the measurement by $\mathbf{m} \equiv (m_1, \dots, m_d)$. In $d = 2$ dimensions we identify $m_1 = \hat{\tau}_1$ and $m_2 = \hat{n}_{\text{tot}}$, where the mean $\langle \mathbf{m} \rangle_x = \boldsymbol{\mu}(x)$ is given in (5.24). Moreover, with the covariance (5.25) the conditional probability distribution reads

$$P(\mathbf{m}|x) = \frac{e^{l(\mathbf{m}|x)}}{\sqrt{(2\pi)^d \det[\boldsymbol{\Sigma}_{\mathbf{m}|x}(x)]}}, \quad (5.39)$$

where

$$l(\mathbf{m}|x) = -\frac{1}{2}[\mathbf{m} - \boldsymbol{\mu}(x)]^\top \boldsymbol{\Sigma}_{\mathbf{m}|x}(x)^{-1}[\mathbf{m} - \boldsymbol{\mu}(x)]. \quad (5.40)$$

In the long time limit the covariance matrix $\boldsymbol{\Sigma}_{\mathbf{m}|x}$ and the conditional mean $\boldsymbol{\mu}(x)$ grow linearly in time, i.e., $\boldsymbol{\mu}(x), \boldsymbol{\Sigma}_{\mathbf{m}|x} \sim t$, which implies that the probability weight becomes sharply distributed around $\mathbf{m} \approx \boldsymbol{\mu}(x)$, where $x \in \mathbb{R}$.

In the following we use saddle-point approximation to determine the marginal distribution $P(\mathbf{m})$ for the long time limit, as schematically shown in Fig. 5.4. The approximation will become exact in the limit $t \rightarrow \infty$. The green solid curve in Fig. 5.4 corresponds to all points $x \in \mathbb{R}$, where $\mathbf{m} = \boldsymbol{\mu}(x)$. The dotted blue ellipse corresponds to width of the conditional distribution (5.39) for a single signal value x around $\boldsymbol{\mu}(x) = (\mu_1(x), \mu_2(x))^\top$.

Since mean and conditional covariance increase both linearly in time, one can identify $\mathbf{m} - \boldsymbol{\mu}(x) \sim \sqrt{t}$ and $\partial_x \boldsymbol{\mu}(x) \sim t$, which with (5.40) yields

$$\frac{\partial^2}{\partial x^2} l(\mathbf{m}|x) \approx -\frac{\partial \boldsymbol{\mu}(x)^\top}{\partial x} \boldsymbol{\Sigma}_{\mathbf{m}|x}(x)^{-1} \frac{\partial \boldsymbol{\mu}(x)}{\partial x}. \quad (5.41)$$

This expression (5.41) determines the curvature of $l(\mathbf{m}|x)$ in the limit $t \rightarrow \infty$. For a specific point \mathbf{m} we obtain the marginal probability distribution using Eqs. (5.39) and (5.41) with saddle-point approximation

$$P(\mathbf{m}) \equiv \int dx P(\mathbf{m}|x) P(x) \approx \frac{P(x^*(\mathbf{m})) e^{l(\mathbf{m}|x^*)}}{\sqrt{(2\pi)^{d-1} \det[\boldsymbol{\Sigma}_{\mathbf{m}|x}(x^*)] \frac{\partial \boldsymbol{\mu}(x^*)^\top}{\partial x} \boldsymbol{\Sigma}_{\mathbf{m}|x}(x^*)^{-1} \frac{\partial \boldsymbol{\mu}(x^*)}{\partial x}}}, \quad (5.42)$$

where $x^* = x(\mathbf{m})$ maximizes (5.40) for a given \mathbf{m} , which are both geometrically indicated as two points connected with a straight red solid line in Fig. 5.4.

The mutual information between signal x and measurement \mathbf{m}

$$I[x:\mathbf{m}] = \int d\mathbf{m} \int dx P(x) P(\mathbf{m}|x) \ln \frac{P(\mathbf{m}|x)}{P(\mathbf{m})} \quad (5.43)$$

can be calculated with (5.39) and (5.42) and the relation

$$l(\mathbf{m}|x) - l(\mathbf{m}|x^*) = \frac{1}{2} \frac{\partial^2 l(\mathbf{m}|x)}{\partial x^2} (x - x^*)^2 + \mathcal{O}(x - x^*)^3, \quad (5.44)$$

which becomes $-1/2 = \ln \sqrt{1/e}$ after averaging over (x, \mathbf{m}) . Finally, from $x = x^*$ follows the long time limit approximation

$$I[x:\mathbf{m}] \approx \int dx P(x) \ln \left[\frac{1}{P(x)} \sqrt{\frac{\frac{\partial \boldsymbol{\mu}(x)^\top}{\partial x} \boldsymbol{\Sigma}_{\mathbf{m}|x}(x)^{-1} \frac{\partial \boldsymbol{\mu}(x)}{\partial x}}{2\pi e}} \right] \equiv \mathcal{I}^\infty \quad (5.45)$$

We note that this approximation (5.45) becomes exact in the long time limit ($t \rightarrow \infty$). In the following two paragraphs we illustrate the validity of this approximation.

First, we consider a Gaussian distributed signal $P(x) = (2\pi\mathcal{E}_x^2)^{-1/2} \exp[-x^2/(2\mathcal{E}_x^2)]$. In Fig. 5.5 we confirm that the approximation \mathcal{I}^∞ (5.45) approaches the exact value of the mutual information \mathcal{I} in the long time limit. Even for strong signals ($\mathcal{E}_x = 2$) the approximation \mathcal{I}^∞ from Eq. (5.45) can be used to calculate the mutual information, whereas the weak signal approximation (5.11) fails at any time. For narrow-width Gaussian signals the approximation (5.11) works even for “finite time”. Note that we used the same parameters in Figs. 5.3(a) and 5.5(a).

As second example, we use a uniformly distributed signal, where $P(x)$ is constant in a interval $x_{\min} \leq x \leq x_{\max}$. We compare in Fig. 5.6 the exact mutual information \mathcal{I} (blue open circles) and the approximation \mathcal{I}^∞ (solid red line) for $x_{\min} = -1$ and $x_{\max} = 1$. We confirm \mathcal{I}^∞ approaches \mathcal{I} in the long time limit ($t \rightarrow \infty$). Moreover, we note that the convergence to the exact solution is more slowly than for Gaussian signal with the same width.

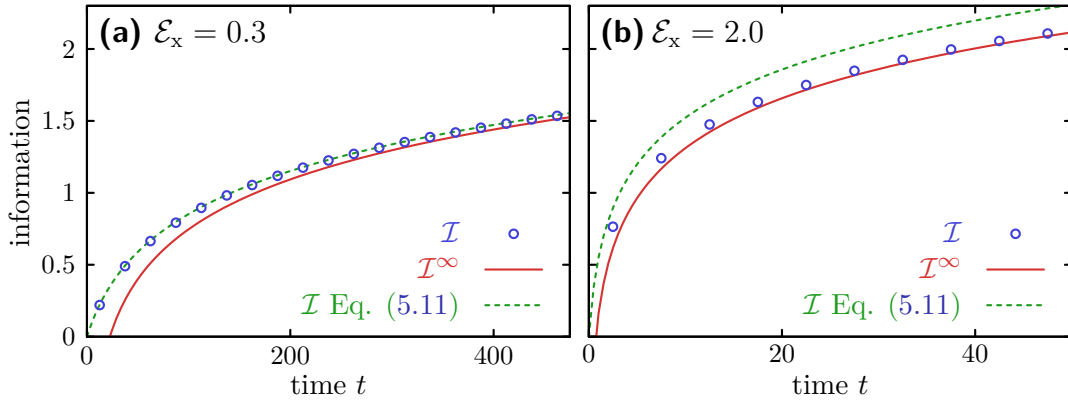


Figure 5.5| The exact mutual information (blue open circles) is compared with both approximations \mathcal{I}^∞ (solid red line) and the approximation from (5.11) (dashed green line), where the latter assumes a weak signal $\mathcal{E}_x^2 \ll 1$. In both figures the approximation \mathcal{I}^∞ approaches the exact result in the long time limit ($t \rightarrow \infty$). (a) The weak signal approximation from (5.11) is fairly accurate even for finite time. (b) For strong signal $\mathcal{E}_x > 1$ the approximation from (5.11) fails at any time, approximation \mathcal{I}^∞ becomes exact in the long time limit ($t \rightarrow \infty$). Parameters: Rates $w_{01} = e^x, w_{10}$; asymmetry parameter $\alpha = 0$; number of sensors $N = 1$. (a) Signal standard deviation $\mathcal{E}_x = 0.3$ [same parameters as in Fig. 5.3(a)]. (b) $\mathcal{E}_x = 2$.

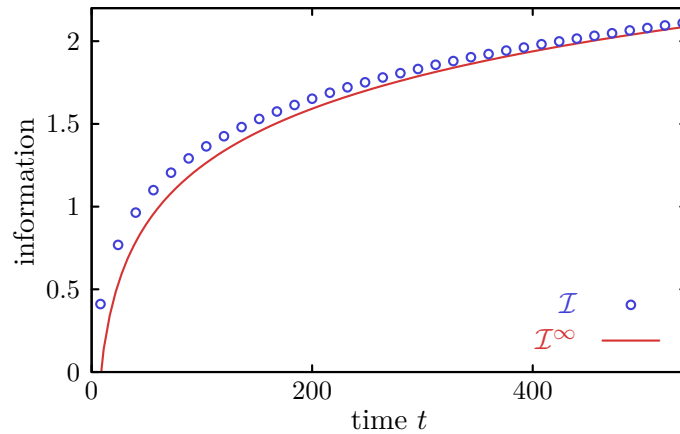


Figure 5.6| Exact mutual information \mathcal{I} (blue open circles) versus long time limit approximation \mathcal{I}^∞ (solid red line) for non-Gaussian signal. The signal is uniformly distributed within the interval $-1 \leq x \leq 1$, i.e., $P(x) = 1/2$ for $|x| \leq 1$ and $P(x) = 0$ for $|x| > 1$. Parameters: Rates $w_{01} = e^x, w_{10} = 1$; asymmetry parameter $\alpha = 0$.

With approximation (5.45), we obtain the long time limit approximation for the coarse-grained mutual information $\tilde{\mathcal{I}}$ as defined in (5.5) in a quite similar way. First, we consider $d = 1$, where $m_1 \equiv \hat{\tau}_1$, which has a signal-dependent mean $\langle m_1 \rangle_x = \mu_1(x)$ and the conditional variance $\langle m_1^2 \rangle_x - \langle m_1 \rangle_x^2 = [\Sigma_{m|x}(x)]_{11}$. Using (5.45), the approximation for coarse-grained mutual information becomes

$$I[x:m] \approx \int dx P(x) \ln \left[\frac{1}{P(x)} \sqrt{\frac{\left| \frac{\partial \mu_1(x)}{\partial x} \right|^2}{2\pi e [\Sigma_{m|x}(x)]_{11}}} \right] \equiv \tilde{\mathcal{I}}^\infty, \quad (5.46)$$

which becomes exact in the limit $t \rightarrow \infty$. We note that from (5.25) follows $[\Sigma_{m|x}(x)]_{11} = 2w_{01}(x)w_{10}(x)t/[w_{01}(x) + w_{10}(x)]^3$.

From the difference between (5.45) and (5.46) we obtain the information gain from the number of jump events

$$\Delta \mathcal{I}^\infty \equiv \lim_{t \rightarrow \infty} (\mathcal{I}^\infty - \tilde{\mathcal{I}}^\infty) = \lim_{t \rightarrow \infty} \int dx P(x) \frac{1}{2} \ln \left[\frac{[\Sigma_{m|x}(x)]_{11} \frac{\partial \mu(x)}{\partial x}^\top \Sigma_{m|x}(x)^{-1} \frac{\partial \mu(x)}{\partial x}}{\left| \frac{\partial \mu_1(x)}{\partial x} \right|^2} \right]. \quad (5.47)$$

The same calculation as for (5.31), where we have used the definition of the asymmetry parameter (5.2) and (5.24), yields

$$\frac{\partial \boldsymbol{\mu}}{\partial x} = \frac{\partial}{\partial x} \begin{pmatrix} \mu_1(x) \\ \mu_2(x) \end{pmatrix} = \frac{\partial}{\partial x} \begin{pmatrix} \langle \hat{\tau}_1 \rangle_x \\ \langle \hat{n}_{\text{tot}} \rangle_x \end{pmatrix} \approx \frac{w_{01}(x)w_{10}(x)t}{[w_{01}(x) + w_{10}(x)]^2} \begin{pmatrix} 1 \\ 2(1 - \alpha)w_{10}(x) - 2\alpha w_{01}(x) \end{pmatrix}, \quad (5.48)$$

which with the signal-dependent covariance matrix (5.25) finally results in

$$\Delta \mathcal{I}^\infty = \int dx P(x) \frac{1}{2} \ln (4\alpha^2 - 4\alpha + 2). \quad (5.49)$$

This proves our main result (5.6) since the approximations for the mutual information $\mathcal{I} \approx \mathcal{I}^\infty$ (5.45) and the coarse-grained mutual information $\tilde{\mathcal{I}} \approx \tilde{\mathcal{I}}^\infty$ (5.46) become exact in the limit $t \rightarrow \infty$.

This result for a single sensor can easily be adopted to a sensor array with N sensors. First, the long time limit implies $\hat{n}_{01} \approx \hat{n}_{10}$. Second, the mean and covariance of $(\hat{\tau}, \hat{n}_{\text{tot}})$, which appears in the path weight (5.7), where $\hat{\tau}_1 = \sum_{i=1}^N \hat{\tau}_1^{(i)}$ and $\hat{n}_{\text{tot}} \equiv \sum_{i=1}^N [\hat{n}_{01}^{(i)} + \hat{n}_{10}^{(i)}]$, is proportional to the number of sensors. Since the replacement $\boldsymbol{\mu}(x) \rightarrow N\boldsymbol{\mu}(x)$ and $\Sigma_{m|x}(x) \rightarrow N\Sigma_{m|x}(x)$ does not alter the expression (5.47), we obtain the same gain of information from the number of jump events for the single sensor case and the sensor array with N sensors.

5.3.4 Method from References [198, 203, 204] for joint dispersion

In this section we derive a method that can be used to calculate the dispersion of random variables $(\hat{\tau}_y$ and $\hat{n}_{yy'})$ for networks with more than two states, where it might be difficult to determine generating function $\mathcal{G}(\mathbf{s}, t)$ or the maximum eigenvalue of the modified

generator $\mathcal{L}(\mathbf{s})$. Thereby, we generalize the methods from Refs. [198, 203, 204] to the joint dispersion of jump-related variables $\hat{n}_{yy'}$ and persistence time $\hat{\tau}_y$. We emphasize, the following method does not require either the generating function $\mathcal{G}(\mathbf{s}, t)$ or the eigenvalues of $\mathcal{L}(\mathbf{s})$, which will be replaced step-by-step.

The modified generator $\mathcal{L}(\mathbf{s})$ has one maximum eigenvalue (with maximum real part), which we denote by $\lambda_{\max}(\mathbf{s})$, where $\lambda_{\max}(\mathbf{s})|_{\mathbf{s}=1} = 0$. In the long time limit ($t \rightarrow \infty$), the generating function is dominated by the contribution of the maximum eigenvalue

$$\mathcal{G}(\mathbf{s}, t) = \mathcal{V}^\top e^{\mathcal{L}(\mathbf{s})t} \mathbf{P}_0 \approx \Phi(\mathbf{s}) e^{\lambda_{\max}(\mathbf{s})t}, \quad (5.50)$$

where we have identified the term $\Phi(\mathbf{s})$, which must satisfy $\Phi(\mathbf{s})|_{\mathbf{s}=1} = 1$. Using the general properties $\Phi(\mathbf{s})|_{\mathbf{s}=1}$ and $\lambda_{\max}(\mathbf{s})|_{\mathbf{s}=1} = 0$ simplifies the calculations remarkably. In the following we use $a \equiv s_{yy'}$ and $b \equiv s_{\tilde{y}\tilde{y}'}$, where y, y', \tilde{y} and \tilde{y}' are states of the system. Using (5.50) it is then straight forward to show that

$$\left. \frac{\partial \mathcal{G}(\mathbf{s}, t)}{\partial a} \right|_{\mathbf{s}=1} = \left. \frac{\partial \lambda_{\max}}{\partial a} \right|_{\mathbf{s}=1} t + \left. \frac{\partial \phi(\mathbf{s})}{\partial a} \right|_{\mathbf{s}=1} \approx \left. \frac{\partial \lambda_{\max}}{\partial a} \right|_{\mathbf{s}=1} t \quad (5.51)$$

holds in the long time limit. Similarly, one obtains

$$\left. \frac{\partial^2 \mathcal{G}(\mathbf{s}, t)}{\partial a \partial b} \right|_{\mathbf{s}=1} - \left. \frac{\partial \mathcal{G}(\mathbf{s}, t)}{\partial a} \right|_{\mathbf{s}=1} \left. \frac{\partial \mathcal{G}(\mathbf{s}, t)}{\partial b} \right|_{\mathbf{s}=1} \approx \left. \frac{\partial^2 \lambda_{\max}}{\partial a \partial b} \right|_{\mathbf{s}=1} t. \quad (5.52)$$

In these two steps we have mapped derivatives of the generating function to derivatives of the maximum eigenvalue. Hence, the derivatives of the generating function can be replaced by derivatives of the maximum eigenvalue (5.51) and (5.52).

Denoting the i -th eigenvalue by $\lambda_i(\mathbf{s})$, the characteristic polynomial of the modified generator $\mathcal{L}(\mathbf{s})$ reads

$$\chi(\lambda) \equiv \det[\mathcal{L}(\mathbf{s}) - \lambda \mathbf{1}] = \prod_i [\lambda_i(\mathbf{s}) - \lambda] \equiv C_0(\mathbf{s}) - C_1(\mathbf{s})\lambda + C_2(\mathbf{s})\lambda^2 + O(\lambda)^3, \quad (5.53)$$

where we have defined the coefficient $C_i(\mathbf{s})$ in the second step. In the following paragraph we will demonstrate that these coefficients can be used to calculate [190]

$$\frac{\partial \lambda_{\max}(\mathbf{s})}{\partial a} = \left[\frac{1}{C_1} \frac{\partial C_0}{\partial a} \right]_{\mathbf{s}=1} \quad (5.54)$$

and [190]

$$\frac{\partial^2 \lambda_{\max}(\mathbf{s})}{\partial a \partial b} = \frac{1}{C_1} \frac{\partial^2 C_0}{\partial a \partial b} \Big|_{\mathbf{s}=1} + \frac{2C_2}{C_1^3} \frac{\partial C_0}{\partial a} \frac{\partial C_0}{\partial b} \Big|_{\mathbf{s}=1} - \frac{1}{C_1^2} \left[\frac{\partial C_0}{\partial a} \frac{\partial C_1}{\partial b} + \frac{\partial C_0}{\partial b} \frac{\partial C_1}{\partial a} \right]_{\mathbf{s}=1}. \quad (5.55)$$

The next paragraph will demonstrate that Eqs. (5.54) and (5.55) indeed hold. We note the joint dispersion of jump related variables and persistence can be calculated with formulas (5.20) and (5.21), whereas thanks to Eqs. (5.51)-(5.55) the generating function and the eigenvalues of the modified generator do not need to be known for the long time limit.

Note that calculating the dispersion from the characteristic polynomial of the modified is generally much simpler than calculating the dispersion from the eigenvalues of the modified generator, since zeros of a polynomial are generally harder to determine than just evaluating the polynomial at specific points. An example, for applying this method to the two level sensor system from Fig. 5.1 is shown in Appendix D of Ref. [190] [see equations (D9)-(D12) therein].

In this paragraph we prove (5.54) and (5.55). From the definition of the characteristic polynomial from (5.53) we can identify the coefficients by

$$C_0(\mathbf{s}) = \prod_i \lambda_i(\mathbf{s}), \quad C_1(\mathbf{s}) = \sum_i \prod_{j \neq i} \lambda_j(\mathbf{s}), \quad C_2(\mathbf{s}) = \sum_{i < j} \prod_{k \neq i, j} \lambda_k(\mathbf{s}), \quad (5.56)$$

where λ_i is the i -th eigenvalue of the modified generator $\mathcal{L}(\mathbf{s})$. Setting $\mathbf{s} = 0$ yields $\lambda_i(\mathbf{s})|_{\mathbf{s}=1} \neq 0$ for $i \neq \max$ and $\lambda_{\max}(\mathbf{s})|_{\mathbf{s}=1} = 0$. Therefore, from (5.56) follows

$$C_0(\mathbf{s})|_{\mathbf{s}=1} = 0, \quad C_1(\mathbf{s})|_{\mathbf{s}=1} = \prod_{i \neq \max} \lambda_i(\mathbf{s}) \Big|_{\mathbf{s}=1}, \quad C_2(\mathbf{s})|_{\mathbf{s}=1} = \sum_{i \neq \max} \prod_{j \neq i, \max} \lambda_j(\mathbf{s}). \quad (5.57)$$

The first derivative at of the first two coefficient in (5.56) with respect to $a = s_{yy'}$ become

$$\frac{\partial C_0(\mathbf{s})}{\partial a} = \sum_i \frac{\partial \lambda_i(\mathbf{s})}{\partial a} \prod_{j \neq i} \lambda_j(\mathbf{s}) \quad \text{and} \quad \frac{\partial C_1(\mathbf{s})}{\partial a} = \sum_i \sum_{j \neq i} \frac{\partial \lambda_j(\mathbf{s})}{\partial a} \prod_{k \neq i, j} \lambda_k(\mathbf{s}). \quad (5.58)$$

For $\mathbf{s} = 1$ the first derivatives read

$$\begin{aligned} \frac{\partial C_0(\mathbf{s})}{\partial a} \Big|_{\mathbf{s}=1} &= \frac{\partial \lambda_{\max}(\mathbf{s})}{\partial a} \prod_{j \neq \max} \lambda_j(\mathbf{s}) \Big|_{\mathbf{s}=1} = \frac{\partial \lambda_{\max}(\mathbf{s})}{\partial a} C_1(\mathbf{s}) \Big|_{\mathbf{s}=1} \\ \frac{\partial C_1(\mathbf{s})}{\partial a} \Big|_{\mathbf{s}=1} &= \sum_{i \neq \max} \frac{\partial \lambda_{\max}(\mathbf{s})}{\partial a} \prod_{k \neq \max, i} \lambda_k(\mathbf{s}) \Big|_{\mathbf{s}=1} + \sum_{j \neq \max} \frac{\partial \lambda_j(\mathbf{s})}{\partial a} \prod_{k \neq j, \max} \lambda_k(\mathbf{s}) \Big|_{\mathbf{s}=1} \\ &= \frac{\partial \lambda_{\max}(\mathbf{s})}{\partial a} C_2(\mathbf{s}) \Big|_{\mathbf{s}=1} + \sum_{i \neq \max} \frac{\partial \lambda_i(\mathbf{s})}{\partial a} \prod_{j \neq i, \max} \lambda_j(\mathbf{s}) \Big|_{\mathbf{s}=1} \end{aligned} \quad (5.59)$$

where we have used that the maximum eigenvalue vanishes at $\mathbf{s} = 1$; in the second step of the first line we have inserted second expression from (5.57); from the second to the third line we have used the third relation from (5.57) and changed summation indices of the remaining sum. The first line in (5.59) immediately proofs (5.54). Taking the derivative of the first expression of (5.58) with respect of b yields

$$\frac{\partial^2 C_0(\mathbf{s})}{\partial a \partial b} = \sum_i \frac{\partial^2 \lambda_i(\mathbf{s})}{\partial a \partial b} \prod_{j \neq i} \lambda_j(\mathbf{s}) + \sum_{i \neq j} \frac{\partial \lambda_i(\mathbf{s})}{\partial a} \frac{\partial \lambda_j(\mathbf{s})}{\partial b} \prod_{k \neq i, j} \lambda_k(\mathbf{s}). \quad (5.60)$$

With a similar calculations, as performed above, this expression for $\mathbf{s} = 1$ becomes

$$\begin{aligned} \frac{\partial^2 C_0(\mathbf{s})}{\partial a \partial b} \Big|_{\mathbf{s}=1} &= \frac{\partial^2 \lambda_{\max}(\mathbf{s})}{\partial a \partial b} C_1(\mathbf{s}) \Big|_{b_{\mathbf{s}}=1} + \frac{\partial \lambda_{\max}(\mathbf{s})}{\partial a} \sum_{i \neq \max} \frac{\partial \lambda_i(\mathbf{s})}{\partial b} \prod_{j \neq i, \max} \lambda_j(\mathbf{s}) \Big|_{\mathbf{s}=1} \\ &+ \frac{\partial \lambda_{\max}(\mathbf{s})}{\partial b} \sum_{i \neq \max} \frac{\partial \lambda_i(\mathbf{s})}{\partial a} \prod_{j \neq i, \max} \lambda_j(\mathbf{s}) \Big|_{\mathbf{s}=1}. \end{aligned} \quad (5.61)$$

Resolving Eq. (5.61) for $\partial^2 \lambda_{\max} / (\partial a \partial b)|_{\mathbf{s}=1}$ and inserting Eqs. (5.57) and (5.59) yields finally (5.55).

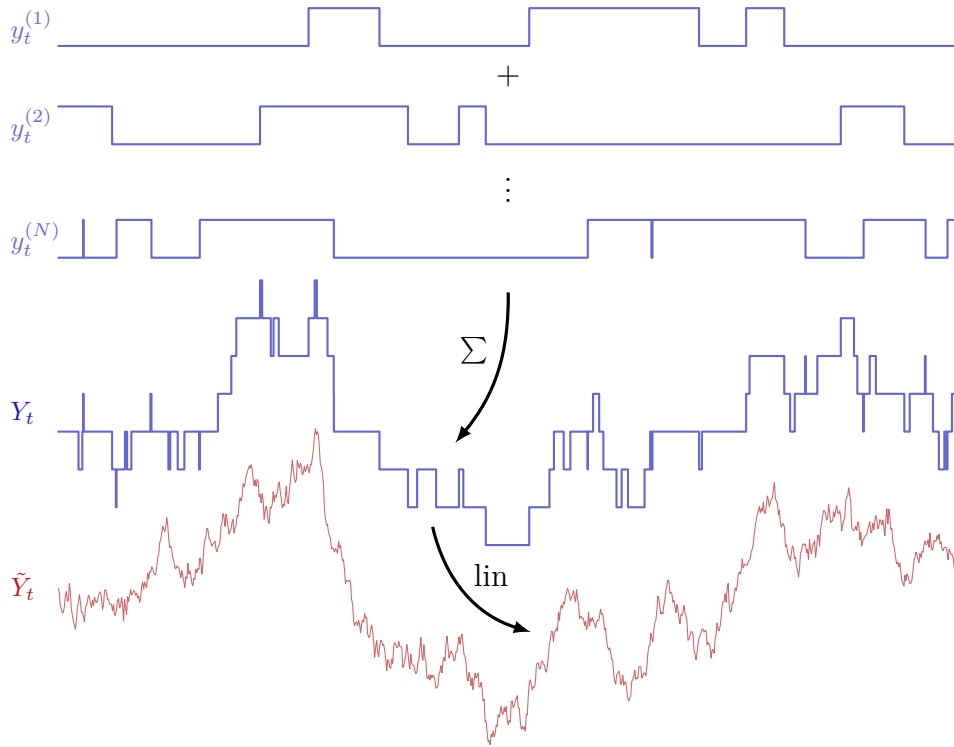


Figure 5.7| Two levels of coarse graining. First, $\mathbf{y}_t \equiv (y_t^{(1)}, y_t^{(2)}, \dots, y_t^{(N)}) \rightarrow Y_t \equiv \sum_{i=1}^N y_t^{(i)}$. Second, linear noise approximation $Y_t \rightarrow \tilde{Y}_t$.

5.4 Continuous approximation schemes

Chemical networks, for instance, the signaling networks in individual cells, typically contain about $N = 10^4 \gg 1$ signaling molecules. For such networks it is useful not to try to resolve each individual component at the molecular level, but rather to use continuous approximation schemes as, for example, a deterministic rate equations or a stochastic Brownian motion [33, 34, 200–202, 205, 206]. For our inference problem the approximation with stochastic Brownian motion is particularly interesting [33, 34, 200–202], since it considers fluctuations arising from the discreteness of the system. In Fig. 5.7 we show schematically the approximation scheme for our binary sensor problem. Importantly, we will show that such approximation schemes lose information compared with the original system dynamics, which is precisely given by Eq. (5.6).

Before using this approximation scheme one has to consider the total sensor activity $Y_t \equiv \sum_{i=1}^N y_t^{(i)}$ of the sensor array (see first step in Fig. 5.7). Since each sensor is measuring the signal independently one can verify that $\mathcal{I}_N = I[x:Y_0^t]$, where $Y_0^t \equiv \{Y_{t'}\}_{0 \leq t' \leq t}$ denotes the time history of the total sensor activity $Y_{t'}$ within the time interval $0 \leq t' \leq t$, i.e., the path weight (5.7) is a functional of just Y_0^t and x . The linear noise approximation \tilde{Y}_t is now used to approximate the total activity ($\tilde{Y}_t \simeq Y_t$) with a Langevin equation. The approximation, as illustrated in Fig. 5.7, is usually quite accurate for $N \gtrsim 10$ and weak changes of the signal x ($\mathcal{E}_x^2 \ll 1$). A systematical derivation of the linear noise approximation for the cellular two-component network involving a series expansion of the

corresponding master equation is shown in Appendix 4.A. Here we can use a simpler approach, where we identify three core properties of the sensor dynamics that determine the dynamics of \tilde{Y}_t . First, the correct mean behavior requires for the long time limit $\langle \tilde{Y}_\infty \rangle_x \approx \langle Y_\infty \rangle_x = Nw_{01}(x)/[w_{01}(x) + w_{10}(x)]$. A first order Taylor expansion of $\langle Y_\infty \rangle_x$ with respect to x yields,

$$\langle \tilde{Y}_\infty \rangle_x = Np_0 + Np_0(1 - p_0)x, \quad (5.62)$$

where we have used $p_0 = w_{01}(0)/[w_{01}(0) + w_{10}(0)]$ and the local detailed balance relation (5.1). Second, the mean $\langle Y_t \rangle_x$ decays exponentially to $\langle Y_\infty \rangle_x$ with rate $\omega_y \equiv w_{01}(0) + w_{10}(0)$, which characterizes the relaxation rate of the sensor. Third, in the steady state the variance of the total sensor activity reads $\langle Y_\infty^2 \rangle_x - \langle Y_\infty \rangle_x^2 \approx Np_0(1 - p_0)$. Adopting this three core properties of the original system dynamic results in the linear Langevin equation

$$\dot{\tilde{Y}}_t = -\omega_y(\tilde{Y}_t - \langle \tilde{Y}_\infty \rangle_x) + \xi_t, \quad (5.63)$$

where ξ_t is standard white noise with zero mean $\langle \xi_t \rangle_x = 0$ and covariance $\langle \xi_t \xi_{t'} \rangle_x = 2D\delta(t - t')$, where the diffusion constant is given by $D = N\omega_y p_0(1 - p_0)$.

This process (5.63) is the well-known Ornstein-Uhlenbeck process. For such processes optimal filtering strategies exist, known as Kalman-Bucy filters, which estimate a normally distributed signal $x \sim \mathcal{N}(0, \mathcal{E}_x^2)$ from the coarse-grained time history \tilde{Y}_0^t with the least variance, which we denote by $\mathcal{E}^2(t)$; see, e.g., Refs. [88, 120, 185, 190] or Appendix 4.C. More precisely, the variance of the estimate $\mathcal{E}^2(t)$ must satisfy the Riccati equation (4.161), where one has to replace the parameters from (5.63) in the following way. Setting $D_x = \omega_x = 0$ (static signal), $\omega_r = \omega_y$, $D_r = D$, and $\phi = Np_0(1 - p_0) = D/\omega_y$, the Riccati equation (4.161) becomes $\frac{d}{dt}\mathcal{E}^2(t) = \frac{1}{2}D\mathcal{E}^2(t)$, with the initial condition $\mathcal{E}^2(0) = \mathcal{E}_x^2$ the solution becomes $\mathcal{E}^2(t) = 2\mathcal{E}_x^2/[2 + \mathcal{E}_x^2 Dt]$. Due to the Gaussian nature of the coarse-grained process the mutual information is then given by [190]

$$\mathcal{I}_N^{\text{lin}} \equiv I[x:\tilde{Y}_0^t] = \frac{1}{2} \ln \frac{\mathcal{E}_x^2}{\mathcal{E}^2(t)} = \frac{1}{2} \ln \left[1 + \frac{1}{2}\mathcal{E}_x^2 N\omega_y p_0(1 - p_0)t \right]. \quad (5.64)$$

Comparing Eqs. (5.11) and (5.64), we find the coarse-grained process \tilde{Y}_t loses information about the original process Y_t , which is given by

$$\mathcal{I}_N - \mathcal{I}_N^{\text{lin}} \approx \frac{1}{2} \ln (4\alpha^2 - 4\alpha + 2) \quad (5.65)$$

for $t \rightarrow \infty$. This result is precisely the information loss from the number of jump events, which we have found in Eq. (5.6). The information of the linearized process (5.64) equals the approximation of coarse-grained mutual information for weak signals (5.12), i.e., $\mathcal{I}_N^{\text{lin}} \approx \tilde{\mathcal{I}}_N$. Hence, the linear noise approximation loses the information compared with the original system dynamics that is hidden in the discontinuous jump events. For example, the persistence time is fully captured by the coarse-grained system dynamics, which can be understood as follows. The linear noise approximation adopts the correct dynamics of the mean $\langle y_t \rangle_x$ and its correlations $\langle y_t y_{t'} \rangle_x$, implying it includes the persistence time $\hat{\tau}_1 \equiv \int_0^t y_{t'} dt'$ up to its second moment. Since the long time limit renders $\hat{\tau}_1$ normally distributed,

the linear noise approximation precisely includes the information from $\hat{\tau}_1$. Therefore, $\Delta\mathcal{I}$ from (5.6) also determines the information loss of the linear noise approximation compared with the original system dynamics. This insight constitutes the second main result of this chapter: The asymmetry parameter from (5.2) determines whether the linear noise approximation loses information on the trajectory level or not. For example, for $\alpha = 1/2$ as it applies to the model from Fig. 5.3(d), the information loss vanishes, making the linear noise approximation accurate on the trajectory level. Whereas for all “natural values” of the asymmetry parameter ($0 \leq \alpha \leq 1$) the linear noise approximation loses information on the trajectory level which is bounded by 1/2 bit per measurement.

5.5 Discussion and outlook

We have shown that the asymmetry parameter, quantifying the load distribution of a free energy change caused by a signal [see Eq. (5.2)], plays a central role for the information acquisition of binary sensory networks. The asymmetry parameter determines the additional information about the signal that can only be obtained from the number of jump events. For example, if the forward and backward transition rates are symmetrically influenced by a signal ($\alpha = 1/2$) the number of jump events do not contain any additional information about the signal, i.e., simple time integration methods can reach highest sensory performance. Under natural condition, where $0 \leq \alpha \leq 1$, the additional information that can be gained from the number of jump events is bounded by 1/2 bit. Notably, the information gain from the number of jump events is independent of the number of binary sensors N measuring the same signal.

Moreover, the linear noise approximation, which is a continuous Brownian motion quite useful for systems with a large copy number ($N \gg 1$), adopts the probability distribution of the sensor state y_t and its time correlations up to the second moment $\langle y_t y_{t'} \rangle_x$ on the ensemble level, whereas it loses information on the trajectory level compared with the original system that is precisely the information that is only accessible with the number of discontinuous jump events. Consequently, the asymmetry parameter determines also whether or not the linear noise approximation loses information on the trajectory level compared with the original system dynamics. Analogously, for $\alpha = 1/2$ the linear noise approximation is surprisingly accurate. For $0 \leq \alpha \leq 1$ the linear noise approximation loses up to 1/2 bit of information per measurement irrespective of the number of individual copies N .

For future studies, it will be interesting to study sensors that measure not just a single signal but rather multiple signal with a single sensor unit [194]. Moreover, multi-state systems can have nonequilibrium affinities which trigger currents which allow to infer additional information about a signal even for symmetric influence of the signal on the transition rates. For example, the dissipation of chemical free energy can reduce the dispersion of jump-related variables [207]; see also Refs. [198, 208–212]. The method, which is described in Sec. 5.3.4, allows to calculate the joint dispersion of jump-related variables and persistence time variables for networks with more than two states. Furthermore, it will be worthwhile to investigate the implications to continuously varying signal ramps [120, 169, 192], which require more than just a single signal estimate.

Finally, a single-electron box [50–52], as it has been used to realize a feedback-driven

engine, may be a promising nonbiological example to investigate information about a change of voltage that can be inferred from the time history of the state of the single-electron box. For example, Ref. [213] has recently studied current fluctuations for varying gate voltage.

6 Nonequilibrium sensing and its analogy to kinetic proofreading

For a paradigmatic model of chemotaxis, we analyze the effect of how a nonzero affinity driving receptors out of equilibrium affects sensitivity. This affinity arises whenever changes in receptor activity involve ATP hydrolysis. The sensitivity integrated over a ligand concentration range is shown to be enhanced by the affinity, providing a measure of how much energy consumption improves sensing. With this integrated sensitivity we can establish an intriguing analogy between sensing with nonequilibrium receptors and kinetic proofreading: the increase in integrated sensitivity is equivalent to the decrease of the error in kinetic proofreading. The influence of the occupancy of the receptor on the phosphorylation and dephosphorylation reaction rates is shown to be crucial for the relation between integrated sensitivity and affinity. This influence can even lead to a regime where a nonzero affinity decreases the integrated sensitivity, which corresponds to anti-proofreading. This chapter is adopted from [177].

6.1 Introduction

Bacterial chemotaxis, a process by which the cell directs its motion in response to external ligand concentration, is a canonical example of biological sensing. Experiments with *E. coli* have provided much insight into chemotaxis [171, 214], making this bacterium sensory system a particularly well understood example. In *E. coli* chemotaxis, the sensitivity is a key observable quantifying the response in activity inside the cell due to a change in the external ligand concentration.

Stochastic models for *E. coli* [167, 176, 215, 216] receptors often assume that changes in activity are described by an equilibrium process involving only conformational changes, leading to an equilibrium Monod-Wyman-Changeux (MWC) model [172, 173]. However, chemical reactions where the receptor changes from an inactive to an active state often involve free energy consumption through, for example, the hydrolysis of adenosine triphosphate (ATP). A stochastic model including this feature must have transition rates that break detailed balance leading to a nonzero affinity, corresponding to the chemical potential difference involved in ATP hydrolysis, which drives the process out of equilibrium.

Two recent studies have analyzed the effect of such an affinity in models related to the *E. coli* sensory network. Tu [145] has considered the effect of the driving affinity on both the dwell-time distribution and the sensitivity in a model for the flagellar motor switching between run and tumble. Skoge et al. [148] have shown that nonequilibrium receptors can increase the signal-to-noise ratio for fixed sensitivity.

Beyond *E. coli* chemotaxis, the effect of energy dissipation in biological processes involving information processing has received much attention recently [92, 94, 95, 119, 144,

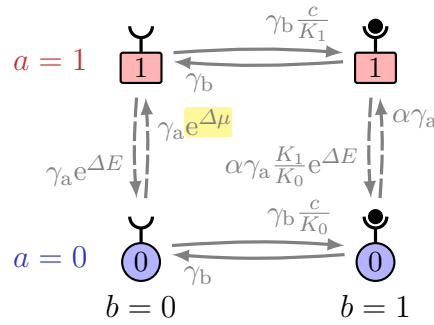


Figure 6.1 | Four-state model for a single receptor. Vertical transitions correspond to a change in activity, while horizontal transitions correspond to a change in the occupancy of the receptor. The phosphorylation rates in (6.4) are chosen as $\kappa_+^0 = \gamma_b e^{\Delta\mu}$ and $\kappa_-^0 = \gamma_a e^{\Delta E}$. The dephosphorylation rates in (6.5) are chosen as $\omega_+^1 = \alpha \gamma_a (K_1/K_0) e^{\Delta E}$ and $\omega_-^1 = \alpha \gamma_a$.

146, 149–151, 170, 181]. A prominent example among such processes is kinetic proofreading [20, 21, 162, 163], which is a dissipative error reduction mechanism related to copying biochemical information. As this error reduction is achieved through free energy consumption, a nonzero affinity driving the process out of equilibrium is also present in kinetic proofreading. Specifically, relations between the error and the driving affinity have been obtained [154, 163] (see also [147, 155–158, 217] for other recent works).

In this chapter, we consider a nonequilibrium model for *E. coli* receptors including ATP hydrolysis in the chemical reactions that involve changes in activity. We quantify the effect of having a nonzero driving affinity on sensing by analyzing an integrated sensitivity, which is an integral of the sensitivity over a concentration range. This observable is shown to have a simple relation with the affinity driving the process out of equilibrium. We show that sensing with nonequilibrium receptors and kinetic proofreading can be viewed as equivalent problems, with the increase in the integrated sensitivity in nonequilibrium sensing being analogous to the error reduction in kinetic proofreading.

The transition rates for changes in activity are assumed to depend on whether the receptor is occupied by a ligand or empty. We show that this dependency is quite important for the relation between sensitivity and the driving affinity. There is even a regime where energy dissipation leads to a decrease in the integrated sensitivity, which is equivalent to an anti-proofreading regime in kinetic proofreading [157].

6.2 Nonequilibrium receptor model

The single receptor model we analyze in this chapter is defined as follows (see Fig. 6.1). There are two binary variables a and b characterizing the state of the receptor, with $b = 1$ if the receptor is occupied by a ligand (bound) and $b = 0$ if the receptor is free (unbound), and $a = 1$ if the receptor is active and $a = 0$ if the receptor is inactive.

In equilibrium the free energy of the four different states can be written as [119, 173] (see also Sec. 4.3.2)

$$F(a, b) \equiv a\Delta E - b \ln \frac{c}{K_a}, \quad (6.1)$$

where ΔE is the conformational energy difference between active and inactive for a free receptor ($b = 0$), K_a is the dissociation constant that depends on the activity a , and c is the external ligand concentration. Setting Boltzmann's constant and the temperature to $k_B T \equiv 1$, the equilibrium stationary probability is $P_{a,b} \propto \exp[-F(a,b)]$. Denoting the coarse-grained probability by $P_a \equiv \sum_{b'} P_{a,b'}$, we obtain

$$\frac{P_0}{P_1} \Big|_{\text{eq}} = e^{\Delta E} \left(\frac{1 + \frac{c}{K_0}}{1 + \frac{c}{K_1}} \right), \quad (6.2)$$

where $P_0 = 1 - P_1$. The average activity

$$\langle a \rangle_c \equiv \sum_a a P_a \quad (6.3)$$

is just $\langle a \rangle_c = P_1$. It is assumed that the dependence of the dissociation constant on the activity is such that $K_1 > K_0$, i.e., the free energy barrier for binding a ligand to an inactive receptor is smaller. Hence, from Eq. (6.2) the average activity is a decreasing function of the concentration. This single receptor MWC model already contains the key feature of self-regulation. However, in order to have cooperativity, which is another important feature of the MWC model, we need more than one binding site [173]. The generalization of the model to an arbitrary number of binding sites is contained in Sec. 6.5.2. For our present purposes it is more convenient to restrict our discussion to a single binding site.

We now consider a nonequilibrium model that includes ATP hydrolysis. For simplicity we assume that when the receptor is unbound only phosphorylation takes place and when the receptor is bound only dephosphorylation occurs. A more general model with phosphorylation and dephosphorylation occurring for both bound and unbound states, and the implications of this generalization are discussed in Sec. 6.5. The phosphorylation reaction is represented as



where κ_+^0 and κ_-^0 denote transition rates. The dephosphorylation reaction reads



where ω_+^1 and ω_-^1 are transition rates.

With the free energy (6.1), the generalized detailed balance relation [18] imposes the following constraints on the rates. First, we have

$$\ln \frac{\kappa_+^0 \omega_+^1}{\kappa_-^0 \omega_-^1} = \Delta\mu + \ln \frac{K_1}{K_0}, \quad (6.6)$$

where $\Delta\mu = \mu_{\text{ATP}} - \mu_{\text{ADP}} - \mu_{\text{P}_i}$ is the free energy dissipated in one ATP hydrolysis. Second, the transition rates from $b = 0$ to $b = 1$, denoted by w_{01}^a , and from $b = 1$ to $b = 0$, denoted by w_{10}^a , fulfill the relation

$$\ln \frac{w_{01}^a}{w_{10}^a} = \ln(c/K_a). \quad (6.7)$$

With these two constraints the logarithm of the product of the transition rates in a cycle in the clockwise direction in Fig. 6.1 is precisely $\Delta\mu$, which is the affinity driving the process out of equilibrium. For simplicity we use the specific transition rates given in Fig. 6.1. The parameters γ_a and γ_b set the time-scale of the active/inactive and bound/unbound transitions, respectively. The parameter α is related to redistributing energy weights among the transition rates in such way that the constraints (6.6) and (6.7) are still fulfilled.

A reasonable assumption is that ligand binding is much faster than activity changes, i.e., $\gamma_a/\gamma_b \ll 1$ [167]. With this assumption, calculating the stationary probability distribution using standard methods [39, 218] we obtain

$$\frac{P_0}{P_1} = e^{\Delta E - \Delta\mu} \left(\frac{1 + \frac{c}{K_0}}{1 + \frac{c}{K_1}} \right) \left(\frac{1 + \alpha \frac{c}{K_0}}{1 + \alpha \frac{c}{K_0} e^{-\Delta\mu}} \right). \quad (6.8)$$

Comparing with the equilibrium expression (6.8) there is the extra term of the second brackets, which becomes 1 for $\Delta\mu = 0$. The precise effect of this extra term in sensing is discussed in the next section. For this discussion it is convenient to define the effective dissociation constants

$$\tilde{K}_0 \equiv \frac{K_0}{\alpha} \quad \text{and} \quad \tilde{K}_1 \equiv \frac{K_0}{\alpha} e^{\Delta\mu}. \quad (6.9)$$

6.3 Integrated sensitivity

A key observable in sensing is the sensitivity

$$R(c, \Delta E) \equiv -4 \frac{\partial}{\partial \ln c} \langle a \rangle_c = -4 \frac{\partial P_1}{\partial \ln c}, \quad (6.10)$$

which is the response of the average activity to small changes in ligand concentration. It is convenient to rewrite the sensitivity as

$$R(c, \Delta E) = 4P_0P_1 \frac{\partial}{\partial \ln c} \ln \frac{P_0}{P_1} \leq \frac{\partial}{\partial \ln c} \ln \frac{P_0}{P_1}, \quad (6.11)$$

where the inequality comes from $P_0P_1 \leq 1/4$. From Eq. (6.8) it follows that the upper bound on the right hand side of Eq. (6.11) does not depend on ΔE . Hence, for given c there is an optimal conformational free energy difference that maximizes the sensitivity

$$\Delta E^*(c) = \Delta\mu + \ln \left(\frac{1 + \frac{c}{K_1}}{1 + \frac{c}{K_0}} \right) + \ln \left(\frac{1 + \alpha \frac{c}{K_0} e^{-\Delta\mu}}{1 + \alpha \frac{c}{K_0}} \right), \quad (6.12)$$

which is obtained from Eq. (6.8) with $P_0P_1 = 1/4$. A free energy close to this optimal value can be achieved through an adaptation system that uses the methylation levels to adjust ΔE in accordance with the external concentration [95]. From now on we set $\Delta E = \Delta E^*(c)$ and denote this maximal sensitivity by $R(c) \equiv R(c, \Delta E^*(c))$.

For the equilibrium case, expressed in Eq. (6.2), the sensitivity becomes

$$R_{\text{eq}}(c) = \frac{c}{c + K_0} - \frac{c}{c + K_1}. \quad (6.13)$$

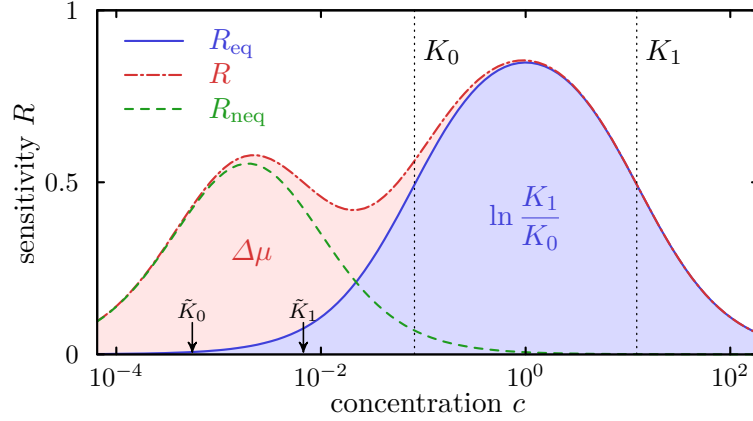


Figure 6.2| Increase in sensitivity $R(c)$ through nonequilibrium driving. The blue shaded region under the curve corresponds to the equilibrium contribution $\ln(K_1/K_0)$, while the red shaded region highlights the additional nonequilibrium enhancement, which is equal to the driving affinity $\Delta\mu$. The parameters are set to $K_1 = 1/K_0 = e^{2.5}$, $\alpha = e^5$, and $\Delta\mu = 2.5$.

Whereas out of equilibrium, with the ratio of probabilities in Eq. (6.8), we obtain

$$R(c) = R_{\text{eq}}(c) + R_{\text{neq}}(c), \quad (6.14)$$

with

$$R_{\text{neq}}(c) = \frac{c}{c + \left(\frac{K_0}{\alpha}\right)} - \frac{c}{c + \left(\frac{K_0 e^{\Delta\mu}}{\alpha}\right)} = \frac{c}{c + \tilde{K}_0} - \frac{c}{c + \tilde{K}_1}. \quad (6.15)$$

Therefore, the effect of adding a driving affinity $\Delta\mu$ to the single receptor is to increase the sensitivity by $R_{\text{neq}}(c)$. Particularly, the sensitivity of this single receptor out of equilibrium is equal to the sensitivity of a equilibrium model that has a second binding site with dissociation constant \tilde{K}_a , as given by (6.9). This situation is represented in Fig. 6.2, where we show the equilibrium contribution to sensitivity peaking between the concentration range $K_0 \leq c \leq K_1$ and the nonequilibrium contribution peaking between the range $\tilde{K}_0 \leq c \leq \tilde{K}_1$. Calculating the maximum of $R_{\text{neq}}(c)$, with c as the optimizing parameter, we obtain the inequality

$$R_{\text{neq}}(c) \leq \frac{e^{\Delta\mu/2} - 1}{e^{\Delta\mu/2} + 1}. \quad (6.16)$$

We note that an enhancement on sensitivity due to a nonequilibrium driving affinity has been shown in [145] (see also [148]).

As a first main result, we obtain that the integrated sensitivity I has the following simple relation with the driving affinity $\Delta\mu$,

$$I \equiv \int_{-\infty}^{\infty} d(\ln c) R(c) = \Delta\mu + \ln \frac{K_1}{K_0}, \quad (6.17)$$

where we used Eqs. (6.13), (6.14) and (6.15). This result for the integrated sensitivity provides a precise quantification of the effect of free energy dissipation on sensing. The

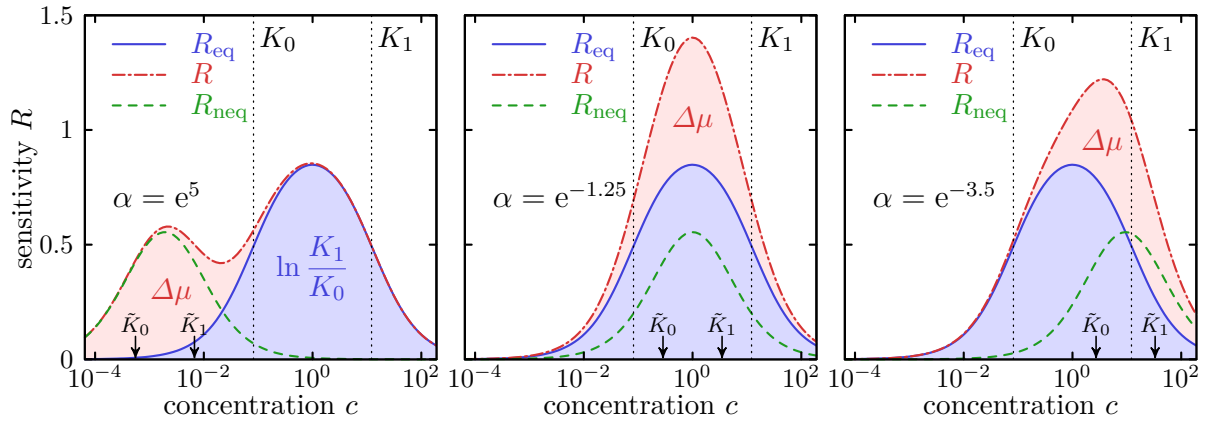


Figure 6.3 | Effect of parameter α on the sensitivity $R(c)$. The parameter α is indicated in the figures, $K_1 = 1/K_0 = e^{2.5}$, and $\Delta\mu = 2.5$. For $\alpha = e^5$ the driving affinity increases the range for which the sensitivity is non-negligible, while in the other two cases we can see a clear increase in the sensitivity in the equilibrium range $K_0 \leq c \leq K_1$, with $\alpha = e^{1.25}$ corresponding to the optimal increase in the equilibrium range.

integral represents the area under the curves in Fig. 6.2 where the equilibrium contribution $R_{\text{eq}}(c)$ yields $\ln(K_1/K_0)$ and the nonequilibrium contribution rises the area under the curve by $\Delta\mu$.

From the expressions (6.13) and (6.15) it follows that $R_{\text{eq}}(c) \leq 1$ and $R_{\text{neq}}(c) \leq 1$, respectively. The effect of the driving affinity on the sensitivity is twofold: it can increase the concentration range for which the sensitivity is non-negligible and it can increase the sensitivity in the equilibrium range $K_0 \leq c \leq K_1$. The nonequilibrium enhancement can even lead to $R(c) > 1$ within this region.

The influence of the parameter α as determined by Eq. (6.15) on these two effects is shown in Fig. 6.3, which indicates that there is an optimal α for which the effect of $\Delta\mu$ is mostly to increase the sensitivity in the equilibrium range $K_0 \leq c \leq K_1$. To quantify the enhancement of sensitivity in this equilibrium range we define the integral

$$\begin{aligned}
 I_{K_0, K_1}^{\text{neq}} &\equiv \int_{\ln K_0}^{\ln K_1} d(\ln c) R_{\text{neq}}(c) \\
 &= \ln \left(\frac{K_1 + \frac{K_0}{\alpha}}{K_1 + \frac{K_0}{\alpha} e^{\Delta\mu}} \right) - \ln \left(\frac{K_0 + \frac{K_0}{\alpha}}{K_0 + \frac{K_0}{\alpha} e^{\Delta\mu}} \right), \tag{6.18}
 \end{aligned}$$

We point out that $I_{K_0, K_1}^{\text{neq}} \leq \Delta\mu$ due to Eq. (6.17) and $I_{K_0, K_1}^{\text{neq}} \leq \ln(K_1/K_0)$ due to $R_{\text{neq}}(c) \leq 1$. Maximizing this integral with respect to α we obtain

$$I_{K_0, K_1}^{\text{neq, opt}} \equiv \max_{\alpha} I_{K_0, K_1}^{\text{neq}} = \ln \left[\frac{K_1}{K_0} \left(\frac{e^{\Delta\mu/2} + \sqrt{\frac{K_0}{K_1}}}{e^{\Delta\mu/2} + \sqrt{\frac{K_1}{K_0}}} \right)^2 \right], \tag{6.19}$$

where the maximum is obtained for $\alpha = \sqrt{K_0/K_1} \exp(\Delta\mu/2)$, which leads to dissociation constants that satisfy $\tilde{K}_0 \tilde{K}_1 = K_0 K_1$. Hence, expression (6.19) provides the optimal sensitivity enhancement due to the driving affinity $\Delta\mu$ within the equilibrium concentration

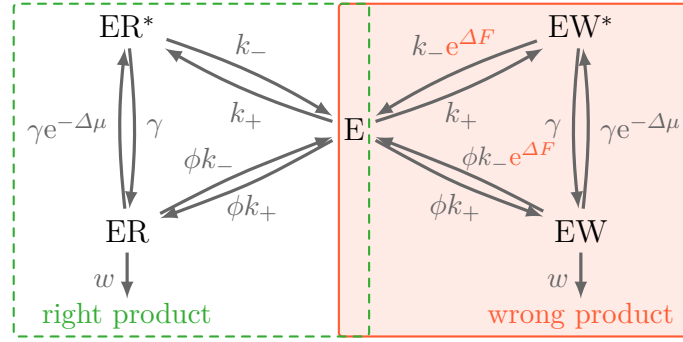


Figure 6.4| Model for kinetic proofreading. The difference in the transition rates for the two cycles is in the free energy term $e^{\Delta F}$ in the transition from EW to E and from EW* to E, which is related to the higher free energy of EW in comparison to ER. The rate at which information is written w is assumed to be small compared to the other transition rates.

range $K_0 \leq c \leq K_1$ for given $\Delta\mu$, K_0 , and K_1 . We note that the effect of increasing the sensitivity beyond the equilibrium range can represent an important advantage for the cell. This increase is quantified by $I - \ln(K_1/K_0) - I_{K_0, K_1}^{\text{neq}}$. A more quantitative relation could arise from studying the sensitivity integrated over some concentration range of interest. Our choice in Eq. (6.18) is motivated by the fact that $I_{K_0, K_1}^{\text{neq}}$ is convenient for the analogy between nonequilibrium sensing and kinetic proofreading.

6.4 Analogy with kinetic proofreading

In this section we establish an explicit analogy between sensing with nonequilibrium receptors and kinetic proofreading, with the integrated sensitivity in Eq. (6.18) playing the role of the error reduction due to dissipation in kinetic proofreading.

6.4.1 Kinetic proofreading

The model for kinetic proofreading is illustrated in Fig 6.4. Two substrates $S = R, W$, with R being the “right” substrate and W being the “wrong” substrate, can bind to the enzyme E. In equilibrium, the substrate R is copied to a template with higher probability due to a free energy difference ΔF . Specifically, this free energy difference between state EW and ER leads to an equilibrium error

$$\epsilon_{\text{eq}} = \exp(-\Delta F), \quad (6.20)$$

where the error is defined as the ratio between the probability of writing W and the probability of writing R to the template [20, 21].

In the kinetic proofreading scheme phosphorylated forms of the substrates are added, leading to the additional states EW* and ER*. The transitions in Fig. 6.4 involve substrate binding and unbinding in the phosphorylated form



and in the dephosphorylated form



as well as the hydrolysis reaction



A cycle $E \rightarrow ES^* \rightarrow ES \rightarrow E$ turns one phosphorylated substrate S^* turned into a dephosphorylated substrate S and a phosphate P_i , leading to a chemical energy release of $\Delta\mu = \mu_{S^*} - \mu_S - \mu_{P_i}$, which is assumed to be the same for the right substrate $S = R$ and the wrong substrate $S = W$. More precisely, we assume $\mu_{R^*} - \mu_R = \mu_{W^*} - \mu_W$. The specific transition rates are shown in Fig. 6.4, where k_- , k_+ , γ , and ϕ are kinetic parameters. Moreover, w is the rate at which the substrate S is written to the template, which we assume to be much slower than the other transition rates, i.e., we assume the limit $w \rightarrow 0$.

The error is given by

$$\epsilon \equiv \frac{P_{EW}}{P_{ER}} = \left(\frac{(e^{-\Delta\mu} + \phi)\gamma + \phi k_-}{(e^{-\Delta\mu} + \phi)\gamma e^{\Delta F} + \phi k_- e^{2\Delta F}} \right) \left(\frac{(1 + \phi)\gamma + \phi k_- e^{\Delta F}}{(1 + \phi)\gamma + \phi k_-} \right), \quad (6.24)$$

where P_{EW} and P_{ER} denote the stationary probabilities of states EW and ER , respectively. Hence, as first observed by Hopfield and Ninio [20, 21], with energy dissipation the error can be smaller than ϵ_{eq} . The maximal error reduction $\epsilon/\epsilon_{\text{eq}} = e^{-\Delta F}$ takes place for an appropriate choice of the kinetic parameters and the formal limit $\Delta\mu \rightarrow \infty$.

6.4.2 Non-equilibrium sensing vs. kinetic proofreading

The minimal error ϵ_{opt} for fixed free energy difference ΔF and driving affinity $\Delta\mu$, that is obtained by optimizing ϵ in Eq. (6.24) with respect to the kinetic parameters, is given by [147, 154]

$$\frac{\epsilon_{\text{opt}}}{\epsilon_{\text{eq}}}(\Delta F, \Delta\mu) = e^{-\Delta F} \left(\frac{e^{\frac{\Delta\mu}{2}} + e^{\frac{\Delta F}{2}}}{e^{\frac{\Delta\mu}{2}} + e^{-\frac{\Delta F}{2}}} \right)^2, \quad (6.25)$$

Since this function is bounded by $e^{-\Delta\mu}$ and by $e^{-\Delta F}$, the following inequality holds [154],

$$\epsilon \geq \epsilon_{\text{opt}} \geq \exp(-\Delta F - \Delta\mu). \quad (6.26)$$

Comparing expression (6.25) for the maximal error reduction in kinetic proofreading with expression (6.19) for the maximal increase in the integrated sensitivity in nonequilibrium sensing, a quite transparent analogy arises, as shown in Figs. 6.5(a) and 6.5(b). Both expressions are the same with the increase in sensitivity in the equilibrium range $I_{K_0, K_1}^{\text{neq, opt}}$ being analogous to $-\ln(\epsilon_{\text{opt}}/\epsilon_{\text{eq}})$ and the ratio of the dissociation constants K_1/K_0 being analogous to $e^{\Delta F}$. Whereas in kinetic proofreading a driving affinity $\Delta\mu$ decreases the error, in nonequilibrium sensing $\Delta\mu$ increases the integrated sensitivity in the equilibrium range $K_0 \leq c \leq K_1$.

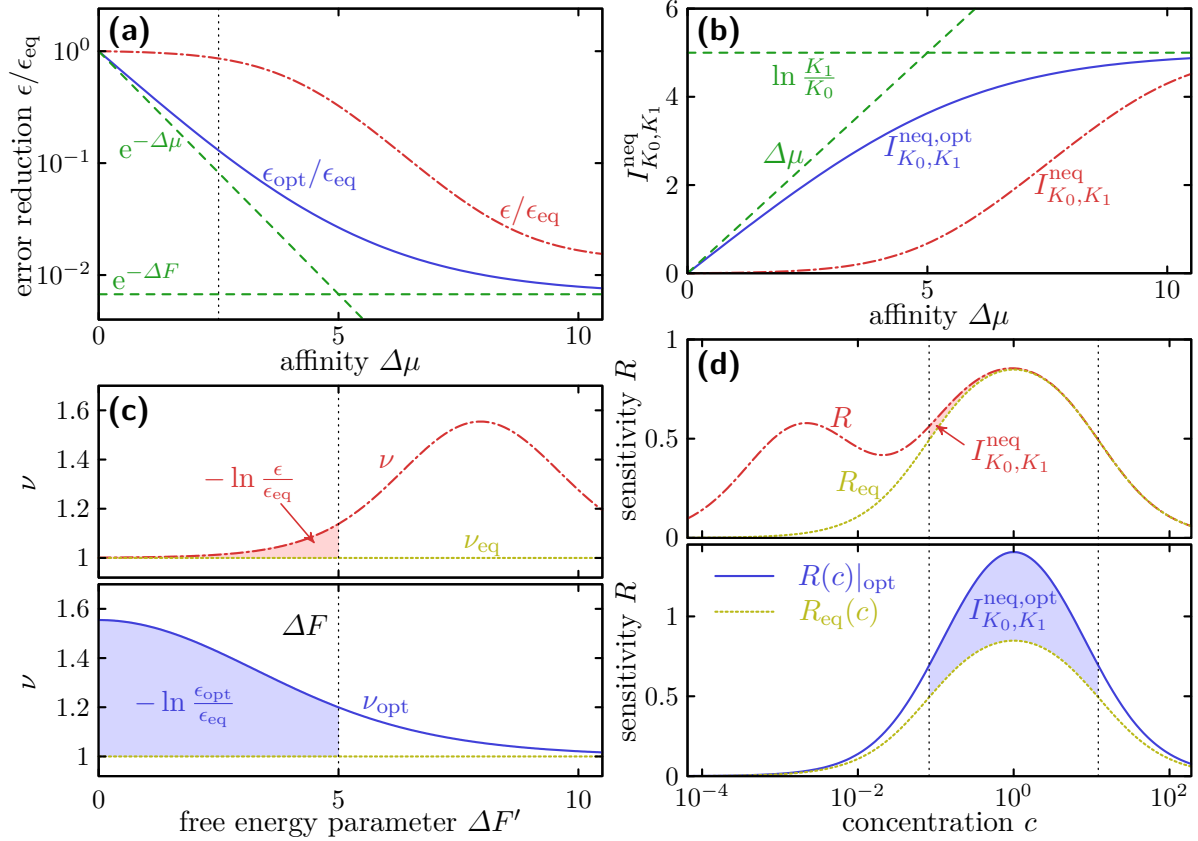


Figure 6.5| Kinetic proofreading (left panel) versus nonequilibrium sensing (right panel). (a) Error reduction $\epsilon/\epsilon_{\text{eq}}$ and optimal error reduction $\epsilon_{\text{opt}}/\epsilon_{\text{eq}}$, as given by (6.25), as functions of the affinity $\Delta\mu$. The green dashed lines indicate the asymptotically reached bounds $\epsilon_{\text{opt}}/\epsilon_{\text{eq}} \geq e^{-\Delta\mu}$ and $\epsilon_{\text{opt}}/\epsilon_{\text{eq}} \geq e^{-\Delta F}$. (b) Nonequilibrium contribution to the sensitivity integrated in the equilibrium range $I_{K_0, K_1}^{\text{neq}}$ and its optimized value $I_{K_0, K_1}^{\text{neq, opt}}$, as given by (6.19), as functions of the affinity $\Delta\mu$. The green dashed lines indicate the asymptotically reached bounds $I_{K_0, K_1}^{\text{neq}} \leq \Delta\mu$ and $I_{K_0, K_1}^{\text{neq}} \leq \ln(K_1/K_0)$. (c) The discriminatory index ν as a function of the free energy difference $\Delta F'$. The lower panel shows $\nu_{\text{opt}} \equiv -\partial_{\Delta F} \ln \epsilon_{\text{opt}}(\Delta F, \Delta\mu)$, i.e., the discriminatory index associated with the minimal error (6.25). The highlighted areas illustrate relation (6.28). (d) The sensitivity $R(c)$ and the sensitivity $R(c)|_{\text{opt}}$, which is associated with $I_{K_0, K_1}^{\text{neq, opt}}$. The highlighted areas illustrate relation (6.18). Parameters are set in the following way: $\Delta F = \ln(K_1/K_0) = 5$ with $K_1 = 1/K_0$ in (a) and (b); $\Delta\mu = 2.5$ in (c) and (d); in (b) and (d) $I_{K_0, K_1}^{\text{neq}}$ is obtained from (6.18) with $\alpha = e^5$; in (a) and (c) $\epsilon/\epsilon_{\text{eq}}$ is obtained from (6.24) with $k_- = \gamma = 1$, $\phi = 10^{-4}$. The dotted vertical line in (a) and (b) indicate the affinity $\Delta\mu = 2.5$. The dotted vertical line in (c) indicates $\Delta F = 5$.

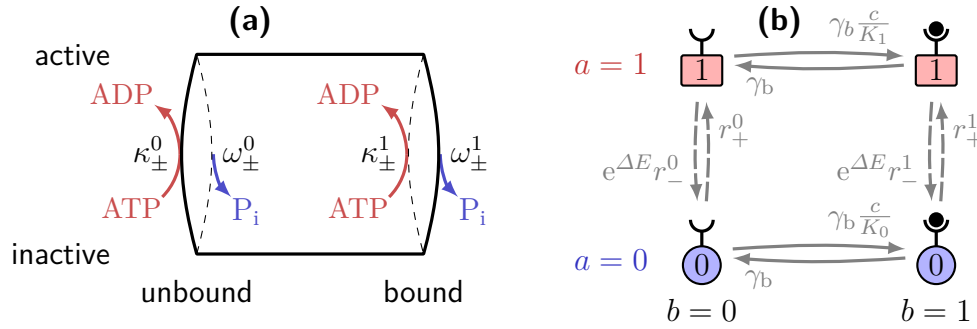


Figure 6.6 | Four-state system with phosphorylation and dephosphorylation for both $b = 0$ and $b = 1$. (a) Full model with two links for the vertical transitions. The dashed links indicate transition rates that are zero in the model of Fig. 6.1. (b) Total rates as given by (6.33) and (6.34). The coarse-grained entropy production (6.44) is calculated with these total transition rates.

A recently introduced quantity in kinetic proofreading is the discriminatory index [157]

$$\nu(\Delta F) \equiv -\frac{\partial}{\partial \Delta F} \ln \epsilon, \quad (6.27)$$

where ϵ is given by (6.24). Due to $\epsilon_{\text{eq}} = e^{-\Delta F}$ the discriminatory index is $\nu_{\text{eq}} = 1$ in equilibrium, with a larger index $\nu \geq 1$ requiring energy dissipation. We can rewrite (6.27) as

$$-\ln \frac{\epsilon}{\epsilon_{\text{eq}}} = \int_0^{\Delta F} d\Delta F' [\nu(\Delta F') - 1]. \quad (6.28)$$

Comparing this equation with (6.18) we observe that the discriminatory index is analogous to the sensitivity $R(c)$, with $\nu(\Delta F') - 1$ being the nonequilibrium contribution. In Figs. 6.5(c) and 6.5(d) we show the comparison between discriminatory index in proofreading and sensitivity in nonequilibrium sensing. Murugan et al. [157] have shown that the integral from $-\infty$ to ∞ of $\nu(\Delta F) - 1$ can be equal to $\Delta\mu$. This result is equivalent to our equality (6.17).

6.5 Effect of the occupancy of the receptor on phosphorylation and dephosphorylation rates

6.5.1 Single receptor

We now generalize the model from Fig. 6.1 to include phosphorylation and dephosphorylation reactions for both $b = 0$ and $b = 1$. With this generalization there are two links for the vertical transitions in Fig. 6.6(a). These reactions happen with transition rates



where $b = 0, 1$. For thermodynamic consistency, the following constraints must be fulfilled:

$$\Delta\mu = \ln \frac{\kappa_+^b \omega_+^b}{\kappa_-^b \omega_-^b} \quad (6.30)$$

for $b = 0, 1$,

$$\ln \frac{\kappa_+^0 \omega_+^1}{\kappa_-^0 \omega_-^1} = \Delta\mu + \ln \frac{K_1}{K_0}, \quad (6.31)$$

and

$$\ln \frac{\kappa_+^1 \omega_+^0}{\kappa_-^1 \omega_-^0} = \Delta\mu - \ln \frac{K_1}{K_0}, \quad (6.32)$$

where we used the free energy (6.1) for the second and third equations. Whereas the presence of two links is important for calculating the rate of dissipation in this model [18], for the purpose of calculating the stationary probabilities we consider the total transition rates from inactive to active

$$r_+^b \equiv \kappa_+^b + \omega_-^b \quad (6.33)$$

and from active to inactive

$$e^{\Delta E} r_-^b \equiv \kappa_-^b + \omega_+^b, \quad (6.34)$$

which are indicated in Fig. 6.6(b). We choose the rates κ_-^b and ω_+^b to be proportional to $e^{\Delta E}$, which leads to r_-^b independent of ΔE . Assuming that the binding/unbinding transitions are much faster, the ratio of stationary probabilities (6.8) for this more general model becomes

$$\frac{P_0}{P_1} = e^{\Delta E} \left(\frac{1 + \frac{c}{K_0}}{1 + \frac{c}{K_1}} \right) \left(\frac{r_-^0 + (\frac{c}{K_1}) r_-^1}{r_+^0 + (\frac{c}{K_0}) r_+^1} \right) \equiv e^{\Delta E} \left(\frac{1 + \frac{c}{K_0}}{1 + \frac{c}{K_1}} \right) \chi(c). \quad (6.35)$$

As in Sec. 6.3 the sensitivity (6.11) is maximized for $P_0/P_1 = 1$, which is achieved at

$$\Delta E^*(c) = \ln \left(\frac{1 + \frac{c}{K_1}}{1 + \frac{c}{K_0}} \right) - \ln \chi(c), \quad (6.36)$$

The equilibrium contribution to the maximal sensitivity is still given by (6.13), while the nonequilibrium contribution becomes

$$R_{\text{neq}}(c) \equiv \frac{\partial}{\partial(\ln c)} \ln \chi(c) = \frac{1}{c} \frac{\chi'(c)}{\chi(c)}. \quad (6.37)$$

The integrated sensitivity then reads

$$\begin{aligned} I &= \int_{-\infty}^{\infty} d(\ln c) [R_{\text{neq}}(c) + R_{\text{eq}}(c)] = \ln \frac{K_1}{K_0} + \ln \frac{\chi(\infty)}{\chi(0)} \\ &= \ln \left(\frac{r_+^0 r_-^1}{r_-^0 r_+^1} \right). \end{aligned} \quad (6.38)$$

For $\Delta\mu \geq 0$, from Eqs. (6.30), (6.33), and (6.34), we obtain

$$\frac{\omega_-^b}{\omega_+^b} \leq \frac{r_+^b}{e^{\Delta E} r_-^b} \leq \frac{\kappa_+^b}{\kappa_-^b}. \quad (6.39)$$

With these inequalities, we obtain that the integrated sensitivity (6.38) is bounded by

$$I = \ln \left(\frac{r_+^0 r_-^1}{r_-^0 r_+^1} \right) \leq \ln \frac{\kappa_+^0 \omega_+^1}{\kappa_-^0 \omega_-^1} = \ln \frac{K_1}{K_0} + \Delta\mu, \quad (6.40)$$

where we used (6.31) in the last equality. As shown in Sec. 6.5.2, this inequality can also be generalized to an arbitrary number of binding sites.

The influence of how the occupancy of the receptor affects the reaction rates for activity on the relation between the integrated sensitivity I and the driving affinity $\Delta\mu$ can be seen with the following examples. First, if we choose transition rates satisfying the relation

$$\frac{K_0 r_-^1}{K_1 r_+^1} = \frac{r_-^0}{r_+^0}, \quad (6.41)$$

the function $\chi(c)$ in (6.35) becomes independent of c . In this case, from (6.37) we obtain $R_{\text{neq}}(c) = 0$, which implies $I = \ln(K_1/K_0)$. Hence, it is possible to have a dissipative model with ATP consumption that has the same sensitivity as the equilibrium case. Second, we consider the case where phosphorylation happens only if the receptor is bound and dephosphorylation occurs only if the receptor is unbound, which is the opposite of the model in Fig. 6.1. In this case $\kappa_{\pm}^0 = \omega_{\pm}^1 = 0$, leading to

$$I = \ln \frac{\kappa_-^1 \omega_-^0}{\kappa_+^1 \omega_+^0} = \ln \frac{K_1}{K_0} - \Delta\mu, \quad (6.42)$$

where we used (6.40) and (6.32). This result shows that the integrated sensitivity can also decrease with energy dissipation. The regime for which the integrated sensitivity is decreased by $\Delta\mu$ is equivalent to an anti-proofreading regime recently studied in [157].

A more precise analysis of the relation between I and energy dissipation can be achieved by considering the entropy production σ [18]. For the present model this entropy production is the rate of ATP consumption. Using the stationary probability $P_{a,b}$ we define the probability current $J_b \equiv P_{0,b} \kappa_+^b - P_{1,b} \kappa_-^b$. With this current the entropy production can be written as

$$\sigma = (J_0 + J_1) \Delta\mu, \quad (6.43)$$

by using the fact that σ is a sum of currents multiplying cycle affinities [18]. The energy dissipation σ is non-zero whenever $\Delta\mu \neq 0$. Besides σ , we can consider a coarse-grained entropy production $\tilde{\sigma}$, which does not take into account the two channels for the vertical transitions in Fig. 6.6(a): it is obtained by considering the single links with rates r_{\pm}^b in Fig. 6.6(b). This coarse-grained entropy production provides a lower bound on the full entropy production, i.e., $\sigma \geq \tilde{\sigma}$ [103]. For the model in Fig. 6.6(b),

$$\tilde{\sigma} = J\mathcal{A}. \quad (6.44)$$

leading to

$$\frac{P_0}{P_1} = e^{\Delta E} \left(\frac{1 + \frac{c}{K_0}}{1 + \frac{c}{K_1}} \right)^N \chi(c), \quad (6.48)$$

where

$$\chi(c) = \frac{\sum_{b=0}^N \binom{N}{b} \left(\frac{c}{K_1} \right)^b r_-^b}{\sum_{b=0}^N \binom{N}{b} \left(\frac{c}{K_0} \right)^b r_+^b}. \quad (6.49)$$

This expression generalizes (6.35) to the case of N binding sites. Following the same procedure from Sec. 6.5, similarly to (6.36) the sensitivity (6.11) is maximized for

$$\Delta E^*(c) = N \ln \left(\frac{1 + \frac{c}{K_1}}{1 + \frac{c}{K_0}} \right) - \ln \chi(c), \quad (6.50)$$

where, similarly to (6.37), the nonequilibrium contribution to sensitivity becomes

$$R_{\text{neq}}(c) = \frac{\partial}{\partial(\ln c)} \ln \chi(c) = \frac{1}{c} \frac{\chi'(c)}{\chi(c)}. \quad (6.51)$$

Hence, the integrated sensitivity reads

$$\begin{aligned} I &= \int_{-\infty}^{\infty} d(\ln c) [R_{\text{eq}}(c) + R_{\text{neq}}(c)] = N \ln \frac{K_1}{K_0} + \ln \frac{\chi(\infty)}{\chi(0)} \\ &= \ln \left(\frac{r_+^0 r_-^N}{r_-^0 r_+^N} \right). \end{aligned} \quad (6.52)$$

The transition rates for this model must fulfill the constraint

$$\ln \left(\frac{\kappa_+^0 \omega_+^N}{\kappa_-^0 \omega_-^N} \right) = N \ln \frac{K_1}{K_0} + \Delta\mu. \quad (6.53)$$

From the inequalities (6.39) we finally obtain

$$I \leq N \ln \frac{K_1}{K_0} + \Delta\mu, \quad (6.54)$$

which generalizes inequality (6.40) to the case of N binding sites.

6.6 Conclusion

We have characterized the enhancement of sensitivity by a nonequilibrium driving affinity that arises from ATP hydrolysis in the chemical reactions involving an activity change. For the single receptor model from Sec. 6.2, the integrated sensitivity I was shown to have a simple relation with the driving affinity in Eq. (6.17). We have shown that a dissipative sensing model can lead to both an increase in the concentration range for

Nonequilibrium sensing	$I_{K_0, K_1}^{\text{neq}}$	R	$\ln(K_1/K_0)$	$I \leq \ln(K_1/K_0) + \Delta\mu$
Kinetic proofreading	$-\ln(\epsilon/\epsilon_{\text{eq}})$	ν	ΔF	$\epsilon \geq \exp(-\Delta F - \Delta\mu)$

Table 6.1 | Nonequilibrium sensing compared to kinetic proofreading.

which the sensitivity is non-negligible and an increase in the sensitivity in the equilibrium range. The second effect is quantified by $I_{K_0, K_1}^{\text{neq}}$, which is defined in Eq. (6.18).

We have shown that nonequilibrium sensing is equivalent to kinetic proofreading, with the analogous parameters, observables and relations summarized in Tab. 6.1. Most prominently, while in nonequilibrium sensing a driving affinity leads to an increase in the sensitivity integrated over the equilibrium range, in kinetic proofreading a driving affinity decreases the error. In kinetic proofreading the equivalent of sensitivity is the discriminatory index introduced in [157].

The influence of the occupancy of the receptor on the phosphorylation and dephosphorylation rates is of fundamental importance for the relation between integrated sensitivity and the affinity. As we have shown in Sec. 6.5, it is even possible to have a regime where energy dissipation leads to a decrease on the integrated sensitivity, which is analogous to the anti-proofreading regime from [157].

Our results demonstrate that measurements of the integrated sensitivity could unveil how the occupancy of the receptor affects the phosphorylation and dephosphorylation rates. It is certainly intriguing to speculate whether real chemotaxis networks evolved in such a way that this influence optimizes the enhancement of sensitivity due to energy consumption.

7 Concluding perspectives

We have developed a framework called stochastic thermodynamics of bipartite systems, which can be used to investigate feedback-driven engines. This framework allows for a transparent interpretation of a Maxwell's demon. We have introduced the learning rate, which characterizes the reduction of uncertainty about a controlled subsystem due to the dynamics of Maxwell's demon. The learning rate also bounds the rate at which the entropy in the medium is reduced due to the dynamics of the controlled subsystem. We have shown that the learning rate is a tighter bound on the entropy reduction in the medium due to the dynamics of the controlled subsystem than the transfer entropy rate, which is another information theoretic quantity. Moreover, we showed that the transfer entropy rate, unlike the learning rate, is *not* bounded by the thermodynamic cost required to maintain the feedback that must be invested by the demon. This insight constitutes one of the main results of this thesis and has been summarized in Eq. (3.47). Extensions of these inequalities have been proposed, including generalizations to non-stationary states [88, 96, 138], multipartite systems with more than two parts [134], partially masked systems [135, 136], a linear response theory [133], and, most importantly, the first experimental test of the first line of (3.47), presented in [52].

Stochastic thermodynamics of bipartite system is not restricted to feedback-driven engines. It has also been successfully applied to another problem: a sensor that measures a fluctuating signal. Considering the fluctuating signal as one part of a system and the sensor that measures the signal as the second part, we apply the methods derived in chapter 3 to this physical scenario. In this setup, the learning rate of the sensor l_y characterizes the rate at which the uncertainty about the signal is reduced due to the dynamics of the sensor. It is shown that the learning rate of the sensor is bounded by the entropy production of the sensor σ_y , which allows us to define an efficiency $\eta = l_y/\sigma_y \leq 1$ that relates the information a sensor acquires with its state to the thermodynamic cost to maintain the dynamics of the sensor. This constitutes the second main result of the thesis. The inequalities are analyzed with three models that are inspired by the *E. coli* sensory network. These specific models allow us to relate the entropy production of a sensor to the chemical energy that is consumed by the sensor and to the work that is delivered by the signal to the sensor. In particular, if the sensor internally consumes chemical energy, the learning rate will not need to be bounded by the rate at which the signal delivers energy to the system.

The sensory capacity has been defined as the ratio between the learning rate of the sensor and the transfer entropy rate from the signal to the sensor $C = l_y/\mathcal{T}_{x \rightarrow y} \leq 1$. The sensor capacity is a purely information theoretic quantity that characterizes the performance of a sensor. A sensor reaches the maximal sensory capacity $C = 1$ if the instantaneous state of the sensor carries the same amount of information about a signal as the full time history of the sensor. We show that the sensory capacity of a sensor can

be increased with the addition of a dissipative memory, which stores information from the time history of the sensor in the instantaneous state of the memory. Most importantly, a general tradeoff has been identified: maximal sensor capacity $C = 1$ implies the efficiency satisfies $\eta \leq 1/2$, which constitutes the third main result of this thesis. We note this tradeoff holds for arbitrary sensory networks and implies that a sensor cannot be a perfect noise filter and simultaneously be energetically efficient. A detailed analysis of a specific linear two-component network revealed a more detailed tradeoff including, amongst other things, $\eta = 1 \Rightarrow C = 0$. It remains to be seen whether this holds also for arbitrary nonlinear networks. We presented some tools in Sec. 4.6.3 that could simplify further theoretical or experimental investigations of the sensory capacity, e.g., a simple analytical estimate of the sensory capacity $\tilde{C} \equiv I_y/\overline{\mathcal{T}}_{x \rightarrow y}$ could be used.

Experiments that investigate the relation between the learning rate and the rate of dissipated energy of a sensor are still lacking. One aforementioned experiment has analyzed the learning rate (information flow) for feedback-driven engines using a single electron transistor [52] at low temperatures. Other promising experiments could involve colloidal systems in a potential. As a first example, we propose a signal to be generated by a stochastically moving laser trap, where the sensor state represents the position of a trapped colloidal particle. A second example would be a trapped colloidal particle in a two dimensional shear flow, where the shear rate couples the motion perpendicular to the shear flow with the motion parallel to the shear flow. Hence, the x-coordinate of the particle could represent the signal and the y-coordinate the sensor “trying to infer the x-coordinate”. An experimental realization of a sensor with an internal memory would be even more challenging. For example, one may think merging the previously mentioned ideas by using a fluctuating laser trap for a colloidal particle within a constant linear shear flow, which might have a dynamics of the form (4.93). For future work it will be promising to link these ideas to the thermodynamic of coarse-graining with hidden slow degrees of freedoms [97, 103], where the hidden slow degree of freedom could be interpreted as a fluctuating signal.

In chapter 5 we have investigated the information loss of a specific class of inference strategies that are based on time-averaging. For binary sensors (e.g., receptors) measuring independently a stochastic signal (e.g., ligand concentration) this information loss is bounded by 0.5 bit, irrespective of the number of sensors. As our fourth main result, we derive an expression for this information loss that depends on an asymmetry parameter α determining the load distribution of the free energy change due to the signal among the forward and backward rates of the sensor. For a symmetric influence of the signal on the sensor ($\alpha = 1/2$), this information loss vanishes, whereas for natural values, $0 \leq \alpha \leq 1$, the information loss is bounded by 0.5 bit per measurement. It is shown that this information can be regained from using the number of jump events. As an implication we identify the same information loss when using the linear noise approximation to approximate large discrete chemical networks by a continuous Brownian motion. In the latter case, the information loss arises from a simplification of the dynamics.

For future work it would be worthwhile to investigate the implications to continuously fluctuating signal as presented in chapter 4, which involve more than a single measurement. Furthermore, a systematic generalizations of the framework to sensors with more than two states measuring multiple signals [194] and the effect of non-zero affinities on

the dispersion of jump related variables [207] could be interesting.

The last subject of the thesis contains models of receptors that are driven out of equilibrium by an ATP hydrolysis reaction. It is shown that the chemical energy from the ATP hydrolysis reaction can be used to increase the sensitivity of a receptor to changes in the external ligand concentration. The increase of the sensitivity integrated over a concentration range is shown to be bounded by the chemical energy liberated by the hydrolysis of an ATP molecule. This constitutes the fifth main result of this thesis and demonstrates how energy consumption can improve sensing.

It turned out that there is a clear analogy to kinetic proofreading, where the increase of the sensitivity due to a nonequilibrium driving force is analogous to the decrease of the error in kinetic proofreading. It will be interesting to investigate other biological systems, as for example, heat shock proteins, which are known to be nonequilibrium machines that achieve ultra-affinity for their substrates [219].

Bibliography

- [1] K. Sekimoto, *Kinetic characterization of heat bath and the energetics of thermal ratchet models*, *J. Phys. Soc. Jpn.* **66**, 1234 (1997).
- [2] K. Sekimoto, *Langevin equation and thermodynamics*, *Prog. Theor. Phys. Supp.* **130**, 17 (1998).
- [3] K. Sekimoto, *Stochastic energetics*, (Springer, Berlin Heidelberg, 2010).
- [4] C. Jarzynski, *Nonequilibrium equality for free energy differences*, *Phys. Rev. Lett.* **78**, 2690 (1997).
- [5] C. Jarzynski, *Equilibrium free-energy differences from nonequilibrium measurements: a master-equation approach*, *Phys. Rev. E* **56**, 5018 (1997).
- [6] G. E. Crooks, *Entropy production fluctuation theorem and the nonequilibrium work relation for free energy differences*, *Phys. Rev. E* **60**, 2721 (1999).
- [7] G. E. Crooks, *Path-ensemble averages in systems driven far from equilibrium*, *Phys. Rev. E* **61**, 2361 (2000).
- [8] U. Seifert, *Entropy production along a stochastic trajectory and an integral fluctuation theorem*, *Phys. Rev. Lett.* **95**, 040602 (2005).
- [9] J. Liphardt, S. Dumont, S. B. Smith, I. Tinoco, and C. Bustamante, *Equilibrium information from nonequilibrium measurements in an experimental test of Jarzynski's equality*, *Science* **296**, 1832 (2002).
- [10] D. Collin, F. Ritort, C. Jarzynski, S. B. Smith, and C. Bustamante, *Verification of the Crooks fluctuation theorem and recovery of RNA folding free energies*, *Nature* **437**, 231 (2005).
- [11] S. Schuler, T. Speck, C. Tietz, J. Wrachtrup, and U. Seifert, *Experimental test of the fluctuation theorem for a driven two-level system with time-dependent rates*, *Phys. Rev. Lett.* **94**, 180602 (2005).
- [12] C. Tietz, S. Schuler, T. Speck, U. Seifert, and J. Wrachtrup, *Measurement of stochastic entropy production*, *Phys. Rev. Lett.* **97**, 050602 (2006).
- [13] G. M. Wang, E. M. Sevick, E. Mittag, D. J. Searles, and D. J. Evans, *Experimental demonstration of violations of the second law of thermodynamics for small systems and short time scales*, *Phys. Rev. Lett.* **89**, 050601 (2002).
- [14] D. M. Carberry, J. C. Reid, G. M. Wang, E. M. Sevick, D. J. Searles, and D. J. Evans, *Fluctuations and irreversibility: an experimental demonstration of a second-law-like theorem using a colloidal particle held in an optical trap*, *Phys. Rev. Lett.* **92**, 140601 (2004).

- [15] V. Blickle, T. Speck, L. Helden, U. Seifert, and C. Bechinger, *Thermodynamics of a colloidal particle in a time-dependent nonharmonic potential*, *Phys. Rev. Lett.* **96**, 070603 (2006).
- [16] O.-P. Saira, Y. Yoon, T. Tanttu, M. Möttönen, D. V. Averin, and J. P. Pekola, *Test of the Jarzynski and Crooks fluctuation relations in an electronic system*, *Phys. Rev. Lett.* **109**, 180601 (2012).
- [17] J. V. Koski, T. Sagawa, O.-P. Saira, Y. Yoon, A. Kutvonen, P. Solinas, M. Möttönen, T. Ala-Nissila, and J. P. Pekola, *Distribution of entropy production in a single-electron box*, *Nat. Phys.* **9**, 644 (2013).
- [18] U. Seifert, *Stochastic thermodynamics, fluctuation theorems and molecular machines*, *Rep. Prog. Phys.* **75**, 126001 (2012).
- [19] W. Bialek, *Biophysics: searching for principles*, (Princeton University Press, 2012).
- [20] J. J. Hopfield, *Kinetic proofreading: a new mechanism for reducing errors in biosynthetic processes requiring high specificity*, *Proc. Natl. Acad. Sci. USA* **71**, 4135 (1974).
- [21] J. Ninio, *Kinetic amplification of enzyme discrimination*, *Biochimie* **57**, 587 (1975).
- [22] R. Landauer, *Irreversibility and heat generation in the computing process*, *IBM J. Res. Dev.* **5**, 183 (1961).
- [23] A. Bérut, A. Arakelyan, A. Petrosyan, S. Ciliberto, R. Dillenschneider, and E. Lutz, *Experimental verification of Landauer's principle linking information and thermodynamics*, *Nature* **483**, 187 (2012).
- [24] Y. Jun, M. Gavrilov, and J. Bechhoefer, *High-precision test of Landauer's principle in a feedback trap*, *Phys. Rev. Lett.* **113**, 190601 (2014).
- [25] J. C. Maxwell, *Theory of heat*, (Longmans, London, 1871).
- [26] L. Szilard, *Über die Entropieverminderung in einem thermodynamischen System bei Eingriffen intelligenter Wesen*, *Z. Phys.* **53**, 840 (1929).
- [27] S. Toyabe, T. Sagawa, M. Ueda, E. Muneyuki, and M. Sano, *Experimental demonstration of information-to-energy conversion and validation of the generalized Jarzynski equality*, *Nat. Phys.* **6**, 988 (2010).
- [28] C. W. Gardiner, *Handbook of stochastic methods*, 3rd ed., (Springer, Berlin, 2004).
- [29] E. M. Purcell, *Life at low Reynolds number*, *Am. J. Phys.* **45**, 3 (1977).
- [30] D. T. Gillespie, *Exact stochastic simulation of coupled chemical reactions*, *J. Phys. Chem.* **81**, 2340 (1977).
- [31] U. Seifert, *Stochastic thermodynamics of single enzymes and molecular motors*, *Eur. Phys. J. E* **34**, 26 (2011).
- [32] C. Van den Broeck and M. Esposito, *Ensemble and trajectory thermodynamics: a brief introduction*, *Physica A* **418**, 6 (2015).
- [33] N. G. van Kampen, *Stochastic processes in physics and chemistry*, 3rd ed., (Elsevier, Amsterdam, 2007).

- [34] P. C. Bressloff, *Stochastic processes in cell biology*, (Springer International Publishing, Cham, 2014).
- [35] C. Shannon, *A mathematical theory of communication*, *Bell Syst. Tech. J.* **27**, 379 (1948).
- [36] T. M. Cover and J. A. Thomas, *Elements of information theory*, 2nd ed., (Wiley-Interscience, Hoboken, NJ, 2006).
- [37] D. J. C. MacKay, *Information theory, interference, and learning algorithms*, (Cambridge University Press, 2003).
- [38] M. Esposito and C. Van den Broeck, *Three detailed fluctuation theorems*, *Phys. Rev. Lett.* **104**, 090601 (2010).
- [39] J. Schnakenberg, *Network theory of microscopic and macroscopic behavior of master equation systems*, *Rev. Mod. Phys.* **48**, 571 (1976).
- [40] H. Qian, *Nonequilibrium steady-state circulation and heat dissipation functional*, *Phys. Rev. E* **64**, 022101 (2001).
- [41] D. Hartich, A. C. Barato, and U. Seifert, *Stochastic thermodynamics of bipartite systems: transfer entropy inequalities and a Maxwell's demon interpretation*, *J. Stat. Mech.* (2014) P02016.
- [42] C. H. Bennett, *The thermodynamics of computation—a review*, *Int. J. Theor. Phys.* **21**, 905 (1982).
- [43] H. S. Leff and A. F. Rex, eds., *Maxwell's demon 2: entropy, classical and quantum information, computing*, (IOP Publishing, Bristol, 2003).
- [44] K. Maruyama, F. Nori, and V. Vedral, *Colloquium: the physics of Maxwell's demon and information*, *Rev. Mod. Phys.* **81**, 1 (2009).
- [45] T. Sagawa, *Thermodynamics of information processing in small systems*, *Prog. Theor. Phys.* **127**, 1 (2012).
- [46] J. M. R. Parrondo, J. M. Horowitz, and T. Sagawa, *Thermodynamics of information*, *Nat. Phys.* **11**, 131 (2015).
- [47] R. Landauer, *Dissipation and noise immunity in computation and communication*, *Nature* **335**, 779 (1988).
- [48] I. L. Markov, *Limits on fundamental limits to computation*, *Nature* **512**, 147 (2014).
- [49] É. Roldán, I. A. Martínez, J. M. R. Parrondo, and D. Petrov, *Universal features in the energetics of symmetry breaking*, *Nat. Phys.* **10**, 457 (2014).
- [50] J. V. Koski, V. F. Maisi, T. Sagawa, and J. P. Pekola, *Experimental observation of the role of mutual information in the nonequilibrium dynamics of a Maxwell demon*, *Phys. Rev. Lett.* **113**, 030601 (2014).
- [51] J. V. Koski, V. F. Maisi, J. P. Pekola, and D. V. Averin, *Experimental realization of a Szilard engine with a single electron*, *Proc. Natl. Acad. Sci. USA* **111**, 13786 (2014).

- [52] J. V. Koski, A. Kutvonen, I. M. Khaymovich, T. Ala-Nissila, and J. P. Pekola, *On-chip Maxwell's demon as an information-powered refrigerator*, *Phys. Rev. Lett.* **115**, 260602 (2015).
- [53] A. Bérut, A. Petrosyan, and S. Ciliberto, *Detailed Jarzynski equality applied to a logically irreversible procedure*, *EPL* **103**, 60002 (2013).
- [54] H. Touchette and S. Lloyd, *Information-theoretic limits of control*, *Phys. Rev. Lett.* **84**, 1156 (2000).
- [55] H. Touchette and S. Lloyd, *Information-theoretic approach to the study of control systems*, *Physica A* **331**, 140 (2004).
- [56] F. J. Cao and M. Feito, *Thermodynamics of feedback controlled systems*, *Phys. Rev. E* **79**, 041118 (2009).
- [57] A. E. Allahverdyan, D. Janzing, and G. Mahler, *Thermodynamic efficiency of information and heat flow*, *J. Stat. Mech.* (2009) P09011.
- [58] M. Esposito and C. Van den Broeck, *Second law and Landauer principle far from equilibrium*, *EPL* **95**, 40004 (2011).
- [59] S. Still, D. A. Sivak, A. J. Bell, and G. E. Crooks, *Thermodynamics of prediction*, *Phys. Rev. Lett.* **109**, 120604 (2012).
- [60] T. Sagawa and M. Ueda, *Generalized Jarzynski equality under nonequilibrium feedback control*, *Phys. Rev. Lett.* **104**, 090602 (2010).
- [61] M. Ponmurugan, *Generalized detailed fluctuation theorem under nonequilibrium feedback control*, *Phys. Rev. E* **82**, 031129 (2010).
- [62] J. M. Horowitz and S. Vaikuntanathan, *Nonequilibrium detailed fluctuation theorem for repeated discrete feedback*, *Phys. Rev. E* **82**, 061120 (2010).
- [63] D. Abreu and U. Seifert, *Thermodynamics of genuine nonequilibrium states under feedback control*, *Phys. Rev. Lett.* **108**, 030601 (2012).
- [64] T. Sagawa and M. Ueda, *Fluctuation theorem with information exchange: role of correlations in stochastic thermodynamics*, *Phys. Rev. Lett.* **109**, 180602 (2012).
- [65] T. Sagawa and M. Ueda, *Nonequilibrium thermodynamics of feedback control*, *Phys. Rev. E* **85**, 021104 (2012).
- [66] A. Kundu, *Nonequilibrium fluctuation theorem for systems under discrete and continuous feedback control*, *Phys. Rev. E* **86**, 021107 (2012).
- [67] S. Ito and T. Sagawa, *Information thermodynamics on causal networks*, *Phys. Rev. Lett.* **111**, 180603 (2013).
- [68] A. C. Barato and U. Seifert, *Unifying three perspectives on information processing in stochastic thermodynamics*, *Phys. Rev. Lett.* **112**, 090601 (2014).
- [69] F. J. Cao, L. Dinis, and J. M. R. Parrondo, *Feedback control in a collective flashing ratchet*, *Phys. Rev. Lett.* **93**, 040603 (2004).
- [70] R. Dillenschneider and E. Lutz, *Memory erasure in small systems*, *Phys. Rev. Lett.* **102**, 210601 (2009).

- [71] Y. Fujitani and H. Suzuki, *Jarzynski equality modified in the linear feedback system*, *J. Phys. Soc. Jpn.* **79**, 104003 (2010).
- [72] J. M. Horowitz and J. M. R. Parrondo, *Thermodynamic reversibility in feedback processes*, *EPL* **95**, 10005 (2011).
- [73] J. M. Horowitz and J. M. R. Parrondo, *Designing optimal discrete-feedback thermodynamic engines*, *New J. Phys.* **13**, 123019 (2011).
- [74] J. M. Horowitz, T. Sagawa, and J. M. R. Parrondo, *Imitating chemical motors with optimal information motors*, *Phys. Rev. Lett.* **111**, 010602 (2013).
- [75] L. Granger and H. Kantz, *Thermodynamic cost of measurements*, *Phys. Rev. E* **84**, 061110 (2011).
- [76] D. Abreu and U. Seifert, *Extracting work from a single heat bath through feedback*, *EPL* **94**, 10001 (2011).
- [77] M. Bauer, D. Abreu, and U. Seifert, *Efficiency of a Brownian information machine*, *J. Phys. A: Math. Theor.* **45**, 162001 (2012).
- [78] T. Munakata and M. L. Rosinberg, *Entropy production and fluctuation theorems under feedback control: the molecular refrigerator model revisited*, *J. Stat. Mech.* (2012) P05010.
- [79] T. Munakata and M. L. Rosinberg, *Feedback cooling, measurement errors, and entropy production*, *J. Stat. Mech.* (2013) P06014.
- [80] M. Esposito and G. Schaller, *Stochastic thermodynamics for “Maxwell demon” feedbacks*, *EPL* **99**, 30003 (2012).
- [81] L. Granger and H. Kantz, *Differential Landauer’s principle*, *EPL* **101**, 50004 (2013).
- [82] G. Diana, G. B. Bagci, and M. Esposito, *Finite-time erasing of information stored in fermionic bits*, *Phys. Rev. E* **87**, 012111 (2013).
- [83] D. Andrieux and P. Gaspard, *Nonequilibrium generation of information in copolymerization processes*, *Proc. Natl. Acad. Sci. USA* **105**, 9516 (2008).
- [84] D. Andrieux and P. Gaspard, *Information erasure in copolymers*, *EPL* **103**, 30004 (2013).
- [85] P. Strasberg, G. Schaller, T. Brandes, and M. Esposito, *Thermodynamics of a physical model implementing a Maxwell demon*, *Phys. Rev. Lett.* **110**, 040601 (2013).
- [86] M. Bauer, A. C. Barato, and U. Seifert, *Optimized finite-time information machine*, *J. Stat. Mech.* (2014) P09010.
- [87] H. Sandberg, J.-C. Delvenne, N. J. Newton, and S. K. Mitter, *Maximum work extraction and implementation costs for nonequilibrium Maxwell’s demons*, *Phys. Rev. E* **90**, 042119 (2014).
- [88] J. M. Horowitz and H. Sandberg, *Second-law-like inequalities with information and their interpretations*, *New J. Phys.* **16**, 125007 (2014).
- [89] J. Bechhoefer, *Hidden Markov models for stochastic thermodynamics*, *New J. Phys.* **17**, 075003 (2015).

- [90] M. Esposito and J. M. R. Parrondo, *Stochastic thermodynamics of hidden pumps*, *Phys. Rev. E* **91**, 052114 (2015).
- [91] L. B. Kish and C. G. Granqvist, *Energy requirement of control: comments on Szilard's engine and Maxwell's demon*, *EPL* **98**, 68001 (2012).
- [92] A. C. Barato, D. Hartich, and U. Seifert, *Information-theoretic versus thermodynamic entropy production in autonomous sensory networks*, *Phys. Rev. E* **87**, 042104 (2013).
- [93] A. C. Barato, D. Hartich, and U. Seifert, *Rate of mutual information between coarse-grained non-Markovian variables*, *J. Stat. Phys.* **153**, 460 (2013).
- [94] P. Mehta and D. J. Schwab, *Energetic costs of cellular computation*, *Proc. Natl. Acad. Sci. USA* **109**, 17978 (2012).
- [95] G. Lan, P. Sartori, S. Neumann, V. Sourjik, and Y. Tu, *The energy-speed-accuracy trade-off in sensory adaptation*, *Nat. Phys.* **8**, 422 (2012).
- [96] J. M. Horowitz and M. Esposito, *Thermodynamics with continuous information flow*, *Phys. Rev. X* **4**, 031015 (2014).
- [97] J. Mehl, B. Lander, C. Bechinger, V. Blickle, and U. Seifert, *Role of hidden slow degrees of freedom in the fluctuation theorem*, *Phys. Rev. Lett.* **108**, 220601 (2012).
- [98] S. Rahav and C. Jarzynski, *Fluctuation relations and coarse-graining*, *J. Stat. Mech.* (2007) P09012.
- [99] S. Pigolotti and A. Vulpiani, *Coarse graining of master equations with fast and slow states*, *J. Chem. Phys.* **128** (2008).
- [100] A. Gomez-Marin, J. M. R. Parrondo, and C. Van den Broeck, *Lower bounds on dissipation upon coarse graining*, *Phys. Rev. E* **78**, 011107 (2008).
- [101] É. Roldán and J. M. R. Parrondo, *Estimating dissipation from single stationary trajectories*, *Phys. Rev. Lett.* **105**, 150607 (2010).
- [102] A. Puglisi, S. Pigolotti, L. Rondoni, and A. Vupani, *Entropy production and coarse graining in Markov processes*, *J. Stat. Mech.* (2010) P05015.
- [103] M. Esposito, *Stochastic thermodynamics under coarse graining*, *Phys. Rev. E* **85**, 041125 (2012).
- [104] B. Altaner and J. Vollmer, *Fluctuation-preserving coarse graining for biochemical systems*, *Phys. Rev. Lett.* **108**, 228101 (2012).
- [105] S. Bo and A. Celani, *Entropy production in stochastic systems with fast and slow time-scales*, *J. Stat. Phys.* **154**, 1325 (2014).
- [106] E. Zimmermann and U. Seifert, *Effective rates from thermodynamically consistent coarse-graining of models for molecular motors with probe particles*, *Phys. Rev. E* **91**, 022709 (2015).
- [107] G. Diana and M. Esposito, *Mutual entropy production in bipartite systems*, *J. Stat. Mech.* (2014) P04010.
- [108] D. Mandal and C. Jarzynski, *Work and information processing in a solvable model of Maxwell's demon*, *Proc. Natl. Acad. Sci. USA* **109**, 11641 (2012).

- [109] A. C. Barato and U. Seifert, *An autonomous and reversible Maxwell's demon*, [EPL](#) **101**, 60001 (2013).
- [110] S. Deffner and C. Jarzynski, *Information processing and the second law of thermodynamics: an inclusive, Hamiltonian approach*, [Phys. Rev. X](#) **3**, 041003 (2013).
- [111] S. Deffner, *Information-driven current in a quantum Maxwell demon*, [Phys. Rev. E](#) **88**, 062128 (2013).
- [112] A. C. Barato and U. Seifert, *Stochastic thermodynamics with information reservoirs*, [Phys. Rev. E](#) **90**, 042150 (2014).
- [113] J. Hoppenau and A. Engel, *On the energetics of information exchange*, [EPL](#) **105**, 50002 (2014).
- [114] N. Merhav, *Sequence complexity and work extraction*, [J. Stat. Mech.](#) (2015) P06037.
- [115] N. Shiraishi, T. Matsumoto, and T. Sagawa, *Measurement-feedback formalism meets information reservoirs*, [New J. Phys.](#) **18**, 013044 (2016).
- [116] A. B. Boyd, D. Mandal, and J. P. Crutchfield, *Identifying functional thermodynamics in autonomous Maxwellian ratchets*, [New J. Phys.](#) **18**, 023049 (2016).
- [117] N. Merhav, *Relations between work and entropy production for general information-driven, finite-state engines*, [ArXiv e-prints](#) (2016) arXiv:1611.01965.
- [118] D. Mandal, H. T. Quan, and C. Jarzynski, *Maxwell's refrigerator: an exactly solvable model*, [Phys. Rev. Lett.](#) **111**, 030602 (2013).
- [119] A. C. Barato, D. Hartich, and U. Seifert, *Efficiency of cellular information processing*, [New J. Phys.](#) **16**, 103024 (2014).
- [120] D. Hartich, A. C. Barato, and U. Seifert, *Sensory capacity: an information theoretical measure of the performance of a sensor*, [Phys. Rev. E](#) **93**, 022116 (2016).
- [121] T. Schreiber, *Measuring information transfer*, [Phys. Rev. Lett.](#) **85**, 461 (2000).
- [122] M. Prokopenko and J. T. Lizier, *Transfer entropy and transient limits of computation*, [Sci. Rep.](#) **4**, 5394 (2014).
- [123] M. Prokopenko and I. Einav, *Information thermodynamics of near-equilibrium computation*, [Phys. Rev. E](#) **91**, 062143 (2015).
- [124] T. D. Nielsen and F. V. Jensen, *Bayesian networks and decision graphs*, 2nd ed., (Springer-Verlag, New York, 2007).
- [125] M. E. Dumitrescu, *Some informational properties of Markov pure-jump processes*, [Časopis pro pěstování matematiky](#) **113**, 429 (1988).
- [126] C. S. Calude and M. Dumitrescu, *Entropic measures, Markov information sources and complexity*, [Appl. Math. Comput.](#) **132**, 369 (2002).
- [127] P. Jacquet, G. Seroussi, and W. Szpankowski, *On the entropy of a hidden Markov process*, [Theor. Comput. Sci.](#) **395**, 203 (2008).
- [128] T. Holliday, A. Goldsmith, and P. Glynn, *Capacity of finite state channels based on Lyapunov exponents of random matrices*, [IEEE Trans. Inf. Theory](#) **52**, 3509 (2006).

- [129] É. Roldán and J. M. R. Parrondo, *Entropy production and kullback-leibler divergence between stationary trajectories of discrete systems*, *Phys. Rev. E* **85**, 031129 (2012).
- [130] S. Ito, *Backward transfer entropy: informational measure for detecting hidden Markov models and its interpretations in thermodynamics, gambling and causality*, *Sci. Rep.* **6**, 36831 (2016).
- [131] R. E. Spinney, J. T. Lizier, and M. Prokopenko, *Transfer entropy in physical systems and the arrow of time*, *Phys. Rev. E* **94**, 022135 (2016).
- [132] G. E. Crooks and S. E. Still, *Marginal and conditional second laws of thermodynamics*, *ArXiv e-prints* (2016) arXiv:1611.04628.
- [133] S. Yamamoto, S. Ito, N. Shiraishi, and T. Sagawa, *Linear irreversible thermodynamics and Onsager reciprocity for information-driven engines*, *Phys. Rev. E* **94**, 052121 (2016).
- [134] J. M. Horowitz, *Multipartite information flow for multiple Maxwell demons*, *J. Stat. Mech.* (2015) P03006.
- [135] N. Shiraishi and T. Sagawa, *Fluctuation theorem for partially masked nonequilibrium dynamics*, *Phys. Rev. E* **91**, 012130 (2015).
- [136] N. Shiraishi, S. Ito, K. Kawaguchi, and T. Sagawa, *Role of measurement-feedback separation in autonomous Maxwell's demons*, *New J. Phys.* **17**, 045012 (2015).
- [137] J. Fuchs, S. Goldt, and U. Seifert, *Stochastic thermodynamics of resetting*, *EPL* **113**, 60009 (2016).
- [138] M. L. Rosinberg, T. Munakata, and G. Tarjus, *Stochastic thermodynamics of Langevin systems under time-delayed feedback control: second-law-like inequalities*, *Phys. Rev. E* **91**, 042114 (2015).
- [139] T. Brandes, *Feedback between interacting transport channels*, *Phys. Rev. E* **91**, 052149 (2015).
- [140] C. Cafaro, S. A. Ali, and A. Giffin, *Thermodynamic aspects of information transfer in complex dynamical systems*, *Phys. Rev. E* **93**, 022114 (2016).
- [141] P. H. Algoet and T. M. Cover, *A sandwich proof of the Shannon-McMillan-Breiman theorem*, *Ann. Prob.* **16**, 899 (1988).
- [142] A. Crisanti, G. Paladin, and A. Vulpiani, *Products of random matrices*, (Springer-Verlag, Berlin, 1993).
- [143] H. C. Berg and E. M. Purcell, *Physics of chemoreception*, *Biophys. J.* **20**, 193 (1977).
- [144] G. De Palo and R. G. Endres, *Unraveling adaptation in eukaryotic pathways: lessons from protocells*, *PLoS Comput. Biol.* **9**, e1003300 (2013).
- [145] Y. Tu, *The nonequilibrium mechanism for ultrasensitivity in a biological switch: sensing by Maxwell's demons*, *Proc. Natl. Acad. Sci. USA* **105**, 11737 (2008).
- [146] H. Qian and T. C. Reluga, *Nonequilibrium thermodynamics and nonlinear kinetics in a cellular signaling switch*, *Phys. Rev. Lett.* **94**, 028101 (2005).

- [147] H. Qian, *Phosphorylation energy hypothesis: open chemical systems and their biological functions*, *Ann. Rev. Phys. Chem.* **58**, 113 (2007).
- [148] M. Skoge, S. Naqvi, Y. Meir, and N. S. Wingreen, *Chemical sensing by nonequilibrium cooperative receptors*, *Phys. Rev. Lett.* **110**, 248102 (2013).
- [149] A. H. Lang, C. K. Fisher, T. Mora, and P. Mehta, *Thermodynamics of statistical inference by cells*, *Phys. Rev. Lett.* **113**, 148103 (2014).
- [150] C. C. Govern and P. R. ten Wolde, *Optimal resource allocation in cellular sensing systems*, *Proc. Natl. Acad. Sci. USA* **111**, 17486 (2014).
- [151] C. C. Govern and P. R. ten Wolde, *Energy dissipation and noise correlations in biochemical sensing*, *Phys. Rev. Lett.* **113**, 258102 (2014).
- [152] N. B. Becker, A. Mugler, and P. R. ten Wolde, *Optimal prediction by cellular signaling networks*, *Phys. Rev. Lett.* **115**, 258103 (2015).
- [153] P. R. ten Wolde, N. B. Becker, T. E. Ouldridge, and A. Mugler, *Fundamental limits to cellular sensing*, *J. Stat. Phys.* **162**, 1395 (2016).
- [154] H. Qian, *Reducing intrinsic biochemical noise in cells and its thermodynamic limit*, *J. Mol. Biol.* **362**, 387 (2006).
- [155] H. Qian, *Cooperativity and specificity in enzyme kinetics: a single-molecule time-based perspective*, *Biophys. J.* **95**, 10 (2008).
- [156] A. Murugan, D. A. Huse, and S. Leibler, *Speed, dissipation, and error in kinetic proofreading*, *Proc. Natl. Acad. Sci. USA* **109**, 12034 (2012).
- [157] A. Murugan, D. A. Huse, and S. Leibler, *Discriminatory proofreading regimes in nonequilibrium systems*, *Phys. Rev. X* **4**, 021016 (2014).
- [158] P. Sartori and S. Pigolotti, *Kinetic versus energetic discrimination in biological copying*, *Phys. Rev. Lett.* **110**, 188101 (2013).
- [159] R. Rao and L. Peliti, *Thermodynamics of accuracy in kinetic proofreading: dissipation and efficiency trade-offs*, *J. Stat. Mech.* (2015) P06001.
- [160] P. Gaspard, *Template-directed copolymerization, random walks along disordered tracks, and fractals*, *Phys. Rev. Lett.* **117**, 238101 (2016).
- [161] P. Gaspard, *Kinetics and thermodynamics of DNA polymerases with exonuclease proofreading*, *Phys. Rev. E* **93**, 042420 (2016).
- [162] C. H. Bennett, *Dissipation-error tradeoff in proofreading*, *BioSystems* **11**, 85 (1979).
- [163] M. Ehrenberg and C. Blomberg, *Thermodynamic constraints on kinetic proofreading in biosynthetic pathways*, *Biophys. J.* **31**, 333 (1980).
- [164] N. Barkai and S. Leibler, *Robustness in simple biochemical networks*, *Nature* **387**, 913 (1997).
- [165] U. Alon, M. G. Surette, N. Barkai, and S. Leibler, *Robustness in bacterial chemotaxis*, *Nature* **397**, 168 (1999).

- [166] J. E. Keymer, R. G. Endres, M. Skoge, Y. Meir, and N. S. Wingreen, *Chemosensing in Escherichia coli: two regimes of two-state receptors*, *Proc. Natl. Acad. Sci. USA* **103**, 1786 (2006).
- [167] Y. Tu, T. S. Shimizu, and H. C. Berg, *Modeling the chemotactic response of Escherichia coli to time-varying stimuli*, *Proc. Natl. Acad. Sci. USA* **105**, 14855 (2008).
- [168] V. Sourjik and N. S. Wingreen, *Responding to chemical gradients: bacterial chemotaxis*, *Curr. Opin. Cell Biol.* **24**, 262 (2012).
- [169] G. Aquino, L. Tweedy, D. Heinrich, and R. G. Endres, *Memory improves precision of cell sensing in fluctuating environments*, *Sci. Rep.* **4**, 5688 (2014).
- [170] S. Bo, M. Del Giudice, and A. Celani, *Thermodynamic limits to information harvesting by sensory systems*, *J. Stat. Mech.* (2015) P01014.
- [171] H. C. Berg and D. A. Brown, *Chemotaxis in Escherichia coli analysed by three-dimensional tracking*, *Nature* **239**, 500 (1972).
- [172] J. Monod, J. Wyman, and J.-P. Changeux, *On the nature of allosteric transitions: a plausible model*, *J. Mol. Biol.* **12**, 88 (1965).
- [173] S. Marzen, H. G. Garcia, and R. Phillips, *Statistical mechanics of Monod-Wyman-Changeux (MWC) models*, *J. Mol. Biol.* **425**, 1433 (2013).
- [174] C. Van den Broeck, *Thermodynamic efficiency at maximum power*, *Phys. Rev. Lett.* **95**, 190602 (2005).
- [175] U. Seifert, *Efficiency of autonomous soft nanomachines at maximum power*, *Phys. Rev. Lett.* **106**, 020601 (2011).
- [176] B. A. Mello and Y. Tu, *Effects of adaptation in maintaining high sensitivity over a wide range of backgrounds for Escherichia coli chemotaxis*, *Biophys. J.* **92**, 2329 (2007).
- [177] D. Hartich, A. C. Barato, and U. Seifert, *Nonequilibrium sensing and its analogy to kinetic proofreading*, *New J. Phys.* **17**, 055026 (2015).
- [178] G. Lan and Y. Tu, *Information processing in bacteria: memory, computation, and statistical physics: a key issues review*, *Rep. Prog. Phys.* **79**, 052601 (2016).
- [179] D. A. Clark and L. C. Grant, *The bacterial chemotactic response reflects a compromise between transient and steady-state behavior*, *Proc. Natl. Acad. Sci. USA* **102**, 9150 (2005).
- [180] A. Celani and M. Vergassola, *Bacterial strategies for chemotaxis response*, *Proc. Natl. Acad. Sci. USA* **107**, 1391 (2010).
- [181] P. Sartori, L. Granger, C. F. Lee, and J. M. Horowitz, *Thermodynamic costs of information processing in sensory adaptation*, *PLoS Comput. Biol.* **10**, e1003974 (2014).
- [182] S. Ito and T. Sagawa, *Maxwell's demon in biochemical signal transduction with feedback loop*, *Nat. Commun.* **6**, 7498 (2015).

- [183] P. Sartori and Y. Tu, *Noise filtering strategies in adaptive biochemical signaling networks*, *J. Stat. Phys.* **142**, 1206 (2011).
- [184] M. Hinczewski and D. Thirumalai, *Noise control in gene regulatory networks with negative feedback*, *J. Phys. Chem. B* **120**, 6166 (2016).
- [185] B. Øksendal, *Stochastic differential equations*, (Springer, Berlin Heidelberg, 2003).
- [186] J. Bechhoefer, *Feedback for physicists: a tutorial essay on control*, *Rev. Mod. Phys.* **77**, 783 (2005).
- [187] K. Brandner, K. Saito, and U. Seifert, *Thermodynamics of micro- and nano-systems driven by periodic temperature variations*, *Phys. Rev. X* **5**, 031019 (2015).
- [188] M. Bauer, K. Brandner, and U. Seifert, *Optimal performance of periodically driven, stochastic heat engines under limited control*, *Phys. Rev. E* **93**, 042112 (2016).
- [189] R. W. Cottle, *Manifestations of the Schur complement*, *Linear Algebra Appl.* **8**, 189 (1974).
- [190] D. Hartich and U. Seifert, *Optimal inference strategies and their implications for the linear noise approximation*, *Phys. Rev. E* **94**, 042416 (2016).
- [191] R. G. Endres and N. S. Wingreen, *Maximum likelihood and the single receptor*, *Phys. Rev. Lett.* **103**, 158101 (2009).
- [192] T. Mora and N. S. Wingreen, *Limits of sensing temporal concentration changes by single cells*, *Phys. Rev. Lett.* **104**, 248101 (2010).
- [193] B. Hu, W. Chen, W.-J. Rappel, and H. Levine, *Physical limits on cellular sensing of spatial gradients*, *Phys. Rev. Lett.* **105**, 048104 (2010).
- [194] T. Mora, *Physical limit to concentration sensing amid spurious ligands*, *Phys. Rev. Lett.* **115**, 038102 (2015).
- [195] G. Aquino, N. S. Wingreen, and R. G. Endres, *Know the single-receptor sensing limit? Think again*, *J. Stat. Phys.* **162**, 1353 (2016).
- [196] C. C. Govern and P. R. ten Wolde, *Fundamental limits on sensing chemical concentrations with linear biochemical networks*, *Phys. Rev. Lett.* **109**, 218103 (2012).
- [197] P. Mehta, A. H. Lang, and D. J. Schwab, *Landauer in the age of synthetic biology: energy consumption and information processing in biochemical networks*, *J. Stat. Phys.* **162**, 1153 (2016).
- [198] A. C. Barato and U. Seifert, *Dispersion for two classes of random variables: general theory and application to inference of an external ligand concentration by a cell*, *Phys. Rev. E* **92**, 032127 (2015).
- [199] S. Goldt and U. Seifert, *Stochastic thermodynamics of learning*, *Phys. Rev. Lett.* **118**, 010601 (2017).
- [200] J. Elf and M. Ehrenberg, *Fast evaluation of fluctuations in biochemical networks with the linear noise approximation*, *Genome Res.* **13**, 2475 (2003).
- [201] G. Tkačik and A. M. Walczak, *Information transmission in genetic regulatory networks: a review*, *J. Phys.: Condens. Matter* **23**, 153102 (2011).

- [202] J. M. Horowitz, *Diffusion approximations to the chemical master equation only have a consistent stochastic thermodynamics at chemical equilibrium*, *J. Chem. Phys.* **143**, 044111 (2015).
- [203] Z. Koza, *General technique of calculating the drift velocity and diffusion coefficient in arbitrary periodic systems*, *J. Phys. A: Math. Gen.* **32**, 7637 (1999).
- [204] A. Wachtel, J. Vollmer, and B. Altaner, *Fluctuating currents in stochastic thermodynamics. I. Gauge invariance of asymptotic statistics*, *Phys. Rev. E* **92**, 042132 (2015).
- [205] M. Polettini, A. Wachtel, and M. Esposito, *Dissipation in noisy chemical networks: the role of deficiency*, *J. Chem. Phys.* **143**, 184103 (2015).
- [206] R. Rao and M. Esposito, *Nonequilibrium thermodynamics of chemical reaction networks: wisdom from stochastic thermodynamics*, *Phys. Rev. X* **6**, 041064 (2016).
- [207] A. C. Barato and U. Seifert, *Thermodynamic uncertainty relation for biomolecular processes*, *Phys. Rev. Lett.* **114**, 158101 (2015).
- [208] A. C. Barato and U. Seifert, *Universal bound on the Fano factor in enzyme kinetics*, *J. Phys. Chem. B* **119**, 6555 (2015).
- [209] P. Pietzonka, A. C. Barato, and U. Seifert, *Universal bounds on current fluctuations*, *Phys. Rev. E* **93**, 052145 (2016).
- [210] P. Pietzonka, A. C. Barato, and U. Seifert, *Affinity- and topology-dependent bound on current fluctuations*, *J. Phys. A: Math. Theor.* **49**, 34LT01 (2016).
- [211] T. R. Gingrich, J. M. Horowitz, N. Perunov, and J. L. England, *Dissipation bounds all steady-state current fluctuations*, *Phys. Rev. Lett.* **116**, 120601 (2016).
- [212] M. Polettini, A. Lazarescu, and M. Esposito, *Tightening the uncertainty principle for stochastic currents*, *Phys. Rev. E* **94**, 052104 (2016).
- [213] S. Singh, J. T. Peltonen, I. M. Khaymovich, J. V. Koski, C. Flindt, and J. P. Pekola, *Distribution of current fluctuations in a bistable conductor*, *Phys. Rev. B* **94**, 241407(R) (2016).
- [214] H. C. Berg, *E. coli in motion*, (Springer, New York, 2004).
- [215] Y. Tu, *Quantitative modeling of bacterial chemotaxis: signal amplification and accurate adaptation*, *Ann. Rev. Biophys.* **42**, 337 (2013).
- [216] D. Clausznitzer, G. Micali, S. Neumann, V. Sourjik, and R. G. Endres, *Predicting chemical environments of bacteria from receptor signaling*, *PLoS Comput. Biol.* **10**, e1003870 (2014).
- [217] H. Qian, *Cyclic conformational modification of an enzyme: serial engagement, energy relay, hysteretic enzyme, and Fischer's hypothesis*, *J. Phys. Chem. B* **114**, 16105 (2010).
- [218] T. L. Hill, *Free energy transduction and biochemical cycle kinetics*, (Dover Publications, Mineola, New York, 2005).
- [219] P. De Los Rios and A. Barducci, *Hsp70 chaperones are non-equilibrium machines that achieve ultra-affinity by energy consumption*, *eLife* **3**, e02218 (2014).

Danksagung (Acknowledgement)

Allen voran möchte ich mich bei meinem Hauptgutachter **Professor Dr. Udo Seifert** für die hilfreichen Ratschläge, das Interesse an meiner Arbeit, das stetige Vertrauen und die dadurch entstandenen Freiheiten bedanken. **Professor Dr. Siegfried Dietrich** danke ich für die schnelle Übernahme des Mitberichts und ein angenehmes Gespräch. Weiterer Dank geht an **Professor Dr. Massimiliano Esposito** für das Anfertigen des externen Gutachtens. Für eine erfolgreiche Zusammenarbeit, aus der ein Großteil der hier präsentierten Ergebnisse entstand, danke ich **Dr. Andre C. Barato**. Bei unserer Sekretärin **Frau Anja Steinhauser** möchte ich mich für die unermüdliche Unterstützung hinsichtlich Organisation sowie den reibungslosen Ablauf bedanken.

Besonderer Dank geht an **Sebastian Goldt**, vor allem für das inhaltliche und sprachliche Korrekturlesen meiner Arbeit sowie die zahlreichen interessanten Gespräche und Tipps.

Außerdem möchte ich mich bei den außerordentlich motivierten Studierenden bedanken, die ich während meiner Promotion bei ihren erfolgreichen Abschlussarbeiten begleiten durfte. Darunter sind die Masterarbeiten von **Andreas Marsing**, **Basile Nguyen**, **Michael Schmid** und **Michael Oechsle** sowie die Bachelorarbeiten von **Jorge Manuel Sánchez** und **Andreas Ehrmann** zu nennen, die es mir ermöglichten, neue Einblicke in andere Themen zu erhalten. Vielen Dank für die Erfahrung, die ich mit euch sammeln durfte!

Vielen Dank auch an **Michael Bauer** und **Robert Wulfert** für Ratschläge und Einblicke (auch abseits der Physik). Für die fachlichen Exkurse (besonders auf der STAT-PHYS26 in Lyon) danke ich **Patrick Pietzonka**. Darüber hinaus möchte ich mich bei allen DoBaMa's und Ehemaligen für die unterhaltsamen Mittags- bzw. Kaffeepausen bedanken.

Meinen Großeltern **Marie Luise Stark** und **Egon Stark** danke ich für das große Interesse an meiner Arbeit sowie die Unterstützung auch schon während des Studiums. Für die Unterstützung in allen Lebenslagen geht mein herzlicher Dank an meine Frau **Patrizia Hartich**: ohne dich wäre so manches Hindernis viel größer gewesen.

Ehrenwörtliche Erklärung

Ich erkläre, dass ich diese Arbeit selbständig verfasst und keine anderen als die angegebenen Quellen und Hilfsmittel verwendet habe.

Stuttgart, den 23.01.2017

David Hartich